Title
Stress-Induced Dynamic Interactions in Bacteria: from Individuals to Communities

Author
Lee, Dong-yeon

Publication Date
2018

UNIVERSITY OF CALIFORNIA SAN DIEGO

Stress-Induced Dynamic Interactions in Bacteria: from Individuals to Communities

A dissertation submitted in partial satisfaction of the
requirements for the degree Doctor of Philosophy

in

Biology

by

Dong-yeon Lee

Committee in charge:

Professor Gürol M. Süel, Chair
Professor Terence Hwa
Professor Kit Pogliano
Professor Massimo Vergassola
Professor Roy Wollman

2018

The Dissertation of Dong-yeon Lee is approved, and it is acceptable in quality and form for publication on microfilm and electronically:

Chair

University of California San Diego

2018

TABLE OF CONTENTS

LIST OF FIGURES

LIST OF TABLES

ACKNOWLEDGMENTS

First and foremost, I would like to thank God, who strengthened me at all the time and provided everything I needed along the journey. Life as a graduate student was not easy and things didn’t go as I wanted, but it was a great chapter of my life that I’ve learned so much from amazing people and I’ve supported by beautiful hearts.

I would like to express the deepest appreciation to my mentor, Gürol M. Süel. Without his guidance and support in every aspect, I wouldn’t be able to go through all the tough times and grow this much. He has been always there providing invaluable insights, encouragements, and teaching me how to become a better scientist. I could not ask for a better teacher. I would like to also appreciate my committee members; Terence Hwa, Kit Pogliano, Roy Wollman, and Massimo Vergassola for their sincere advice and support. Committee meetings were always helpful and enjoyable.

I feel very grateful for being a member of Süel lab. I learned so much from every single person, both current and former lab members. They have been a great role model, a guide, and a supporter not only academically but also for my whole life during my graduate school. I wouldn’t forget our countless discussions and laughs on everything. I am honored to be a part of great collaborative work described in almost every chapter of my thesis. Thank for all the authors. I would like to express a special thanks to my long collaborator, Letícia Galera-Laporta, who has been dedicated so many extra hours with enthusiasm, fueled me when I was exhausted, and being a great friend and supporter at all time. I am very lucky to be able to grow together with her and the members of the Süel lab.

Thank you to everyone that gave me a support like the one from family members throughout each step of graduate school. Someone once asked me how I could live alone so well in this foreign country. My simple answer was “I am not alone here”. My family and old friends are not here, but I’ve been with great individuals inside and outside of the lab and two schools I’ve been in. Amazing housemates, journal club members, POSTECH alumni, and church families to name a few.

Most importantly, I would like to thank my family for their unconditional love and support. This would not have been possible without them.

Chapter 2 and Appendix A, in full, contain materials being prepared for publication. Dong-yeon D. Lee, Liyang Xiong, San Ly, Lev Tsimring and Gürol M Süel. The dissertation author was the primary investigator and author of the material contains the chapter.

Chapter 3 and Appendix B, in full, are a reprint of the material Jintao Liu, Arthur Prindle*, Jacqueline Humphries*, Marçal Gabalda-Sagarra*, Munehiro Asally*, Dong-yeon D. Lee, San Ly, Jordi Garcia-Ojalvo, and Gürol M. Süel. “Metabolic co-dependence gives rise to collective oscillations within biofilms“ *Nature* vol. 523, 550–554. 2015 (*equal contribution). The dissertation author participated in discussions, some of the experimental designs, and strain constructions.

Chapter 4 and Appendix C, in full, are a reprint of the material Jintao Liu, Rosa Martinez-Corral*, Arthur Prindle*, Dong-yeon D. Lee, Joseph Larkin, Marçal Gabalda-Sagarra, Jordi Garcia-Ojalvo, and Gürol M. Süel. “Coupling between distant biofilms and emergence of nutrient time-sharing“ *Science*, vol. 356, Issue 6338, 638-642. 2017 (*equal contribution). The dissertation author participated in discussions, strain constructions, experiments for supplementary materials, and reviewer responses.

Chapter 5 and Appendix D, in full, are a reprint of the material Jatin Narula*, Anna Kuchina*, Dong-yeon D. Lee, Masaya Fujita, Gürol M. Süel, Oleg A. Igoshin. “Chromosomal Arrangement of Phosphorelay GenesCouples Sporulation and DNA Replication“ Cell 162, 328–337. 2015 (*equal contribution). The dissertation author performed experiments regarding translocated *kinA* strains, which were used in Figure 5.4, 5.5, and 5.8.

Chapter 6, in full, is currently being prepared for submission for publication of the material. Dong-yeon D. Lee, Leticia Galera-Laporta, Maja Bialecka-Fornal, Eun Chae Moon, Jordi Garcia-Ojalvo, and Gürol M. Süel. The dissertation author is shared primary author of this paper with Leticia Galera-Laporta.

VITA

2010	B. S. in Biological Sciences, Pohang University of Science and Technology, South Korea.
2012 – 2018	Research Assistant, University of California San Diego
2013 – 2015	Teaching Assistant, University of California San Diego
2018	Ph. D. in Biology, University of California San Diego

PUBLICATIONS

1. **Lee D.D.**, Prindle A., Liu J, and Süel G.M. Snapshot: Electrical Communication in Biofilms. *Cell*, 2017; Volume 170, Issue 1, 214-214

2. Liu J., Martinez-Corral R., Prindle A., **Lee D.D.**, Larkin J., Gabalda-Sagarra M., Garcia-Ojalvo J. and Süel G.M. Coupling between distant biofilms and emergence of nutrient time-sharing. *Science*, 2017; Volume 356, Issue 6338, 638-642

3. Narula J.*, Kuchina A.*, **Lee D.D.,** Fujita M., Süel G.M., and Igoshin O.A. Chromosomal arrangement of phosphorelay genes couples sporulation and DNA replication. *Cell*, 2015; Volume 162, Issue 2, 328-337

4. Liu J., Prindle A.*, Humphries J.*, Gabalda-Sagarra M.*, Asally M.*, **Lee D.D.**, Ly S., Garcia-Ojalvo J., and Süel G.M. Metabolic co-dependence gives rise to collective oscillations within biofilms. *Nature*. 2015; 523(7562)

ABSTRACT OF THE DISSERTATION

Stress-Induced Dynamic Interactions in Bacteria: from Individuals to Communities

by

Dong-yeon Lee

Doctor of Philosophy in Biology

University of California San Diego, 2018

Professor Gürol Mehmet Süel, Chair

Bacteria often encounter stress conditions, where cells need to address conflicting demands. For instance, a bacterium may need to save resources and use energy to defend simultaneously. Moreover, many, if not all, cellular processes are dynamic: oscillatory behaviors, like cell cycle regulators, or transient pulses, like neuronal activities, are much common than one may expect. How can a cell coordinate multiple and dynamic cellular processes to establish a right response? This dissertation thesis attempts to account these questions focusing on its dynamic characteristics. It mainly consists of two parts: studies in communities, namely biofilms (Chapters 2-4), and in individual cells (Chapters 5-6).

In the first part, three examples of how *Bacillus subtilis* biofilm cells deal with conflicting demands are considered. Utilizing time-lapse imaging techniques, we dissected coupling mechanisms under nitrogen stress. For instance, biofilm cells couple nitrogen metabolism among neighbors, which could account for an unexpected emerging pattern across more than 100 times of a cell-length scale (Chapter 2). Based on this insight, we could also explain the oscillatory growth of 2D biofilm in a microfluidic device: metabolic codependence between interior and exterior cells of a biofilm results in the oscillatory growth. It is noteworthy that biofilms exerting this behavior are more resistant to external attacks (Chapter 3). The discovery was then expanded to understand multiple biofilm cases. We found that nearby biofilms coordinate their growth and nitrogen consumption dynamics, which enhances overall growth (Chapter 4).

In the second part, two studies are presented as examples of how dynamic processes are coordinated at the single-cell level. By investigating *B. subtilis* sporulation, we demonstrated that chromosomal arrangement of two key regulators ensures the coordination between a cell cycle and a cellular differentiation under starvation (Chapter 5). We could also show that two of the most ancient and fundamental properties of a cell, ribosomes and membrane potential, are coupled through magnesium ions under ribosome-perturbing stresses (Chapter 6). Taken together, these examples emphasize an interesting concept that can be applied across multiple scales: cells can coordinate their cellular processes not through a specific master regulator, but through the dynamic characteristics of the interactions.

I

INTRODUCTION

1 Introduction

1.1 Dynamics, heterogeneity, and time-lapse microscopy

"… Blessed are those who believe without seeing." John 20:29 (partial)

This famous bible phrase, in fact, implies that it is much easier to believe or know something if one sees it. In that sense, advancement of microscopy has been played a vital role in modern biology, especially in cell biology and microbiology. It is little controversial but generally accepted that the first person described bacteria with a microscope is Antonie van Leeuwenhoek, using his own home-made microscope in 1676 (Lane 2015). Surprisingly, it took over 150 years of optical development to reproduce the same quality of images with a practical binocular microscope around 1850 (Riddell 1854). It took a rapid growth from then, and soon people started to take pictures through a microscope instead of hand-drawing the specimen. One step further, people began to take time-lapse images, I mean films, with a microscope in the early 1900's. It is interesting that the motivation of one of the first filmmakers, Julius Ries, was that he thought students would never believe the cell theory unless they saw the live motion of cell division with their own eyes (Landecker 2009). Nowadays, time-lapse microscopy is one of the indispensable tools to describe dynamic biological systems.

Are some scientists just enticed by beautiful images/movies generated with multiple fluorescent reporters through microscopy? Many scientists, including me, would not be able to deny that we are fascinated by amazingly artistic images of cells, but more importantly, we are thrilled by biological questions that time-lapse microscopy can uniquely answer;

dynamics and heterogeneity. All living systems need to cope with the ever-changing environment. Then, logically thinking, it seems obvious that cells would use the dynamic characteristics of the environment and their own regulations. However, we only begin to appreciate the importance of such aspects in a living system. For instance, Long Cai and his colleges (2008) demonstrated that calcium concentration modulates the frequency of nuclear localization of a transcription factor Crz1, which coordinates gene regulation in yeast (Cai, Dalal, and Elowitz 2008). Also, Gürol Süel and his colleges (2006) elegantly illustrated that certain gene regulatory circuits can exhibit excitable dynamics driven by noise. As a consequence, stochastic and transient cellular differentiation can be induced for only small percent of cells in an isogenic bacterial population under stress (Süel et al. 2006). It is important to point out that these studies look at the system in an operational point of view instead of static interactions of molecules in a pathway.

How can a highly dynamic and heterogeneous system operate faithfully for itself and together with its neighbors? How can it coordinate responses to multiple and sometimes confusing environmental cues? It is clear that coordination of cellular processes is essential for proper adjustment, especially under stress. For example, a cell may find itself in a trouble if it only slows down its genomic replication but not cell division during starvation. I am fascinated by how cells and cellular processes are dynamically coupled to each other to coordinate themselves under stress. This dissertation thesis is meant to provide six independent, but interconnected examples of spatial and temporal coordination under stress. These dynamic processes were studied using *Bacillus subtilis* both in a community and at a single-cell level. Before proceeding to each chapter, I would like to introduce the model system, *B. subtilis* in its community and single cell forms, and basic techniques used throughout the studies, and provide a general overview of the chapters.

1.2 Model systems

1.2.1 *Bacillus subtilis* as a model organism for multi-scale studies.

Bacillus subtilis, one of the first described bacteria, has been the most popular model organism for gram-positive bacteria. This rod-shaped bacterium, which found in soils and human guts, has several characteristics as a good model organism. First of all, it is genetically amenable. It can naturally differentiate into a genetic competence state, which takes up extracellular DNA from surrounding medium (Dubnau 1991). Secondly, the whole genome sequence is available. Also, the Bacillus Genetic Stock Center (BGSC) provides various mutants of the laboratory strain 168. Lastly, various cell types and basic gene circuits necessary for the cell types are already known in *B. subtilis*. Indeed, the spoluration and biofilm formation of *B. subtilis* were already described in 1877 by Ferdinand Cohn (Vlamakis et al. 2013). The vast amount of knowledge of *B. subtilis* becomes a solid ground to ask complex questions.

Under stress condition, this simple bacteria can take many options. Most well-known options are forming a biofilm and becoming a spore. There are many other differentiated cell types under stress; competent cells, swarming cells, and matrix-producing cells, to name a few. A biofilm, a community form of lifestyle that many bacteria encapsulated by the self-produced matrix, can shelter all these types of cells (López and Kolter 2010). Therefore, *B. subtilis* is the best model organism for this study because 1) it is a well-known and simple bacteria, 2) it needs to coordinate the gene expression to differentiate into a right cell type as like the stem cells, and 3) it also encounters coordination problems with neighboring cells to successfully develop into a biofilm as like the case of multicellular organisms.

1.2.2 Bacterial Biofilms

A biofilm is a community of microorganisms, which are encased in an extracellular matrix (Fig. 1.1). Most bacteria reside in a biofilm associated with any natural and artificial surfaces (J. William Costerton et al. 1987). It has been widely studied in the past few decades because it is a simple model for a multicellular development as well as tightly connected to industrial and general health problems (Hall-Stoodley, Costerton, and Stoodley 2004; Bryers 2008; Morikawa 2006). A biofilm developmental process is generally classified into four distinct steps: initial attachment, growth and differentiation, maturation and sporulation, and biofilm dispersal (Stoodley et al. 2002). It has been also known that biofilms are not a mere collection of cells in a matrix but the structurally organized community. Hera Vlamakis and her colleagues (2008) claimed that the formation of a structured biofilm itself governs cellular differentiation inside of a *B. subtilis* biofilm (Vlamakis et al. 2008). Using fixed biofilms at various time points, they showed that motile, matrix-producing, and sporulating cells are localized distinct places and this organization is dynamic. However, it is still unclear what can drive the organization of different cell types in a biofilm.

It is interesting that the genetic signaling pathways required for differentiation is more or less known at the single cell level, yet it has not been placed into the context of a biofilm development. How does a single cell recognizes where it is located in a biofilm and behave accordingly? How does a biofilm ensure the proportion of certain cell types in a heterogeneous population? The most probable hypothesis would be that cells use the fact that they may experience different metabolic needs based on the location. Metabolic organization inside of a biofilm has been suggested and some of the properties have been measured, yet there are very scarce data corresponding to the cell differentiation pattern over time (Stewart and Franklin 2008; Freilich et al. 2011; Dietrich et al. 2013; Cole et al. 2015).

Besides its beauty as a simple developmental model, a biofilm itself significantly affects human lives (Hall-Stoodley, Costerton, and Stoodley 2004; Bryers 2008; Parsek and Singh 2003). It is important to study biofilms specifically because bacteria in a biofilm show quite different physiology compared to its free-living form. For instance, biofilms are very resilient to a shear stress (Persat et al. 2015). Dental plaques or clogged industrial pipes are good examples. Moreover, it can show 1000 times higher resistance to antibiotic stress (Nickel et al. 1985; Gristina et al. 1987), which poses serious problems in public health. The negative aspects of biofilms result in extensive researches on how to eradicate them. Yet, how bacteria in biofilms react to the stress individually and collectively is largely unknown.

Recent studies of gut microbiome bring the light into the importance of the biofilm physiology itself. It becomes clear that bacterial biofilms in our guts are organized in space and time and continuously influence its host, us (Cong et al. 2016; Ferraris, Choe, and Patel 2018; Z. Wang and Zhao 2018). For example, bacterial metabolism can affect host metabolism by breaking down non-digestible substances into digestible pieces or consuming them. It would be great if one can magically monitor every interaction altogether, but researchers even fail to grow more than half of the gut microbiome in pure culture (Browne et al. 2016). Fortunately, fundamental principles of the interactions could be captured in a single species biofilm. Even in a single species biofilm, differentiated cells in different regions would create diverse interactions among them (Hense et al. 2012). Understanding the interaction between cells in a community or in neighboring communities could give us new insights into the general communication methods between bacteria and host cells.

1.3 General experimental procedures

1.3.1 Strain constructions

Except for the chapter 5 that used *Bacillus subtilis* PY79 strains, all other experiments were done with wild-type *B. subtilis* NCIB 3610 strain. *B. subtilis* PY79 is often referred to as a domesticated or lab strain, which does not form a biofilm and is much easier to manipulate its genome. The wild-type strain was a gift from Wade Winkler (University of Maryland). Regardless of the parental strain, all mutants were constructed in the same way – construct a vector to target a desired genomic change and transform it into a parental strain. I would like to introduce the common method here and provide individual information, such as promoter or primer names, in each chapter.

The original vectors used in the studies are as follows: ECE174, integrating into the *sacA* locus (constructed by R. Middleton and obtained from the Bacillus Genetic Stock Center); pLD30 designed to integrate into the *amyE* locus (kind gift from Jonathan Dworkin, Columbia University); ECE173, designed to integrate into the *gltA* locus (Middleton and

Hofmeister 2004)(constructed by R. Middleton and obtained from the Bacillus Genetic Stock Center); per449, a generic integration vector constructed for integration into the gene of interest (kind gift from Wade Winkler, UT Southwestern); and the bi-functional cloning plasmid pHP13 carrying the replication origin of the cryptic *B. subtilis* plasmid pTA1060 (5 copies per genome) (Haima, Bron, and Venema 1987). These vectors are shuttle vectors that can be amplified in *Escherichia coli*, and thus all molecular clonings were performed in *E. coli* for convenience. Cloned vectors with desired change were confirmed by direct sequencing and then integrated into the chromosome of the wild-type strain by a standard one-step transformation procedure (Jarmer et al. 2002). Finally, chromosomal integrations were confirmed by colony PCR using the corresponding primers.

1.3.2 Growth conditions

B. subtilis strains were grown in LB culture or on LB agar plates at 37 °C. When appropriate, antibiotics were supplemented in LB at the following final concentrations: 5 μg/ml chloramphenicol, 300 μg/ml spectinomycin (100 μg/ml for PY79), or 9 μg/ml neomycin (5 μg/ml for PY79), 5 μg/ml erythromycin, and 5 μg/ml phleomycin. Except for Chapter 5, a single colony of desired strain was picked from overnight grown on LB plate and cultured in LB at 37 °C until saturated. Growth condition for Chapter 5 is drastically different from other chapters and will be described in the chapter. Depending on the experiment, saturated cultures are either pre-cultured in MSgg media for an additional hour and spotted 1μl on MSgg-agar pad or resuspended in MSgg media and loaded in a microfluidics plate. MSgg media composition is as following: 5 mM potassium phosphate buffer (pH 7.0), 100 mM MOPS buffer (pH 7.0, adjusted using NaOH), 2 mM $MgCl_2$, 700 μM $CaCl_2$, 50 μM $MnCl_2$, 100 μM $FeCl_3$, 1 μM $ZnCl_2$, 2 μM thiamine HCl, 0.5% (v/v) glycerol and 0.5% (w/v) monosodium glutamate. The MSgg medium was made from stock solutions on the day of the experiment, and the stock solution for glutamate was made new each week.

1.3.3 Agar- or agarose-based pad

Agar or agarose-based nutrient pads have been extensively used to image single cells or biofilms growing on a solid surface. It has multiple advantages: 1) it is transparent, and thus good for imaging, 2) bulk agar or agarose stores nutrients that are provided to cells over time through diffusion, and 3) solid surface usually limits motility, and thus it enables researchers to observe certain cells for a long period time. Many researchers could track natural heterogeneity in gene expression at the single-cell level as well as to follow the developmental process of bacterial biofilms using this system (Megason and Fraser 2007; Asally et al. 2012).

Traditional agar or agarose pads, however, have clear limitations. For instance, high-resolution single cell measurement is generally limited by cell growth because cells eventually overcome gentle pressure from the pads and grow in multiple layers. Also, cells use up nutrients and excrete waste during growth. It means the condition keep changes during the experiment. These limitations can be not an obstacle at all or even better for certain studies; for example, the sporulation process - cells don’t grow much anyway - or other developmental processes based on the local changes made by cellular activities. On the other hand, some questions required intentional media change in the middle of an experiment or maintaining constant media condition cannot be addressed with this system.

Studies in Chapter 1 and 5 were done with traditional agar or agarose pad.

1.3.4 Microfluidics devices

Microfluidic devices, as the name suggested, confine fluids on a micro or sub-micrometer scale. Microfluidic devices used in biology are mostly made of poly-di-methyl-siloxane (PDMS), which is optically clear, biocompatible and gas permeable (Friend and Yeo 2010). It may have various designs and functions from simple to complicate depending on the purpose of the use, and this flexibility contributes significantly to increase the range of questions to be asked. For instance, it becomes very easy to manage the media composition by flowing the same or different media with desirable speeds and durations.

Jintao Liu, a former postdoc in our lab and currently an assistant professor at Tsinghua University, developed a new method to observe biofilm growth using a commercial system. We used the CellASIC ONIX Microfluidic Platform and the Y04D microfluidic plate (Yeast plate, EMD Millipore). It provides unconventionally large chambers, allowing the formation of colonies containing millions of cells, yet still leaves room for media flow. Media flow in the microfluidic chamber was driven by a pneumatic pump from the CellASIC ONIX Microfluidic Platform, and the pressure from the pump was kept stable during the experiments. For biofilm experiments using the microfluidic system, it is worth note that the media becomes limited once a biofilm grows at a certain point due to increased consumption rather than a change in media composition. Studies in Chapter 3,4, and 6 are done in microfluidic devices.

1.3.5 Imaging

Bacterial growth and gene expressions were observed with fluorescent time-lapse microscopy at 30 °C with an IX81 or IX83 inverted microscope (Olympus), ORCA-ER digital camera or ORCA-flash4.0LT (Hamamatsu), and a motorized stage (ASI). Custom Visual Basic software in combination with the Image Pro Plus (Media Cybernetics) was used to automated image acquisition and microscope control for the Chapter 1, 5 studies and MetaMorph Advanced version 7.8.4.0 for the rest chapters. Time-lapse images were taken with various magnifications using from the 2.5x to the 100x objective lens depending on the scale of interest.

1.4 Overview of the thesis

This dissertation thesis discusses bacterial stress responses focus on its dynamic characteristics. The main body consists of two parts, part I: biofilm studies (Chapters 2-4) and part II: single cell studies (Chapters 5-6). The first part is based on the dynamics of nitrogen metabolic stress in biofilms. Each chapter is well connected but attempts to answer its unique questions regarding organization (Chapter 2) and coordination (Chapter 3) of nitrogen metabolism during a biofilm development and between biofilms (Chapter 4) under stress. The second part focuses more on the dynamic response to stresses at the single-cell level (Chapter 5 and 6). It is very interesting the ways that dynamic cellular processes are coupled in both examples. Each chapter asks independent questions and describes interesting phenomena (Fig. 1.2).

In chapter 2, I asked how individual cells can affect each other's metabolism in spatially structured communities like biofilms. I utilized *B. subtilis* biofilms grown on MSgg-agar system to investigate the spatiotemporal dynamics of nitrogen metabolism in a structured community. I observed the emergence of unexpected global patterns of nitrogen stress reporter. Various mutants regarding the glutamate-glutamine regulation suggest that the peripheral cells of the biofilms experience ammonia limitation, which is made by interior cells. Moreover, an agent-based mathematical model and single-cell experiments reveal that this global pattern can be explained by a simple cell-cell coupling of nitrogen metabolism with ammonia.

At the similar time, a postdoc in our lab, Jintao Liu, observed interesting biofilm growth oscillations in a microfluidics device, which he adapted commercial yeast plates for biofilm studies (The details of the system can be found in chapter 1.3.4). We puzzled by this interesting growth oscillation for a long time. Inspired by the ring patterns in 3D biofilms described in chapter 2, we hypothesized that the growth oscillation is due to a long-range metabolic codependence between interior and periphery cells in a biofilm. Indeed, we could explain the growth oscillation with the same pathway described in chapter 2. This published work is described in Chapter 3.

In chapter 4, I would like to introduce the work that we expanded the concepts in chapter 3 to ask coordination between multiple biofilms. Specifically, we asked if two spatially separated biofilms can modulate each other's metabolic regulations under nutrient limitation stress. Together with Jintao's beautiful work described in Chapter 3, this work is heavily grounded on Arthur Prindle's work on electrochemical signaling in biofilms (Prindle et al. 2015). Briefly, metabolically triggered electrical cell-to-cell signaling couples metabolic states among cells interior and periphery of a biofilm. The interplay between competition for shared nutrient, glutamate, and communication through ions, potassium, during nitrogen metabolic stress results in an interesting behavior; dynamic time-sharing between two biofilms.

Coupling and coordination under stress are not only important between two different entities but also important in individual cells. Chapter 5 describes outstanding work mainly done by Jatin Narula and Anna Kuchina. In this work, the coordination between cell cycle, chromosome replication, and cellular differentiation process, sporulation, has been studied. A bacterium can become a spore under extreme stress conditions including nitrogen limitation, and it needs to coordinate the sporulation process with chromosome replication. In this work, mathematical modeling and various genetic mutants successfully demonstrate that chromosomal arrangement of two sporulation pathway genes plays a critical role in coupling sporulation commitment to the cell cycle. The simplicity of this process – just an arrangement of genes on the chromosome determines the timing – is itself beautiful and it also suggests that this type of coordination mechanism can be widely applicable in variety stress-response settings.

In Chapter 6, the last chapter in the main body, I would like to discuss how two fundamental properties of a cell are connected. Two of the most fundamental properties of all living cells are ribosome-mediated protein synthesis and an electrochemical potential across the cell membrane. We asked if ribosome, which is full of ions, can influence the membrane potential dynamics. Using direct chemical or genetic perturbations of the ribosome, we could show that the ribosome perturbation can transiently increase the membrane potential in *B. subtilis* cells. Ions are one of the most prevalent components of a living cell and at the same time are one of the most ignored elements. This study implies a new dynamic connection through ions between two fundamental properties in a cell.

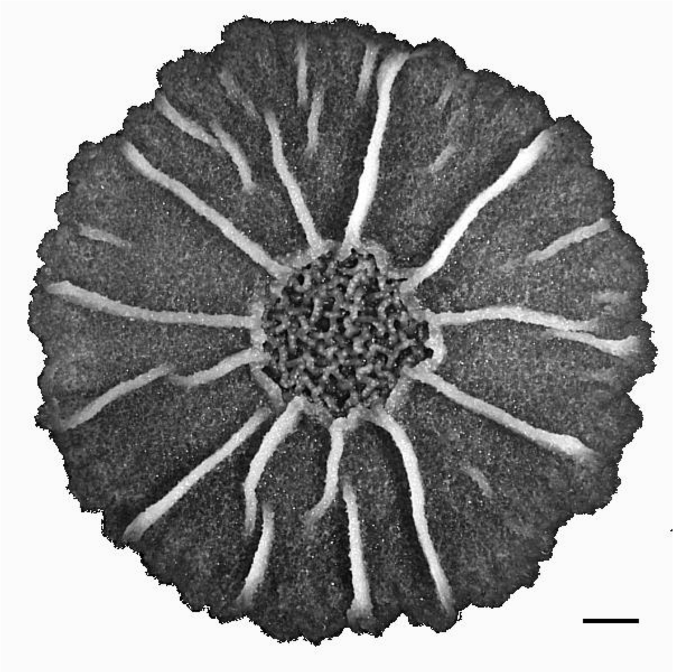

Figure 1.1 A *Bacillus subtilis* biofilm.
A Three-day-old B. subtilis biofilm grown on MSgg-agar plate. The picture was taken with a stereoscope and the scale bar is 1mm.

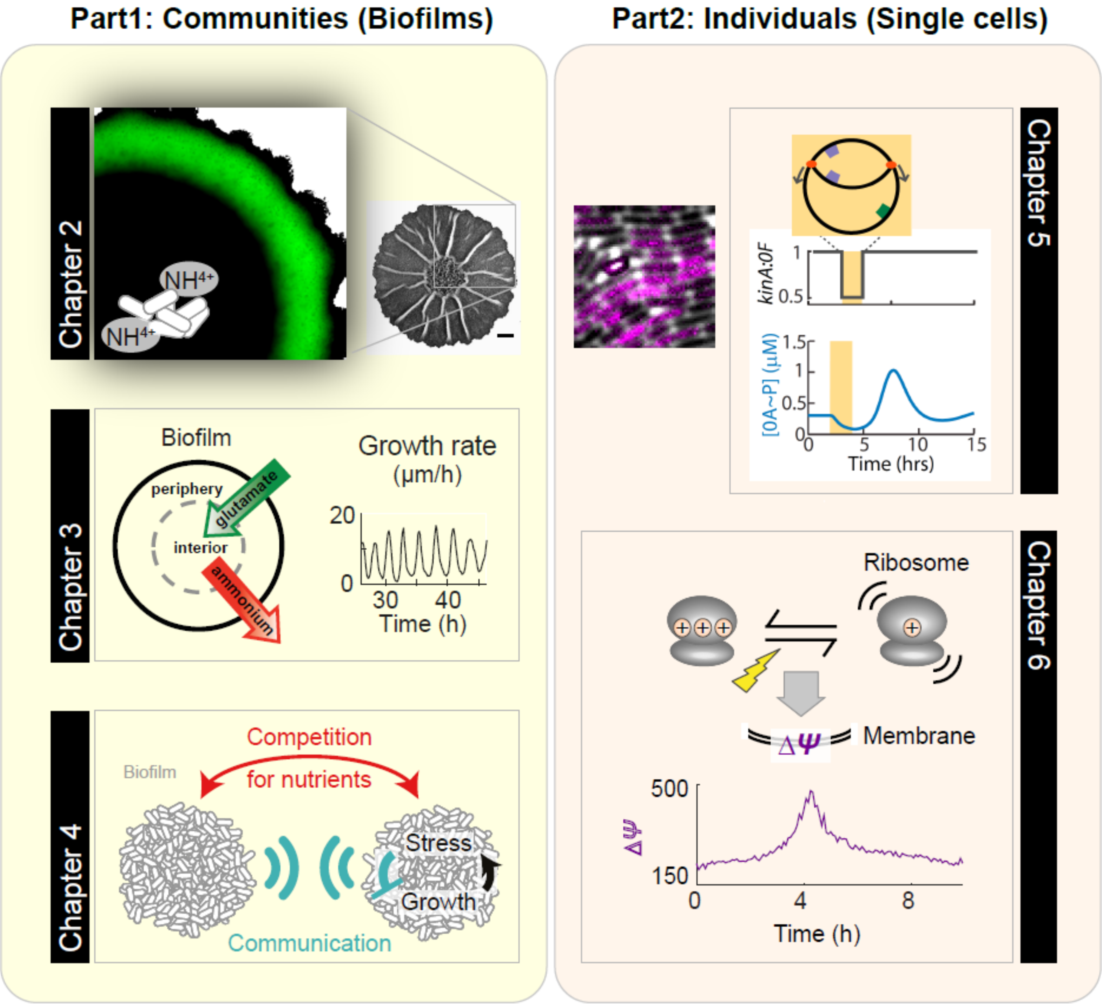

Figure 1.2 Overview of the dissertation thesis.
A schematic summarizes each chapter. The dissertation thesis consists of two parts, part I: biofilm studies (Chapters 2-4) and part II: single cell studies (Chapters 5-6). The first part is based on the dynamics of nitrogen metabolic stress in biofilms. Each chapter is well connected but attempts to answer its unique questions regarding organization (Chapter 2) and coordination (Chapter 3) of nitrogen metabolism during a biofilm development and between biofilms (Chapter 4) under stress. The second part focuses more on the dynamic response to stresses at the single-cell level (Chapter 5 and 6). Chapter 5 examines the coupling between cell cycle and cell differentiation into a spore, and Chapter 6 investigates the coupling between ribosomes and membrane potential dynamics.

II

SPATIO-TEMPORAL COORDINATION OF BACTERIAL BIOFILMS UNDER NITROGEN STARVATION

2 Nitrogen metabolism becomes globally organized during biofilm development

2.1 Abstract

Much of our knowledge of metabolism is derived from the study of liquid cell cultures and population averages. It remains unclear how individual cells can affect each other's metabolism in spatially structured communities. We utilized *B.subtilis* biofilms to investigate the spatiotemporal dynamics of nitrogen metabolism in a structured community. We observe the emergence of an unexpected spatial ring pattern indicating localized nitrogen stress. Using mixed biofilms comprised of strains with genetically modified nitrogen metabolism, we identified ammonium as the metabolic coupling agent. Integration of mathematical modeling with single-cell measurements suggests that cells on the biofilm edge act as a sink for ammonium, giving rise to the counterintuitive ring pattern. We also show how ammonium mediated coupling of nitrogen metabolism is a fundamental cellular process even outside the biofilm context. Spatial coupling of cellular metabolism among individual cells can thus generate unexpected and global patterns during biofilm development.

2.2 Introduction

In typical liquid cultures, extracellular conditions are well mixed and interactions among cells are averaged over time and space. However, most bacteria reside in biofilm communities, where cells are densely packed and confined in space, which enables sustained local interactions (Hall-Stoodley, Costerton, and Stoodley 2004). As a result, intracellular processes, such as metabolism, can be affected by the activity of neighboring cells. Therefore, in a structured community, intracellular processes such as metabolism may depend on the context of the collective and may thus be better understood when the spatial dimension is taken into consideration.

To investigate metabolic regulation in a developing biofilm, we focused on nitrogen metabolism, which is essential for biomass production. Specifically, we investigated *B. subtilis* biofilms, which have served as a model system for studying biofilm development on defined medium containing glutamate as the only nitrogen source (Branda et al. 2001; Asally et al. 2012). Glutamate is the most abundant amino acid in the cell (Newsholme et al. 2003; Tempest, Meers, and Brown 1970) and, together with glutamine, acts as the major donor of amino groups to nitrogen-containing molecules (Gunka and Commichau 2012; Newsholme et al. 2003). Thus, maintaining sufficient glutamate and glutamine levels is essential for cells to increase their biomass. While cells can take up glutamate from the media, they need to synthesize glutamine from glutamate through ammonium incorporation using the enzyme glutamine synthetase (GS) (Figure 1A) (Fisher and Sonenshein 1977). Glutamine biosynthesis is crucial for maintenance of cellular nitrogen homeostasis and ammonium assimilation in cells. Therefore, cells closely monitor glutamine availability to adjust their nitrogen metabolism. In particular, glutamine inhibits the activity of TnrA, a central transcription factor for nitrogen metabolism genes (L V Wray, Zalieckas, and Fisher 2001; Lewis V Wray and Fisher 2005). Under nitrogen-limited conditions, TnrA activates the expression of multiple genes including *nasA*, encoding a nitrate importer, and *nrgA*, encoding an ammonium importer, to secure nitrogen availability (Figure 1A) (Lewis V.

Wray et al. 1996; Yoshida et al. 2003). Accordingly, inadequate production of glutamine from glutamate results in expression of TnrA, which in turn regulates central nitrogen metabolism.

Here, we investigated the regulation of nitrogen metabolism during biofilm development as a function of space and time. Utilizing fluorescent promoter reporters, genetic perturbations, and mixed strain biofilms, we discovered that nitrogen metabolism regulated by TnrA becomes spatially organized into a ring pattern during biofilm development. We identified that the ring pattern is mediated by ammonium, which couples nitrogen metabolism of cells that reside in different regions of a biofilm. Furthermore, we demonstrated with mathematical modeling and quantitative single-cell measurements that the coupling of metabolic states is not limited to the context of biofilms, but can be reconstituted at the single cell level. Together, our findings present direct evidence of spatiotemporal metabolic organization during biofilm development. Furthermore, we provide an intuitive explanation for the unexpected organization of the nitrogen stress response into a global ring pattern within the biofilm. These results reveal that the metabolic state of individual bacteria residing in biofilms is determined collectively, resulting in the nonlinear spatial organization.

2.3 Results

2.3.1 Regulation of nitrogen metabolism becomes organized in space and time during biofilm development.

To investigate nitrogen metabolism during *B. subtilis* biofilm development, we monitored a genetically encoded reporter for nitrogen stress response. Specifically, we measured *nasA* promoter activity (P_{nasA}-*yfp*, Figure 1B and Movie S1, green) using fluorescence time-lapse imaging. The *nasA* promoter is activated by TnrA, which is a central transcriptional regulator of nitrogen metabolism. Instead of nitrogen stress being homogeneously distributed in space, we observed a prominent and unexpected ring-shaped P_{nasA} expression pattern near the biofilm edge that emerged at approximately 33 hours (32.7 ± 0.8 hrs, mean ± SEM, n=10) into biofilm development (Figure 1D, green). This ring indicates a localized and timed nitrogen stress response. We confirmed that the pattern of P_{nasA} expression was indeed dependent on TnrA activity. Specifically, we disrupted the TnrA binding site of the *nasA* promoter reporter, which eliminated the signal and ring-like expression pattern (Figure S1A). Furthermore, another representative TnrA regulated promoter P_{nrgA} showed the same expression pattern as P_{nasA} (Figure S1B). Finally, the specificity of the P_{nasA} expression pattern was in direct contrast to the global expression profile of the IPTG-inducible promoter P_{HS} in the same biofilm (P_{HS}-*cfp*, Figures 1C-D and Movie S1, magenta). These data show that the activity of the TnrA, a master regulator of nitrogen metabolism, becomes organized in space and time during biofilm development.

The ring pattern of TnrA regulation provoked the question of whether this pattern is specific to nitrogen metabolism or a common feature shared by other metabolic pathways, such as carbon metabolism. Accordingly, we measured the promoter activity of two genes, specifically *citZ* and *sucC*, which are regulated by a central regulator of carbon metabolism, CcpA (Blencke et al., 2003; Kim et al., 2002). We find that the expression patterns of these carbon-regulated promoters are similar to the expression profile of the globally expressed constitutive P_{HS} promoter (Figures S1C-D). Therefore, the observed ring pattern appears to be specific to regulation of nitrogen metabolism and not carbon metabolism. This suggests that the developing biofilm experiences a highly localized and timed nitrogen specific stress that gives rise to the spatial organization of nitrogen metabolism.

2.3.2 Genetic perturbations reveal the limiting factor responsible for the pattern of nitrogen stress.

Next, we attempted to identify the limiting factor that is responsible for the observed nitrogen stress response pattern. Since the stress response indicates a limitation in glutamine (Figure 1A), either the GS enzyme or its substrates (glutamate and ammonium) could be limited in the ring-like region identified by *nasA* expression.

To test whether the GS enzyme is the limiting factor, we exogenously overexpressed GS from the inducible P_{HS} promoter (Figure 2A). This genetic perturbation did not interfere with biofilm growth (Figure S2A) or the nitrogen stress response pattern (Figure 2B). Nor could we detect any difference in the maximal intensity of P_{nasA}-*yfp* expression in the ring (Figure 2C), showing that GS overexpression cannot alleviate the nitrogen limitation. These results indicate that the nitrogen stress response is not due to GS enzyme limitation.

We then asked whether one of the two substrates for glutamine synthesis, glutamate or ammonium, could be the limiting factor. To pursue this question, we overexpressed the enzyme glutamate dehydrogenase (GDH) from the IPTG inducible promoter (P_{HS}-GDH) (Figure 2D). GDH breaks down glutamate to produce ammonium (Belitsky and Sonenshein 1998; Commichau et al. 2008). Therefore, overexpression of GDH will consume glutamate while supplying more ammonium, allowing us to identify the limiting substrate. Interestingly, overexpression of GDH eliminated the nitrogen stress pattern in the biofilm (Figure 2E and Figure S2B), and the maximal intensity of P_{nasA} expression dropped by 84% ± 5% compared to wild-type (Figure 2F, mean ± SEM, n = 7). Since GDH overexpression alleviates the nitrogen stress, we conclude that ammonium, but not glutamate, is the limiting factor that triggers the nitrogen stress response.

2.3.3 Biofilm cells gradually experience nitrogen limitation from the edge.

According to the ring pattern of the nitrogen stress, ammonium is not limited to the biofilm interior, but rather limited at the edge. This is an unexpected observation since the periphery of the biofilm has more access to nutrients. Is the ring pattern generated because inner cells are dormant, and thus cannot respond to the same ammonium limitation? Alternatively, inner cells may produce or retain sufficient ammonium to meet their needs, while cells at the biofilm periphery cannot. To discriminate between these possibilities, we tested if we can move the location of the stressed region (ring) by modulating ammonium production. Specifically, we lowered the glutamate concentration in the medium, which in turn would decrease ammonium production. This perturbation not only increased the nitrogen stress response as expected (Figure 3A) but also moved the ring inward (Figure 3B). This inward shift of the ring's location is evident even after we corrected for less overall growth in low glutamate medium (Figure 3C and Figure S3A). As a complementary experiment, we induced GDH overexpression to globally increase ammonium production. As expected P_{nasA} expression decreased with increased GDH induction (Figure 3D), and the location of the ring moved further out toward the edge until the pattern disappeared completely (Figures 3E-F, and S3B). Together, these results suggest that while cells throughout the biofilm can produce and consume ammonium, consumption near the edge seems to outweigh production, giving rise to the ring-like P_{nasA} expression pattern.

Motivated by these findings, we sought to understand the P_{nasA} ring formation process more deeply. We closely followed changes of reporter expression during the emergence of the ring pattern. This analysis shows that the nitrogen stress response starts near the biofilm edge, but then propagates inward, increasing the thickness of the ring (Figures 3G and 3H). We note that the observed increase of ring thickness is only transient, arguing against it being a result of nutrient depletion in the medium over time. If nutrient depletion were the cause, then ring thickness would be expected to continuously increase. Together, the results show the ring pattern of the nitrogen stress response cannot be exclusively due to nutrient depletion during biofilm growth.

2.3.4 Nitrogen metabolic states of cells are coupled through ammonium within a biofilm.

Given that nitrogen stress first arises at the biofilm edge and then propagates towards the interior, we hypothesized that edge cells may represent a sink that depletes ammonium from interior cells. In other words, the high metabolic demands of peripheral cells cause them to effectively 'steal' ammonium from interior cells; thereby giving rise to the ring-shaped stress response pattern within the biofilm. This mechanism assumes that ammonium can be shared among neighboring cells. Indeed, while ammonium production is an intracellular process, ammonium is in equilibrium with ammonia, which can diffuse through the cell membrane and be shared among cells (Boogerd et al. 2011). Therefore, we directly tested the concept that the ring-shaped stress pattern can be caused by cells acting as a sink for ammonium. Specifically, we grew mixed biofilm consortia that were comprised equally of wild-type and GDH-overexpression strains. In these mixed biofilms, the GDH strain is the dominant ammonium source, thereby designating wild-type cells effectively as the sink for ammonium. Since cells within the biofilm grow in spatially segregated lineages (Hallatschek et al. 2007), this approach allows us to test the sink hypothesis by investing if two strains with differences in ammonium production and consumption can affect each other's nitrogen metabolism (Figure 4A).

As expected, we find that the GDH-overexpression strain acts as a source of ammonium, while the wild-type strain becomes a sink. Specifically, we find that the wild-type strain when grown together with the GDH-overexpression strain exhibits a reduction in nitrogen stress (Figures 4B-C and Figure S4A). Therefore, ammonium overproduction in the GDH-overexpression strain can alleviate nitrogen stress in the neighboring wild-type strain. Furthermore, maximal P_{nasA} expression of the GDH overexpression strain in the mixed biofilms was more than two-fold higher compared to a biofilm comprised only by the GDH-overexpression strain (Figures 4D-E and Movie S2). This result further confirms that wild-type cells act as a sink for ammonium and can thereby induce nitrogen stress in the neighboring GDH overexpression strain. Accordingly, wild-type cells do not just utilize 'leftover' ammonium from the GDH overexpression strain, but rather act as a sink that can deplete ammonium. Therefore, ammonium appears to couple nitrogen metabolic states among neighboring cells within a biofilm, where some cells can act as a source and others as a sink for ammonium.

2.3.5 Coupling of nitrogen metabolism among individual cells.

The apparent ability of ammonium to couple metabolic activity within the biofilm suggests the intriguing possibility that such coupling could also be observed at the single cell level, outside the context of the biofilm (Figure 5A). To explore this hypothesis in detail, we turned to mathematical modeling. Specifically, we used a combination of discrete agent-based and continuum modeling (Figure 5B) to stimulate growth and metabolic activity of individual bacteria in a population. A more detailed description of our computational approach is given in Supplementary Text. Briefly, bacteria were modeled as soft spherocylinders that grow, divide, and are pushed by the contact forces with neighboring cells. Each "bacterium" was associated with a set of differential equations for concentrations of its intracellular glutamate $G_i(t)$, ammonium $A_i(t)$, GDH enzyme $H_i(t)$, housekeeping proteins $R_i(t)$, and concentration of the YFP reporter $Y_i(t)$ (Figure 5B). This agent-based model was augmented by partial differential equations simulating spatiotemporal dynamics of extracellular glutamate $G(x,t)$ and ammonium $A(x,t)$ (Figure 5B). These reaction-diffusion equations describe the linear diffusion of these compounds throughout the integration domain and exchange of ammonium and glutamate between the cells and the environment. We used this model to simulate the two-dimensional biofilm growth and ring pattern and obtained good agreement between simulations and experimental observations (Compare Figure 1C with Figure S5A).

The agent-based model also allowed us to simulate the ammonium coupling at the single cell level and generated specific predictions (Figure 5C and Figure S5D). To test these modeling predictions, we measured the nitrogen stress response in single cells outside the context of the biofilm. To approximate the nutrient competition within the dense biofilm, we grew cells on reduced glutamate concentration. Consistent with modeling predictions, we find that wild-type cells experience nitrogen stress, while GDH-overexpressing cells do not (Figure 5D). In contrast, GDH-overexpressing cells exhibit high nitrogen stress when they reside next to wild-type cells (Figure 5D bottom). Quantification of these single-cell measurements shows that these results are not only qualitatively, but also quantitatively consistent with modeling prediction (Figures 5E-F). Specifically, results show that the ratio of P_{nasA} expression of GDH-overexpressing cells to wild-type cells approaches one when cells are mixed (Figures S4C, 0.86 ± 0.002). This is also quantitatively similar to the fluorescence ratio observed in biofilms (Compare Figures S4B-D, the P_{nasA} ratio is 0.89 ± 0.09 in mixed biofilms). Together, these findings confirm that even outside the context of the structured biofilm, GDH overexpressing cells can act as a source, while wild-type cells act as a sink for ammonium. Therefore, metabolic coupling among neighboring cells appears to be a fundamental cellular property that is not limited to, but more pronounced in the context of the densely packed biofilm community.

2.4 Discussion

Here, we present the discovery that the nitrogen stress response becomes globally organized in space to form an unexpected ring pattern during biofilm development. Our results suggest that the ring arises due to differences in ammonium demand and production among cells in different regions of the biofilm. In other words, one subpopulation of cells becomes a source and the other a sink for ammonium. Specifically, our data indicate that the consumption of ammonium outweighs production near the biofilm edge, which creates a source-and-sink relationship between the interior and the periphery of the biofilm. As a result, a ring-like nitrogen stress response pattern emerges during biofilm development. We show that this spatiotemporal pattern at the level of the biofilm can be successfully recapitulated by an agent-based mathematical model that simulates the metabolic dynamics of individual cells in a large population. Accordingly, the ring pattern emerges when peripheral cells deplete ammonium from cells that are located closer to the biofilm interior. Interestingly, ammonium uptake is known as a "futile cycle", because cells spend ATP to take up ammonium, which they cannot fully retain as it can be lost in the form of ammonia (Boogerd et al. 2011; M. Kim et al. 2012). In the biofilm, community, bacteria appear to utilize this seemingly problematic property of ammonium to couple nitrogen metabolic states among neighboring cells and give rise to a global organization.

The diffusive property of ammonia combined with its role in nitrogen stress in individual cells, suggests that it can serve to spatially organize a community-level activity. Particularly, when cells are not provided external ammonium but have to produce their own, extracellular ammonium in the community reflects the activities of neighboring cells. Furthermore, a recent study of *B. subtilis* biofilms in a microfluidic device provided evidence for metabolic co-dependence among distant cells, which gave rise to global oscillations in colony growth rate (Liu et al. 2015). These studies show that ammonium production by biofilm cells can determine collective behavior. Intriguingly, the metabolic oscillations described in that work also suggest that it may be possible to observe more than one ring within a biofilm, which could give rise to a concentric pattern of multiple rings.

Our findings also suggest that ammonium may play a signaling role to organize cellular activity during biofilm development. We note that that self-produced ammonia has been shown to serve as a signaling molecule during community development in other biological systems such as yeast and *Dictyostelium* (Singleton, Kirsten, and Dinsmore 2006; Schindler and Sussman 1977; Zdena Palková and Vachova 2003; Z Palková et al. 1997). Similarly, the TnrA mediated nitrogen stress response in *B. subtilis* is known to control genes that are either directly or indirectly regulating biofilm formation (Yoshida et al. 2003; L. Wang et al. 1997; Kobayashi 2007; Perego et al. 1991). Furthermore, recent work has suggested that bacterial biofilm development can be affected by high ambient ammonium concentrations (Nijland and Burgess 2010). We now show that bacteria may indeed use ammonium in a manner that is reminiscent of a signaling molecule, such that it can couple the metabolic states of individual cells within the community. Therefore, it will be interesting to pursue in future studies whether ammonium mediated coupling of metabolic states serves an active role in the organization of the complex multicellular structures formed by bacterial biofilms.

2.5 Method

2.5.1 Strain Construction

Promoter-reporter constructs were chromosomally integrated into either *amyE* locus (pDL30 vector) or *sacA* locus (pSac-cm vector). Both loci are nonessential and widely used regions for chromosomal integration. All metabolic reporter constructs, P_{nasA}-*yfp*, P_{nrgA}-*cfp*, P_{citZ}-*cfp*, and P_{sucC}-*cfp*, were a kind gift from the Elowitz lab (Caltech, CA). $P_{nasA(mut)}$-*yfp* construct was made based on P_{nasA}-*yfp*. It contains two point mutations in the well-characterized TnrA binding sequence (TGTCACAAAAACTTACA → TATCGCAAAAACTTACA). These mutations were characterized in Nakano et al.'s paper in 1995. Consistent with the study, this strain does not have fluorescent signal in both biofilm and single cell conditions (Figure 2.1 and 2.6A. Single cell condition data is not presented here). All constructs were confirmed by sequencing before NCIB 3610 transformation.

Both IPTG (Isopropyl β-D-1-thiogalactopyranoside)-inducible constructs for *B.subtilis* were made using pDR111 plasmid, a pHyperspank promoter containing a vector that integrates into *amyE* locus. To make P_{HS}-GS ($P_{hyperspank}$-*glnA*) construct, the *glnA* gene and RBS were PCR amplified from NCIB 3610 with primers 5'-GCGTCGACAGAGGAGGAATTTTACCAAATGGC-3' and 5'-CGGCTAGCGTGCCAAGGGATTGAGATATT-3' and cloned into SalI- and NheI-digested pDR111. To make P_{HS}-GDH ($P_{hyperspank}$-*rocG*) construct, the *rocG* gene and RBS were PCR amplified from NCIB 3610 with primers 5'-CCGTCGACACAATGAGGTGAAAAAGATGTCAGCA-3' and 5'-AGGCTAGCGTCTAACAGGTGATCACCTTTCTC-3' and cloned into pDR111 in the same way with P_{HS}-GS construct. All cloned regions were confirmed by direct sequencing.

2.5.2 Growth and Imaging conditions

B. subtilis strains were grown as described in 1.xx. general method. The saturated culture was then diluted to OD600 of 1.3 in MSgg media, pre-cultured for an additional hour, and spotted on the plate (modified MSgg-agar medium described above, 3 mm thickness, dried overnight). After spotting, biofilms were grown in 30 °C chamber. For mixed-strain biofilms, MSgg pre-cultures were mixed in equal portions right before spotted. For single-cell imaging, the same MSgg-agar pad described above was used except that the glutamate is diluted 500-fold (final 0.003 % glutamate). Cells were grown in the same way with biofilm movies and diluted 16-fold before spotted. Pads were dried and placed into a coverslip-bottom Willco dish for imaging. This protocol is optimized to observe nitrogen stress response at the single-cell level.

2.5.3 Image Analysis

Time-lapse data and snapshot analysis were performed by custom software developed with MATLAB (MathWorks) and ImageJ (National Institutes of Health, http://imagej.nih.gov/ij/).

Fluorescence across a biofilm radius in Figure 2.1D was measured as flow. The location of the biofilm radius was determined from bright field images. First, the location of the center of the biofilm was determined by fitting circles to multiple bright field images from a filmstrip obtained during biofilm development. Once the biofilm center was determined, fluorescence intensity was measured for a continuous series of concentric circles, originating from the biofilm center to the edge. The fluorescence intensity values for each concentric circle were averaged, providing a measure of intensity from the center to the edge of the biofilm. This was done for multiple time points (12, 24, and 36 hr) and for each biofilm, the traces were normalized by the minimal and maximal intensities across all time points. For each time point plot, one line represents one biofilm. Five independent biofilms for each reporter were shown in each plot.

The maximal P_{nasA}-*yfp* intensity in biofilms used in Figures 2.2, 2.3 and 2.4 are measured as follow. First, to compare all data, including mixed biofilms in which only half of the population has the reporter, the maximal P_{nasA}-*yfp* intensity relative to that of WT was calculated for each biofilm. To minimize artifacts associated with this approach, maximal P_{nasA}-*yfp* intensities were determined 1) only from the area inside of the biofilm, as determined by the corresponding bright field image, and 2) by the 5th most maximal value at the time point. Each data set is normalized by the P_{nasA}-*yfp* intensity of the WT, P_{nasA}-*yfp* labeled strain in the same experimental set before determining the maximal value. Since modulation of ring location also affects the timing of the ring emergence, data for Figure 3 were obtained from a maximum projection after 37 hr for each condition. A maximum projection is obtained by taking the maximum value for each pixel during the first 37 hr period. Otherwise, the maximal P_{nasA}-*yfp* intensity was obtained from a snapshot at 36 hr.

Ring location in Figure 2.3 was calculated based on the location of the biofilm center which is described the first part of the method. Biofilm size was determined from bright field images at around 37 hr. To get the ring location, a maximum projection of *yfp* was acquired first as described in the second part of the method. Then, an intensity plot across the radius from the maximum projection was obtained as described the first part of the method. The ring center was determined by obtaining the location of the peak *yfp* value in the intensity plot.

Tracking the changes in P_{nasA}-*yfp* expression and the inner boundary of the PnasA-yfp ring in Figure 2.3 was done as follows. To track the change in P_{nasA}-*yfp* expression, we performed image differencing on individual *yfp* snapshots for the entire time course (images were taken every 40 mins). Specifically, the difference between two consecutive *yfp* images was calculated by finding the positive difference between each pixel in each image. Resulting images were gathered as an image stack. Then, a kymograph along the biofilm radius was acquired from the difference image stack. Figure 3G shows a representative kymograph during the emergence of a ring pattern (x and y-axis are flipped so that the x-axis shows time and the y-axis shows the distance from the center of a biofilm). The inward boundary of the change in P_{nasA}-*yfp* expression was obtained from a kymograph and seven of them were averaged to generate Figure 2.3H.

For single-cell data, we averaged mean P_{nasA}-*yfp* intensity from individual cells because we can avoid potential issues in biofilms with cell density (or the number of cells expressing P_{nasA}-*yfp*). Data were obtained from three independent experiments. A total of 1007 cells (pure WT: 302, WT in mixed population: 174, pure P_{HS}-GDH: 360, P_{HS}-GDH in mixed population: 171) were manually detected as a region of interest (roi) from the phase images using ImageJ. Mean YFP intensity of a roi was determined as P_{nasA}-*yfp* intensity. Then, intensities were normalized within the same experimental set.

Chapter 2, in full, contains materials being prepared for publication. Dong-yeon D. Lee, Liyang Xiong, San Ly, Lev Tsimring and Gürol M Süel. The dissertation author was the primary investigator and author of the material contains the chapter.

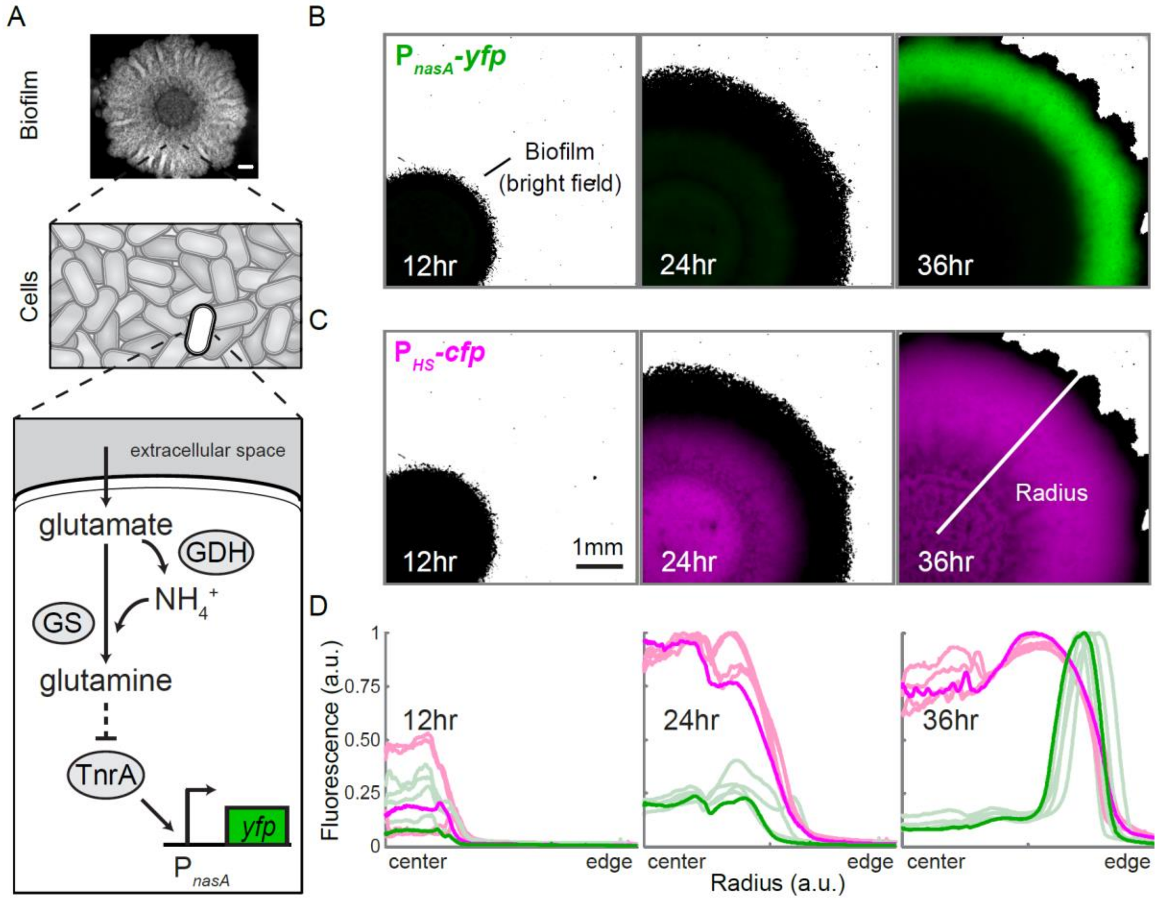

Figure 2.1 Nitrogen metabolism is organized in space and time during biofilm development.

(A) A simplified diagram illustrating the glutamine production pathway in *Bacillus subtilis*. All cells in *B.subtilis* biofilm (top, 3.5-day old, scale bar = 1mm) have the same genetic background. Nitrogen limitation can be detected through the use of the P_{nasA}-*yfp* reporter (bottom). **(B)** Filmstrip of TnrA activity over time, monitored by P_{nasA}-*yfp* (green). Fluorescent images are merged with the bright field to indicate the boundaries of the biofilm (scale bar = 1 mm). See also Figures 2.2A-B.
(C) Filmstrip of constitutive gene expression over time from the same biofilm shown in (B). An IPTG-inducible promoter driving CFP expression, P_{HS}-*cfp* (1 mM IPTG, magenta) was measured and merged with corresponding bright field images (scale bar = 1 mm). See also Figures 2.2C-D.
(D) Fluorescent intensities of P_{nasA}-*yfp* and P_{HS}-*cfp* (green and magenta, respectively) along the indicated radius (white line) during biofilm development (n = 5 biofilms for each reporter). Darker lines show intensities for the biofilm shown in panels B and C.

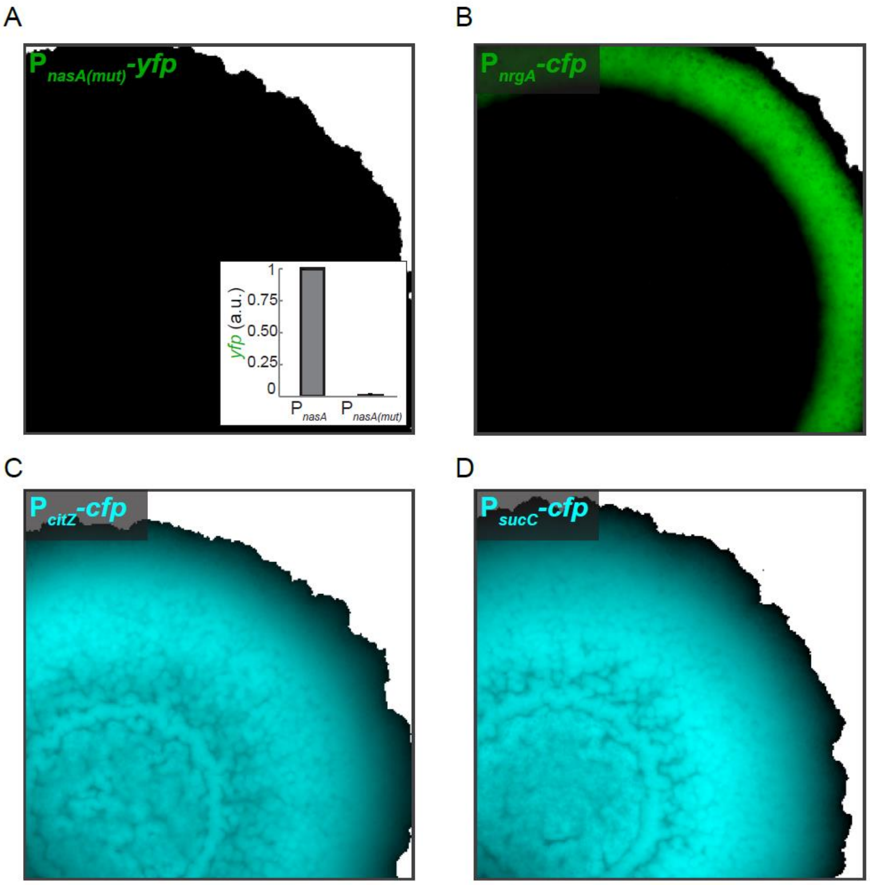

Figure 2.2 Global pattern of TnrA regulation is specific to nitrogen metabolism. **(A)** Disruption of the TnrA binding site in the *nasA* promoter reporter results in the elimination of P_{nasA}-*yfp* signal. Pseudocolored fluorescent images were merged with bright field images. Inset is the quantification of YFP signal from the original P_{nasA} and mutated P_{nasA} reporters (mean ± SEM, n = 4). Here, YFP intensities are normalized against the original P_{nasA} reporter. **(B)** Promoter reporter activity of the *nrgA* gene, another representative TnrA regulon gene, at 36 hr. The pseudocolored fluorescent image was merged with bright field image. **(C)** Promoter reporter activity of the *citZ* gene, which is subject to carbon catabolite repression, at 36 hr. The pseudocolored fluorescent image was merged with bright field image. **(D)** Promoter reporter activity of the *sucC* gene, another gene that is subject to carbon catabolite repression, at 36 hr. The pseudocolored fluorescent image was merged with bright field image.

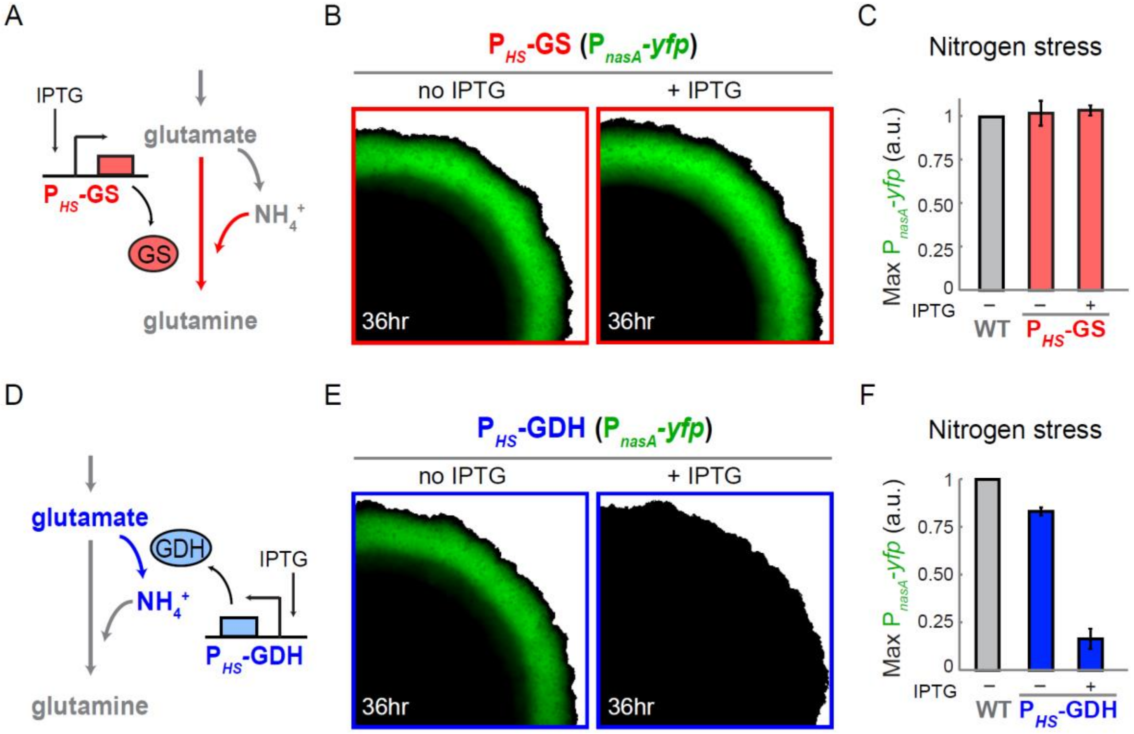

Figure 2.3 Genetic perturbations identified the limiting factor that is responsible for the nitrogen metabolic pattern.

(A) To test if glutamate synthetase (GS, red) is the limiting factor, additional GS was introduced via expression from an IPTG inducible promoter (P_{HS}-*glnA*, referred to throughout this text as P_{HS}-GS). **(B)** The additional GS (+ 1 mM IPTG) does not affect the nitrogen stress response (P_{nasA}-*yfp*, green) at 36hr. See also Figure 2.4A. **(C)** Maximal P_{nasA}-*yfp* intensity at 36hr (mean ± SEM, n = 7 biofilms for WT, n = 8 biofilms for - IPTG, n = 9 biofilms for + 1 mM IPTG). **(D)** To determine whether glutamate or ammonium is the limiting factor, additional glutamate dehydrogenase (GDH, blue) was introduced via expression from an IPTG inducible promoter (P_{HS}-*rocG*, referred to throughout this text as P_{HS}-GDH). **(E)** The additional GDH (+ 1 mM IPTG) eliminates the pattern of nitrogen stress response (P_{nasA}-*yfp*, green) at 36hr. See also Figure 2.4B. **(F)** Maximal P_{nasA}-*yfp* intensity at 36hr (mean ± SEM, n = 8 biofilms for WT, n = 12 biofilms for '- IPTG', n = 7 biofilms for '+ 1 mM IPTG').

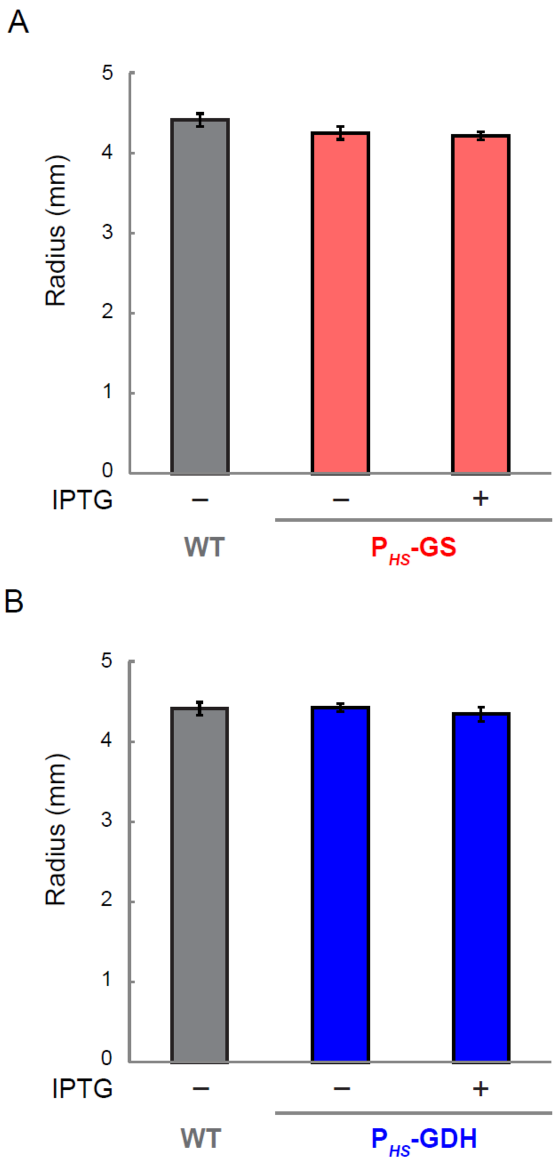

Figure 2.4 Minimal change in biofilm growth due to genetic perturbations.
Mean biofilm radius after 36 hr of growth of WT and (A) P_{HS}-GS, or (B) P_{HS}-GDH strains with and without addition of 1 mM IPTG to induce each enzyme overexpression (mean ± SEM, n = 7, 10, 13, 8 and 9 for WT, P_{HS}-GS without or with IPTG, and P_{HS}-GDH without or with IPTG, respectively).

Figure 2.5 Ring-shaped pattern of nitrogen stress is formed by active production and consumption of ammonium in cells.

(A) Maximal P_{nasA}-*yfp* intensity depending on the initial glutamate concentration (mean ± SEM, n = 7 biofilms for 34 mM glutamate, n = 5 for 68 mM glutamate, and n = 15 for 102 mM glutamate). **(B)** P_{nasA}-*yfp* expression (green) for each glutamate concentration was merged with the corresponding bright field image. Relative distances from the center to the edge are marked with ticks, and the center of the ring is marked with a dashed line. **(C)** Relative ring locations shown in panel B were quantified for multiple biofilms (mean ± SEM, data was obtained from the same biofilms shown in panels A and B). See also Figure2.6A. **(D)** Maximal P_{nasA}-*yfp* intensity in GDH overexpression strain depending on IPTG induction level (mean ± SEM, n = 5 biofilms for 0 and 100 μM IPTG, n = 6 biofilms for 5 μM IPTG, and n = 7 biofilms for 10 μM IPTG). The Intensities were normalized against WT intensity within the same experimental set. **(E)** P_{nasA}-*yfp* expression (green) in GDH overexpression strain at each IPTG concentration was merged with the corresponding bright field image. Relative distances from the center to the edge are marked with ticks, and the center of the ring is marked with a dashed line. **(F)** Relative ring locations shown in panel E were quantified for multiple biofilms (mean ± SEM, data was analyzed from the same biofilms with D). Gray box in 100 μM IPTG is due to the absence of a ring to quantify under this condition. See also Figure 2.6B. **(G)** The change in P_{nasA}-*yfp* expression (green) at each time point was merged with the corresponding bright field image. The transient inward propagation of the nitrogen stress response makes the ring pattern thicker. **(H)** Quantitative time trace of the inner boundary of the increased P_{nasA}-*yfp* expression shown in panel G (mean ± SEM, n = 7). The time point at which the ring began to move inward is set to zero.

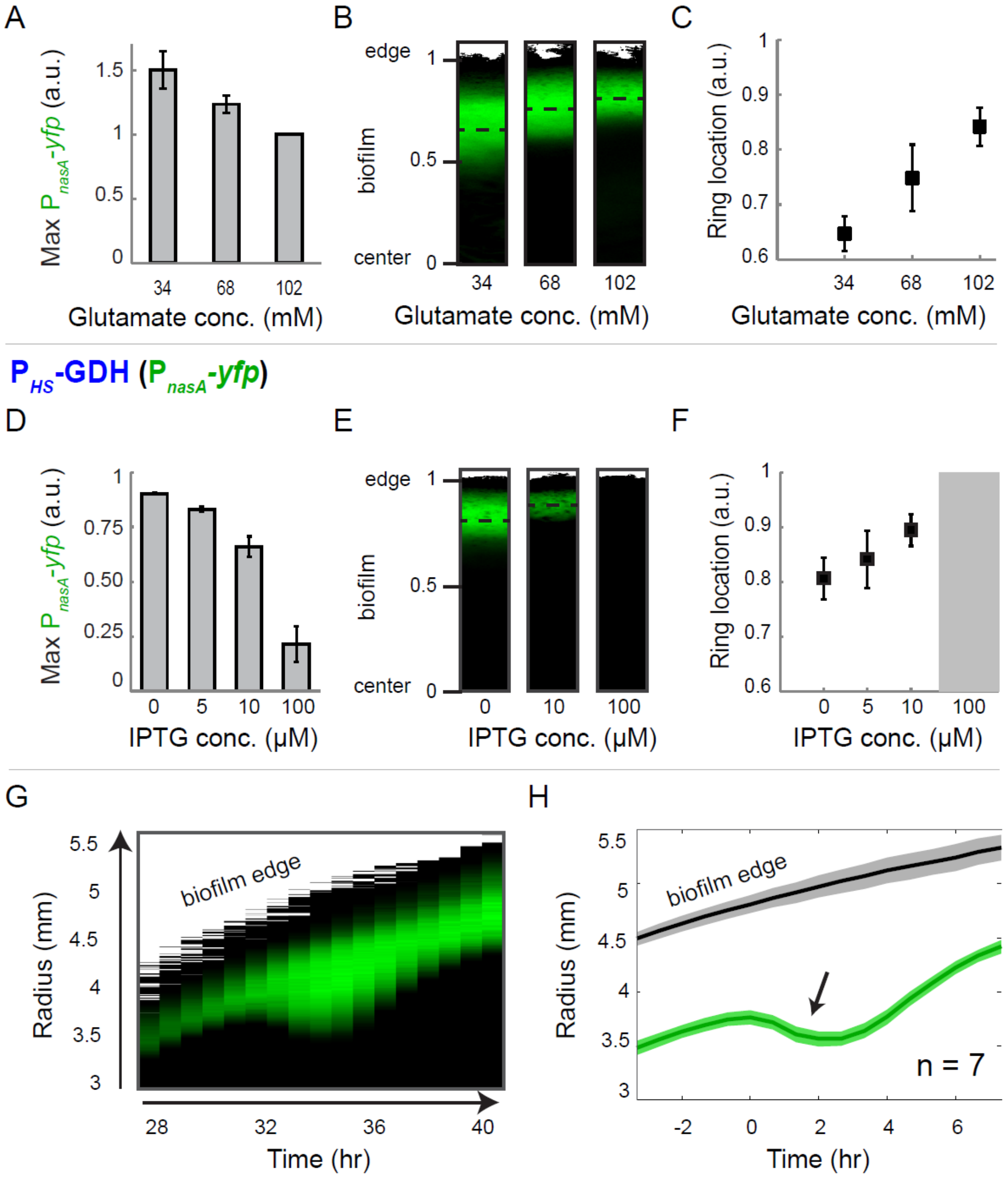
A
Max P_nasA-yfp (a.u.)
1.5
1
0.5
0
34
68
102
Glutamate conc. (mM)
B
edge
biofilm
center
1
0.5
0
34
68
102
Glutamate conc. (mM)
C
Ring location (a.u.)
1
0.9
0.8
0.7
0.6
34
68
102
Glutamate conc. (mM)
P_HS-GDH (P_nasA-yfp)
D
Max P_nasA-yfp (a.u.)
1
0.75
0.50
0.25
0
0
5
10
100
IPTG conc. (μM)
E
edge
biofilm
center
1
0.5
0
0
10
100
IPTG conc. (μM)
F
Ring location (a.u.)
1
0.9
0.8
0.7
0.6
0
5
10
100
IPTG conc. (μM)
G
Radius (mm)
5.5
5
4.5
4
3.5
3
biofilm edge
28
32
36
40
Time (hr)
H
Radius (mm)
5.5
5
4.5
4
3.5
3
biofilm edge
n = 7
-2
0
2
4
6
Time (hr)

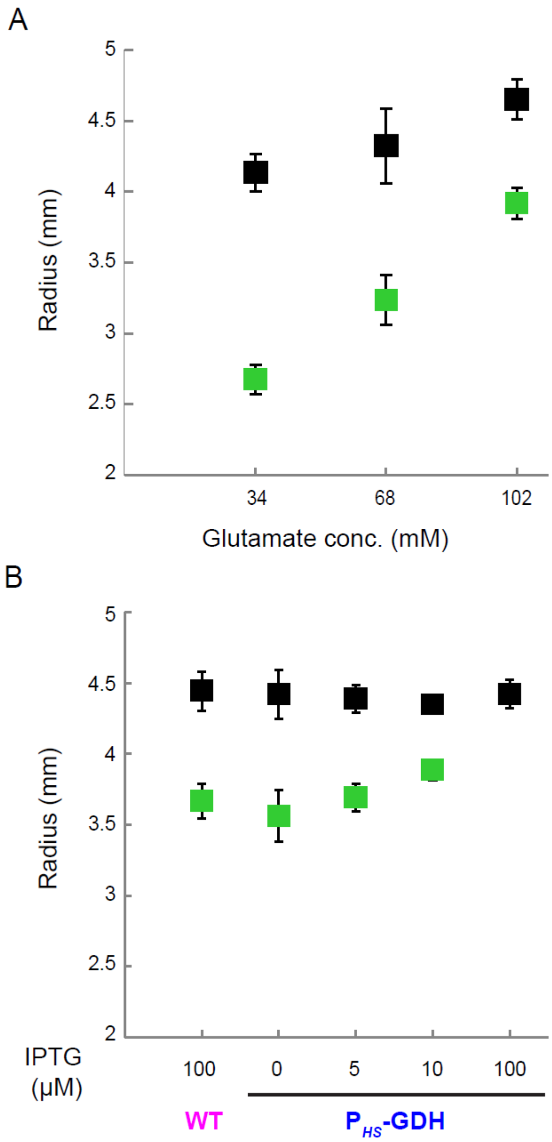

Figure 2.6 Radius of the ring center and biofilm size in various conditions.
(A) The real ring center (green squares) and biofilm size (black squares) used to quantify the relative ring location shown in Figure 2.5C. **(B)** The real ring center (green squares) and biofilm size (black squares) used to quantify the relative ring location shown in Figure 2.5F.

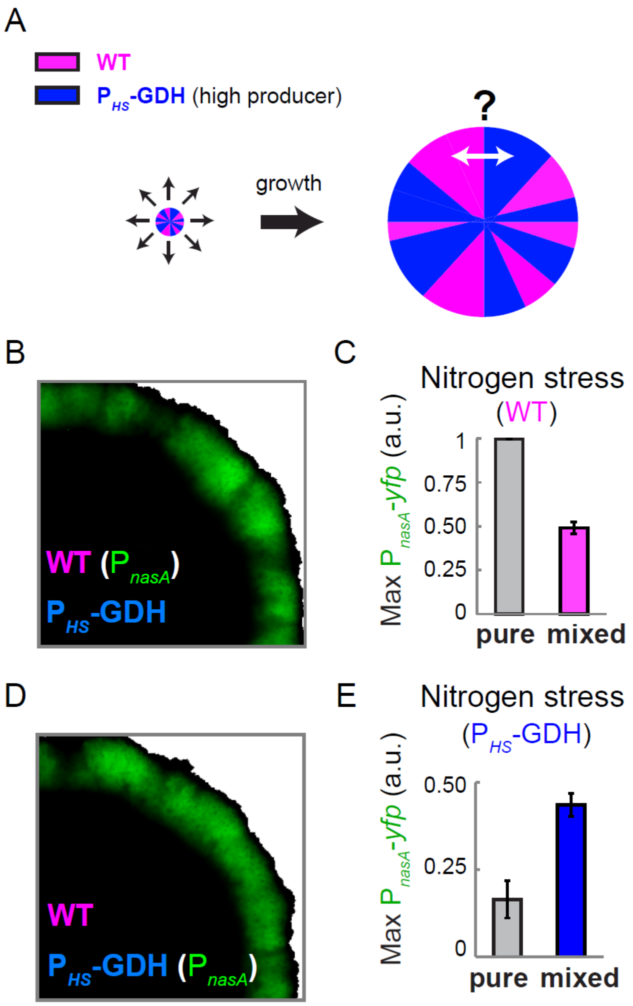

Figure 2.7 **Nitrogen stress responses in mixed biofilms are coupled between different strains.**

(A) Mixed biofilms are comprised of equal amounts WT and GDH-overexpression strains. Biofilm cells grow in segregated lineages. **(B)** P_{nasA}-*yfp* expression (green) in a mixed biofilm with only the WT strain containing the P_{nasA}-*yfp* reporter. **(C)** Maximal P_{nasA}-*yfp* intensity of WT strain in pure (WT only, n = 6) and in mixed (WT and P_{HS}-GDH, n = 14) biofilms, respectively (mean ± SEM). See also Figure 2.9A. **(D)** P_{nasA}-*yfp* expression (green) in a mixed biofilm with only the P_{HS} –GDH strain containing the P_{nasA}-*yfp* reporter. **(E)** The maximal P_{nasA}-*yfp* intensity of P_{HS} –GDH strain in pure (P_{HS} –GDH only, n =7) and mixed (WT and P_{HS}-GDH, n = 7) biofilms, respectively (mean ± SEM). Pure P_{HS} –GDH biofilm data is from Figure 2.2F. See also Figure 2.9B.

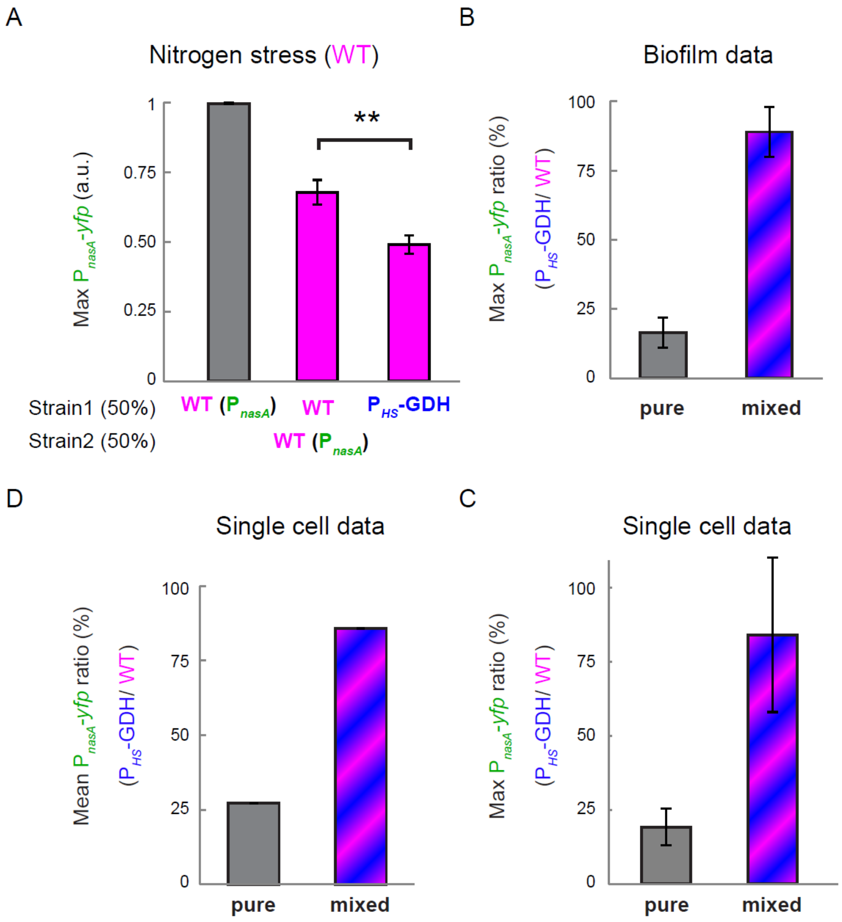

Figure 2.8 **P$_{nasA}$-*yfp* intensity in pure and mixed populations.**
(A) The maximal P$_{nasA}$-*yfp* intensity in mixed biofilms consisting of a 1:1 ratio of the indicated strains. Strain2 is always the WT strain with P$_{nasA}$-*yfp* reporter. Maximal intensity from a biofilm consisting of unlabeled and P$_{nasA}$-*yfp* labeled cells (middle, mean ± SEM, n =8) is decreased compared to that in pure WT P$_{nasA}$-*yfp* labeled biofilms (left), but it is also distinct from that in mixed biofilms containing the P$_{HS}$-GDH strain (right, ** $p < 0.008$, Student's t-test). For consistent data analysis, the P$_{nasA}$ intensity data given in figure 3 were all normalized by the P$_{nasA}$-*yfp* intensity from a pure WT biofilm (P$_{nasA}$-*yfp* reporter strain in non-mixed condition) within the same experimental set. **(B)** The maximal P$_{nasA}$-*yfp* intensity of the P$_{HS}$-GDH strain relative to that of the wild-type strain in biofilms (mean ± SEM). Biofilm data shown here were derived from the same experiments that produced Figures 2.3 and 2.7. **(C)** The maximal P$_{nasA}$-*yfp* intensity of the P$_{HS}$-GDH strain relative to that of the wild-type strain in single cells (mean ± SEM, n = 3). Single cell data shown here were derived from the same experiments used in Figures 2.9E and 2.9F, but instead of using mean P$_{nasA}$-*yfp* intensity, we use the maximal P$_{nasA}$-*yfp* intensity for each experimental set. **(D)** Mean P$_{nasA}$-*yfp* intensity of the P$_{HS}$-GDH strain relative to that of the wild-type strain in single cells (mean ± SEM). Single cell data shown here were derived from the same experiments that used in Figures 5E and 5F. Error bars are too tight to be shown on behalf of a number of data set. The conclusion from this mean P$_{nasA}$-*yfp* intensity data is comparable with the one from maximal P$_{nasA}$-*yfp* intensity data.

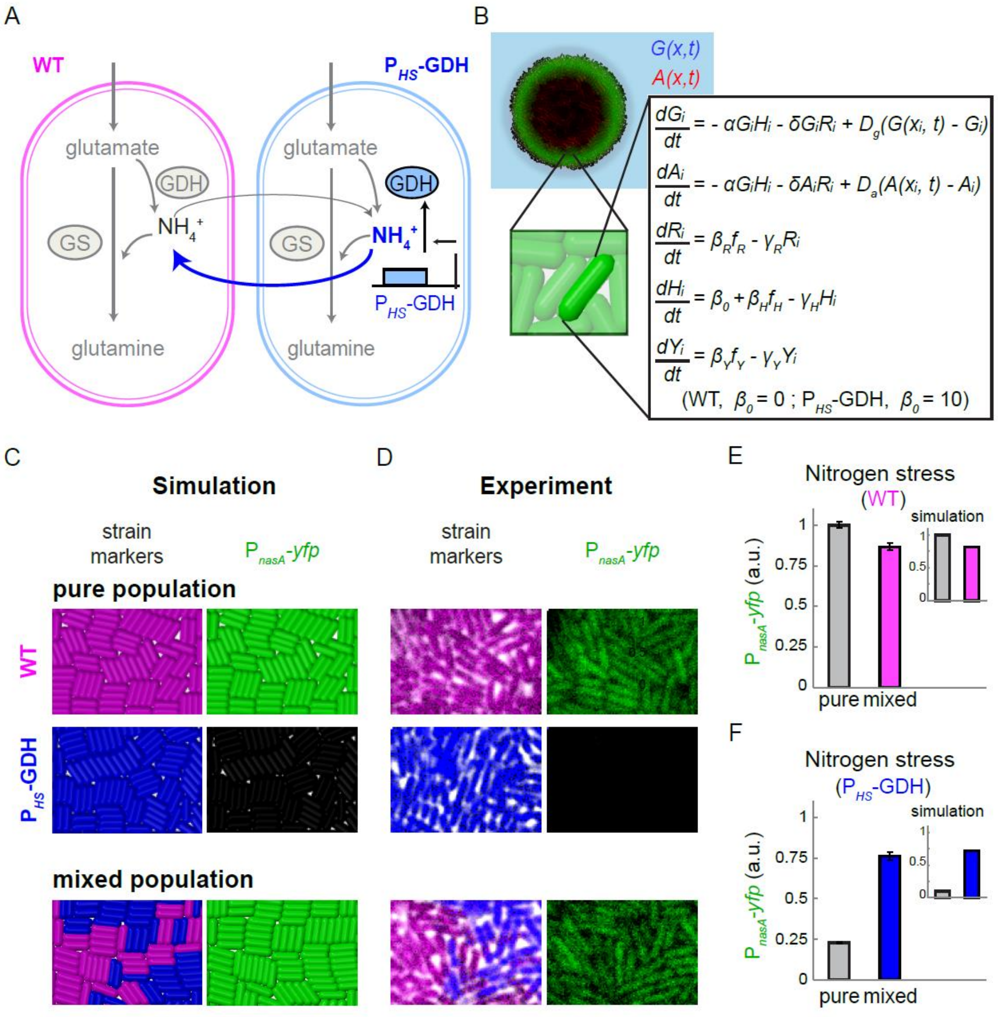

Figure 2.9 Nitrogen metabolic states are coupled at single cell level.

(A) In our "shared ammonium" hypothesis, ammonium made by cells is shared among its neighbors, and thus mediates metabolic coupling between distinct strains. P_{HS} –GDH strain produces and loses more ammonium than WT strain, acting as an ammonium source. **(B)** A combination of a discrete agent-based and a continuum model is used to test the "shared ammonium" hypothesis. Each hypothetical "bacterium" behaves based on the set of equations in the box, growing on the field with extracellular glutamate ($G(x, t)$) and ammonium ($A(x, t)$). $G_i(t)$, $A_i(t)$, $R_i(t)$, $H_i(t)$, $Y_i(t)$ are the intracellular amounts of glutamate, ammonium, housekeeping proteins, GDH and PnasA reporter expression, respectively. See also Figure 2.10. **(C)** Simulation results of the nitrogen stress responses in pure (top two) and mixed (bottom) populations. Both strain marker (left) and nitrogen stress reporter (right, P_{nasA}-*yfp*, green) are presented. **(D)** Experimental results of the nitrogen stress responses in pure (top two) and mixed (bottom) populations. Both strain markers (left, WT: P_{rpsD}-*mCherry*, magenta, P_{HS} –GDH: P_{rpsD}-*cfp*, blue) and nitrogen stress reporter (right, P_{nasA}-*yfp*, green) are presented. **(E)** Mean P_{nasA}-*yfp* intensity from each WT cell in pure (gray, n = 302 cells) and in mixed (magenta, n = 174 cells) populations (mean ± SEM). Simulation results are shown as an inset. **(F)** Mean P_{nasA}-*yfp* intensity from each P_{HS} -GDH cell in pure (gray, n = 360 cells) and in mixed (blue, n = 171 cells) populations (mean ± SEM). Simulation results are shown as an inset. See also Figures 2.9C-D.

Table 2.1 *Bacillus subtilis* strains used in this study

Strain	Genotype	Source
WT	*Bacillus subtilis* NCIB 3610	(Irnov and Winkler 2010)
P$_{HS}$-*cfp*, P$_{nasA}$-*yfp*	*amyE::* P$_{hyperspank}$-*cfp*, *sacA::* P$_{nasA}$-*yfp* (Sp^{R}, Cm^{R})	This study
P$_{HS}$-GS, P$_{nasA}$-*yfp*	*amyE::* P$_{hyperspank}$-*glnA*, *sacA::* P$_{nasA}$-*yfp* (Sp^{R}, Cm^{R})	This study
P$_{HS}$-GDH, P$_{nasA}$-*yfp*	*amyE::* P$_{hyperspank}$-*rocG*, *sacA::* P$_{nasA}$-*yfp* (Sp^{R}, Cm^{R})	This study
P$_{rpsD}$-*mCherry*, P$_{nasA}$-*yfp*	*amyE::* P$_{prpsD}$-*mCherry*, *sacA::* P$_{nasA}$-*yfp* (Sp^{R}, Cm^{R})	This study
P$_{HS}$-GDH, P$_{rpsD}$-*cfp*, P$_{nasA}$-*yfp*	*amyE::* P$_{prpsD}$-*cfp*, P$_{hyperspank}$-*rocG*, *sacA::* P$_{nasA}$-*yfp* (Sp^{R}, Cm^{R})	This study
P$_{nrgA}$-*cfp*, P$_{nasA(mut)}$-*yfp*	*amyE::* P$_{nrgA}$-*cfp*, *sacA::* P$_{nasA(mut)}$-*yfp* (Sp^{R}, Cm^{R})	This study
P$_{citZ}$-*cfp*, P$_{nasA}$-*yfp*	*amyE::* P$_{citZ}$-*cfp*, *sacA::* P$_{nasA}$-*yfp* (Sp^{R}, Cm^{R})	This study
P$_{sucC}$-*cfp*, P$_{nasA}$-*yfp*	*amyE::* P$_{sucC}$-*cfp*, *sacA::* P$_{nasA}$-*yfp* (Sp^{R}, Cm^{R})	This study

3 Metabolic codependence gives rise to collective oscillations within biofilms

3.1 Abstract

Cells that reside within a community can cooperate and also compete with each other for resources. It remains unclear how these opposing interactions are resolved at the population level. Here we investigated such an internal conflict within a microbial biofilm community: Cells in the biofilm periphery not only protect interior cells from external attack but also starve them through nutrient consumption. We discovered that this conflict between protection and starvation is resolved through the emergence of long-range metabolic codependence between peripheral and interior cells. As a result, biofilm growth halts periodically, increasing nutrient availability for the sheltered interior cells. We show that this collective oscillation in biofilm growth benefits the community in the event of a chemical attack. These findings indicate that oscillations support population-level conflict resolution by coordinating competing metabolic demands in space and time, suggesting new strategies to control biofilm growth.

3.2 Introduction

Cooperation and competition are complex social interactions that can play critical roles in biological communities. Cooperative behavior often increases the overall fitness of the population through processes such as division of labor and production of common goods (Ben-Jacob, Cohen, and Levine 2000; Eldar 2011; Gregor et al. 2010; Wingreen and Levin 2006). At the same time, individuals in a community compete with each other for limited resources, such as nutrients (Hibbing et al. 2010; Oliveira, Niehus, and Foster 2014). Here we investigated bacterial biofilms (D. Davies 2003; Donlan and Costerton 2002; Vlamakis et al. 2008; Yildiz and Visick 2009) to determine how the conflict between the opposing social behaviors of cooperation and competition could be resolved at the community level to increase overall fitness.

Biofilms typically form under environmental stress conditions, such as nutrient limitation (Berk et al. 2012; J. W. Costerton 1999; Hall-Stoodley, Costerton, and Stoodley 2004). As these bacterial communities grow larger, the supply of nutrients to interior cells becomes limited due to an increase in nutrient consumption associated with the growth of multiple layers of cells in the biofilm periphery. Severe nutrient limitation for interior cells is detrimental to the colony since the sheltered interior cells are critical to the survival of the biofilm community in the event of an external challenge. This defines a fundamental conflict between the opposing demands for biofilm growth and maintaining the viability of protected (interior) cells (Fig. 3.1A). The identification of possible mechanisms that ensure the viability of the protected interior cells is fundamental to understanding biofilm development (Asally et al. 2012; Wilking et al. 2013).

In order to directly investigate how *Bacillus subtilis* biofilms continue expanding while sustaining interior cells, we converted the potentially complex three-dimensional problem to a simpler two-dimensional scenario using microfluidics. Specifically, we used growth chambers that are unconventionally large in the lateral, x-y dimensions (3 × 3 mm), while confining biofilm thickness (z-dimension) to only a few micrometers (Fig. 3.1B). Therefore, biofilm expansion in this device is predominantly limited to two dimensions, creating a “pancake-like” configuration. In fact, biofilms often form in confined aqueous environments and thus this microfluidic chamber may better mimic those growth conditions (Berk et al. 2012; J. W. Costerton 1999; Hall-Stoodley, Costerton, and Stoodley 2004). This experimental set-up is thus ideal to interrogate how biofilms can reconcile the opposing benefits of growth and protection during biofilm development.

3.3 Results

3.3.1 Oscillations in biofilm growth

Unexpectedly, we observed oscillations in biofilm expansion despite constant media flow within the microfluidic device (Fig. 3.1C, D, and 3.5A). Specifically, biofilms exhibit a periodic reduction in colony expansion that is self-sustained and can last for more than a day (Fig. 3.1E and 3.5B). The period of oscillations has a mean of 2.5 ± 0.8 hours (s.d., n = 63 colonies), which is less than the duration of the average cell replication time of 3.4 ± 0.2 hours (s.d., n = 21 cell cycles) under this growth condition (Fig. 3.1F). Moreover, oscillations only arise when the biofilm exceeds a certain colony size. In particular, quantitative measurements obtained from 53 individual biofilms indicate that oscillations emerge in colonies that exceed an average diameter of 580 ± 85 μm (s.d., n = 53 colonies), which corresponds to approximately one million cells (Fig. 3.1G, H). Together, these data show that oscillations arise during biofilm formation and are self-sustained.

Given that biofilms typically form under nutrient-limited conditions and bacterial growth is generally controlled by metabolism, we hypothesized that metabolic limitation plays a key role in the observed periodic halting of biofilm expansion. In particular, after determining that carbon source limitation did not play an essential role in the oscillations (Fig. 3.6), we focused on nitrogen limitation. The standard biofilm growth media (MSgg, see Methods: Growth conditions) used to study *B. subtilis* biofilm development contains glutamate as the only nitrogen source16. In most organisms including *B. subtilis*, glutamate is combined with ammonium by glutamine synthetase (GS) to produce glutamine, which is essential for biomass production and growth (Fig. 3.2A) (Gunka and Commichau 2012). Cells can obtain the necessary ammonium from glutamate through the enzymatic activity of glutamate dehydrogenase (GDH), expressed by the rocG or gudB genes in the undomesticated *B. subtilis* used in this study (Fig. 3.2A)(Stannek et al. 2015; Belitsky and Sonenshein 1998; Zeigler et al. 2008). To determine whether biofilms experience glutamine limitation, we measured the expression of nasA, one of several genes activated in response to a lack of glutamine (Nakano et al. 1995). Results show that biofilms indeed experience glutamine limitation during growth. Specifically, supplementation of growth media directly with glutamine reduced nasA promoter expression but did not affect the expression of a constitutive promoter, confirming glutamine limitation within the biofilm (Fig. 3.2B). More strikingly, the addition of exogenous glutamine eliminated periodic halting of biofilm growth (Fig. 3.2C and 3.7A). These findings suggest that glutamine limitation plays a critical role in the observed oscillations during biofilm expansion.

The synthesis of glutamine requires both glutamate and ammonium, therefore we investigated which of these substrates could be responsible for the observed glutamine limitation. Glutamate is provided in the media and is thus readily available to cells in the periphery of the biofilm. On the other hand, consumption of glutamate by peripheral cells is likely to limit its availability to cells in the biofilm interior (Fig. 3.2D). One may thus expect that oscillations in biofilm expansion could be due to periodic pausing of cell growth in the biofilm interior. Accordingly, we set out to establish whether interior or peripheral cells exhibited changes in growth. By tracking physical movement within the biofilm, we uncovered that only peripheral cells grow and that oscillations in biofilm expansion, therefore, arise exclusively from periodic halting of peripheral cell growth (Fig. 3.2E and 3.8A). This finding was further confirmed by single-cell resolution analysis that directly showed a periodic reduction in the growth of peripheral cells (Fig. 3.8B). This surprising pausing of cell growth in the periphery, despite unrestricted access to glutamate, suggests that glutamate cannot be the limiting substrate for glutamine synthesis. Consistent with this expectation, biofilm oscillations were not quenched by supplementation of the media with glutamate (Fig. 3.2F). Therefore, it is not glutamate, but ammonium that appears to be the limiting substrate for glutamine synthesis in the biofilm periphery.

Since cells can self-produce ammonium from glutamate, we next sought to determine how peripheral cells could experience periodic ammonium limitation despite a constant supply of glutamate in the media. It is well known that ammonium production is a highly regulated process that is dependent on the metabolic state of the cell and the ambient level of ammonium in the environment (Kleiner 1985). In particular, since ammonium is in equilibrium with ammonia vapor, which can freely cross the cell membrane and be lost to the extracellular media (Castorph and Kleiner 1984), the production of ammonium is known as a “futile cycle”. Cells therefore preferentially use extracellular (ambient) ammonium for growth, rather than producing their own (Boogerd et al. 2011; Jayakumar et al. 1986; M. Kim et al. 2012). Since peripheral cells are exposed to media flow, they are particularly susceptible to this futile cycle of ammonia loss. In this sense, since ammonium is not provided in the media, even if all cells produce ammonium, the biofilm interior will be the major source for ambient ammonium (Fig. 3.2D). Consequently, the simplifying hypothesis is that growth of peripheral cells relies on ammonium produced within the biofilm. To test this conjecture, we supplemented the media with 1 mM ammonium, which eliminated the periodic halting in biofilm expansion (Fig. 3.2G, 3.7B and 3.9A). When additional ammonium was suddenly removed from the media, growth in the biofilm periphery halted as expected (Fig. 3.9B). These findings indicate that peripheral cells preferentially rely on extracellular ammonium produced within the biofilm for their growth.

3.3.2 Metabolic codependence between the biofilm periphery and interior

The results described above evoke the intriguing possibility that ammonium limitation for peripheral cells may arise due to glutamate limitation for interior cells. Specifically, persistent consumption of glutamate by peripheral cells can deprive the interior cells of the necessary glutamate for ammonium production. In order to explore this nontrivial hypothesis, we turned to mathematical modeling to develop a conceptual framework and generate experimentally testable predictions. Our model describes separately the metabolic dynamics of interior and peripheral cells and the metabolite exchange between them, where the distinction of the two subpopulations depends on nutrient availability (see Chapter 3.6 Mathematical Model). The model thus consists of two main assumptions (Fig. 3.3A): First, consumption of glutamate during growth of peripheral cells deprives interior cells of this nutrient and thus inhibits ammonium production in the biofilm interior. Second, the growth of peripheral cells depends predominantly on ammonium that is produced by metabolically stressed interior cells. A model based on these two simplifying assumptions (Fig. 3.3B) generates oscillations consistent with our experimental observations (Fig. 3.3C-E) and reproduces the effects of supplementing the media with glutamine, glutamate, and ammonium (Fig. 3.3F-H, and 3.10, and Chapter 3.6 Mathematical Model). The model also accounts for the observed slight increase of the oscillation period by considering an increase in the ratio of interior to peripheral cells over time (Fig. 3.5B and 3.10F). Therefore, this simple model shows that periodic halting in biofilm growth can result from metabolic codependence between cells in the biofilm periphery and interior that is driven by glutamate consumption and ammonium production, respectively.

The metabolic codependence between interior and peripheral cells gives rise to the surprising prediction that external attack could promote growth within the biofilm. Specifically, the killing of peripheral cells will eliminate their glutamate consumption, which will increase glutamate availability in the biofilm and thereby promote the growth of interior cells (Fig. 3.4A). To test this hypothesis, we measured cell death and growth within oscillating biofilms (Fig. 3.4B, top and 3.11). When we exposed the biofilm to media containing hydrogen peroxide (H2O2), we observed increased cell death predominantly in the biofilm periphery (Fig. 3.4B, bottom and 3.12). As predicted, the death of peripheral cells led to the growth of interior cells (Fig. 3.4C and 3.12). To verify that this response is not uniquely triggered by H_2O_2, we exposed biofilms to the antibiotic chloramphenicol and again observed the growth of interior cells (Fig. 3.12). These findings further support our hypothesis that glutamate consumption by peripheral cells limits its availability in the biofilm.

3.3.3 The benefit of biofilm oscillations

Our model also assumes that glutamate starvation of the biofilm interior reduces the production of ammonium that can support peripheral cell growth. This assumption provokes the question as to why peripheral cells do not simply overcome their dependence on extracellular ammonium by increasing intracellular production (Commichau et al. 2008; Detsch 2003). To address this question, we constructed a strain that contains an inducible copy of the GDH gene rocG (Fig. 3.4D). We confirmed that GDH overexpression was not toxic to individual cells and did not affect their growth rate (Fig. 3.13). In contrast, the induction of GDH expression in the biofilm quenched growth oscillations (Fig. 3.4E and 3.7C) and resulted in high levels of cell death in the colony interior (Fig. 3.4F, top). This result explains why peripheral cells do not appear to utilize the simple strategy of overcoming their dependence on extracellular ammonium: such a strategy would result in the continuous growth of peripheral cells, starving and ultimately causing the death of sheltered interior cells within the biofilm. The periodic halting of peripheral cell growth due to extracellular ammonium limitation thus promotes the overall viability of the biofilm.

The ability of the biofilm to regenerate itself in the event of an external attack suggested that killing the biofilm interior first would be a more effective strategy for biofilm extermination. Accordingly, we exposed the GDH overexpression strain to hydrogen peroxide and again measured growth and death. As described above, GDH induction causes the death of interior cells. Exposing the GDH overexpression strain to hydrogen peroxide resulted in more effective global killing throughout the biofilm (Fig. 3.4F, G, bottom). While in the wild-type biofilm interior cells begin to grow in response to an external attack, metabolic independence between interior and peripheral cells in the GDH strain interferes with this defense mechanism (Fig. 3.4H). This outcome is also consistent with modeling predictions (Fig. 3.4H, inset). Oscillations in biofilm growth that are driven by metabolic codependence thus promote the resilience of the biofilm community by sustaining the viability of the sheltered interior cells that are most likely to survive in the event of an environmental stress (Fig. 3.4I).

3.4 Discussion

The data presented here reveal that intracellular metabolic activity within biofilms is organized in space and time, giving rise to codependence between interior and peripheral cells. Even though bacteria are single-celled organisms, the metabolic dynamics of individual cells can thus be regulated in the context of the community. This metabolic codependence can, in turn, give rise to collective oscillations that emerge during biofilm formation and promote the resilience of biofilms against chemical attack. The community-level oscillations also support the ability of biofilms to reach large sizes, while retaining a viable population of interior cells. Specifically, the periodic halting of peripheral cell growth prevents complete starvation and death of the interior cells. This overcomes the colony size limitation for a viable biofilm interior that would otherwise be imposed by nutrient consumption in the biofilm periphery. Metabolic codependence in biofilms, therefore, offers an elegant solution that resolves the social conflict between cooperation (protection) and competition (starvation) through oscillations.

The intriguing discovery of biofilm oscillations presented here also provokes new questions. While cellular processes such as swarming or expression of extracellular matrix components are not required for the observed biofilm oscillations (Fig. 3.14), it will be interesting to pursue whether such cellular processes are influenced by oscillatory dynamics (Anyan et al. 2014). Another question worth pursuing is whether metabolic codependence can also arise in other biofilm-forming species. Perhaps other metabolic branches where metabolites can be shared among cells could also give rise to oscillations in biofilm growth. It will be exciting to pursue these questions in future studies to obtain a better understanding of biofilm development.

Our observations also suggest future strategies to cope with the intriguing resilience of biofilms in the face of environmental stresses, such as antibiotic exposure. In particular, our findings show that straightforward application of stress (such as H_2O_2 or chloramphenicol) to the biofilm counterintuitively promotes growth, effectively rejuvenating the biofilm. Death of the colony periphery relieves the repression on the growth of interior cells, allowing them to regenerate a new biofilm periphery and interior. In contrast, manipulation of the metabolic codependence may yield a more effective approach to control biofilm formation. Specifically, promoting continuous growth of peripheral cells can starve the biofilm interior, leaving behind the exposed peripheral cells that can more easily be targeted by external killing factors. Therefore, the metabolically driven collective oscillations in biofilm expansion described here not only reveal fundamental insights into the principles that govern the formation of multicellular communities but also suggest new strategies for manipulating the growth of biofilms.

3.5 Method

3.5.1 Microfluidics

We used the CellASIC ONIX Microfluidic Platform and the Y04D microfluidic plate (EMD Millipore). In most of the experiments, we used a pump pressure of 1 psi with only one media inlet open (there are 6 media inlets in the Y04D plate), which corresponds to a flow speed of ~16 μm/s in the growth chamber.

A single colony was picked from the plate and inoculated into 3 ml of LB broth in a 50 ml conical tube, and then incubated in 37°C shaker. After 2.5 hours of incubation, the cell culture was centrifuged at 2100 rcf for 1 min, and then the cell pellet was re-suspended in MSgg and then immediately loaded into microfluidics. After the loading, cells in the microfluidic chamber were incubated at 37°C for 90 min, and then the temperature was kept at 30°C for the rest of the experiment.

3.5.2 Data analysis

ImageJ (National Institutes of Health) and MATLAB (MathWorks) were used for image analysis. In-house software was also developed to perform colony detection and quantification of colony expansion. Multiple methods of colony detection were used to ensure the accuracy of the analysis. To detect regions of expansion in a biofilm, we performed image differencing on snapshots of the biofilm from time-lapse microscopy videos. Specifically, we calculated the difference between two consecutive phase contrast images (taken 10 min apart) by finding the absolute difference between each pixel in each image. We then generated an image stack based on these results. The intensity values from the stack correlate with the expansion into the biofilm. The growth area was determined by converting difference images to binary images and then measuring the area of the colony growth region (white pixels). To measure cell replication time, we tracked the length and division of individual cells in the biofilm periphery (Fig. 3.8B).

Chapter 3, in full, is a reprint of the material *Jintao Liu, Arthur Prindle*, Jacqueline Humphries*, Marçal Gabalda-Sagarra*, Munehiro Asally*,* ***Dong-yeon D. Lee****, San Ly, Jordi Garcia-Ojalvo, and Gürol M. Süel. "Metabolic co-dependence gives rise to collective oscillations within biofilms" Nature vol. 523, 550–554. 2015 (*equal contribution).* The dissertation author participated in discussions, some of the experimental designs, and strain construction.

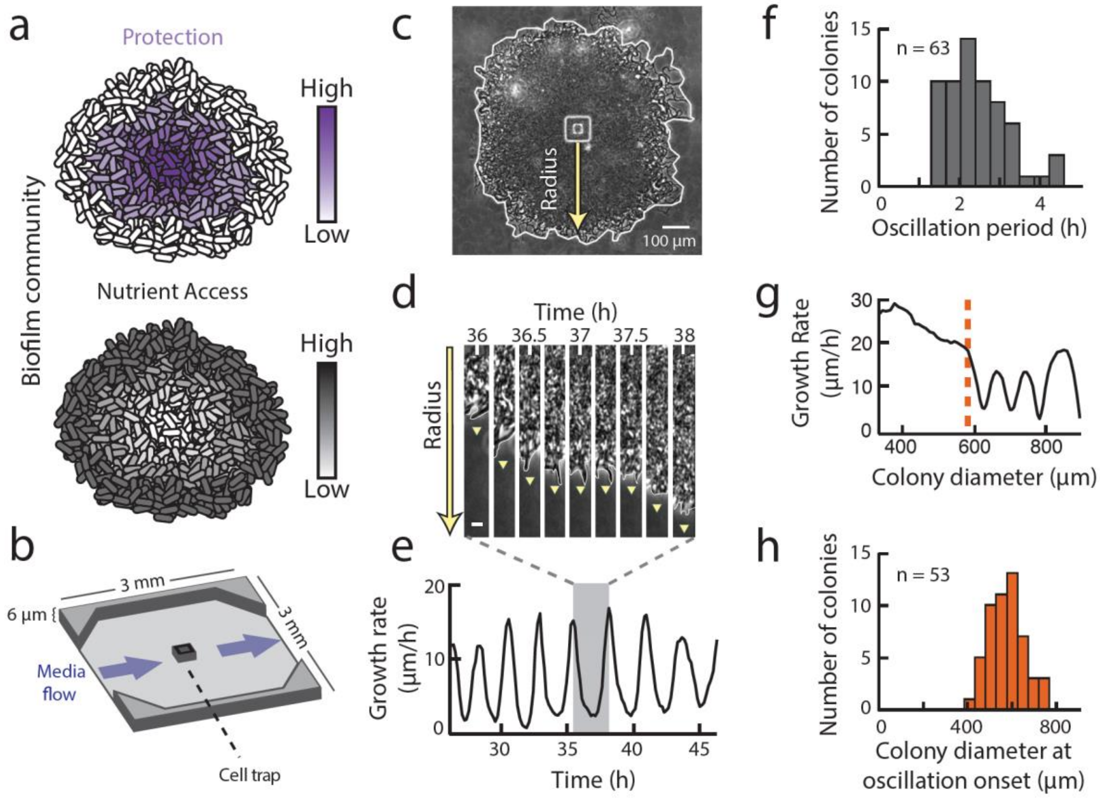

Figure 3.1 Biofilms grown in microfluidic devices show oscillations in colony expansion. **(A)** Biofilms must reconcile opposing demands for protection from external challenges (gradient indicated in purple) and access to nutrients (gradient indicated in gray). **(B)** Schematic of the microfluidic device used throughout this study. The direction of media flow is indicated by the blue arrows. **(C)** Phase contrast image of a biofilm growing in the microfluidic device. The yellow arrow indicates the region of interest in panel D. **(D)** Filmstrip of a radius of the biofilm over time shows a pause in colony expansion. This film strip represents one cycle of biofilm oscillations, indicated by the shaded region in panel E. Scale indicates 5 µm. **(E)** The growth rate over time shows persistent oscillations in colony expansion. **(F)** Histogram of the average period of oscillations for each colony (n = 63 colonies, mean = 2.5 hours, s.d. = 0.8 hours). The cell replication time is approximately 3.4 hours under these conditions (Chapter 3.5.2 Data Analysis). **(G)** Growth rate as a function of colony diameter (which increases in time) shows that early colony growth does not exhibit oscillations. The orange line indicates the diameter (~600 µm) at which this colony initiates oscillations. **(H)** Histogram of the diameter at which a colony begins to oscillate (n = 53 colonies, mean = 576 µm, s.d. = 85 µm).

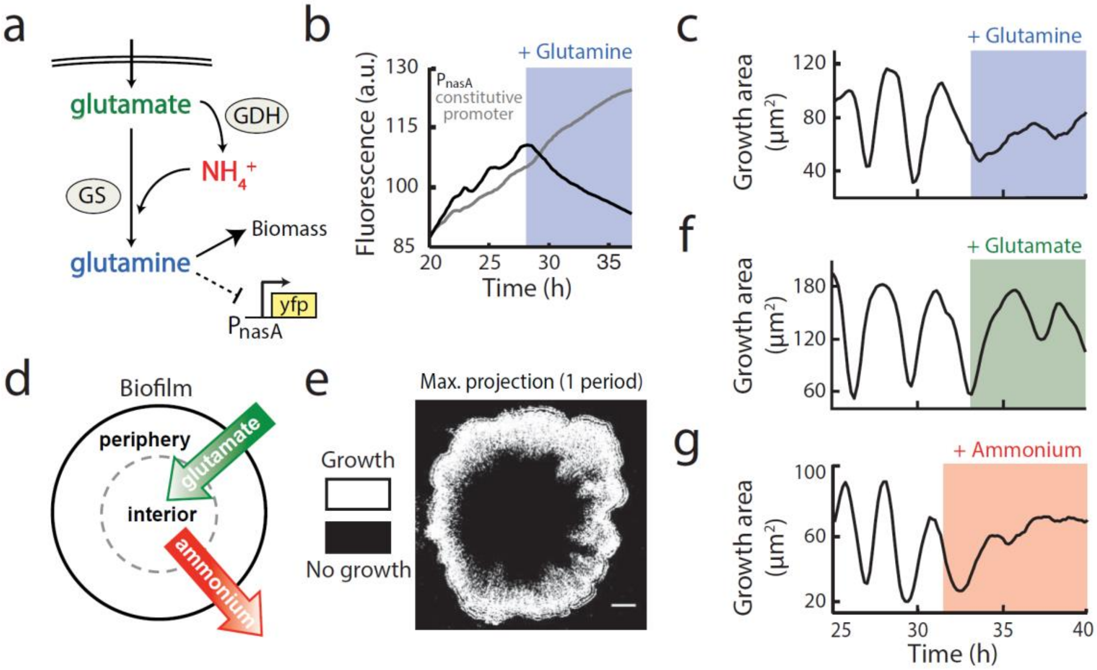

Figure 3.2 Biofilm growth depends specifically on extracellular ammonium availability. **(A)** Colony growth in the MSgg medium depends on the production of glutamine from externally supplied glutamate and self-produced or scavenged ammonium. Glutamine limitation was monitored using YFP expressed from the *nasA* promoter, which is activated upon glutamine limitation[21]. **(B)** Addition of 1 mM glutamine (blue shading) represses expression from the P*nasA*-YFP reporter (black) but does not affect expression from a constitutive reporter (P*hyperspank*-CFP + 1 mM IPTG, gray). **(C)** Growth area (see Chapter 3.5.2 Data Analysis) before and after addition of 1 mM glutamine to an oscillating colony. **(D)** Of the two nutrients required for glutamine production, externally supplied glutamate (green) is most abundant in the biofilm periphery, while biofilm-produced ammonium (red) is most abundant in the biofilm interior. **(E)** Maximum intensity projection over one period of a colony oscillation, made from a difference movie (Chapter 3.5.2 Data Analysis), which shows regions of growth (white) and no growth (black). Scale bar represents 100 µm. **(F)** Growth area of an oscillating colony before and after addition of 30 mM glutamate (green shading). **(G)** Growth area of an oscillating colony before and after addition of 1 mM ammonium (red shading).

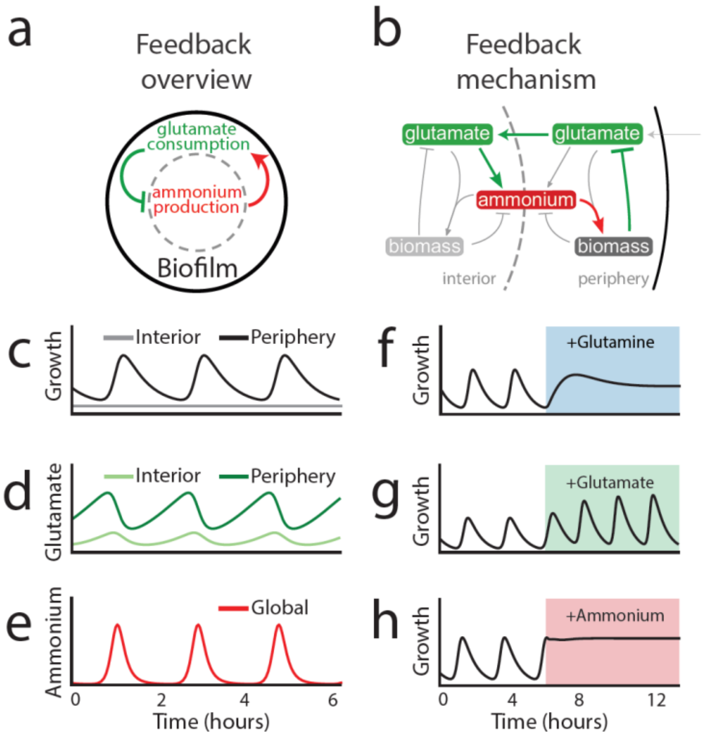

Figure 3.3 Mathematical modeling of a spatial metabolic feedback loop gives rise to oscillations consistent with experimental data.
(A) The production of ammonium in the interior is limited by and at the same time triggers the consumption of glutamate in the periphery (green and red arrows, respectively), producing a delayed negative feedback loop. **(B)** The excess glutamate not consumed by the biofilm periphery diffuses to the interior, where it can be converted into ammonium (green arrows). The ammonium, in turn, enhances growth in the periphery (red arrow) and consequently reduces the supply of glutamate to the interior. Model predictions are shown in (**C-H**): **(C)** Biofilm growth over time. **(D)** Glutamate concentration over time. **(E)** Ammonium concentration over time. **(F)** Colony growth before and after glutamine addition (indicated by blue shading). **(G)** Colony growth before and after addition of glutamate (green shading). **(H)** Colony growth before and after addition of ammonium (red shading).

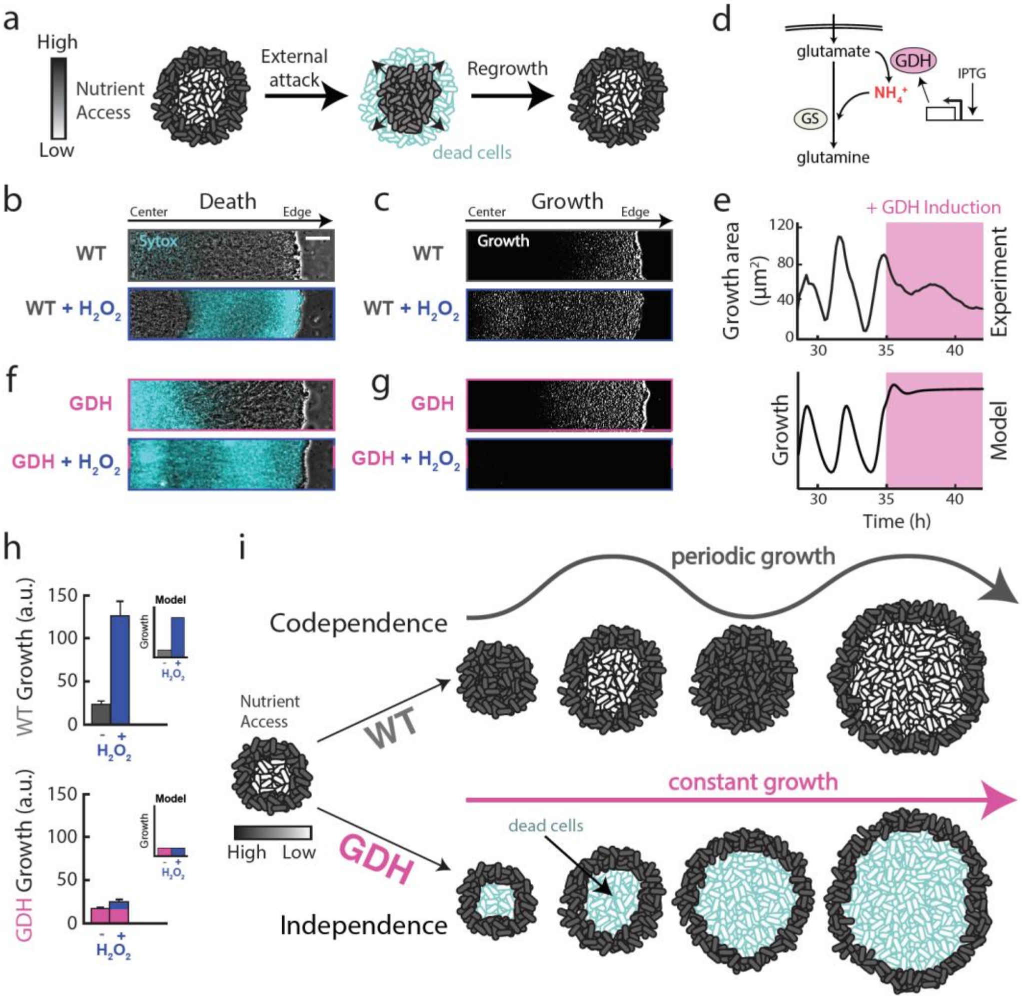

Figure 3.4 Metabolic codependence between interior and peripheral cells gives rise to oscillations that make the colony more resilient to external attack.

(A) Visual representation of the predicted outcome of an external attack on biofilm growth. **(B)** Phase contrast merged with cell death marker (cyan, 1 µM Sytox Green) images of a wild-type biofilm region shows cell death with and without challenge by 2% w/w H_2O_2. Scale bar represents 50 µm. **(C)** In the same biofilm, difference images (white regions indicate cell growth) show wild-type growth with and without challenge by H_2O_2. **(D)** Overexpression of glutamate dehydrogenase (GDH, pink) promotes more production of ammonium from glutamate. **(E)** Experimental (top) and modeling results (bottom) of GDH overexpression (induced with 1 mM IPTG, indicated by pink shading). **(F)** Phase contrast merged with cell death marker (cyan, 1 µM Sytox Green) images of a colony overexpressing GDH with and without challenge by H_2O_2. **(G)** In the same biofilm, difference images show cell growth during GDH overexpression alone, and with a challenge by H_2O_2. **(H)** Quantification of total biofilm growth rate in wild-type (upper, *n* = 4 colonies) and GDH overexpression (lower, *n* = 3 colonies) strains upon challenge with H_2O_2. Error bars represent standard deviations. Modeling data are shown as an inset for each strain. **(I)** Codependence between interior and peripheral cells exhibited in a wild-type strain results in a growth strategy that sustains the viability of interior cells, while independence enforced by a GDH overexpression strain results in starvation of interior cells and reduced resilience to external attack.

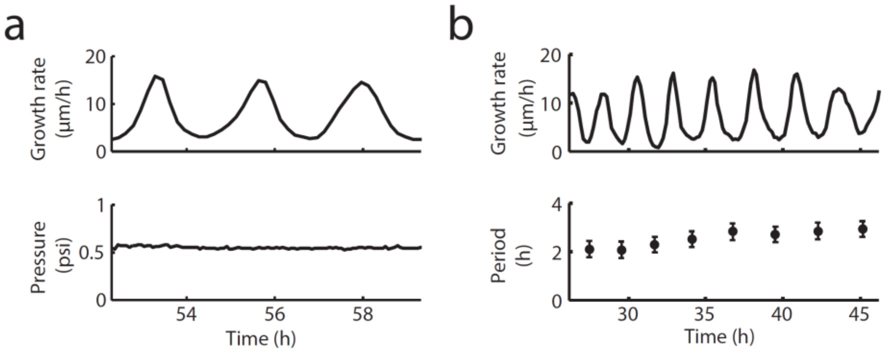

Figure 3.5 **Characterization of biofilm growth oscillations.**
(A) (Top) The growth rate over time of an oscillating colony. (Bottom) The pressure that drives media flow in the microfluidic chamber is constant over time (see Chapter 3.5.1 Microfluidics). **(B)** (Top) The growth rate of an oscillating colony. (Bottom) Period of each oscillation cycle, measured peak to peak. The error bars (±20 min) are determined by the imaging frequency (1 frame/10 min). The period slightly increases over time (see also Fig. 3.10F and Chapter 3.6 Mathematical Model).

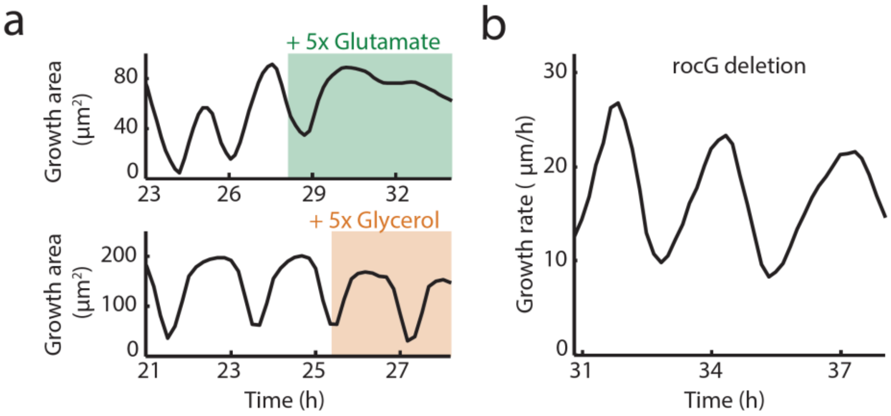

Figure 3.6 **Roles of carbon and nitrogen in biofilm growth oscillations.**
(A) Effect of increasing carbon (glycerol) or nitrogen (glutamate) availability on the oscillations. While increasing glutamate by 5 times of the normal MSgg levels leads to quenching of the oscillation, increasing glycerol by 5 times does not. **(B)** Colony growth of mutant strain with *rocG* deletion. *B. subtilis* NCIB 3610 has two glutamate dehydrogenases (GDH), *rocG* and *gudB*. While *gudB* is constitutively expressed, the *rocG* expression is subject to carbon catabolite repression[18]. The oscillatory growth of the *rocG* deletion strain indicates that carbon-source dependent regulation of *rocG* expression is not required for biofilm oscillations.

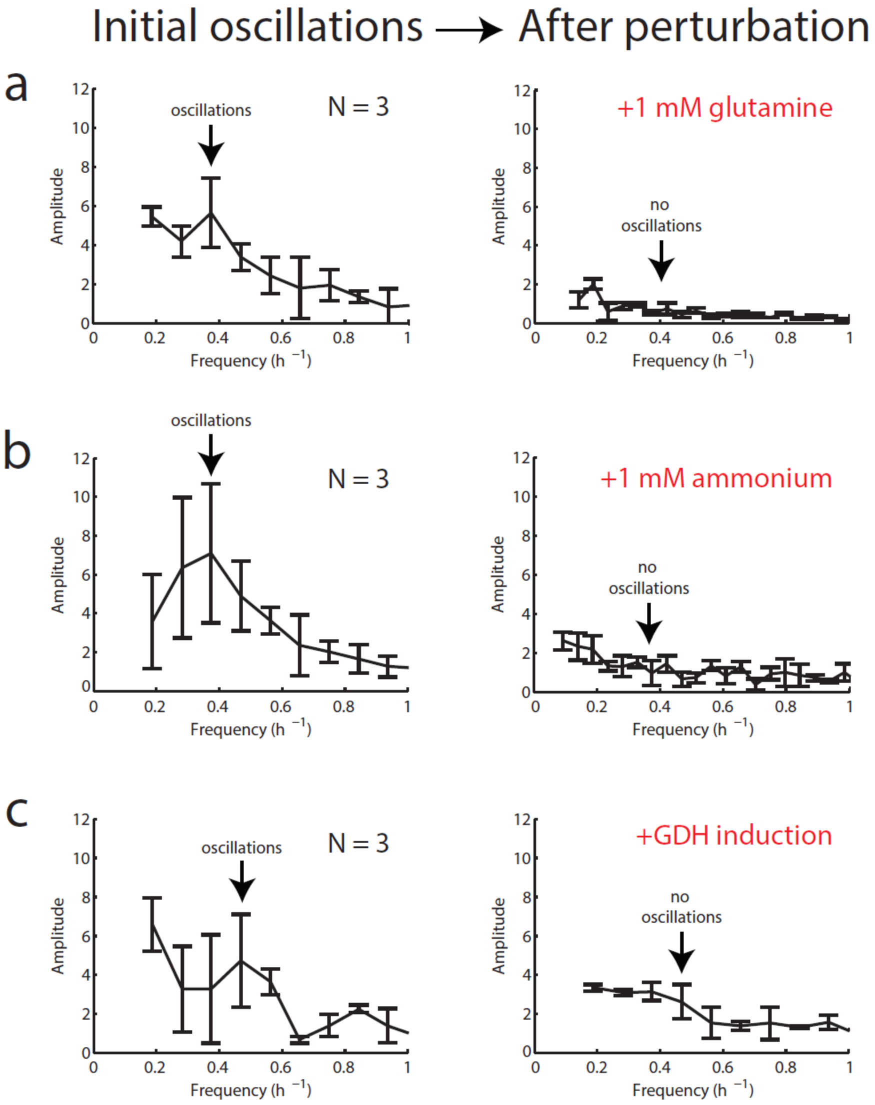

Figure 3.7 Fourier transform of biofilm growth rates before and after addition of indicated substances.

(A) 1 mM glutamine, **(B)** 1 mM ammonium, and **(C)** 1 mM IPTG to induce P*hyperspank*-RocG. The error bars show standard deviations (*n* = 3 colonies for each condition). The arrows indicate the frequency of oscillations for each condition before perturbation (left) and the lack of oscillations after perturbation (right).

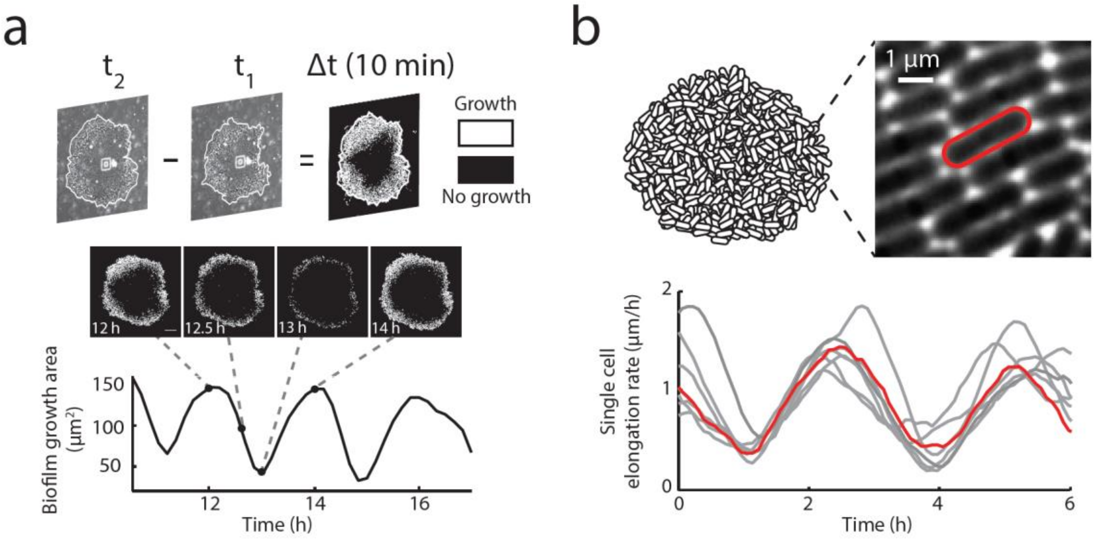

Figure 3.8 Measurements of cell growth within oscillating biofilms.
(A) (Top) Visual representation of the method through which difference movies are generated (Chapter 3.5.2 Data Analysis). Growth is represented by white pixels, and lack of growth is indicated by black pixels. (Middle) Filmstrip and (bottom) growth area over time of an oscillating colony. Dashed lines show the position of each image on the time trace. Scale bar represents 100 µm. **(B)** (Top left) schematic of a biofilm. (Top right) high magnification phase contrast image of biofilm periphery focused at the bottom layer of cells. (Bottom panel) time traces depicting elongation rates of single cells in gray. Highlighted in red is the single cell time trace for the cell outlined in red in the top right panel. The periodic slowdown of the growth of individual peripheral cells is responsible for the observed periodic reduction in biofilm expansion.

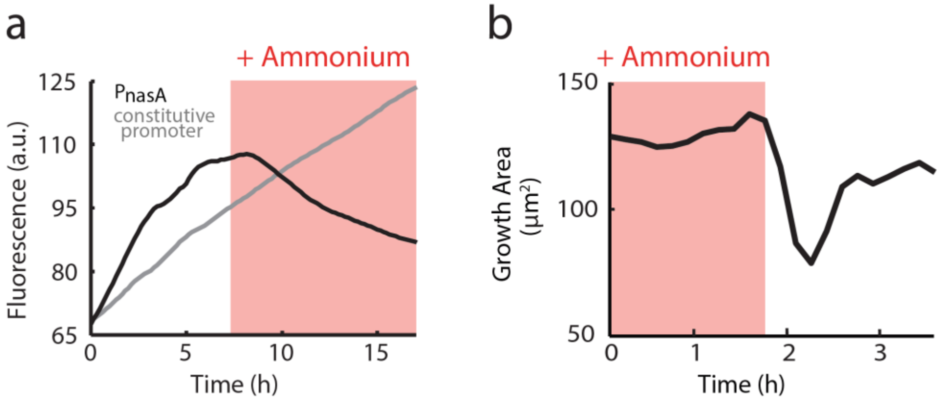

Figure 3.9 Effects of external ammonium on biofilm development.
(A) Addition of external ammonium (red shading, 1 mM) represses expression from the P*nasA*-YFP reporter (black) but does not affect expression from a constitutive reporter (P*hyperspank*-CFP + 1 mM IPTG, gray). **(B)** Removal of external ammonium (red shading, 13 mM) causes halting of colony growth.

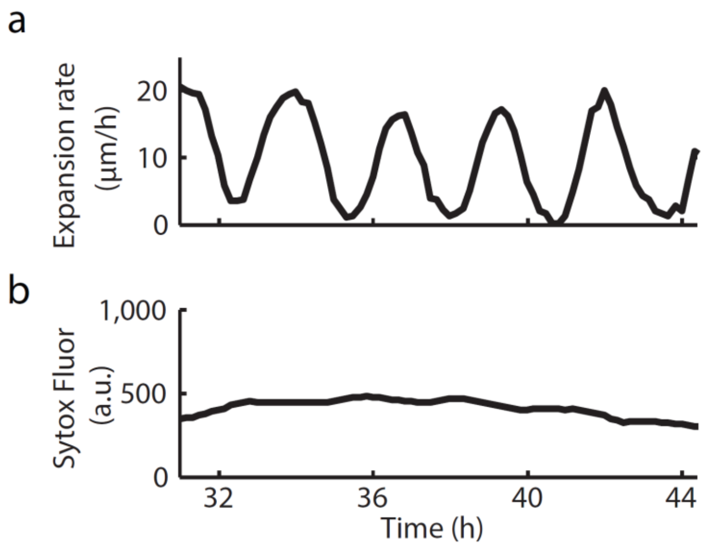

Figure 3.10 Temporal profile of cell death within an oscillating biofilm.
(A) Colony growth rate. **(B)** Average fluorescence intensity of a cell death marker (Sytox Green, 1 µM, Life Technologies) from the same colony shown in A.

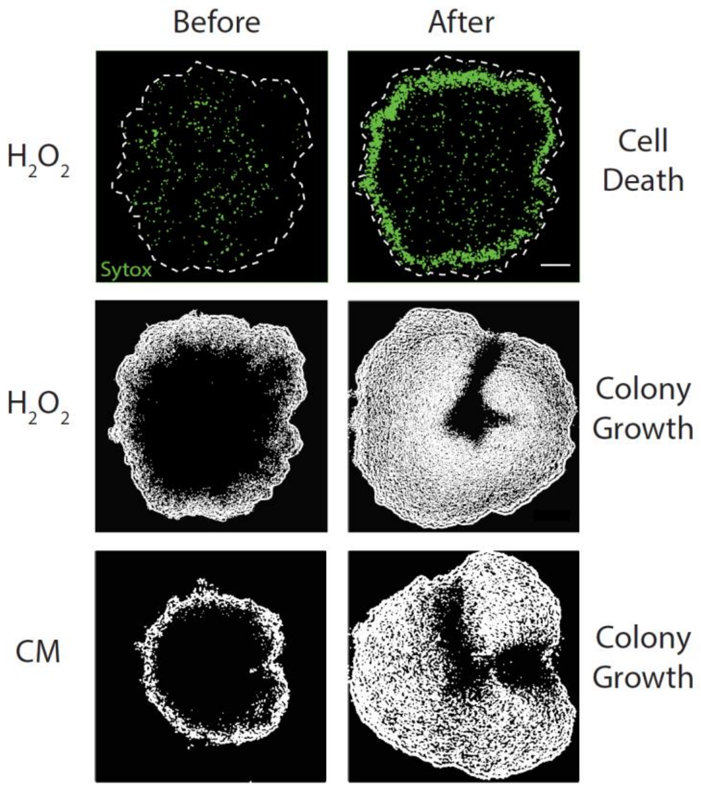

Figure 3.11 Effect of external attack with hydrogen peroxide (H_2O_2, 0.15% v/v) or chloramphenicol (CM, 5 µg/ml).
(Top) cell death is shown by Sytox Green (1 µM). (Middle and bottom) colony growth is shown by image differencing (see Fig. 3.8A and Chapter 3.5.2 Data Analysis). Scale bar represents 100 µm. The white dashed lines indicate colony edge.

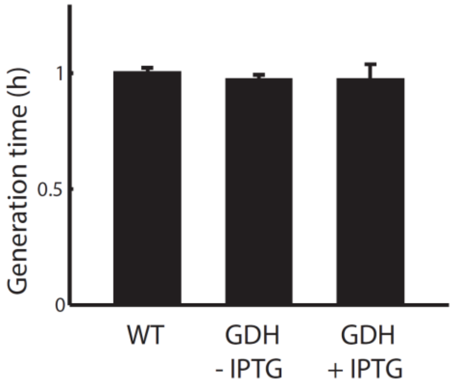

Figure 3.12 Effect of GDH induction on cell growth.
Wild-type and P*hyperspank*-RocG (uninduced or induced with 10 mM IPTG) strains were grown in liquid culture (MSgg medium, 30^{o}C). Cell generation times were measured using OD_{600}. Error bars show standard deviations (*n* = 3 replicates).

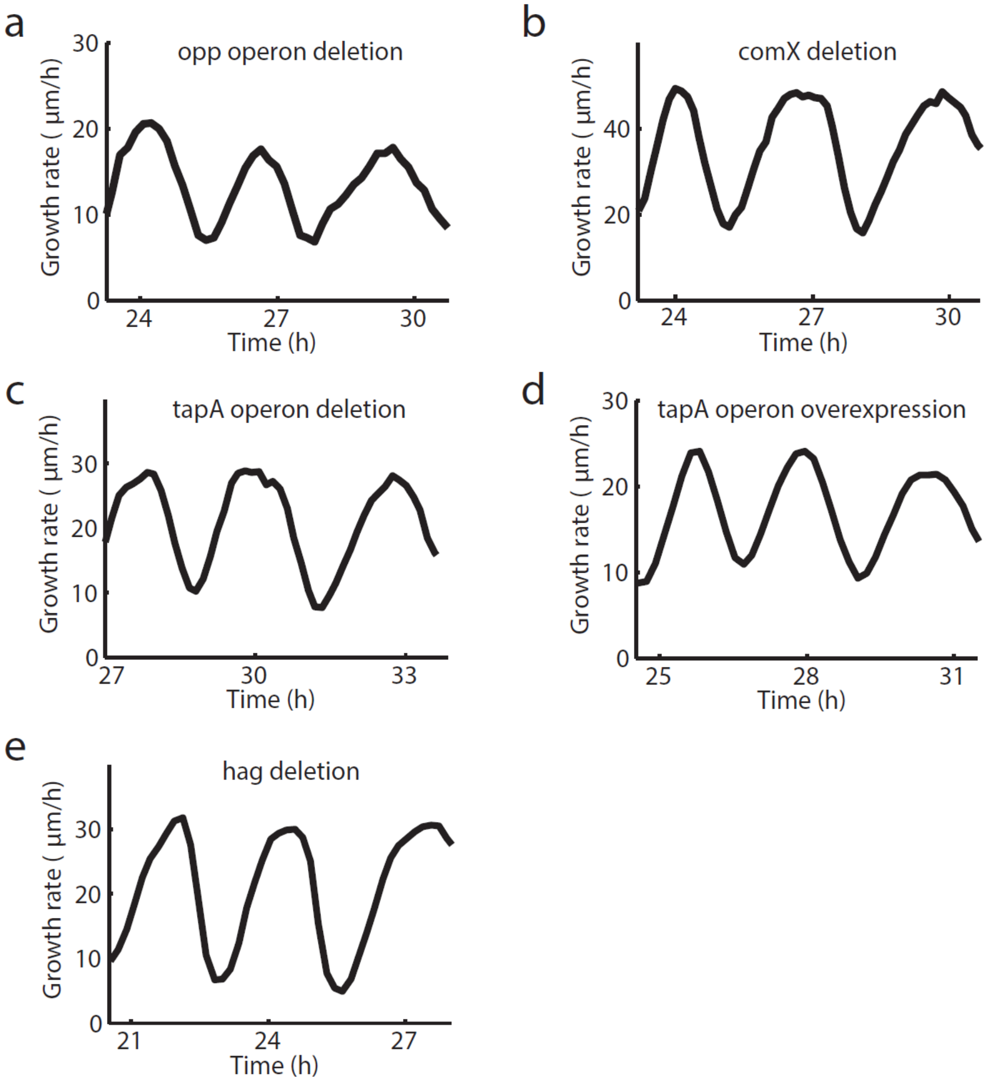

Figure 3.13 Growth rate oscillations persist in various mutant strains.
(A) *opp* operon deletion (deficient in quorum sensing). **(B)** *comX* deletion (deficient in quorum sensing). **(C)** *tapA* operon deletion (extracellular matrix component deletion). **(D)** *tapA* operon overexpression (P*hyperspank*-tapA operon, 1mM IPTG). **(E)** *hag* deletion (deficient in swimming and swarming). These results show that the corresponding genes and processes are not required for biofilm oscillations.

Table 3.1 List of strains used in this study

Strain	Genotype	Source
Wild-type	*B. subtilis* NCIB 3610	(Irnov and Winkler 2010)
P$_{hyp}$-CFP, P$_{nasA}$-YFP	*amyE::* P$_{Hyperspank}$-*cfp*, *sacA::* P*nasA-yfp* (Sp^{R}, Cm^{R})	This study
P$_{hyp}$-RocG	*amyE::* P$_{Hyperspank}$-*rocG* (Sp^{R})	This study
P$_{hyp}$-tapA operon	*amyE::* P$_{Hyperspank}$-*tapA operon* (Sp^{R})	This study
Δ*tapA operon*	*tapA-sipW-tasA::* cat	This study
Δ*oppA-D*	*oppABCD::* cat	This study
Δ*comX*	*comX::* cat	(Asally et al. 2012)
Δ*hag*	*hag::* cat	This study
Δ*rocG*	*rocG::* kan	This study

4 Coupling between distant biofilms and emergence of nutrient time-sharing

4.1 Abstract

Bacteria within communities can interact to organize their behavior. It remains unclear whether such interactions extend beyond a single community to coordinate the behavior of distant populations. We discovered that two *Bacillus subtilis* biofilm communities undergoing metabolic oscillations become coupled through electrical signaling and synchronize their growth dynamics. Coupling increases competition by also synchronizing demand for limited nutrients. As predicted by mathematical modeling, we confirm that biofilms resolve this conflict by switching from in-phase to anti-phase oscillations. This results in time-sharing behavior where each community takes turns consuming nutrients. Time-sharing enables biofilms to counterintuitively increase growth under reduced nutrient supply. Distant biofilms can thus coordinate their behavior to resolve nutrient competition through time-sharing, a strategy used in engineered systems to allocate limited resources.

4.2 Introduction

Biological systems often experience resource limitation (Xavier and Foster 2007; Hibbing et al. 2010; Celiker and Gore 2012; Harcombe et al. 2014; Liu et al. 2015; Kragh et al. 2016; Nadell, Drescher, and Foster 2016). One strategy typically employed in engineered systems to cope with such challenges is known as time-sharing (Bemer 1957; Strachey 1959), in which users take turns consuming resources. Time-sharing requires competing systems to vary their state in time and coordinate their dynamics. In general, coordination only arises from interactions such as communication among functional units, such as cells, to direct systems behavior. For example, bacteria within a population can communicate through various mechanisms, including quorum sensing and electrical cell-to-cell signaling mediated by ion channels (Dunny and Leonard 1997; D. G. Davies et al. 1998; Shapiro 1998; Waters and Bassler 2005; Dietrich et al. 2013; Prindle et al. 2015). However, it remains unclear whether distinct populations of bacteria can act as functional units, and whether cell-to-cell interactions can extend to couple distant populations. Here we study whether two bacterial biofilm communities can coordinate their growth dynamics to engage in timesharing and resolve competition for limited resources.

We studied *B. subtilis* biofilm communities that engage in collective growth-rate oscillations in response to glutamate starvation (Liu et al. 2015). Oscillations are driven by a spatially extended negative feedback loop, where the growth of the biofilm results in glutamate stress within the interior, and this stress, in turn, interferes with biofilm growth (Fig. 4.1A and 4.4) (Liu et al. 2015). Coordination of these growth-rate oscillations within a biofilm is facilitated by potassium ion channel-mediated electrical cell-to-cell signaling (Prindle et al. 2015). Since these long-range electrical signals have been shown to extend beyond the biofilm (Humphries et al. 2017), we hypothesized that neighboring biofilms could potentially affect each other's growth rate. Such biofilms would then also compete directly for nutrients in the shared environment. Therefore, biofilm pairs can be coupled through two basic mechanisms, namely communication and competition for nutrients (Fig. 4.1A).

4.3 Results

To investigate the coupling between biofilms, we used a large (3 mm × 3 mm × 6 µm) microfluidic chamber that can accommodate the growth of two oscillating biofilms separated by approximately 2 mm (Fig. 4.1B). Biofilms were cultured using standard MSgg biofilm-promoting media (17, 18) (glycerol and glutamate as main carbon and nitrogen sources, respectively) and at a steady flow rate (24 µm/s). We used time-lapse phase-contrast microscopy to directly measure colony expansion rate. Electrical signaling dynamics of each biofilm were measured using the fluorescent cationic dye Thioflavin T (ThT), which acts as a Nernstian voltage indicator of bacterial membrane potential (19) (Fig. 4.1C). As reported previously, growth rate and ThT oscillations are anti-correlated (Fig. 4.1D, E) and can be used interchangeably to characterize biofilm dynamics. Our measurements revealed that two distant biofilms can exhibit synchronized oscillations in both growth rate and electrical signaling (Fig. 4.1C-E). The average phase difference between oscillating biofilm pairs was $0.06 \pm 0.07\,\pi$ (s.d., $n = 10$ experiments) and it persisted during the course of the experiment (~10 hours). The observed synchronization suggests not only two distant biofilms interact, but also collective oscillations in each of the two biofilms can become coupled (Fig. 4.5A, C).

We turned to mathematical modeling to examine how the interplay between competition and communication determines synchronization between two oscillating biofilms. Specifically, we modeled the biofilms as two coupled phase oscillators (20–24) to represent their growth dynamics (Appendix C, and see Fig. C.1). We explicitly modeled competition for glutamate, which is used as a nitrogen source in the medium and is required for biofilm growth. The biofilms were also assumed to communicate through known electrical signaling during periods of metabolic stress, which can also couple their growth dynamics (5, 15). Furthermore, we assumed that communication increases with the concentration of glutamate in the medium, as the activity of the potassium ion channel underlying electrical signaling is regulated by glutamate availability (15). With these assumptions, the mathematical model could predict synchronization between two biofilms as a function of glutamate concentration and communication strength.

The model additionally predicted anti-phase oscillations at lower glutamate concentrations in the medium due to enhanced competition (Fig. 4.2A and C.2C). In particular, enhanced competition increases the tendency of the biofilms to halt their growth. Stochastically, one of the biofilms will start this process before the other. This will allow the second biofilm to postpone halting its own growth, thus increasing the phase difference between the biofilms. This process destabilizes the in-phase dynamics, leading to anti-phase oscillations (Fig. C.2C). In contrast, higher concentrations of glutamate promote in-phase oscillations through stronger communication (Fig. C.1). Here enhanced communication forces the two biofilms to share their stress state, leading to synchronized phases (Fig. C.2B). These results show that, depending on the balance between competition and communication, the system of coupled biofilms is predicted to have two attractor states corresponding to in-phase or anti-phase oscillations.

We experimentally tested these predictions by measuring the synchronization between pairs of oscillating biofilms growing under a steady supply of regular (30 mM) or reduced (by 25%) concentration of glutamate. As predicted, we found in-phase oscillations at regular concentrations of glutamate (Fig. 4.2B top, 4.6B, and 4.7) and approximately anti-phase oscillations at lower glutamate concentrations (Fig. 4.2B bottom, 4.5B-C, 4.6A, and 4.7). Consequently, glutamate limitation is sufficient to induce changes in the synchronization between two biofilms.

The model also predicted that the transition from in-phase to anti-phase oscillations depends on communication strength (Fig. 4.2A right, C.2, and see Appendix C). Electrical signaling in *B. subtilis* biofilms is mediated by the YugO ion channel that is gated by a TrkA domain (25–27). To test the effect of communication strength, we used a previously characterized truncated YugO potassium ion channel that lacks the TrkA gating domain. While a complete deletion of the YugO ion channel interferes with biofilm formation (15, 25), the truncated version, lacking the TrkA gating domain, simply decreases the transmission efficiency of electrical signaling without abolishing it completely (15). Such reduced communication within a biofilm may also reduce synchronization between two biofilms. The model predicted that for lower communication strengths, higher glutamate concentrations are needed to reach in-phase oscillations between biofilms (Fig. 4.2A right, and C.2E). Indeed, Δ*trkA* mutant biofilms did not synchronize at regular or 50% increased concentration of glutamate (Fig. 4.2C bottom, 4.6C, 4.7, and 4.8). As predicted, when glutamate concentrations were doubled we observed in-phase oscillations between mutant biofilms (Fig. 4.2C top, 4.6D, and 4.7). Thus, the transition from in-phase to anti-phase oscillations also depends on the communication between biofilms.

The model predicted that the transition to anti-phase dynamics depends on competition strength as well (Fig. 4.2A, left). Accordingly, we constructed a mutant strain that cannot synthesize its own glutamate and thus has a higher demand for externally supplied glutamate. Specifically, we disrupted the *gltA* gene encoding glutamate synthase (Δ*gltA*). This enzyme allows cells to synthesize two glutamate molecules from combining one molecule of glutamine and one of alpha-ketoglutarate (Fig. 4.9) (28). Consequently, two ΔgltA biofilms should experience higher competition for glutamate compared to wild-type biofilms. As predicted, Δ*gltA* biofilms failed to synchronize under baseline glutamate concentrations (Fig. 4.2D, bottom), for which the wild-type biofilms readily synchronized. Glutamate concentration had to be increased by 25% to generate the predicted in-phase oscillations between ΔgltA biofilms (Fig. 4.2D, top). The synchronization dynamics between two biofilms thus also depend on nutrient competition. Together, perturbations to communication and competition strength between biofilms confirm the mathematically predicted 3-dimensional phase diagram that defines the regions where two biofilms oscillate either in-phase or anti-phase (Fig. 4.2E).

We tested whether the observed anti-phase dynamics that would allow time-sharing, provided a benefit for biofilm growth. In the case of in-phase oscillations, each biofilm would effectively obtain only half of the available resources (resource-splitting) during its growth phase (Fig. 4.3A). In contrast, time-sharing would allow each biofilm to take turns in having access to all the resources supplied at a constant rate (Fig. 4.3A). Counterintuitively, biofilm growth would thus increase when nutrient supply is low because the reduction in the concentration of glutamate promotes the transition to time-sharing. Our mathematical model indeed predicted greater biofilm growth when glutamate concentrations were reduced by 25% (Fig. 4.3B, and see Appendix C).

We experimentally tested the prediction that reduced concentrations of glutamate would improve biofilm growth through time-sharing. We first confirmed the basic expectation that two in-phase biofilms compete for nutrients by showing that their time-averaged growth rates are slower compared to that of a single biofilm (Fig. 4.3C, 1x glutamate, and 4.10). We also verified that the growth rate of a single biofilm is slower at reduced concentrations of glutamate (Fig. 4.3C, gray line). In contrast to a single biofilm, two biofilms growing in lower glutamate concentrations had a faster average growth rate than two biofilms growing at higher glutamate concentrations (Fig. 4.3C, black line). Observing a faster growth rate for biofilms growing under lower glutamate concentrations is surprising, yet can be explained by the switch from resource-splitting to time-sharing. At higher glutamate concentrations, in-phase nutrient consumption leads to direct competition and resource-splitting. In contrast, at lower concentrations of glutamate biofilms consume nutrients at different times, and the resulting time-sharing of resources promotes growth. Accordingly, the observed difference in growth rates is accounted for by the phase difference between the biofilms (Fig. 4.3D). These results demonstrate the benefit of time-sharing and reveal that the average growth rate of biofilms is not exclusively defined by absolute nutrient concentrations, but also by the resource sharing strategy between biofilms.

4.4 Discussion

Our data show that bacteria appear to resolve conflicts that arise from competition for resources between distant communities. It remains unclear why biofilms would synchronize their growth in the first place. The fitness benefit of communication among bacteria that allows coordination within a biofilm may bring with it the cost of synchronization between communities. This communication cost may not be restrictive when nutrient concentrations are sufficiently high but could be detrimental when the concentration of nutrients is too low. Our results show that glutamate-dependent modulation of competition and communication allows biofilms to alleviate this cost by engaging in time-sharing when nutrients become more limited. It remains to be determined in future studies whether two biofilms formed by different bacterial species can also engage in time-sharing, or if this behavior is limited to kin populations, due to evolutionary incentives. From another perspective, time-sharing is a common strategy employed in computer science to share computing resources between users (8, 9). This connection between engineered and natural systems may in the future allow us to utilize time-sharing in synthetic biology applications focusing not only on interactions within but also between communities.

4.5 Method

4.5.1 Biofilm oscillations

Oscillations initiated only once the biofilm exceeded a critical size, at which point the biofilm began to experience glutamate starvation (*5*). As the colony size increased, nutrient consumption exceeded the ability of simple diffusion to provide nutrients into the biofilm. The resulting glutamate starvation then triggered oscillations in growth rate. This periodic reduction in the biofilm growth rate reduces nutrient consumption, allowing more nutrients to diffuse into the biofilm. As reported previously, by preventing starvation in this way, the biofilm better tolerates antibiotic attack, since cells sheltered in its interior are more likely to survive (*5*). The distance between two biofilms when oscillations were initiated was ~2 mm. This distance could shrink by ~15% during the course of the experiments as biofilms grow. This reduction in the distance between biofilms did not appear to affect the in-phase or anti-phase dynamics of biofilm pairs.

4.5.2 Data analysis

ImageJ (National Institutes of Health) and MATLAB (MathWorks) were used for image analysis. Python and the SciPy package were used for mathematical modeling. The temporal dynamics of membrane potential was measured by tracking ThT fluorescence at biofilm edge, and the resulting time traces were detrended and normalized. Biofilm growth rate was measured as the expansion speed of biofilm edge. Average growth rates were measured over 3-4 oscillation cycles. Biofilm growth rate and ThT fluorescence are anti-correlated (Figs. 1D-E, and S7). Therefore, we used them interchangeably in this study.

Chapter 4, in full, is a reprint of the material *Jintao Liu, Rosa Martinez-Corral*, Arthur Prindle*, **Dong-yeon D. Lee**, Joseph Larkin, Marçal Gabalda-Sagarra, Jordi Garcia-Ojalvo, Gürol M. Süel. "Coupling between distant biofilms and emergence of nutrient time-sharing" Science, vol. 356, Issue 6338, 638-642. 2017 (*equal contribution).* The dissertation author participated in discussions, strain constructions, experiments for supplementary materials, and reviewer responses.

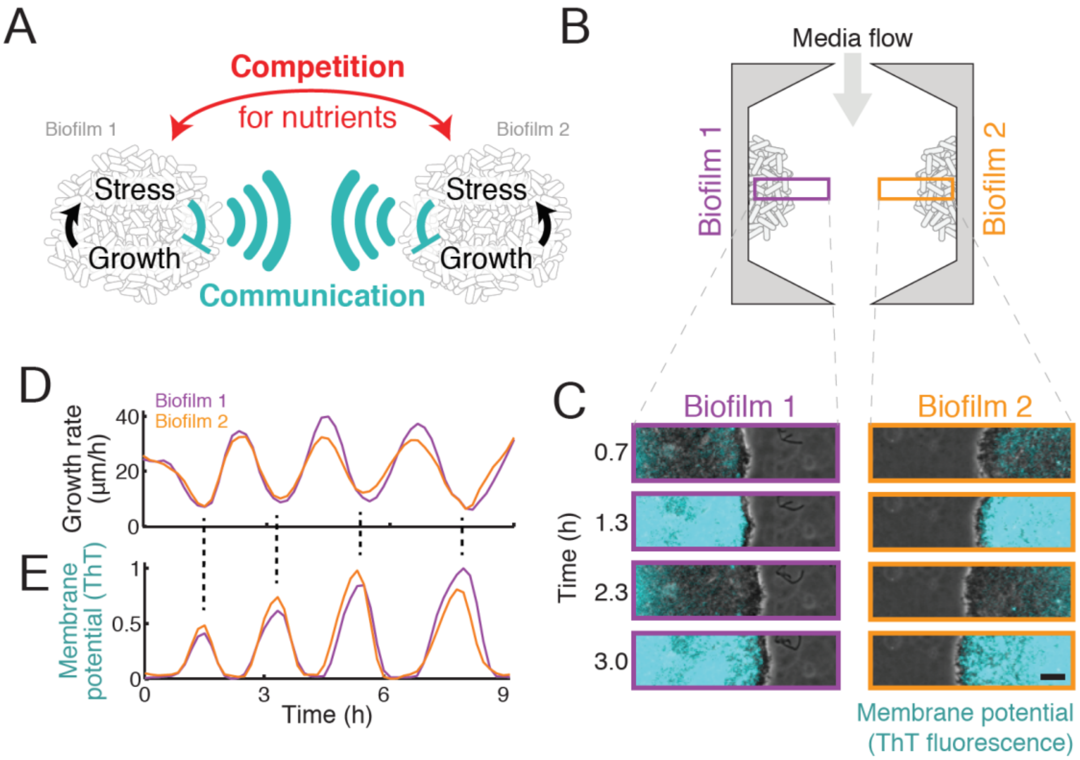

Figure 4.1 Distant biofilms synchronize their growth dynamics.
(A) Individual biofilms undergo metabolic oscillations that periodically halt growth. The metabolic oscillation is facilitated by electrical communication, which can extend beyond one biofilm and couple distant biofilms (cyan signals). In addition, two biofilms can also be coupled through competition for nutrients (red arrows). **(B)** Schematic depicting two biofilms grown on the two sides of a microfluidic chamber, with steady media flow. Purple and orange rectangles represent regions shown in C. **(C)** Filmstrip showing the edges of a biofilm pair over time. Cyan indicates fluorescence of Thioflavin T (ThT), a cationic fluorescent dye that reports membrane potential within the biofilm. Scale bar, 50 μm. **(D)** Growth rate oscillation measured by expansion speed of biofilm edges shown in C. **(E)** Membrane potential oscillation measured from the mean ThT fluorescence at biofilm edges shown in C.

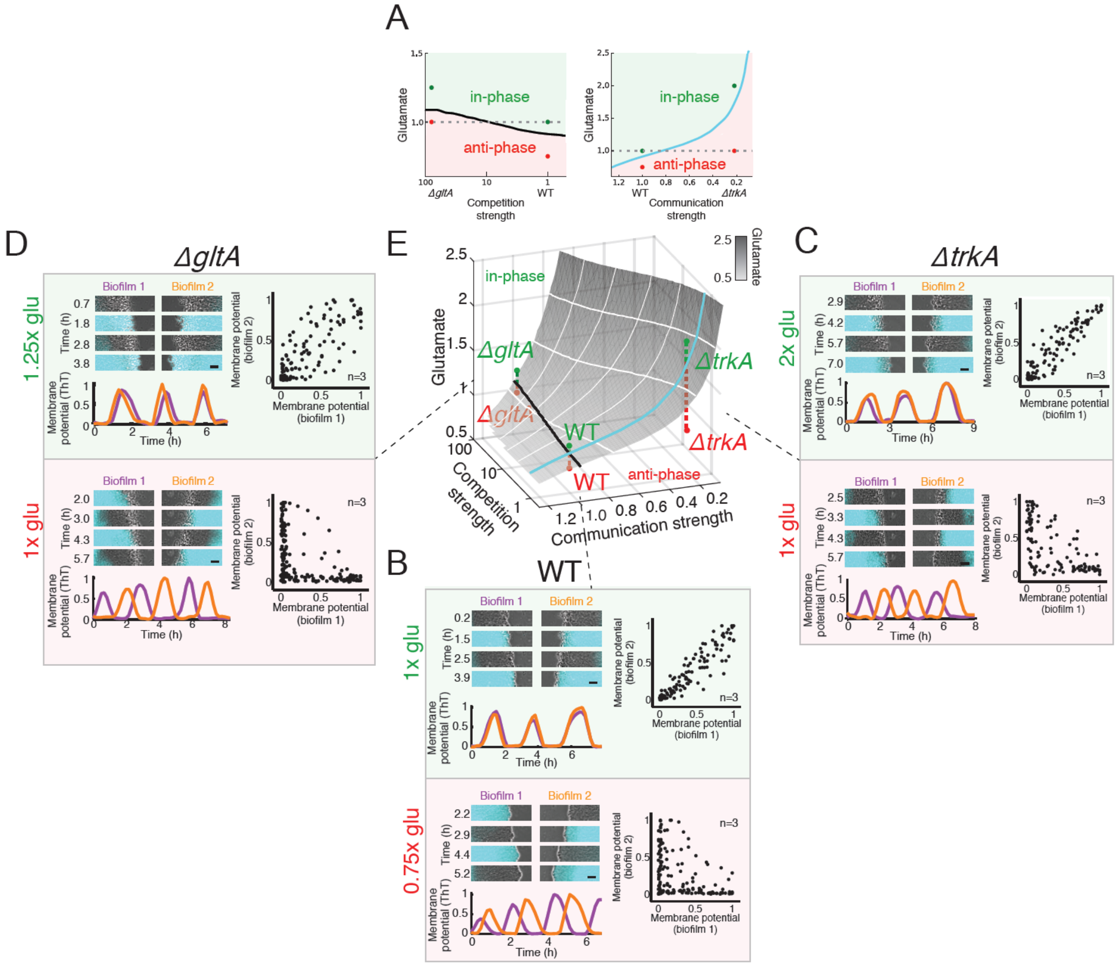

Figure 4.2 Synchronization between biofilms is governed by communication and competition.

(A) Phase diagrams computed using a mathematical model of coupled phase oscillators show in-phase (green-shaded regions) and anti-phase (red-shaded regions) oscillations. The colored dots indicate the experimental validations shown in the following panels. (**B-D**) Experimental results of wild-type **(B)**, *ΔtrkA* **(C)**, and *ΔgltA* **(D)** biofilms. For each strain, the biofilm pairs showed in-phase (approximately 0 phase difference) oscillations at high glutamate concentrations and anti-phase (approximately π phase difference) oscillations at low glutamate concentrations. In each panel, the filmstrip shows the membrane potential oscillation of a representative biofilm pair, with corresponding time traces (color coded by biofilm). The scatterplots show membrane potential of biofilm pairs against each other for individual time points (n = 3 experiments per plot). (**E**) Three-dimensional phase diagram summarizing model prediction and experimental validations. The gray-shaded surface depicts the boundary between regions of in-phase and anti-phase oscillations. The black and cyan lines indicate the corresponding two-dimensional phase diagram boundaries shown in A.

Figure 4.3 Time-sharing resolves nutrient competition between biofilms.

(A) Anti-phase oscillations (time-sharing) allow each biofilm to take turns accessing the full quantity of supplied nutrients during its growth phase. In contrast, in-phase oscillations (resource-splitting) only allow half of the supplied nutrients to each biofilm during its growth phase. **(B)** Model prediction and **(C)** experimental validation of average growth rate for single biofilm (grey line) and biofilm pair (black line) at different glutamate concentrations. **(D)** Biofilm growth rate is determined by the phase difference between biofilm pairs. Pairs of wild-type (solid line), Δ*trkA* (dashed line) and Δ*gltA* (dotted line) biofilms all showed faster growth with anti-phase oscillations (time-sharing) compared to in-phase oscillations (resource-splitting). The blue shading indicates glutamate concentration. Error bars represent s.e.m., *n* = 3 experiments.

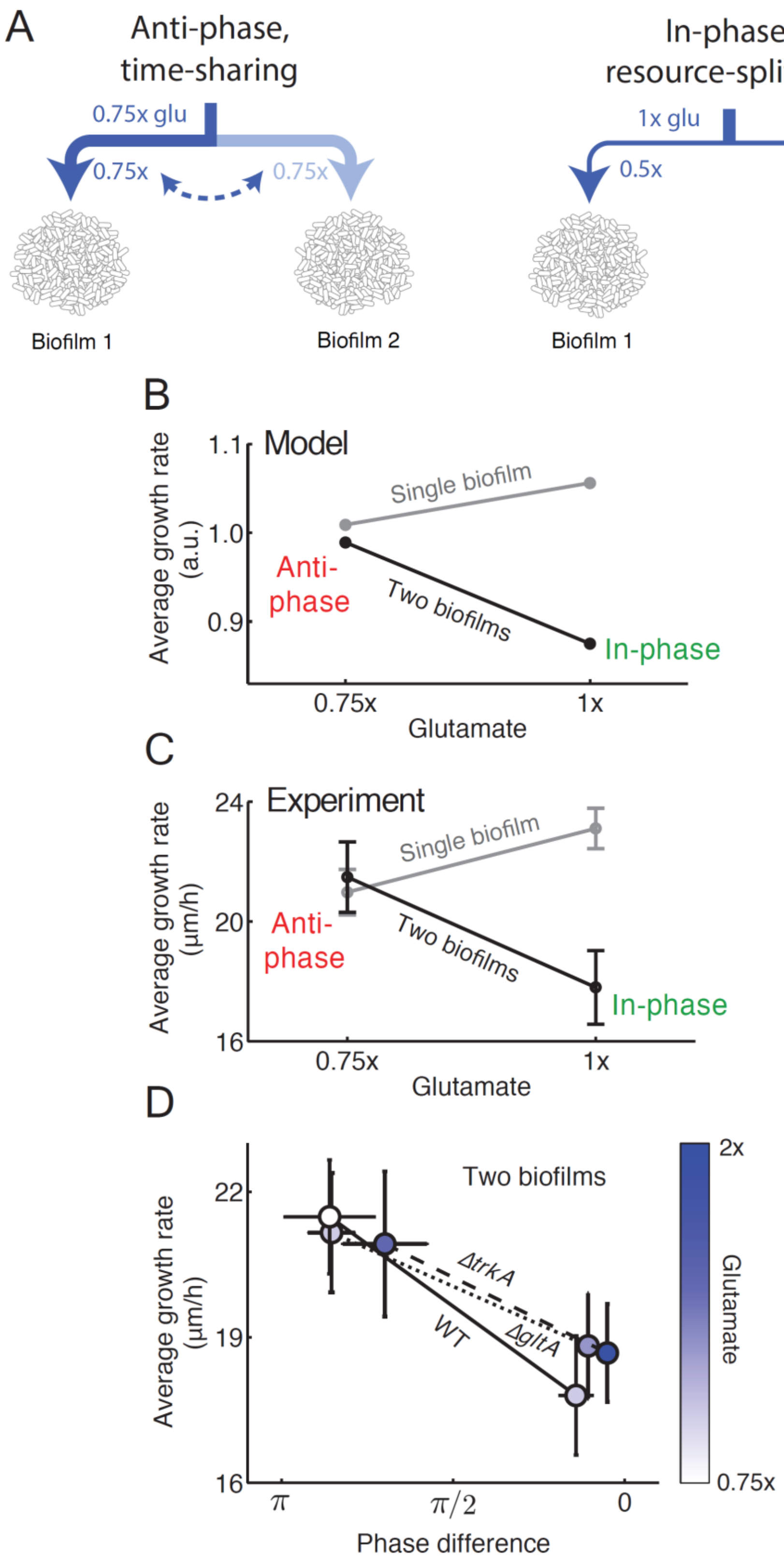
A
Anti-phase, time-sharing
0.75x glu
0.75x
0.75x
Biofilm 1
Biofilm 2
In-phase, resource-splitting
1x glu
0.5x
0.5x
Biofilm 1
Biofilm 2
B
Model
Average growth rate (a.u.)
1.1
1.0
0.9
Single biofilm
Two biofilms
Anti-phase
In-phase
0.75x
1x
Glutamate
C
Experiment
Average growth rate (μm/h)
24
20
16
Single biofilm
Two biofilms
Anti-phase
In-phase
0.75x
1x
Glutamate
D
Two biofilms
Average growth rate (μm/h)
22
19
16
ΔtrkA
WT
ΔgltA
π
π/2
0
Phase difference
2x
Glutamate
0.75x

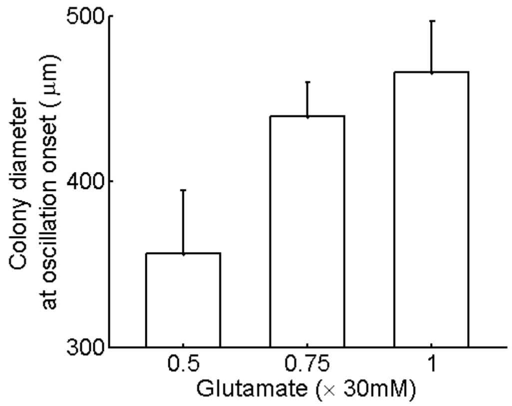

Figure 4.4 The biofilm size at which oscillations emerge increases with the concentration of glutamate.

This illustrates the role of glutamate starvation in biofilm oscillations. At lower glutamate concentration, the biofilm interior becomes starved of glutamate sooner, therefore leading to oscillations at a relatively smaller size. Error bars represent s.t.d., *n* = 24, 12, and 20 for 0.5x, 0.75x, and 1x glutamate respectively.

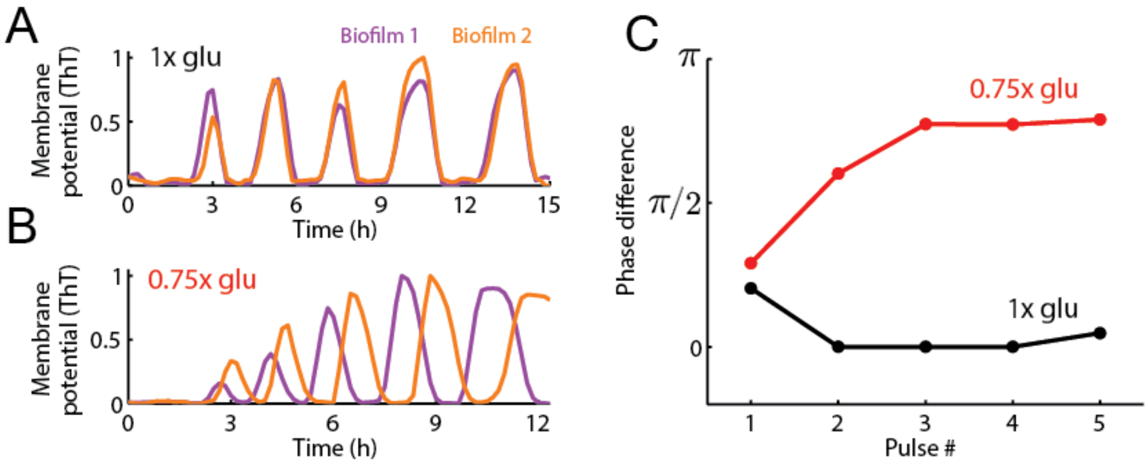

Figure 4.5 Onset of oscillations and evolution of phase regimes.

(A) A pair of wild-type biofilms grown at 1x glutamate concentration (30 mM) started oscillations slightly out of phase, but then become in-phase (approximately 0 phase difference) after one oscillation cycle. **(B)** A pair of wild-type biofilms grown at 0.75x glutamate concentration (22.5 mM) started oscillations slightly out of phase and then become anti-phase (approximately π phase difference) after two oscillation cycles. **(C)** Phase difference as a function of oscillation cycle for the results shown in A and B.

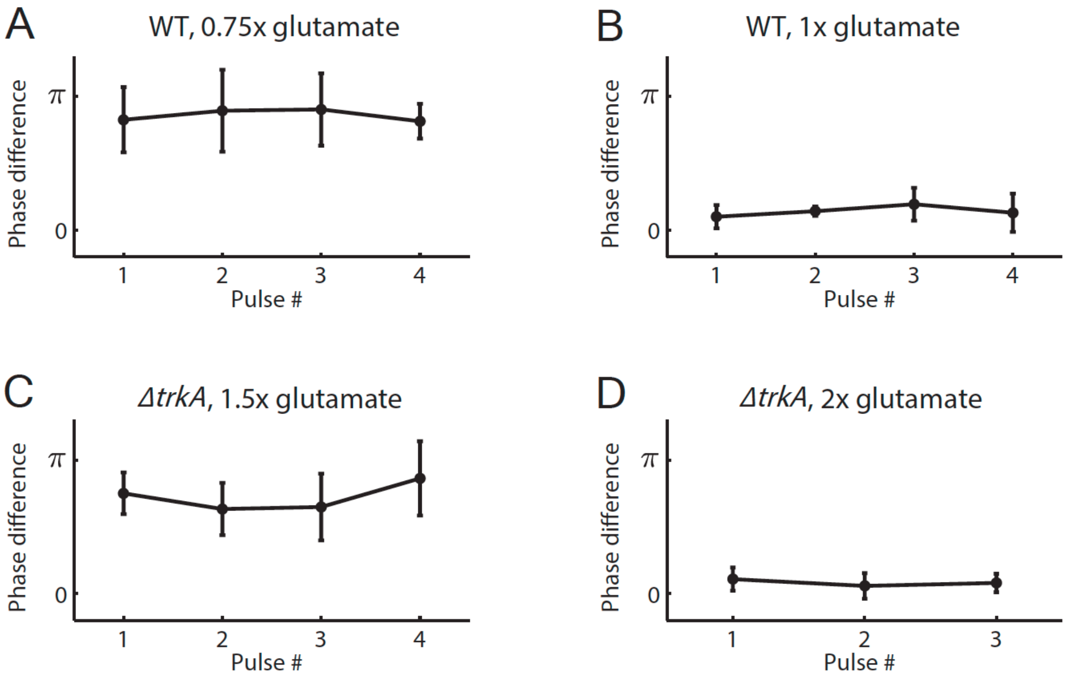

Figure 4.6 Phase difference over pulse number between pairs of biofilms. Anti-phase (approximately π phase difference) oscillations were observed with: **(A)** wild-type biofilms at 0.75x glutamate and **(C)** Δ*trkA* mutant biofilms at 1.5x glutamate. In-phase (approximately 0 phase difference) oscillations were observed with: **(B)** wild-type biofilms at 1x glutamate and **(D)** Δ*trkA* mutant biofilms at 2x glutamate. Error bars represent standard deviations, $n = 3$ experiments.

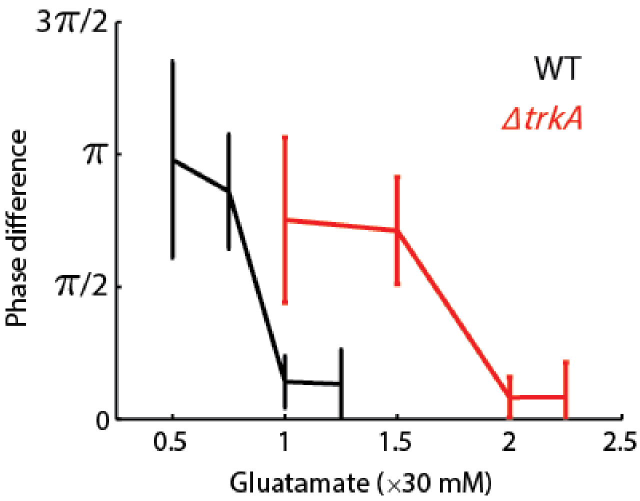

Figure 4.7 Biofilm pairs can show in-phase or anti-phase oscillations.
Biofilm pairs showed in-phase oscillations when grown at high glutamate concentrations, and anti-phase oscillations when grown at low glutamate concentrations. The transition between in-phase and anti-phase oscillations happened at higher glutamate concentration for Δ*trkA* biofilms than for wild-type biofilms.

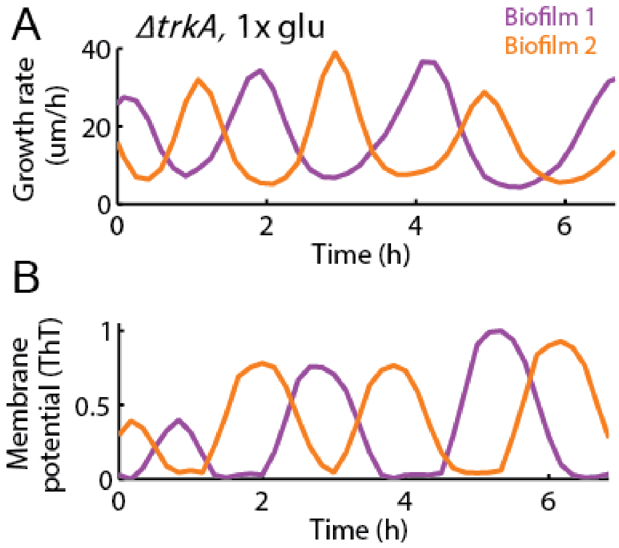

Figure 4.8 Δ*trkA* mutant biofilms showed anti-phase oscillations at regular glutamate concentration (30 mM).
(A) Growth oscillations measured by expansion speed of biofilm edges. Purple and orange curves correspond to two different biofilms in the same microfluidic growth chamber. **(B)** Membrane potential oscillations measured from the mean ThT intensity of the two biofilms in A. In each biofilm, growth rate and ThT fluorescence are anti-correlated (see also Figs. 1D-E). Therefore, we used them interchangeably in this study.

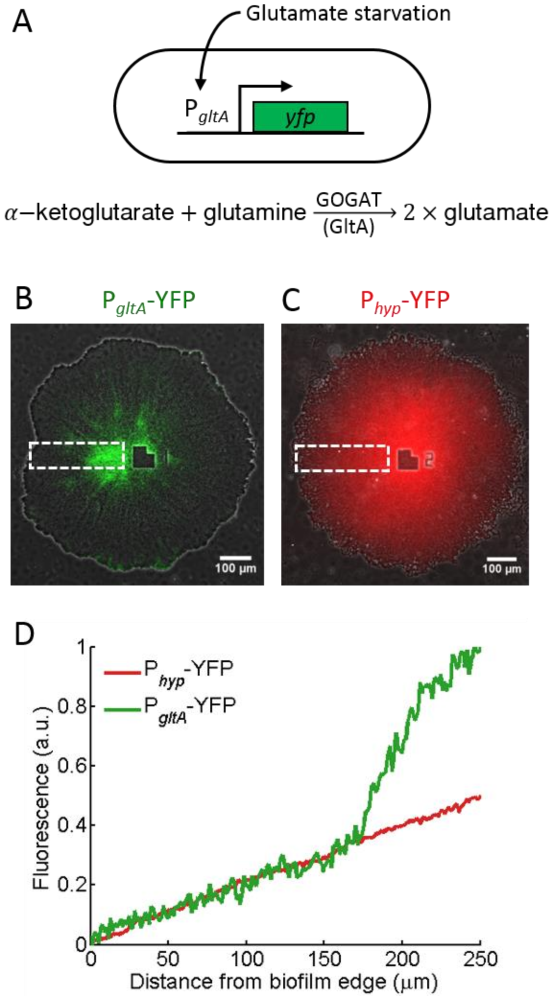

Figure 4.9 Glutamate starvation and expression of glutamate synthase in biofilms.
(A) *B. subtilis* uses the glutamate synthase GOGAT to synthesize glutamate from α-ketoglutarate and glutamine. GOGAT is up-regulated during glutamate starvation. We monitored expression of the large subunit of GOGAT by expressing YFP from the *gltA* promoter (P_{gltA}-YFP). **(B)** Fluorescence image of a biofilm expressing P_{gltA}-YFP (colored green) shows *gltA* is mainly expressed in biofilm interior. **(C)** In contrast, fluorescence image of a biofilm expressing YFP from the IPTG (1 mM) inducible hyperspank promoter (P_{hyp}-YFP) (colored red) shows constitutive expression throughout the biofilm. **(D)** Spatial profiles of P_{gltA}-YFP and P_{hyp}-YFP intensity (from boxes in C, D) illustrate increased *gltA* expression in the biofilm interior relative to constitutive gene expression.

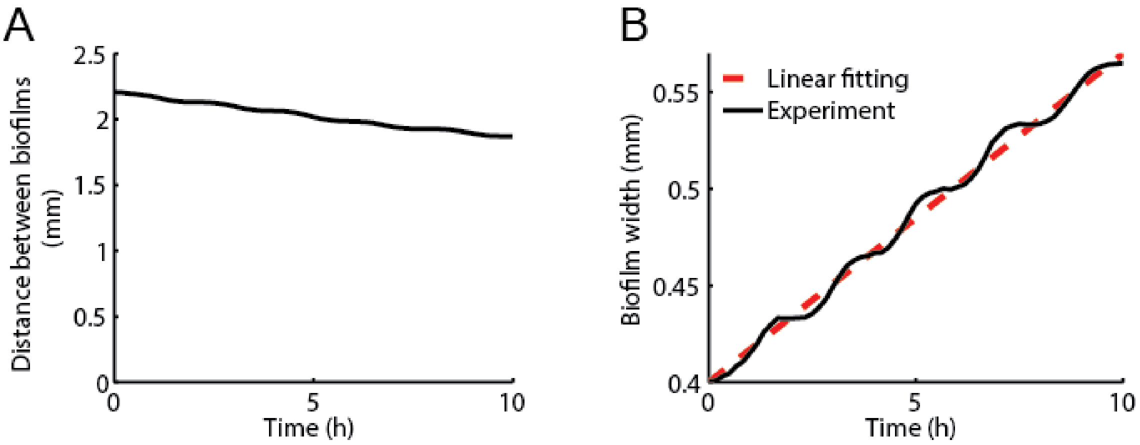

Figure 4.10 Characterization of biofilm growth.
(A) The distance between two biofilms when oscillations were initiated was ~2 mm. This distance could shrink by ~15% during the course of the experiments as biofilms grew. This reduction in the distance between biofilms did not appear to affect the in-phase or anti-phase dynamics of biofilm pairs. **(B)** Biofilm expansion dynamics were stable over many hours and multiple oscillation cycles, and the average growth rate did not change over biofilm size.

III

COUPLED DYNAMICAL PROCESSES IN A BACTERIUM UNDER STRESS

5 Chromosomal arrangement of phosphorelay genes couples sporulation and DNA replication

5.1 Abstract

Genes encoding proteins in a common regulatory network are frequently located close to one another on the chromosome to facilitate co-regulation or couple gene expression to growth rate. Contrasting with these observations, here, we demonstrate a functional role for the arrangement of *Bacillus subtilis* sporulation network genes on opposite sides of the chromosome. We show that the arrangement of two sporulation network genes, one located close to the origin and the other close to the terminus, leads to a transient gene dosage imbalance during chromosome replication. This imbalance is detected by the sporulation network to produce cell-cycle coordinated pulses of the sporulation master regulator Spo0A~P. This pulsed response allows cells to decide between sporulation and continued vegetative growth during each cell cycle spent in starvation. The simplicity of this coordination mechanism suggests that it may be widely applicable in a variety of gene regulatory and stress-response settings.

5.2 Introduction

A recurring theme in recent studies of cellular differentiation networks is that these networks respond to stimuli in a highly dynamic, time-dependent manner (Kuchina, Espinar, Garcia-Ojalvo, et al. 2011; Kuchina, Espinar, Çağatay, et al. 2011). One of the main roles of this dynamical response is to coordinate the expression of genes in the differentiation program with cell-cycle events such as DNA replication and cell division (Doncic, Falleur-Fettig, and Skotheim 2011; Toettcher et al. 2009; J. Veening, Murray, and Errington 2009). Lack of coordination between the differentiation program and the cell-cycle can often result in incomplete/abortive differentiation or even cell death. As a result, uncovering the system-level mechanisms of cell-cycle coordinated differentiation is essential to understand this process. Keeping this in mind, we investigated sporulation in soil bacterium *B. subtilis* to uncover how this differentiation program is coordinated with the cell-cycle.

Sporulation is the last resort of starving *B. subtilis* cells. In response to starvation, *B. subtilis* cells cease vegetative growth and asymmetrically divide to initiate a multistage program that produces stress-resistant and metabolically inert spores (Fig. 5.1A)(Higgins and Dworkin 2012). At the molecular level, the sporulation program is controlled by the master regulator Spo0A (0A) which is active in its phosphorylated (0A~P) form (Jeff Errington 2003). Expression of many downstream sporulation program genes is controlled by 0A~P, and it has been shown that a threshold level of 0A~P commits cells to sporulation (Prahathees Eswaramoorthy et al. 2010; Fujita and Losick 2005; Narula et al. 2012). The activation of 0A itself is regulated by a complex network known as the sporulation phosphorelay (Burbulys, Trach, and Hoch 1991). Since cells need two complete chromosomes to produce a viable spore (Hauser and Errington 1995), the dynamics of 0A activation must be temporally coordinated with the completion of DNA replication. Previous studies have suggested that Sda, an inhibitor of the phosphorelay kinase that activates 0A may be responsible for coordinating 0A activation with DNA replication (J.

Veening, Murray, and Errington 2009). However, it has been recently shown deletion of sda does not completely abolish cell-cycle coupling of 0A activation (Levine et al. 2012). As a result, the central question of how the phosphorelay coordinates 0A activation with the cell-cycle remains unaddressed.

Here we show that the chromosomal arrangement of two phosphorelay genes plays a critical role in coupling 0A activation to DNA replication. The location of these genes on opposite sides of the chromosome – one located close to the origin of replication, the other close to the terminus, leads to a transient imbalance in their gene dosage during chromosome replication. Combined with a delayed negative feedback loop in the phosphorelay this transient imbalance results in the pulsatile activation of 0A that is responsible for coordinating the commitment to sporulation with the cell-cycle.

5.3 Results

5.3.1 0A activity pulses follow the completion of DNA replication

To understand the dynamics of sporulation network response, we employed time-lapse microscopy and simultaneously tracked 0A activity and DNA replication in single *B. subtilis* cells (see Methods). We used fluorescent reporters to measure gene expression from 0A~P-regulated promoters for *spo0A* and *spo0F* (P_{0A} and P_{0F}). In addition, we fluorescently tagged a replisome component, DnaN, so that periods of DNA replication could be detected by the presence of fluorescent DnaN foci (Su'etsugu and Errington 2011). In agreement with previous studies (Levine et al. 2012; Veening et al. 2008), we found that in these conditions cells do not sporulate immediately upon exposure to starvation, but rather complete multiple divisions before finally producing spores. Measurements of the expression level of P_{0A}-*cfp* (Fig. 5.1B) and the cell growth rate (inferred from cell elongation rate) enabled us to compute 0A activity defined as production rate of the reporter protein (Fig. 5.1C). The results revealed that during the multi-cycle progression to spore formation a single pulse of 0A activity is produced every cell-cycle in starvation conditions (Fig. 5.1C). Similar pulsing was observed in the production of fluorescent reporters of other 0A~P-regulated promoters such as P_{0F} (Fig. 5.6). We measured the pulse timing during the cell cycle (Fig. 5.1C) and found that 0A activity pulses always follow the completion of DNA replication (Fig. 5.1D).

This type of 0A activity pulsing has also been reported by other recent studies (Kuchina, Espinar, Garcia-Ojalvo, et al. 2011; Levine et al. 2012; Veening, Murray, and Errington 2009a). Veening and coworkers reported that this pulsatile response is the result of pulsing of Sda, an inhibitor of the kinase that activates 0A (Veening, Murray, and Errington 2009a). However, a more recent study (Levine et al. 2012), has shown that Sda might not be the only mechanism behind 0A activity pulsing since deletion of *sda* does not completely abolish pulsing. As a result, the mechanism underlying this pulsatile response remains unclear.

5.3.2 A hidden negative feedback loop in the phosphorelay

Our first goal was to uncover the mechanism underlying the pulsing of 0A~P. To this end, we built a detailed mathematical model of the sporulation phosphorelay network (Fig. 5.2A) that controls 0A production and phosphorylation (see Appendix D). This network consists of multiple histidine kinases KinA-E, two phosphotransferases Spo0F (0F) and Spo0B (0B), and the master regulator 0A (Hoch, 1993). Among the five kinases, the cytoplasmic protein KinA is the major sporulation kinase (in our conditions) and therefore we have only included this kinase in our model(Eswaramoorthy et al. 2010; Perego et al. 1989). Upon nutrient limitation, KinA auto-phosphorylates and indirectly transfers the phosphate group to 0A via the intermediate proteins 0F and 0B (Fig. 5.2A) (Burbulys, Trach, and Hoch 1991). The expression levels of kinA, 0F and 0A are regulated by 0A~P via direct and indirect transcriptional feedback loops. These post-translational and transcriptional interactions were described using appropriate mass-action and Hill-function type rate laws to build the model of the phosphorelay network (see Appendix D).

Analysis of simulations of this model showed that an increase in 0F levels leads to higher levels of 0A~P and increased expression of 0A targets (Fig. 5.2B). However, this result contradicts previous *in vivo* studies, which indicate that 0F overexpression inhibits sporulation (Chapman and Piggot 1987; Chastanet et al. 2010; Sen, Garcia-Ojalvo, and Elowitz 2011). To resolve this discrepancy, we made a change to the conventionally assumed phosphorelay architecture (Fig. 5.2A without a red arrow) and incorporated substrate inhibition of KinA by 0F into the phosphorelay model (red arrow, Fig. 5.2A). This substrate inhibition effect was based on an in vitro study demonstrating inhibition of phosphotransfer by excess 0F (Grimshaw et al. 1998). The resulting model predicted a non-monotonic dependence of 0A~P on 0F as high 0F concentrations blocked 0A activation (Fig. 5.2B). We verified this inhibition in an engineered strain, $i0F^{amyE}$, in which the native copy of *0F* was replaced by a copy of *0F* expressed from an IPTG-inducible promoter ($P_{hyperspank}$, or P_{hsp}) at the amyE locus. The results indicate inhibition of 0A activity by an excess of *0F* induction (Fig. 5.2C).

Since 0F expression is activated by 0A~P, the substrate inhibition of KinA by 0F results in the negative feedback loop in the phosphorelay. This feature is especially significant since negative feedback loops are known to produce adaptation-like pulsatile responses (Ma et al. 2009). In addition, the inhibition of KinA by 0F made the flux through the phosphorelay very sensitive to the ratio of KinA and 0F concentrations (Fig. 5.7). As a result, any perturbation of the relative KinA/0F ratio can force the negative feedback loop to produce a pulsed 0A~P response.

5.3.3 Chromosomal arrangement of phosphorelay genes provides a pulse triggering perturbation

The sensitivity of the phosphorelay response to the KinA/0F ratio in our model suggested that chromosomal arrangement of *kinA* and *0F* may affect 0A~P dynamics. On the *B. subtilis* chromosome *0F* is located close to the origin (326°-*oriC* proximal) and *kinA* near the terminus (126°-*ter* proximal) of DNA replication (Fig. 5.3A). As a result, replication of *0F* precedes that of *kinA* and each DNA replication cycle produces a transient decrease in the *kinA:0F* gene dosage ratio (Fig. 5.3A). In light of this, we proposed that this arrangement of *0F* and *kinA* genes on the chromosome might couple the phosphorelay output to DNA replication.

Including a DNA replication window in our simulations, we found that this imbalance in *kinA* and *0F* expression inhibits the phosphorelay flux and results in a decrease in 0A~P during replication (Fig. 5.3A). Once DNA replication is completed and the *kinA:0F* ratio returns to one, the delayed negative feedback loop comprised of transcriptional feedback from 0A~P to 0F and the postulated substrate inhibition of KinA by 0F produces an overshoot of 0A~P above its steady state (Fig. 5.3A). These overshoots are manifested as pulses of 0A activity occurring once per cell cycle. Thus, our model explains both the pulsing mechanism and the observed correlation between DNA replication and timing of 0A pulses (compare Fig. 5.1C and Fig. 5.3A). Moreover, comparison of the chromosomal locations of *kinA* and *0F* in 45 different species of spore-forming bacteria that have both these genes showed little variation in their positions relative to the chromosomal origin (Fig. 5.7DE), which suggests that the proposed relative gene dosage pulsing mechanism is evolutionarily conserved.

To uncover the essential design features necessary for the pulsatile 0A~P dynamics, we tested the model response to specific network perturbations. First, we tested the effect of translocating *0F* so that both *kinA* and *0F* are close to the chromosome terminus. Simulations of this mutant *Trans-0F*^{gltA} (Fig. 5.3B and Fig. D.2) showed that the translocation of *0F* close to the terminus eliminated the transient *kinA:0F* decrease during DNA replication. Consequently, simulations of this modified strain showed no 0A~P pulsing and instead the system remained at steady state. In the same fashion, our model shows that elimination of the transient *kinA:0F* ratio decrease by translocation of *kinA* close to the chromosomal origin (*Trans-kinA*^{amyE}) would eliminate 0A~P pulsing (Fig. D.2).

Next, we investigated the role of the negative feedback loop between 0A~P and 0F by testing the effect of assuming that 0F is expressed from an IPTG-inducible P$_{hsp}$ promoter, rather than the native 0A~P regulated P$_{0F}$ promoter. We tested two such inducible engineered strains: *i0F*^{amyE} (P$_{hsp}$-*0F* located close to the origin of replication - Fig. 5.3C) and *i0F*^{gltA} (P$_{hsp}$-*0F* located close to the terminus - Fig. 5.3D). In these inducible strains, the effective *kinA:0F* gene dosage was assumed to depend on the level of 0F expression. Model simulations showed that in the *i0F*^{amyE} strain (Fig. 5.3C), there is a transient decrease in effective *kinA:0F*. This decrease inhibits the phosphorelay phosphate flux and causes a decrease in 0A~P. However, 0A~P does not overshoot before returning to the steady state and there is no pulse (Fig. 5.3C), unlike the results for WT (Fig. 5.3A). Simulations further showed that transient decrease of *kinA:0F* is eliminated by *0F* translocation in the $i0F^{gltA}$ strain (Fig. 5.3D) and that 0A~P stays at steady state in this case. Simulations also predicted that the 0A~P response in these inducible strains depends on the level of 0F, specifically 0A~P levels decrease with increasing 0F expression in both $i0F^{amyE}$ and $i0F^{gltA}$ (Fig. 5.3C and D).

Thus far, our phosphorelay model only included one kinase, KinA, as its deletion (Δ*kinA*) has a most drastic effect on sporulation efficiency under most sporulation conditions (Fig. 5.7A)(LeDeaux, Yu, and Grossman 1995). However, in certain conditions (S7 minimal media), KinB is known to act as the major kinase. To explore the role of KinB we extended our model to include KinB. Notably, the location of *kinB* is ~ 60 degrees further from *oriC* than *0F* (Fig. D.1A). As a result, similar to *kinA* there is a transient period during which gene dosage of *0F* exceeds that of *kinB* resulting in the inhibition of kinase and reduction in 0A activity. According to our mathematical model, upon *kinB* replication relief of this inhibition can be sufficient to trigger a 0A~P pulse (Fig. 5.8C). The lower amplitudes of 0A~P pulses triggered by KinB relative to KinA are consistent with the results of Levine et al. (Levine et al. 2012) who reported 0A-activity pulsing in Δ*kinA* strain. This prediction also explains the reduced sporulation efficiency of this strain (LeDeaux, Yu, and Grossman 1995). Overall these results show that KinB can partially compensate for KinA and trigger pulsing of 0A activity by relying on the same design features as *the kinA:0*F pulsing mechanism.

Based on these results, we constructed a simplified model of the network that can capture the negative-feedback-based 0A~P pulsing mechanism. This model used KinA concentration as a time-varying signal and had just three variables: 0A~P, 0F, and an auxiliary variable to account for a delay in transcriptional activation of 0F by 0A~P (Fig. D.2A). This minimal model also demonstrated that a change in the *kinA:0F* ratio together with ultrasensitive repression of 0A~P by 0F and delayed activation of 0F transcription are necessary and sufficient to produce the observed pulses of 0A~P (Fig. D.2B and C). Elimination of either of these ingredients destroyed the pulsing (Fig. D.2D–G). Notably, the introduction of the positive feedback into the model to mimic the effect of transcriptional activation of *kinA* and *spo0A* by 0A~P enhanced the ultrasensitivity of the repression of 0A phosphorylation by 0F and increased the pulse amplitudes resulting from changes in KinA:0F dosage ratio (Fig. D.2D–G). However, in agreement with the observations of Levine et al. (2012), this positive feedback is not essential for pulsing.

Altogether our model results suggest that two design features of the phosphorelay are crucial for the pulsatile response of 0A~P during starvation: (1) negative feedback between 0A~P and 0F and (2) transient gene dosage imbalance between *kinA* and *0F* resulting from the chromosomal arrangement of these genes. Consequently, our model predicts that disrupting these key features would abolish 0A~P pulsing and thereby affect sporulation (Fig. 5.3B-D and D.1).

5.3.4 Experimental tests confirm the role of gene-dose imbalance and negative feedback in 0A~P pulsing

We tested our modeling predictions by engineering two sets of *B. subtilis* strains. The first set of strains was engineered to examine how the chromosomal arrangement of *kinA* and *0F* and the resulting transient gene dosage imbalance affects 0A~P pulsing (Fig. 5.4A-E). In the first strain, *Trans-0F*^{gltA} (Fig. 5.4B), we eliminated the transient imbalance in the *kinA:0F* ratio by translocation of the *0F* gene to the *gltA* locus close to the terminus. As a control, we engineered a second strain (*Trans-0F*^{amyE}; Fig. 5.4C) by moving the *0F* gene to the *amyE* locus near the origin so that the *kinA:0F* imbalance is retained despite the translocation. Because the entire *0F* gene with the upstream region containing regulatory sequences was translocated in both strains, only the relative gene dosage during replication was perturbed whereas the negative feedback regulation remained intact. As predicted by the model (Fig. 5.3B), pulsing was abolished in the *Trans-0F*^{gltA} strain but not in the *Trans-0F*^{amyE}, which exhibited pulsing similar to the WT cells (Fig. 5.4F-H). The lack of pulsing in the *Trans-0F*^{gltA} resulted solely from the change in chromosomal position of *0F* and not from reduced *0F* expression. Specifically, we measured the activity of P_{0F} at *amyE* and *gltA* loci and found that it displays the same pulsatile behavior with similar expression levels (Fig. 5.6).

Following the same line of thought, we constructed two *Trans-kinA* strains by chromosomally translocating *kinA* to perturb the transient *kinA:0F* imbalance. In *Trans-kinA*^{gltA} (Fig. 5.4D) and *Trans-kinA*^{amyE} (Fig. 5.4E), we moved the *kinA* gene to *gltA* locus near the terminus and the *amyE* locus near the origin respectively. Translocation of *kinA* close to the origin in *Trans-kinA*^{amyE} eliminated the transient imbalance in the *kinA:0F* ratio whereas the *kinA:0F* imbalance was retained in *Trans-kinA*^{gltA}. Similar to the *Trans-0F* strains the negative feedback regulation remained intact in the *Trans-kinA* strains. As predicted by our model, *Trans-kinA*^{gltA} exhibited pulsing similar to the WT cells whereas pulsing was abolished in the *Trans-kinA*^{amyE} strain (Fig. 5.4IJ). However, in contrast to the non-pulsing *Trans-0F*^{gltA} strain, the non-pulsing *Trans-kinA*^{amyE} displayed a high level of 0A activity. This difference can be attributed to the compensatory effect of other kinases (such as KinB) or to the increased expression of *kinA* from the *amyE* locus. Together, the results from these translocation experiments confirm the prediction that transient *kinA:0F* gene dosage imbalance is necessary for 0A pulse generation.

To further establish the role of transient imbalance in *0F* to *kinA* expression rates, we constructed a rescue strain, *iTrans-0F* (Fig. 5.4K). In addition to *0F* translocation to the terminus (*Trans-0F*^{gltA}), we integrated an additional IPTG-inducible copy of *0F* close to the chromosome origin to recover the transient imbalance in *0F* to *kinA* expression rates during replication. In the absence of IPTG, this strain acted like the non-responsive *Trans-0F*^{gltA} strain and showed no 0A~P pulsing. However, at 5µM IPTG the sporulation in the *iTrans-0F* strain was restored similar to the WT strain (Fig. 5.4P). Thus, we concluded that the transient imbalance in *kinA* and *0F* expression resulting from their chromosomal locations acts as an essential trigger for 0A~P pulses.

To test the role of negative feedback between 0A~P and 0F in pulse generation, we created a second set of strains, *i0F*^{amyE} and *i0F*^{gltA} (Fig. 5.4L-O), in which 0F is expressed from the IPTG-inducible P_{hsp} promoter, rather than the native 0A~P regulated promoter. According to our simulations (Fig. 5.3CD), even though 0A~P pulsing in these strains would be disrupted, cells could still accumulate high levels of 0A~P if 0F expression was below the inhibitory range determined in Fig. 5.2C. Indeed, we found that in *i0F*^{amyE} and *i0F*^{gltA} strains, the 0A promoter activity increased gradually over time to levels comparable to that in WT at 5µM IPTG (low 0F expression; Fig. 5.4QR). In contrast, at 20µM IPTG (high 0F expression; Fig. 5.4ST) there was no significant increase in 0A promoter. We also found that, consistent with our model predictions (Fig. 5.3C), 0A promoter activity in *i0F*^{amyE} fluctuates (Fig. 5.4M) due to transient changes in *kinA:0F* expression ratios in this strain. However, these fluctuations did not resemble the adaptation type pulsatile responses of the WT and *Trans-0F*^{amyE} strains. In fact, unlike the WT and *Trans-0F*^{amyE} strains, both *i0F*^{amyE} and *i0F*^{gltA} strains showed no statistically significant difference between the peak 0A activity during a cell-cycle and the 0A activity at the end of the cell cycle (Fig. 5.8). This led us to conclude that 0A activity does not pulse in these strains, thereby confirming our prediction that the negative feedback in the phosphorelay is essential for producing pulses of 0A~P in response to starvation.

5.3.5 Lack of 0A~P pulsing leads to sporulation defects

Notably, the lack of 0A~P pulsing in the *kinA* translocation strain *Trans-kinA*^{amyE} and the inducible *i0F*^{amyE} and *i0F*^{gltA} strains did not prevent them from producing spores (for *i0F* strains this is the case only at 5µM IPTG when 0F expression was low; see Fig. 5.5A). Thus, 0A~P pulsing was not essential for sporulation, but we hypothesized that it was necessary for ensuring that the threshold level of 0A~P activity required for asymmetric septation or σF activation would only be reached in the cells with two complete chromosomes. Accordingly, we predicted that strains with a non-pulsatile accumulation of 0A~P would exhibit an increased frequency of defective sporulation phenotypes resulting from untimely 0A activation.

To determine whether pulsatile 0A activation plays a role in preventing faulty sporulation, we counted the frequency of defects in the pulsing WT and non-pulsing *Trans-kinA*^{amyE} and *i0F*^{gltA} strains. We specifically focused on two types of sporulation defects

(Fig. 5.5B): (i) Asymmetric septation without activation of σF in the forespore and (ii) Activation of σF in the mother cell before asymmetric septation. We found that asymmetric septation without activation of σF causes cells to bud off a small daughter cell that lacks DNA and dies soon after division (Fig. 5.5B). On the other hand, activation of σF in the mother cell causes cell death (Fig. 5.5B). Thus, both types of defects affect the ability of cells to efficiently produce spores. Counting the number of such abnormalities, we found that the frequency of defects per spore produced over 30hrs in starvation conditions was about three-fold higher in the *i0F*^{gltA} strain (14.7% 1.7%; 3 independent measurements >250 spores each) and *Trans-kinA*^{amyE} strain (13.1% 5.8%; 3 independent measurements >100 spores each) relative to the WT strain (5.0% 1.5%; 3 independent measurements, >250 spores each) (Fig. 5.5C). Therefore, we find that 0A~P pulsing plays a key role in preventing defective sporulation.

Next, we examined whether the higher frequency of defects/spore ratio in the non-pulsing *i0F*^{gltA} strain results from lack of proper coordination of sporulation with the cell-cycle. To test this idea, we used time-lapse microscopy data for the *i0F*^{gltA} strain to compute the time of cell-fate decisions both in cell-cycles that successfully produce spores and those that end in defective sporulation. The time of cell-fate decision was defined as the time from the start of the cell-cycle to the time of P$_{spoIIR}$-*cfp* (a σF reporter) activation in the cases of normal sporulation and the mother cell σF activation defect. For the defect of asymmetric septation without σF activation, the time of cell-fate decision was defined as the time from the start of the cell-cycle to the time of asymmetric septation. As shown in Fig. 5.5B and D, cell-cycles that end in sporulation defects reach cell-fate decisions early in the cell-cycle (2-3hrs after the start of the cell-cycle). We note that unlike rich medium conditions, cell-cycle durations in starvation conditions are typically 5-6 hours long. As DNA replication is incomplete early in the cell-cycle, these early cell-fate decisions appear to arise from the attempt to execute the sporulation program without two complete chromosomes. In contrast, in cell-cycles that successfully produce a spore, the timing of cell-fate decisions is typically late in the cell-cycle (>4hrs after the start of the cell-cycle; Fig. 5.5B and D), after the completion of DNA replication. Thus, we concluded that activation of 0A and commitment to sporulation too early in the cell-cycle, before the completion of DNA replication, is responsible for both sporulation defects. Moreover, since these defects occur at a higher frequency in the non-pulsing $i0F^{gltA}$ strain, these results show that the 0A~P pulsing plays a key role in preventing sporulation defects because of its ability to ensure proper coordination of the sporulation program with DNA replication.

5.4 Discussion

Taken together, our results reveal a novel mechanism for coupling cell-fate decisions to DNA replication. Using an ultrasensitive, delayed negative feedback loop to detect the transient imbalance of gene dosage resulting from directional chromosome replication allows *B. subtilis* to use DNA replication itself as the trigger for 0A activation, thereby ensuring that these two do not temporally conflict with each other. Moreover, the pulsatile activation of 0A during every cell cycle offers *B. subtilis* cells an opportunity to evaluate their starvation level and decide between sporulation and continued vegetative growth on a cell-cycle by cell-cycle basis.

One of the key design features that underlie the pulsatile 0A~P dynamics appears to be a negative feedback loop, which is known to be one of the few network motifs capable of generating adaptation-like pulsatile responses (Ma et al. 2009). The crucial component that creates this negative feedback is the substrate inhibition of KinA by 0F through the formation of a dead-end complex that blocks KinA autophosphorylation. This substrate inhibition effect has been demonstrated previously (Grimshaw et al. 1998) but has received little attention in mathematical modeling studies. This effect is however essential for explaining the inhibitory effect of 0F overexpression on sporulation (Chapman and Piggot 1987; Chastanet et al. 2010; Sen, Garcia-Ojalvo, and Elowitz 2011). Our results demonstrate that this negative feedback based on the substrate inhibition of KinA by 0F plays a critical role in coupling 0A~P pulsing to DNA replication. Alternative explanations for 0A~P pulsing suggested by earlier studies invoke either the 0A~P-AbrB-Spo0E negative feedback loop (Schultz et al. 2009) or the inhibition of KinA by Sda (Veening, Murray, and Errington 2009a). However, a pulsing mechanism based on the 0A~P-AbrB-Spo0E negative feedback loop is unlikely since it cannot explain our observations of the cell-cycle coupling of pulses (Fig. 5.1D). In addition, a recent study has shown the Spo0E deletion does not affect pulsing (Levine et al. 2012). On the other hand, the cell-cycle dependent oscillations of Sda provides a viable explanation for the DNA replication-coupled 0A~P pulses. However, our results showing the lack of pulsing in $i0F^{gltA}$ strain where 0A~P-0F negative feedback is perturbed (Fig. 5.3D), suggests that substrate inhibition feedback that we propose here plays the key role in controlling 0A~P dynamics.

Notably, dead-end complex based substrate inhibition mechanisms have been previously postulated to act as a source of ultrasensitivity in the response of bacterial two-component systems and sigma factor regulation (Clarkson et al. 2004; Igoshin, Alves, and Savageau 2008; Igoshin, Price, and Savageau 2006). Our results reveal that these mechanisms can also result in ultrasensitivity in the ratio of the two genes involved in dead-end complex substrate inhibition – specifically the KinA:0F ratio. In the case of sporulation, this ratio sensitive response forms the basis of the coupling of 0A~P pulsing to DNA replication by a gene dosage mechanism. More generally, however, this ratio-sensitive response provides a unique mechanism for the integration of different environmental signals - a feature that may be relevant to wide variety systems that employ phosphorelay networks (Appleby, Parkinson, and Bourret 1996).

The sensitivity of phosphorelay response to the KinA:0F ratio and as a result of their gene dosages also suggests a unique mechanism for growth rate based control of sporulation. In nutrient-rich conditions, for cells with a generation time of less than the time required replication, new rounds of replication begin before the previous round terminates, resulting in multifork replication (Wang and Levin 2009). As a result of multifork replication, cells have multiple copies of the origin-proximal chromosomal region and a single copy of the terminus-proximal region. Consequently, the relative gene dosage of origin-proximal and terminus-proximal genes increases at a high growth rate (Wang and Levin 2009). Considering that *0F* and *kinA* are origin-proximal and terminus-proximal respectively, this implies that the low KinA:0F ratio at high growth rates could prevent 0A activation sporulation in nutrient-rich conditions. A similar origin-terminus relative gene dosage mechanism has been shown to regulate histidine metabolism in response to the growth rate in Salmonella typhimurium (Blanc-Potard, Figueroa-Bossi, and Bossi 1999). Our results suggest that in *B. subtilis*, the *kinA:0F* relative gene dosage sensitive phosphorelay may act similarly and function as a growth rate dependent decision mechanism although this requires further investigation.

Our results also show that to enable the pulsatile 0A~P response strategy, the design of the sporulation network exploits a universal feature of bacterial physiology: the transient imbalance of gene dosage between origin-proximal and terminus-proximal genes during chromosome replication. It is well-known that chromosomal location of genes affects their expression (Block et al. 2012; Klumpp, Zhang, and Hwa 2009) and that clustering of genes facilitates their co-regulation (Lathe et al., 2000). Recent studies have also revealed that origin-proximal location of genes can be used to detect DNA replication stress and trigger bacterial competence (Slager et al. 2014). Our results add to this growing repertoire of functional roles for the chromosomal arrangement of regulatory genes and provide a simple cell-cycle coupling mechanism that could very well be employed in a wide range of other microbial species and stress response mechanisms.

5.5 Method

5.5.1 Strain construction

Table 5.1 lists *B. subtilis* strains used in this study. All strains are isogenic to *B. subtilis* PY79. Gene *spo0F* with it native P_{spo0F} promoter (165 bp upstream) and 43 bp downstream sequence were PCR amplified from *B. subtilis* PY79 with the addition of a terminator upstream (CCAGAAAGTCAAAAGCCTCCGACCG) and ligated to either ECE173 (Pm^R) between BHI and XbaI restriction sites, or pLD30 (Sp^R) between BHI and ERV sites. These constructs were used, respectively, to create *Trans-0F^{gltA}* and *Trans-0F^{amyE}* strains. To create *i0F^{amyE}* strain, the *spo0F* gene was PCR amplified from *B. subtilis* PY79 with the addition of optimal RBS and linker (AAGGAGGAAAGTCACATT) and including 43 bp fragment downstream. It was ligated to a derivative of PLD30, the JDE131 plasmid (Sp^R) next to the P$_{hyperspank}$ promoter (between HindIII and NheI restriction sites). To create *i0F*^{gltA} strain, the region containing P$_{hyperspank}$ promoter, *spo0F,* and *lacI* were subcloned from resulting JDE131 and integrated into ECE173 (Pm^R) between BHI and ERI restriction sites. For *spo0F* deletion construct, the 5' and 3' fragments were PCR amplified using the following primers:

GAGGCGCCCCTGTCGCTTTCTGTCACTTCCTCAG and TCGAATTCGCAAAATACGAATGCCGTATTGATCATCAACGA for 5' arm, GATCTAGAGACATCGACGAAATCAGAGACGCCGTCAAAAAATATCTGCCCCTGAAGTCTAAC and TCGTCGACCCTTCGGAAACACCAAGGATCACTGGAG for 3' arm, and integrated as recombination arms into either per449 (Erm^R) or per449 (Kan^R) vectors between KasI and ERI, or XbaI and SalI restriction sites, respectively. The reporter strains were described previously (Kuchina et al., 2011a; Kuchina et al., 2011b).

5.5.2 Culture preparation

For imaging, *B. subtilis* culture was started from an overnight LB agar plate containing appropriate antibiotics (final concentrations: 5 µg/ml chloramphenicol, 5 µg/ml neomycin, 5µg/ml erythromycin, 5µg/ml phleomycin and 100 µg/ml spectinomycin). Strains containing multiple resistance genes were grown on a combination of no more than three antibiotics at a time. Cells were resuspended in casein hydrolysate (CH) medium (Sterlini and Mandelstam, 1969) and grown at 370C with shaking. After reaching OD 1.8-2.0, cells were washed once and resuspended in 0.5 volume of Resuspension Medium (RM) (Sterlini and Mandelstam, 1969). The resuspended cells were grown at 37°C for 1 hour, then diluted 15-fold and applied onto a 1.5% low-melting agarose pad made with RM-MOPS medium with desired IPTG or glucose concentration, if necessary. The pads were covered, left to air-dry for 1 hour at 37°C and placed into a coverslip-bottom Willco dish for imaging.

5.5.3 Data Analysis

A combination of Schnitzcells software (http://cell.caltech.edu/schnitzcells), custom written MATLAB programs, MicrobeTracker tool (Sliusarenko et al., 2011) and freely available ImageJ plugins (Rasband, W.S., ImageJ, U. S. National Institutes of Health, Bethesda, Maryland, USA, http://imagej.nih.gov/ij/, 1997-2014) was used to analyze microscopy data as described below.

5.5.3.1 Quantification of cell growth rates

The mean cell-growth rate for individual cell-cycles (Fig. 5.1, 5.4 and 5.6) was quantified using the measurements of cell-length in the time-lapse data. We first calculated the instantaneous cell-growth rate at every frame as:

$$\mu(t) = \frac{1}{L(t)}\frac{dL(t)}{dt} = \frac{d\log L(t)}{dt} = \frac{\log(L(t+\Delta t)) - \log(L(t))}{\Delta t}$$

where L(t) is the cell-length at time t and Δt is the time difference between successive frames (20 minutes). For cell-cycles that result in vegetative division, mean growth rate during a cell-cycle was defined as the average of μ(t) over the cell-cycle duration. For cell-cycles that end in sporulation, the mean growth rate was the average of μ(t) over the cell-cycle duration until the asymmetric division. Depending on the strain, the asymmetric division was defined either as P_{spoIIR} activation (for the strains in which a P_{spoIIR} reporter was present) or as the time frame two-hours before the appearance of the phase-bright forespore.

5.5.3.2 Calculation of Promoter Activity

The measurements of promoter activities for P_{0A}-*cfp/yfp* promoters (Fig. 5.1C and 5.4) and the P_{0F}-*yfp* promoter (Fig. 5.6) refer to rate of protein production calculated from fluorescence time-lapse data. Promoter activity for a specific promoter can be estimated from the dynamics of fluorescent reporter expression from that promoter. Given a specific promoter- fluorescent reporter combination, the dynamics of the reporter protein concentration [F] are given by the following equation:

$$\frac{d[F]}{dt} = P_F(t) - (\gamma + \mu(t))[F] \qquad (1)$$

Here PF(t) is the protein production rate or the promoter activity. $\mu(t)$ and γ are the protein dilution and degradation rates respectively. Rearranging equation (1), we find the following expression for the promoter activity PF(t):

$$P_F(t) = \frac{d[F]}{dt} + (\gamma + \mu(t))[F] \qquad (2)$$

The reporter protein concentration, [F], depends on the total amount of fluorescent protein inside the cell, F and the cell volume V : [F]=F/V. Thus we can rewrite equation (2) as:

$$P_F(t) = \frac{d\left(F(t)/V(t)\right)}{dt} + (\gamma + \mu(t))\frac{F(t)}{V(t)} \qquad (3)$$

Approximating the cells as cylinders,

$$V(t) = \pi W^2 L(t) \qquad (4)$$

$$F(t) = M(t)WL(t) \qquad (5)$$

where W is cell width assumed to be constant, L(t) and M(t) are cell-length and mean cell fluorescence respectively. This change in variables makes the estimates of promoter activity less sensitive to segmentation errors (Levine et al., 2012; Rosenfeld et al., 2005). Using equations (4) and (5) in equation (3):

$$P_F(t) = \frac{1}{\pi W}\left[\frac{dM(t)}{dt} + (\gamma + \mu(t))M(t)\right] \tag{6}$$

Using equation (6) the promoter activity $P_F(t)$ can be determined from fluorescence time-series data by using the dilution rate $k_{dil}(t)$ and the derivative of M(t). We used the following approximations to calculate the promoter activity (up to a proportionality constant):

$$\begin{aligned}
&\frac{dM(t)}{dt} = \frac{M(t+\Delta t) - M(t)}{\Delta t}\\
&\mu(t) = \frac{1}{L(t)}\frac{dL(t)}{dt} = \frac{\log(L(t+\Delta t)) - \log(L(t))}{\Delta t}\\
&P_F(t) \propto \frac{M(t+\Delta t) - M(t)}{\Delta t} + \gamma M(t) + \frac{\log(L(t+\Delta t)) - \log(L(t))}{\Delta t}M(t)
\end{aligned} \tag{7}$$

Here Δt is the time difference between successive frames (20 minutes). We used γ=0.1 hr-1 since in our conditions, fluorescent proteins CFP and YFP are stable.

5.5.3.3 Quantification and characterization of promoter activity pulses

Promoter activity time-series determined from fluorescence microscopy were smoothed using the MATLAB smooth function by employing a Savitsky-Golay filter with a 3rd-order polynomial over a sliding window of 5 frames. After smoothing, the time to reach the maximum promoter activity from the start of the cell-cycle and was used to calculate the T_P period (Fig. 1D).

To differentiate pulsing and non-pulsing strains (Fig. D.2), the promoter activity in each cell-cycle was quantified at three-time points: at the start of the cell-cycle, at the point during the cell-cycle where the promoter activity reaches its maximum value and at the end of the cell cycle (Fig. D.2AB). To determine whether the increase in 0A promoter activity during each cell cycle occurs in a pulsatile manner we compared ΔMax, the difference between Peak promoter activity and promoter activity at the start of the cell cycle, and ΔEnd, the difference between the promoter activities at the start and end of the cell cycles. In each strain, we aggregate the data for ΔMax and ΔEnd at each cell cycle and compare their distributions with a two-sample t-test. Statistical significance of the observed differences in ΔMax and ΔEnd is used to detect whether pronounced pulsing can be detected for each strain.

5.5.3.4 Identification of DNA replication periods using DnaN foci

To identify DNA replication windows in time-lapse experiments (Fig. 5.1BC) we expressed a fluorescent DnaN-YFP fusion protein from the IPTG inducible $P_{hyperspank}$ promoter. During DNA replication, the DnaN forms subcellular foci (Su'etsugu and Errington, 2011; Veening et al., 2009). Using the DnaN-YFP fusion protein, these foci can be detected as diffraction-limited spots. We used the SpotFinderF MATLAB program (Sliusarenko et al., 2011) with a signal-to-background ratio of 40 as the minimum peak height to identify DnaN-YFP foci and active DNA replication periods. DNA replication periods identified in this way were used to calculate the difference between the start of the cell-cycle and the end of DNA replication or T_r period (Fig. 5.1D) for each cell-cycle in the time-lapse data.

5.5.3.5 Estimation of the spore fraction

To get an estimate of the sporulation efficiency of the various strains in Fig. 5.3 we calculated a spore fraction for each strain after 25 hrs in starvation conditions (see Fig. 5.5A). The spore fraction was calculated by dividing the number of cells that had formed phase-bright spores by the total number of cells. Three independent measurements were made for each strain with more than 200 cells counted in each instance to calculate the mean and standard deviations of spore fractions.

5.5.3.6 Quantification of sporulation defects

We manually counted the number of both types of sporulation defects (Asymmetric septation without σF activation and Activation of σF in the mother cell) in the time-lapse images of pulsing WT strain (harboring the same integrated reporters and *gltA* knockout as *i0F*^{gltA} strain) and of the non-pulsing *i0F*^{gltA} (at 5µM IPTG) and *Trans-kinA*^{amyE} strains over 30 hrs in starvation conditions. We also counted the total number of spores produced over those 30 hrs to calculate the frequency of defects produced for both strains per spore (Fig. 5.5B). A two-sample t-test was used to determine the statistical significance of the observed differences.

To determine the timing of cell-fate decision in sporulation defects and normal sporulation (Fig. 5.5C) we used time-lapse microscopy data from the non-pulsing *i0F*^{gltA} strain. The timing of the cell-fate decision was defined as the time from the start of the cell-cycle to the time of P$_{SpoIIR}$-*cfp* (a σF reporter) activation in the cases of normal sporulation and mother cell σF activation defect. For the case of asymmetric septation without σF activation defect, the time of cell-fate decision was defined as the time from the start of the cell-cycle to the time of asymmetric septation.

Chapter 5, in full, is a reprint of the material *Jatin Narula*, Anna Kuchina*,* ***Dong-yeon D. Lee****, Masaya Fujita, Gürol M. Süel, Oleg A. Igoshin. "Chromosomal Arrangement of Phosphorelay GenesCouples Sporulation and DNA Replication" Cell 162, 328–337.*

*2015 (*equal contribution).* The dissertation author performed experiments regarding translocated *kinA* strains, which were used in Figure 5.4, 5.5, and 5.8.

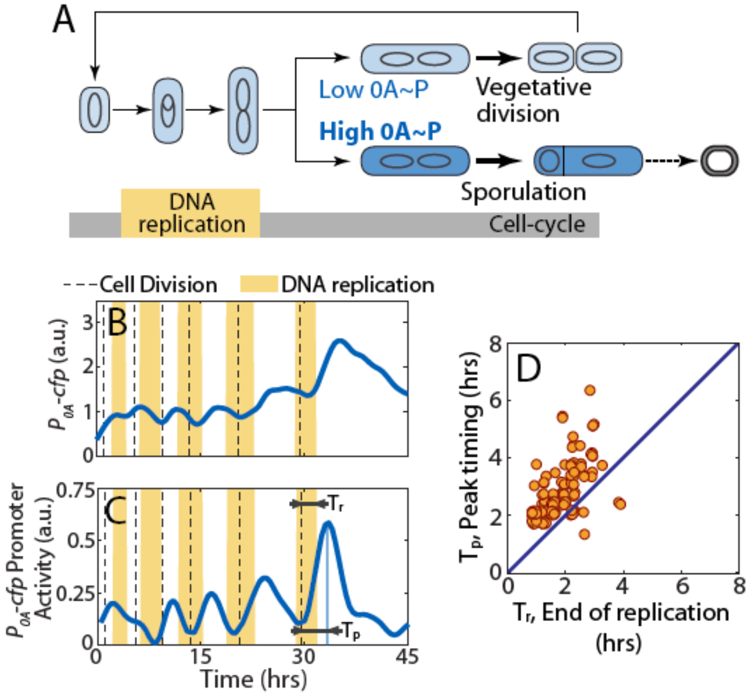

Figure 5.1 Coordination of the sporulation response with the cell-cycle in *B. subtilis*.

(A) Cell-cycle of starving *B. subtilis* cells. In starvation conditions, cells first complete DNA replication and then make a cell-fate decision. They either divide medially and continue with slower vegetative growth or divide asymmetrically and commit to sporulation producing a stress-resistant spore. The cell-fate decision is based on the level of phosphorylated master regulator Spo0A (0A~P). 0A~P exceeding threshold commit cells to sporulation whereas lower levels allow cells to continue growth. The decision must be made after the completion of DNA replication phase (yellow bar) since two complete chromosomes are needed to produce a viable spore.

(B-C) Single-cell time-lapse microscopy using a P_{0A}-*cfp* reporter for 0A~P. The expression level of P_{0A}-*cfp* **(B)** increases in a pulsatile fashion over multiple cell-cycles in starvation media. Its promoter activity (defined as production rate, an indicator of 0A~P level) also shows pulses of increasing amplitude **(C)** over multiple generations during starvation. In B and C, vertical dashed lines indicate cell divisions and yellow shaded regions indicate periods of DNA replication (detected by the presence of DnaN-YFP foci). Note that DNA replication is sometimes initiated just before cell division. For each cell cycle, we can determine the time from birth to end of DNA replication (T_r) and time from birth to peak P_{0A}-*cfp* Promoter activity (T_p) represent respectively.

(D) Measurements of time from birth to end of DNA replication (T_r) and time from birth to peak P_{0A}-*cfp* Promoter activity (T_p) show that $T_p>T_r$ for the vast majority of the cell-cycles implying that 0A activity peaks occur after DNA replication is complete.

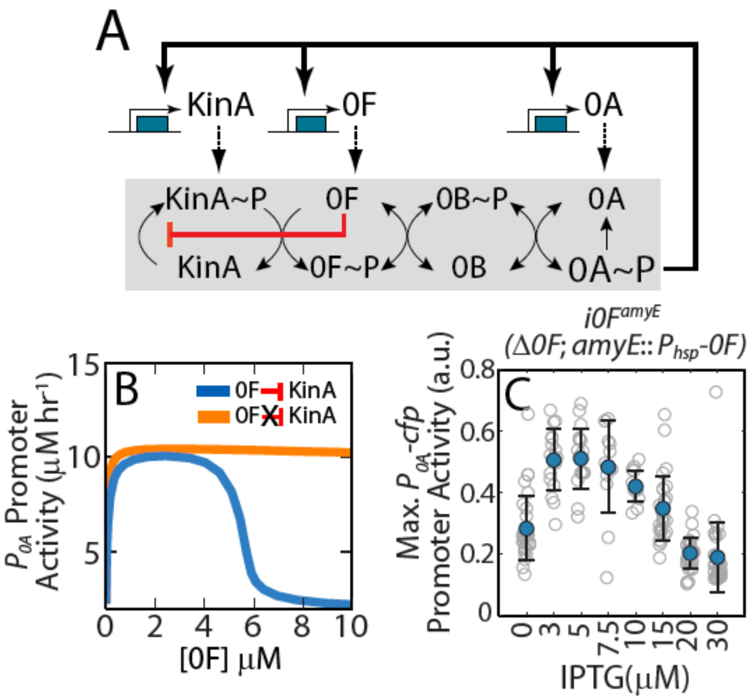

Figure 5.2 Substrate inhibition of 0F by KinA produces a negative feedback in the phosphorelay.

(A) Network diagram of the sporulation phosphorelay network that controls the activity of the master regulator Spo0A (0A). The phosphorelay includes both post-translational and transcriptional regulatory interactions. Post-translationally, the kinases KinA-E (only KinA is shown) transfer phosphoryl groups to the master regulator 0A via the two phosphotransferases Spo0B (0B) and Spo0F (0F). Transcriptionally, 0A~P controls the expression of *kinA*, *0F* and *0A* both directly and indirectly via AbrB and σ^H (not shown) forming multiple transcriptional feedback loops. Our model also includes a substrate inhibition interaction (red blunted arrow) whereby excess 0F can bind to unphosphorylated KinA and block its autophosphorylation. This substrate inhibition creates a negative feedback loop wherein 0A~P activates *0F* expression and 0F inhibits 0A activation by inhibiting KinA. **(B)** Mathematical model predicts steady-state levels of 0A promoter activity as a function of 0F concentration. The results show that, for a phosphorelay with substrate-inhibition of KinA by 0F (blue curve), 0A promoter activity is a non-monotonic function of 0F concentrations and decrease ultrasensitively for [0F]>5μM. In contrast, for a phosphorelay without substrate-inhibition (orange curve), 0A promoter activity monotonically increase to saturated value. **(C)** Predicted non-monotonic dependence of 0A activity on 0F levels is confirmed by engineering inducible 0F strain, $i0F^{amyE}$ (*Δ0F; amyE::*P_{hsp}*-0F*) and measuring maximum 0A promoter activity in the at different levels of 0F induction. Gray empty circles show maximum P_{0A} promoter activity levels achieved by individual cell lineages over 25 hours in starvation conditions at each IPTG concentration. Blue filled circles and error bars indicate the mean and standard deviations of these measurements at each IPTG concentration. Maximum P_{0A} promoter activity decreases at high 0F expression levels (IPTG>10μM) in agreement with the substrate-inhibition effect of *0F* overexpression.

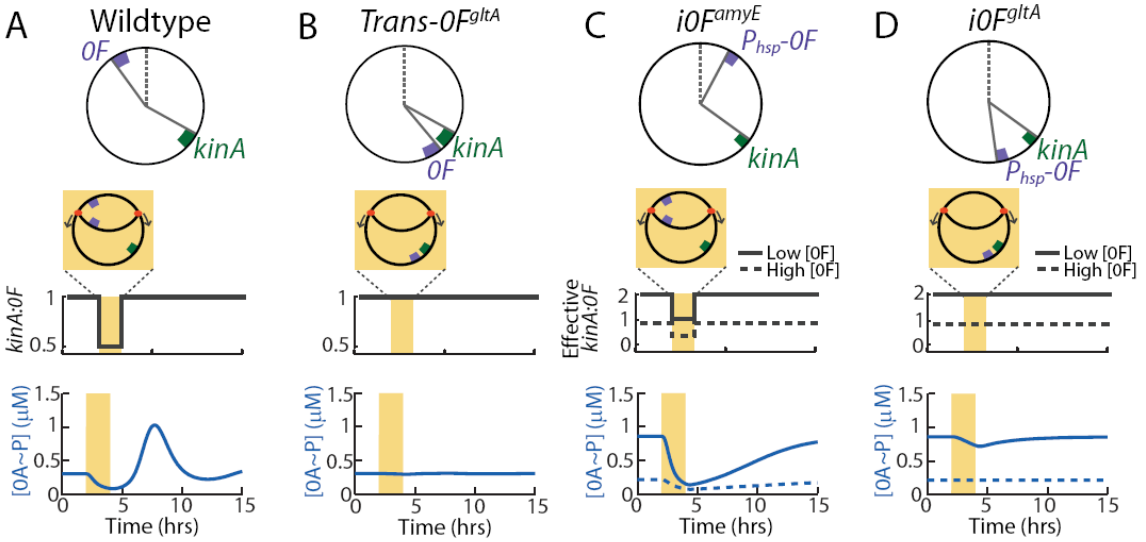

Figure 5.3 Mathematical model identifies the mechanism of 0A~P pulsing and its necessary conditions.

Top panels in **(A-D)** show chromosomal arrangements of *0F* and *kinA* in **(A)** Wildtype (WT) *B. subtilis* and synthetic mutant strains: **(B)** *Trans-0F*^{gltA}, **(C)** *i0F*^{amyE}, **(D)** *i0F*^{gltA}. *0F* is located close to the origin of replication in WT and *i0F*^{amyE} strains and close to the terminus in the *Trans-0F*^{gltA} and *i0F*^{gltA}. *kinA* is located close to the terminus in all strains. Note that *0F* is expressed from the IPTG-inducible P_{hsp} promoter, rather than the native 0A~P regulated P_{0F} promoter in the inducible *i0F*^{amyE} and *i0F*^{gltA} strains.

Middle panels in **(A-D)** show changes in *kinA:0F* gene dosage ratio in the WT and mutant strains. In WT **(A)** and *i0F*^{amyE} **(C)**, *0F* is replicated before *kinA* due to their arrangement on the chromosome. As a result, there is a transient decrease in the *kinA:0F* gene dosage ratio during DNA replication (yellow bar). The translocation of *0F* close to the terminus in a synthetic *Trans-0F*^{gltA} **(B)** and *i0F*^{gltA} **(D)** strains eliminates the transient *kinA:0F* decrease. In the inducible *i0F*^{amyE} and *i0F*^{gltA} strains, the effective *kinA:0F* gene dosage depends on whether the level of 0F expression from the IPTG-inducible P_{hsp} promoter is low (solid line) or high (dashed line).

Bottom panels in **(A-D)** show model predictions for the response of 0A~P levels to the changes in *kinA:0F* ratio in WT and mutant strains. Model simulations show that the transient decrease in *kinA:0F* during DNA replication (yellow bar) in WT **(A)** inhibits the phosphorelay phosphate flux, thereby causing a decrease in 0A~P. Once DNA replication is complete, the phosphorelay produces an overshoot of 0A~P before returning to the steady state resulting in a 0A~P pulse. Model results also predict that that elimination of the transient decrease of *kinA:0F* in the *Trans-0F*^{gltA} strain **(B)** abolishes 0A~P pulsing and instead the system stays at steady state. In the *i0F*^{amyE} strain **(C)**, the transient decrease in effective *kinA:0F* inhibits the phosphorelay phosphate flux and causes a decrease in 0A~P but 0A~P does not overshoot before returning to the steady state and there is no pulse. This 0A~P response depends on the level of 0F expression. Simulations also show that elimination of the transient decrease of *kinA:0F* in the *i0F*^{gltA} strain **(D)** abolishes 0A~P pulsing and instead the system stays at steady state. The steady-state 0A~P level depends on whether *0F* expression from the IPTG-inducible P_{hsp} promoter is low (solid line) or high (dashed line). These results show that 0A~P pulsing is triggered by DNA replication and that both the *kinA-0F* chromosomal arrangement and 0A~P-0F negative feedback are essential for 0A~P pulsing.

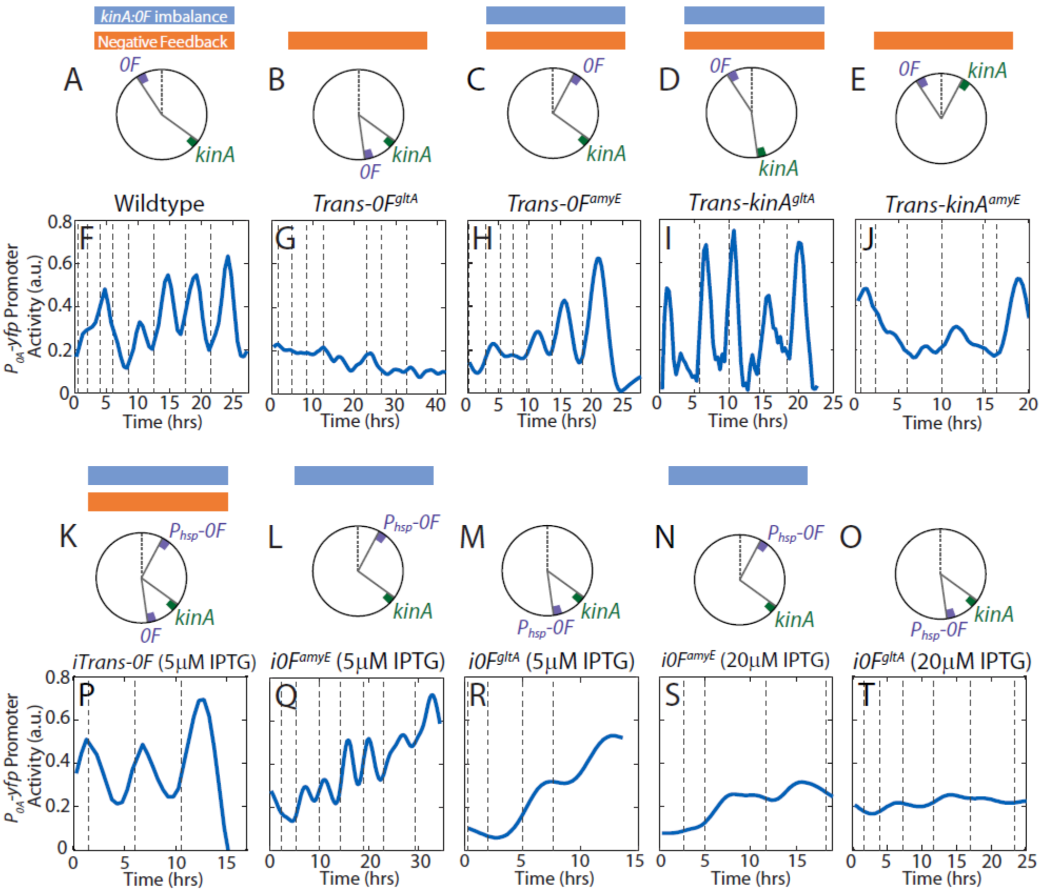

Figure 5.4 0A~P pulsing depend on the *kinA-0F* chromosomal arrangement and transcriptional feedback from 0A~P to 0F negative feedback.
(A-E) Chromosomal arrangements of *0F* and *kinA* in Wildtype *B. subtilis* **(A)**, *Trans-0F*^{gltA} **(B)**, *Trans-0F*^{amyE} **(C)**, *Trans-kinA*^{gltA} **(D)** and *Trans-kinA*^{amyE} **(E)** strains. Blue and orange bars mark strains that have transient *kinA:0F* imbalance and negative feedback respectively. **(F-J)** Measurements of P$_{0A}$-*yfp* activity in single cells during starvation. 0A~P pulses seen in Wildtype *B. subtilis* cells **(F)** are abolished by the translocation of *0F* to the *gltA* locus in the *Trans-0F*^{gltA} strain **(G)** but not by the translocation of *0F* to the *amyE* locus in the *Trans-0F*^{amyE} strain **(H)**. 0A~P pulses are also abolished by the translocation of *kinA* to the *amyE* locus in the *Trans-kinA*^{gltA} strain **(J)** but not by the translocation of *kinA* to the *gltA* locus in the *Trans-0F*^{gltA} strain **(I)**. Note that P$_{0A}$ -*yfp* promoter activity level does not increase in the *Trans-0F*^{gltA} strain. Vertical dashed lines indicate cell divisions. **(K-O)** Chromosomal arrangements of *0F* and *kinA* in *iTrans-0F* **(K)**, *i0F*^{amyE} **(L, N)** and *i0F*^{gltA} strains **(M, O)**. Note that both strains lack the 0A~P-0F negative feedback. **(P-T)** Measurements of P$_{0A}$ -*yfp* activity in single cells during starvation. Addition of an IPTG inducible copy of *0F* near the origin in the *iTrans-0F* strain **(P)** recovers the transient *kinA:0F* imbalance lost in *Trans-0F*^{gltA} strain and rescues the 0A~P pulses seen in wild-type *B. subtilis* cells. 0A activity pulsing is greatly decreased in the *i0F*^{amyE} **(Q, S)** and *i0F*^{gltA} strains **(R, T)** which lack the negative feedback. 0A activity in the *i0F*^{amyE} **(Q)** strain fluctuates due to transient changes in *kinA: P*$_{hsp}$*-0F* but does not pulse (Fig. 5.11). If 0F expression is low (at 5µM IPTG; **Q, R**), both *i0F* strains accumulate high 0A activity levels. High-level expression of *0F* (at 20µM IPTG; **S, T**) blocks 0A activation in both *i0F* strains similar to *Trans-0F*^{gltA}. Vertical dashed lines indicate cell divisions.

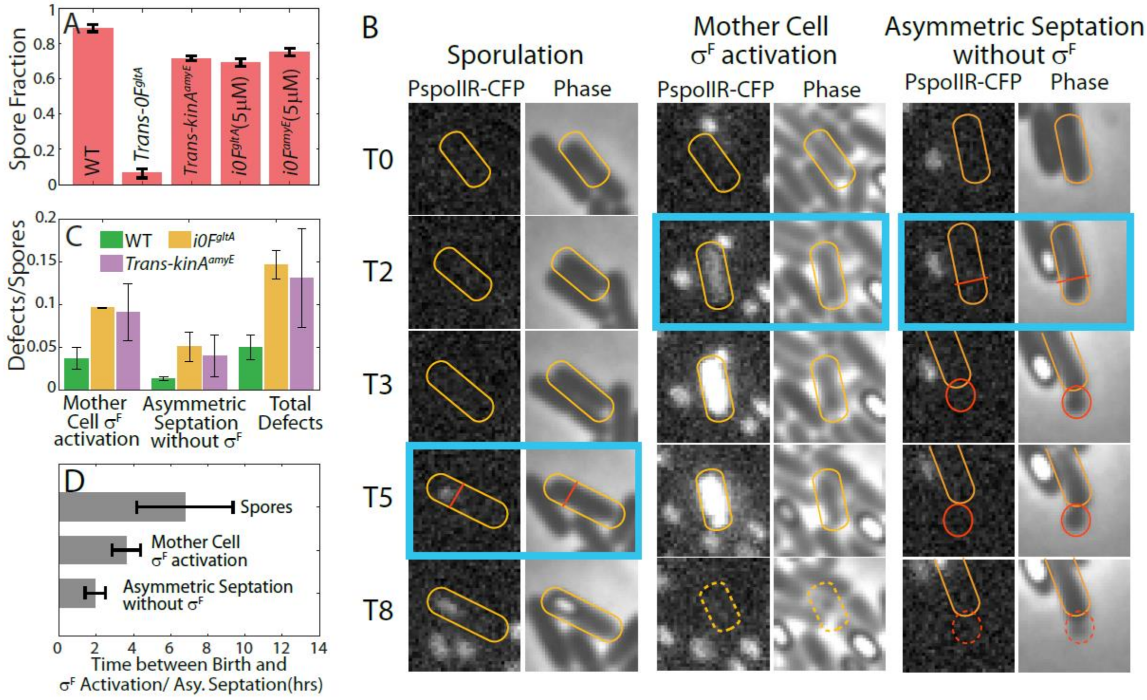

Figure 5.5 Loss of coordination of sporulation program with DNA replication in non-pulsing strains could lead to sporulation defects.

(A) The fraction of cells that have formed spores at 25hrs into starvation in different strains. Bars and error bars show the mean and standard deviation of spore fraction respectively for each strain. Means and standard deviations were calculated using 3 independent measurements for each condition. **(B)** Phase-contrast and fluorescence microscopy (P_{spoIIR}-*cfp*) images from a time-lapse experiment showing the difference in timing of SpoIIR activation/Asymmetric septation in sporulation and sporulation defects. T0 represents the time of birth for each indicated cell (yellow outline). T2, T3 etc. indicate time after birth in hours. Time-point of SpoIIR activation/Asymmetric septation in each case is marked by a blue box. Asymmetric septation and σ^F activation happen late in the cell-cycle (T5) during normal sporulation as compared to the sporulation defect cases. Early activation of σ^F in the whole cell at T2 results in cell death. Early asymmetric septation at T2 produces a small daughter cell (orange outline) which dies without activating σ^F in the forespore. **(C)** Quantification of the number of defects per spore produced over 30hrs in starvation conditions by the pulsing WT strain (green bars) and the non-pulsing strains *i0F*^{gltA} (yellow bars) and *Trans-kinA*^{amyE} (purple bars). Errorbars indicate the standard deviation of 3 independent measurements. The defects/spore ratio is significantly higher for non-pulsing strains for both types of sporulation defects. **(D)** Time difference between birth and SpoIIR (a σ^F reporter) activation/Asymmetric septation in cell-cycles that produce spores and those that end in lysis due to sporulation defects. SpoIIR activation/Asymmetric septation happens significantly earlier in cell-cycles that end sporulation defects.

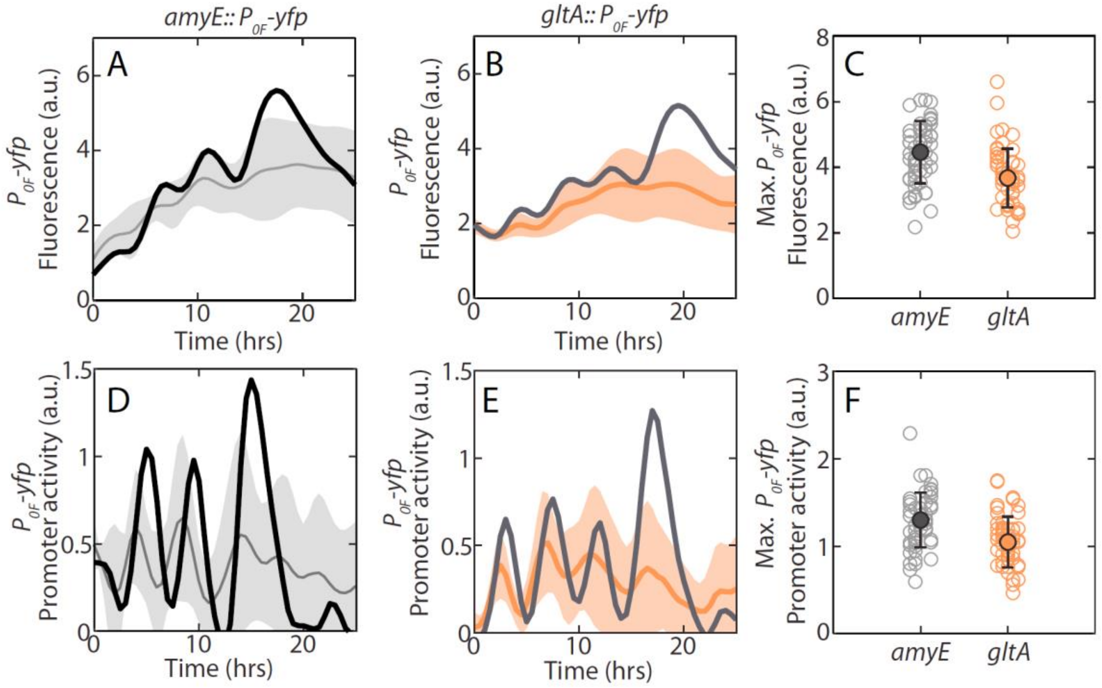

Figure 5.6 Pulsing from P_{0F} Promoters.

Related to Fig. 5.1 and 5.4 **(A and B)** Fluorescence measurements for P_{0F} -*yfp* reporters inserted at *amyE* **(A)** and *gltA* **(B)** loci in WT background. Solid lines and shaded regions show one example lineage trace and the mean expression level over multiple traces respectively. **(C)** Measurements of maximum P_{0F}-*yfp* fluorescence. Empty circles show maximum YFP fluorescence levels achieved by individual cell lineages over 25 hr in starvation conditions. Filled circles and error bars indicate the mean and standard deviations of measurements at each integration location. **(D and E)** Measurements for P_{0F} promoter activity for P_{0F} -*yfp* reporters inserted at *amyE* **(D)** and *gltA* **(E)** loci in WT background. Solid lines and shaded regions show one example lineage trace and the mean expression level over multiple traces respectively. Note that P_{0F} promoter activity pulses similar to P_{0A} promoter activity (see Fig. 5.1C). **(F)** Measurements of maximum P_{0F} promoter activity. Empty circles show maximum P_{0F} promoter activity levels achieved by individual cell lineages over 25 hr in starvation conditions. Filled circles and error bars indicate the mean and standard deviations of measurements at each integration location. Both maximum P_{0F}-*yfp* fluorescence and maximum P_{0F} promoter activity are comparable for the *amyE* and *gltA* locations.

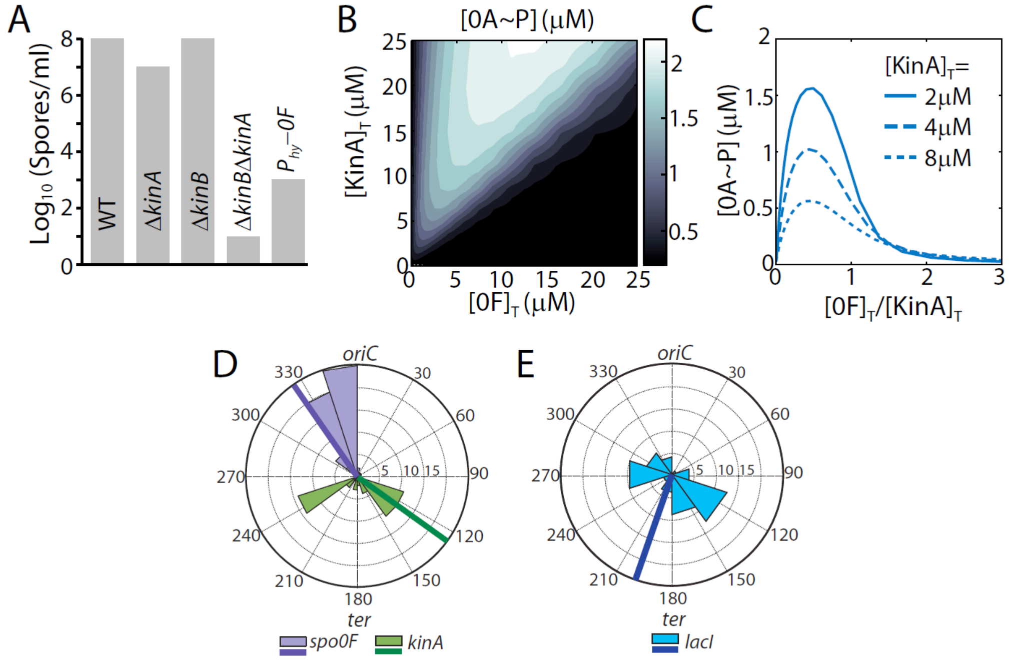

Figure 5.7 Role of 0F/KinA Ratio in Controlling 0A-P.

Related to Fig. 5.2 and 5.3 **(A)** Measurements of sporulation efficiency (spores/ml) in WT and mutant cells. *B. subtilis* strains used are: PY79 (wt), MF1237 (*ΔkinA*), MF1847 (*ΔkinB*), MF1855 (*ΔkinAΔkinB*), and MF2547 (Spo0F overexpression, *amyE*:: $P_{hyperspank}$-*spo0F*) (Eswaramoorthy and Fujita, 2010). Sporulation was induced according to the method of Sterlini and Mandelstam by shifting growth in casein hydrolysate (CH) medium to Sterlini-Mandelstam (SM) medium (Eswaramoorthy et al., 2010; Narula et al., 2012). For 0F overexpression in MF2547, 0.5mM IPTG was added to SM culture. Sporulation efficiency was measured as described previously (Eswaramoorthy et al., 2010). **(B and C)** Mathematical modeling of the post-translational interactions shows the ultrasensitive dependence of [0A_P] on the [0F]T/[KinA]T ratio. Post-translational interactions of the phosphorelay included the substrate-inhibition of KinA by 0F. To isolate the post-translational interactions, the rate of 0A transcription was fixed at 0.4mMhr-1 and the rate of 0F and kinA transcription was varied to calculate their effect on the steady-state levels of phosphorylated 0A ([0A_P]). **(B)** Contour diagram showing steady-state levels 0A_P as a function of [0F]T and [KinA]T concentrations. Steady-state [0A_P] levels always increase with increasing [KinA]T. However, due to the substrate inhibition of KinA by 0F, steady state [0A_P] levels depended non-monotonically on [0F]T concentrations and decreased at high 0F levels. **(C)** Modeling of post-translational interactions show that 0A-P concentration decreases ultrasensitivity for [0F]T/[KinA]T > 1. Note that the ultrasensitivity of this decrease increases at higher KinA concentrations. **(D and E)** *0F* and *kinA* chromosomal locations are evolutionarily conserved in spore-forming bacteria. **(D)** Radial histogram of chromosomal locations of *kinA* (green) and *0F* (purple) in 45 species of spore-forming bacteria (see also Table 5.3). The histograms show that the *0F* is located close to the origin *oriC* and *kinA* is located close to the terminus in all *Bacillus* species. *kinA* and *0F* locations in *B. subtilis* 168 (0F-326_ and kinA-126_) are marked by solid lines. **(E)** Radial histogram of chromosomal locations of *lacI* (blue) in the same 45 species of spore-forming bacteria as A. The histogram shows that unlike *kinA* and *0F*, *lacI* location relative to *oriC* varies widely over different *Bacillus* species.

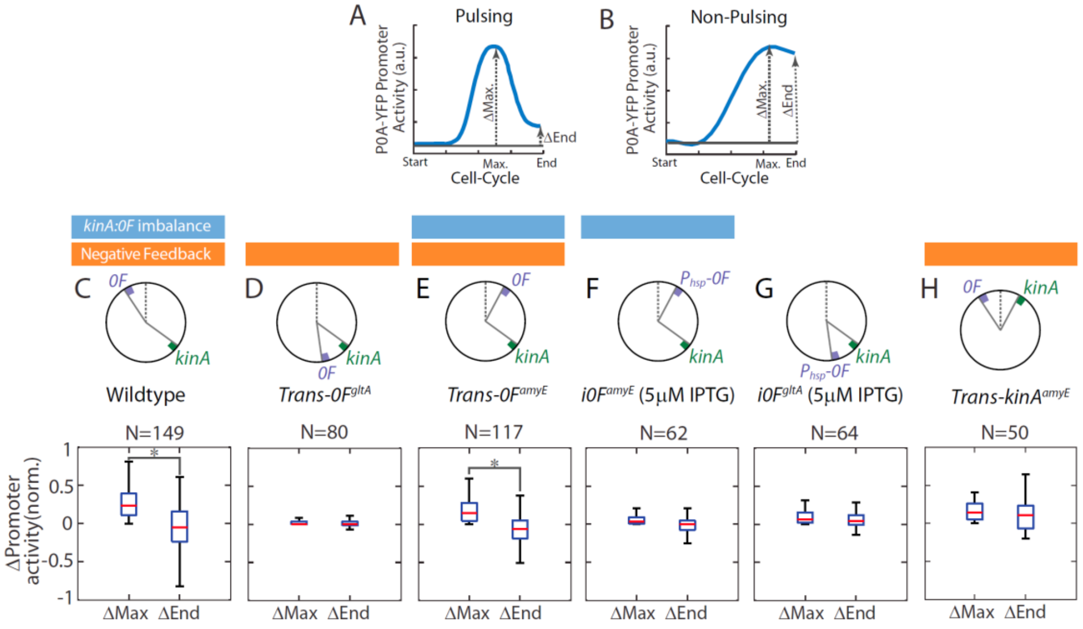

Figure 5.8 Comparison of Pulsing and Non-pulsing Responses

(A and B) Pulsing dynamics **(A)** and Non-pulsing dynamics **(B)** of P_{0A} promoter activity can be distinguished by comparing the maximum change in promoter activity (ΔMax) and the change in the promoter activity at the end of the cell cycle (ΔEnd). Both changes are measured relative to the promoter activity at the start of the cell cycle. The response can be classified as Pulsing dynamics only if ΔMax and ΔEnd differ significantly. **(C–G)** Comparison of ΔMax and ΔEnd in WT **(C)**, *Trans-0F*^{gltA}**(D)**, *Trans-0F*^{amyE}**(E)**, *i0F*^{amyE}**(F)** and *i0F*^{gltA}**(G)** and *Trans-kinA*^{amyE}**(H)**. Note that ΔMax andΔDEnd differ significantly only in WT and *Trans-0F*^{amyE} strains.

Table 5.1 *B. subtilis* strains used in this study

B. subtilis strains as referred in the article	*B. subtilis* strain number	Genotype	Used in Figures
“Wildtype”, WT	AK151	*AmyE*::P$_{spo0A}$-*yfp*, P$_{comG}$-*mCherry* (Sp^{R}) *SacA*:: P$_{spoIIR}$-*cfp* (Cm^{R})	Fig. 5.4A,F; Fig. 5.5; Fig. 5.8; Fig. 5.11
	AK456	*AmyE*::P$_{spo0F}$-*yfp* (Sp^{R})	Fig. 5.6
	AK2111	*GltA*::P$_{spo0F}$-*yfp* (Kan^{R})	Fig. 5.6
	AK2261	*AmyE*:: P$_{hsp}$-*DnaN-YFP* (Sp^{R}) pHP13- P$_{spo0A}$-*cfp*, P$_{comG}$-*mCherry* (Erm^{R})	Fig. 5.1B-D
$i0F^{amyE}$	AK2084	*AmyE*::P$_{hsp}$-*Spo0F* (Sp^{R}) *SacA*:: P$_{spoIIR}$-*yfp* (Cm^{R}) pHP13- P$_{spo0A}$-*cfp* (Erm^{R}) *Spo0F*:: *kan* (Kan^{R})	Fig. 5.4L,Q,N,S; Fig. 5.5A; Fig. 5.8; Fig. 5.11F
$Trans\text{-}0F^{gltA}$	AK2271	*AmyE*::P$_{spo0A}$-*yfp*, P$_{comG}$-*mCherry* (Sp^{R}) *SacA*:: P$_{spoIIR}$-*cfp* (Cm^{R}) *GltA*::P$_{spo0F}$-*Spo0F* (Pm^{R}) *Spo0F*:: *erm* (Erm^{R})	Fig. 5.4B,G; Fig. 5.5A; Fig. 5.8; Fig. 5.11D
$Trans\text{-}0F^{amyE}$	AK2301	*AmyE*:: P$_{spo0F}$-*Spo0F* (Sp^{R}) *SacA*::*P*$_{spo0A}$-*yfp/P*$_{comG}$-*cfp* (Cm^{R}) *Spo0F*:: *erm* (Erm^{R})	Fig. 5.4C,H; Fig. 5.8; Fig. 5.11E
$Trans\text{-}KinA^{gltA}$	AK2323	*GltA*:: P$_{kinA}$-*KinA* (Pm^{R}) *SacA*::*P*$_{spo0A}$-*yfp/P*$_{comG}$-*cfp* (Cm^{R}) *KinA*:: *tet* (Tet^{R})	Fig. 5.4D,I
$Trans\text{-}KinA^{amyE}$	AK2351	*AmyE*:: P$_{kinA}$-*KinA* (Sp^{R}) *SacA*::*P*$_{spo0A}$-*yfp/P*$_{comG}$-*cfp* (Cm^{R}) *KinA*:: *tet* (Tet^{R})	Fig. 5.4E,J; Fig. 5.5A,C; Fig. 5.8
$i0F^{gltA}$	AK2253	*AmyE*::P$_{spo0A}$-*yfp*, P$_{comG}$-*mCherry* (Sp^{R}) *SacA*:: P$_{spoIIR}$-*cfp* (Cm^{R}) *GltA*::P$_{hsp}$-*Spo0F* (Pm^{R}) *Spo0F*:: *erm* (Erm^{R})	Fig. 5.4M,R,O,T; Fig. 5.5A,C; Fig. 5.8; Fig. 5.11G
iTrans-0F	AK2092	*AmyE*::P$_{hsp}$-*Spo0F* (Sp^{R}) *SacA*:: P$_{spoIIR}$-*yfp* (Cm^{R}) *GltA*::P$_{spo0F}$-*Spo0F* (Pm^{R}) pHP13- P$_{spo0A}$-*cfp* (Erm^{R}) *Spo0F*:: *kan* (Kan^{R})	Fig. 5.4K,P

Table 5.2 Genome sizes and chromosomal locations of phosphorelay genes *spo0F* and *kinA* in 45 spore-forming bacteria

Data were drawn from the Pubmed Gene database. Only species which have both *kinA* and *spo0F* were selected. Gene location in degrees is given by the ratio: 360*pos_x^s / G^s, where pos_x^s is the position of the transcriptional start site of gene x (=*kinA* or *spo0F*) in species s (measured clockwise from the origin) and G^s is the genome size of species s. (0^o=360^o=chromosome origin; 180^o=chromosome terminus). (Table continues to the next page)

Species Name	**Genome Size**	***spo0F* Location (degrees/360)**	***kinA* Location (degrees/360)**
Bacillus subtilis subsp. subtilis str. 168	4215606	325.324	125.5358
Bacillus halodurans C-125	4202352	334.6104	160.656
Bacillus megaterium QM B1551	5097129	351.7039	165.9983
Bacillus amyloliquefaciens DSM 7	3980199	325.8056	134.0655
Bacillus subtilis subsp. spizizenii str. W23	4027676	323.492	127.4498
Bacillus pseudofirmus OF4	3858997	342.5017	184.0939
Bacillus pumilus SAFR-032	3704465	323.9976	131.4467
Bacillus amyloliquefaciens FZB42	3918589	325.016	123.1567
Bacillus thuringiensis str. Al Hakam	5257091	348.7712	202.84
Bacillus licheniformis DSM 13 = ATCC 14580	4222645	322.7962	134.3266
Bacillus cereus biovar anthracis str. CI	5196054	347.6662	147.0065
Bacillus thuringiensis BMB171	5330088	348.2211	238.7468
Bacillus cereus Q1	5214195	348.1544	151.8708
Bacillus anthracis str. 'Ames Ancestor'	5227419	348.789	234.2406
Bacillus cereus ATCC 10987	5224283	347.5709	235.4239
Bacillus anthracis str. Ames	5227293	348.7887	234.2375
Bacillus megaterium DSM 319	5097447	351.4806	163.0007
Bacillus cereus E33L	5300915	348.7168	236.0028
Bacillus thuringiensis serovar konkukian str. 97-27	5237682	348.5111	148.329
Bacillus anthracis str. A0248	5227419	348.7821	234.2337
Bacillus anthracis str. CDC 684	5230115	348.7835	57.5361
Bacillus cereus 03BB102	5269628	348.79	238.2591
Bacillus cereus AH820	5302683	347.8941	236.5036
Bacillus cereus G9842	5387334	347.8314	238.9148
Bacillus cereus B4264	5419036	348.8427	243.252
Bacillus cereus AH187	5269030	348.3469	233.8018
Alicyclobacillus acidocaldarius subsp. acidocaldarius Tc-4-1	3124048	339.1574	227.7419
Bacillus licheniformis 9945A	4376305	326.2416	132.4264

Table 5.2 Genome sizes and chromosomal locations of phosphorelay genes *spo0F* and *kinA* in 45 spore-forming bacteria (continued)

Species Name	**Genome Size**	***spo0F* Location (degrees/360)**	***kinA* Location (degrees/360)**
Bacillus subtilis subsp. subtilis 6051-HGW	4215610	325.3242	125.5355
Bacillus subtilis XF-1	4061186	323.4117	130.4759
Bacillus subtilis subsp. natto BEST195	4091591	323.2848	130.1218
Bacillus subtilis QB928	4146839	324.7672	125.8378
Bacillus amyloliquefaciens Y2	4238624	326.7711	115.8335
Paenibacillus polymyxa M1	5864546	10.39716	52.97136
Bacillus amyloliquefaciens subsp. plantarum YAUB9601-Y2	4242774	326.7803	115.9104
Bacillus amyloliquefaciens XH7	3939203	326.5166	182.7644
Bacillus amyloliquefaciens TA208	3937511	326.5049	182.7237
Bacillus megaterium WSH-002	4983975	8.047817	339.2598
Bacillus amyloliquefaciens subsp. plantarum CAU B946	4019861	327.6388	124.9527
Bacillus thuringiensis serovar chinensis CT-43	5486830	348.9355	236.8537
Paenibacillus larvae subsp. larvae DSM 25430	4046337	339.7109	319.8833
Bacillus amyloliquefaciens subsp. plantarum NAU-B3	4196170	327.0585	222.1804
Bacillus amyloliquefaciens subsp. plantarum UCMB5113	3889532	326.1037	124.4399
Bacillus amyloliquefaciens subsp. plantarum UCMB5033	4071167	326.4765	122.2481
Bacillus amyloliquefaciens subsp. plantarum UCMB5036	3910324	325.163	122.767

6 Ribosomal modulation of membrane potential in bacteria

6.1 Abstract

Two of the most fundamental features of all living cells are their utilization of ribosome machines and reliance on electrochemical membrane potentials. However, it remains unclear whether such basic processes are connected, such that one can influence the other. Inorganic ions play an important role in both stabilizing the ribosome complex and establishing the cellular membrane potential. Motivated by this connection, we performed direct chemical and structural perturbations of ribosomes in *Bacillus subtilis* and measured the cellular membrane potential dynamics at the single cell level. We find that ribosome perturbations modulate the membrane potential of bacteria. Specifically, we show that sub-lethal concentrations of antibiotics (kanamycin and spectinomycin) that target the 30S subunit of the ribosome cause transient hyperpolarization events. Similarly, deletion of the ribosomal L34 protein, known to cause ribosome destabilization, also increases the fraction of hyperpolarized cells. In contrast, duplication of the ribosomal L22 protein loop, a stabilizing core component of the ribosome complex, eliminates hyperpolarization. Our results suggest that magnesium ions, known to stabilize the ribosome complex, play a central role in modulating the cellular membrane potential. In particular, magnesium ions suppress hyperpolarization events caused by either antibiotics or the destabilizing L34 ribosomal protein deletion phenotype. Collectively, our results suggest that ribosome

stability can modulate membrane potential, thus revealing an intriguing relationship between these two fundamental cellular properties.

6.2 Introduction

All living cells have an electrochemical potential across their cell membrane. Such membrane potential can be utilized by cells to drive various processes, such as uptake of nutrients. In contrast to well-studied eukaryotic cells such as neurons, far less is known about the membrane potential dynamics of bacteria. Recent experimental advances have revealed that the membrane potential of bacteria is not static. For example, measurements in individual bacteria showed small-amplitude membrane-potential fluctuations with durations on the order of seconds (Kralj et al. 2011). Additionally, measurements in bacterial biofilm communities have revealed a collective modulation of the membrane potential of millions of bacteria (Prindle et al. 2015; Liu et al. 2017). Despite these recent findings, we lack a clear understanding of what intracellular processes can potentially modulate changes in bacterial membrane potential. Regardless of what intracellular mechanisms may be identified and implicated, it is clear that flow of ions across the membrane must be a critical component that gives rise to a change in the electrochemical membrane potential.

Like all living cells, bacteria contain high concentrations of cations such as potassium (~400mM) and magnesium (~100mM)(Milo et al. 2010). Most of these intracellular ions are bound to various molecules in the cells. For example, nearly 200 divalent magnesium ions appear to associate with the ribosome complex, which is comprised of numerous RNA and protein subunits (Schuwirth et al. 2005). It has been shown that divalent magnesium ions, which have a smaller radius than monovalent potassium ions, play an important role in stabilizing the structure of the ribosome complex (Yamamoto et al. 2010; Klein, Moore, and Steitz 2004; Pontes, Sevostyanova, and Groisman 2015). Such stabilization of the ribosome complex impacts directly the growth rate of bacteria since ribosomes are essential for protein synthesis and thus biomass production (Scott et al. 2010). Bacterial growth thus provides a well-established metric for ribosomal stability and activity in cells. From these insights, it is undeniable that ions and their concentration gradients across the cell membrane play an essential role in biological processes.

While ribosomes and membrane potential have each been independently studied in great detail in various biological systems, it remains unclear whether these two fundamental cellular properties are connected in some way. To pursue this question, we explored whether perturbations of the ribosome would cause a change in the membrane potential of bacterial cells (Fig. 6.1A). Our results, detailed below, reveal that either direct chemical or genetic perturbations of the ribosome modulate the membrane potential. Specifically, we find that cells transiently hyperpolarize upon ribosomal perturbations and that the fraction of cells exhibiting this phenotype can be modulated by ribosome perturbations. Our results thus indicate an intriguing connection between ribosomes and the membrane potential. We speculate on the potential implications of this profound connection between these two fundamental cellular processes and discuss ideas for future research directions inspired by our finding.

6.3 Results

We began by quantitatively measuring the membrane potential dynamics of individual *B. subtilis* cells. Bacteria were grown in minimal defined media (MSgg) inside a microfluidic device (Fig. 6.1B) that provides control over growth media conditions and also enables imaging of a monolayer of bacterial cells (Fig. 6.1C). We imaged and tracked cells over time and quantified their growth rates and membrane potential dynamics. For this purpose, we utilized a previously characterized cationic fluorescent membrane potential indicator dye, Thioflavin-T (ThT) (Fig. 6.1C). This dye acts as a Nernstian membrane potential indicator. In other words, the amplitude of the fluorescence signal correlates with the membrane potential, such that more polarized cells exhibit a higher fluorescence signal (ref). Using this experimental approach, we identified a small percentage (3 ± 0.03 %, mean ± 95% CI, $n = 1.4 \times 10^6$) of bacteria that exhibit transient membrane potential hyperpolarization (Fig. 6.1D, E). We ruled out that hyperpolarization of bacteria could, for example, be due to respiration (Fig. 6.2, 7 and 8). In addition, while only a small fraction of cells exhibited this hyperpolarization and the events were not synchronized among cells, these membrane potential transients were reproducible, suggesting a stereotypical behavior (Fig. 6.8). We then determined whether changes in membrane potential correlated with growth by measuring the elongation rate of individual bacteria (Fig. 6.2). Results show that hyperpolarized cells have a lower elongation (growth) rate compared to cells that do not exhibit such changes in their membrane potential (Fig. 6.1F). This finding indicates a negative correlation between membrane potential and ribosome activity as reported by growth rate.

To determine whether there is a causal relationship between ribosome activity and changes in the membrane potential of cells, we utilized two antibiotics that specifically target the 30S subunit of ribosomes, namely spectinomycin and kanamycin (Fig. 6.3A). We used sub-lethal concentrations of those antibiotics (2 and 0.5 mg/L, respectively), as our goal was not to kill bacteria, but rather to perturb ribosomes and simultaneously measure membrane potential dynamics. We find that addition of sub-lethal antibiotic doses increases the fraction of cells that exhibit hyperpolarization approximately thirteen- and six-fold, respectively (Fig. 6.3B and C). Exposing bacteria to antibiotics that target ribosomes thus increases the likelihood of causing a membrane potential change in bacteria.

We further investigated the changes in the membrane potential caused by antibiotic stress. While both spectinomycin and kanamycin target the 30S subunit of the ribosome, the former stops translation while the latter causes mistranslation (Davis 1987). Consequently, it had been argued in the literature that these two antibiotics could have opposite effects on the membrane potential of bacteria (Kohanski et al. 2008). Specifically, kanamycin was suggested to cause depolarization by resulting in expression of aberrant proteins that can no longer sustain cellular polarization. In contrast, spectinomycin is not expected to result in aberrant proteins that could reduce the membrane potential of bacteria. However, our single-cell measurements of membrane potential dynamics show that addition of either antibiotic to growing cells causes similar hyperpolarization transients (Fig. 6.3D, E and 6.8). Furthermore, bacteria exposed to these antibiotics exhibit a similar negative correlation between hyperpolarization and growth rate (Fig. 6.3F and G), reminiscent of the results shown in Fig. 6.1F. Overall, these data show that ribosome-targeting antibiotics increase the probability of membrane potential hyperpolarization in bacterial cells.

Next, we asked whether direct perturbations of ribosomal subunits that alter the structure and stability of the ribosome complex could also cause changes in the membrane potential. Accordingly, we genetically perturbed two different ribosomal subunits that have been shown to have opposite effects on the ribosome complex (Fig. 6.4B). First, we targeted the L22 (L17 in eukaryotes) protein subunit of the ribosome complex, which contains a short loop (position 94 to 100) with two positively charged amino acids (lysine and arginine) (Chiba, Lamsa, and Pogliano 2009). Positive charges are known to stabilize the ribosome complex that contains numerous negatively charged rRNA molecules. Specifically, the L22 subunit has been shown to be important for folding and stabilizing the structural conformation of the 23S rRNA (Fig. 6.4A, left panel and Fig. 6.9)(Ban et al. 2000). In bacteria, duplication of the L22 loop is also known to provide resistance against macrolide antibiotics by crowding out space to which antibiotics can bind (Chiba, Lamsa, and Pogliano 2009). Consistent with L22's ribosome stabilizing property, our measurements show that L22 loop duplication reduces hyperpolarization events in cells (Fig. 6.4CD and Fig. 6.7). Furthermore, the elongation (growth) rate of L22 mutant cells is overall shifted towards higher values compared to wild-type cells (Fig. 6.4E). These results suggest that increased stability of the ribosome complex prevents membrane potential hyperpolarization of bacterial cells.

Conversely, we then focused on another genetic perturbation that has been shown to destabilize bacterial ribosomes, namely deletion of the ribosomal L34 protein subunit (*ΔrpmH*) (Fig. 6.4A, right panel)(Akanuma et al. 2014). We note that the L34 protein contains 18 positively charged residues and thus its deletion leads to a loss of positive charges that are known to stabilize the ribosome complex (Fig. 6.9). As expected, our results show that deletion of L34 leads to an increase (nearly ten-fold) in the fraction of cells that exhibit hyperpolarization (Fig. 6.4FG and Fig. 6.7). This increase in the percentage of hyperpolarized cells upon L34 deletion is similar to the effect of the addition of ribosome targeting antibiotics (Fig. 6.4C and Fig. 6.7). As expected, we also observe a reduced elongation rate in cells with the L34 deletion compared to wild-type cells (Fig. 6.4H). These results indicate that a destabilizing structural perturbation of the ribosome complex increases the probability of membrane potential hyperpolarization in bacterial cells. Taken together, the L34 and L22 genetic perturbation results show that molecular-level direct perturbations of the ribosome structure can either promote or suppress hyperpolarization, respectively. It is thus possible to exert control over the bacterial membrane potential through genetic perturbations of the ribosome complex structure.

How can ribosome perturbations increase the membrane potential? An increase in membrane potential implies either influx of negatively charged ions or efflux of positive ions from the cell. Specifically, if the influx of negative ions drives hyperpolarization, reducing the content of negative ions in the media would reduce the fraction of cells that exhibit hyperpolarization events. In contrast, if efflux of positive ions was responsible for hyperpolarization, then reduction of positive ions in the media would increase their outward gradient from cells and thus increase the fraction of hyperpolarized cells. Therefore, to discriminate between these two scenarios, we equally decreased the negative and positive ion content of the media by removing $CaCl_2$, $MgCl_2$, $FeCl_3$, $MnCl_2$, and $ZnCl_2$. We find that removing ions from the media increases the fraction of hyperpolarized cells by 14-fold, which indicates that hyperpolarization is driven by efflux of positive ions (Fig. 6.5A). When we combine removal of ions with the addition of spectinomycin that targets the ribosome, we observe a non-additive increase in the fraction of hyperpolarized cells reaching almost 95% (Fig. 6.5A). This non-additive effect reveals an interaction between ribosome perturbations and efflux of cations. Ribosome perturbations can thus increase the likelihood of bacterial hyperpolarization events that result from efflux of positive ions.

Next, we focused on divalent magnesium cations since they are the most abundant ion species that associates with the ribosome complex (Fig. 6.5B). Specifically, we asked whether ribosomes could provide a sufficient number of magnesium cations needed to change the cellular membrane potential. Given the typical surface area of a bacterial cell (~5 μm^2), approximately 5,000 divalent magnesium ions are needed to generate a membrane potential of 100mV (Milo et al. 2010). The number of ribosomes in the bacterial cell ranges from a lower bound of about 5,000 all the way up to approximately 100,000 (Milo et al. 2010). Each of these ribosomes can associate with nearly 200 magnesium ions (Fig. 6.5B)(Schuwirth et al. 2005). Assuming the lower bound of 5,000 ribosomes per cell, a release of 5,000 magnesium ions can thus occur if approximately 10% of ribosomes release 5% of their associated magnesium ions. Therefore, complete dissociation of many ribosomes is not required to cause a release of thousands of magnesium ions in the cell. These numbers show that the vast pool of magnesium ions bound to ribosomes in the cell is more than sufficient to generate the number of free ions needed to induce a change in membrane potential.

To further test the role of magnesium ions in the observed hyperpolarization events, we investigated whether an increase of magnesium concentration in the growth media can suppress hyperpolarization of bacteria induced by ribosome perturbations (Fig. 6.5C). Specifically, we transiently increased (for a period of 3 hours) the magnesium concentration in the media ten-fold (from 2mM to 20mM). As expected, the increased magnesium concentration in the growth media reduced the occurrence of hyperpolarization events in the presence of spectinomycin. When the excess magnesium concentration is removed from the media, cells once again exhibit hyperpolarization transients (Fig. 6.5D top). Since changes in ion concentrations in the media can also directly affect the membrane potential, we performed control experiments using other biologically relevant cations, such as potassium, calcium, and sodium. Increasing the potassium, calcium or sodium ion concentrations to similar levels in the media did not effectively suppress hyperpolarization (Fig. 6.5D). Therefore, hyperpolarization of bacteria caused by a ribosome targeting antibiotic can be quenched specifically by increasing the magnesium concentration. Consistent with this result, the addition of excess magnesium was also able to rescue the L34 deletion phenotype (Fig. 6.5E). In particular, the fraction of L34 deletion cells that exhibit hyperpolarization events decreased with increasing magnesium concentration in the media (Fig. 6.5F). As expected, the growth rate defect of the L34 deletion strain was also rescued with increasing concentrations of excess magnesium in the media (Fig. 6.5G). Together, these results suggest that hyperpolarization events in bacterial cells that are induced by ribosome perturbations can be suppressed by magnesium-mediated stabilization of the ribosome complex.

6.4 Discussion

Taken together, the chemical or genetic perturbations of the ribosome explored in this study can modulate the membrane potential of bacteria. Our results reveal that bacteria are more or less likely to hyperpolarize depending on whether the perturbations are destabilizing or stabilizing the ribosome complex, respectively. Consequently, we find a negative correlation between ribosome activity, as reported by the average growth rate of bacteria, and the fraction of hyperpolarized cells in the population (Fig. 6.6). Our work thus defines a relationship between two of the most fundamental properties of any living cell.

While it is beyond the scope of our study, it will also be exciting to engage in future research directions to investigate whether other molecular components may play a contributing role in the connection between ribosomes and the membrane potential. For example, several proteins are known to target non-functional or destabilized ribosome complexes for degradation (Keiler 2015). These proteins could possibly speed up or amplify the effect that ribosome stability could exert on membrane potential. It will be interesting to determine the possible means of control the cell may be able to exert over how ribosome stability can influence the membrane potential.

Our results provoke the question as to whether a cell could potentially benefit from ribosomal stress causing membrane potential hyperpolarization. The intracellular content of cations such as magnesium and calcium is of importance to a range of cellular functions. While magnesium and calcium are both divalent cations and can to some degree be used interchangeably by the cell, several cellular and molecular processes are preferentially dependent on magnesium or calcium. It is thus possible that the cell utilizes hyperpolarization caused by magnesium efflux to increase the influx of calcium or other cations, which are known for example to allow cells to cope with toxic reactive oxygen species that arise during stress (Görlach et al. 2015). Calcium is also a known as a second messenger that is stored in intracellular compartments of eukaryotic cells (Rasmussen et al. 1976). There are no such known intracellular compartments that store magnesium, but our work suggests that ribosomes can effectively serve as magnesium stores that can release their ions upon encountering stress conditions. This suggests the intriguing idea that magnesium could also function as a second messenger. The findings presented here will thus inspire new questions and future research directions that may not have been envisioned prior to our study. For now, our work points to unexplored ways in which cells may cope with stress through ribosomal modulation of the membrane potential that can alter the intracellular composition and concentration of inorganic ions known to regulate numerous biological processes.

6.5 Method

6.5.1 Growth and imaging conditions

Desired *B. subtilis* strains were streaked on a fresh plate a day before the experiment. When appropriate, 5 μg/ml erythromycin or 5 μg/ml chloramphenicol was supplemented in LB. A single colony of the desired strain was picked from overnight grown on LB plate and cultured in LB at 37 °C. Saturated cultures were washed with MSgg medium [5 mM potassium phosphate (pH 7.0), 100 mM 3-(N-morpholino) propanesulfonic acid (pH 7.0), 2 mM MgCl2, 700 μM CaCl2, 50 μM MnCl2, 100 μM FeCl3, 1 μM ZnCl2, 2 μM thiamine, 0.5% glycerol, 0.5% glutamate], and then immediately loaded into the commercial the Y04D microfluidic plate (EMD Millipore). After the loading, cells in the microfluidic chamber were grown in MSgg media at 37 °C for 90 mins, and then the temperature was kept at 30 °C for the whole experiments. For L34 deletion mutant, MSgg media was supplemented with final 20 mM MgCl2 before imaging to ensure the growth. During the imaging, MgCl2 concentration kept in 2mM unless specified. Imaging was performed only near the media inlet and before an apparent biofilm formation. Membrane potential dynamics were measured using the 10μM fluorescent cationic dye Thioflavin-T (ThT) supplemented in the MSgg media.

6.5.2 Time-lapse microscopy

The growth and membrane potential dynamics of *B. subtilis* cells were monitored with fluorescence time-lapse microscopy at 30 °C. Olympus IX-81 and IX-83 inverted microscope with a motorized stage (ASI) were used. Single layers of cells were imaged every 5 min with 40X objective lens. Whenever fluorescence images were taken, we used minimal exposure time that still provides a good signal-to-noise ratio.

6.5.3 Image analysis

The combination of freely available plugins and custom written scripts for Fiji/ImageJ (National Institutes of Health) and MATLAB (MathWorks) were used for image analysis.

Chapter 6, in full, is currently being prepared for submission for publication of the material. Dong-yeon D. Lee, Leticia Galera-Laporta, Maja Bialecka-Fornal, Eun Chae Moon, Jordi Garcia-Ojalvo, and Gürol M. Süel. The dissertation author is shared primary author of this paper with Leticia Galera-Laporta.

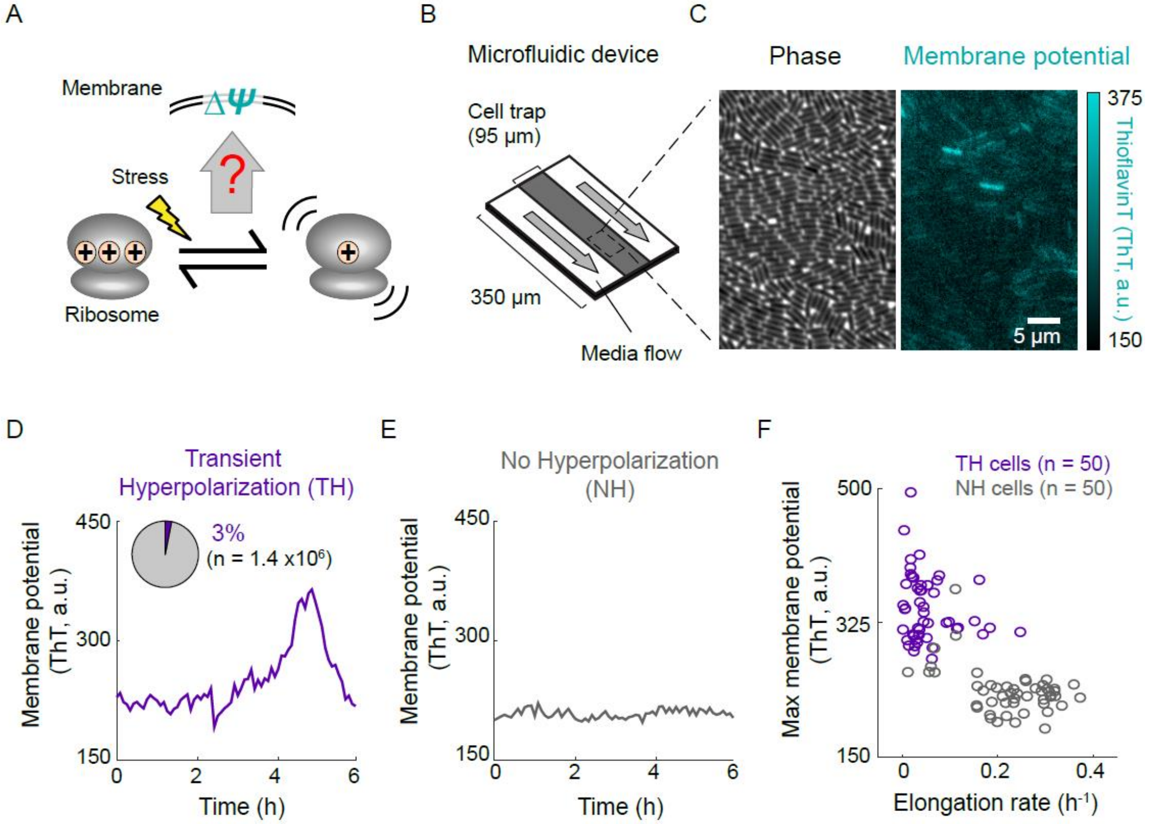

Figure 6.1 Bacterial cells can exhibit spontaneous transient hyperpolarization in membrane potential.

(A) A cartoon illustrates the question whether or not the perturbations of the ribosome could alter the cellular membrane potential. **(B)** A scheme of the microfluidic device used in this study. **(C)** Snapshots of bacterial cells in phase and stained with Thioflavin-T (ThT) used as an indicator of membrane potential. The scale bar on the right illustrates the intensity range of the signal from ThT stained cells. **(D)** Membrane potential fluctuation as a function of time (bottom) for a representative cell exhibiting Transient Hyperpolarization (TH). The pie chart insert shows the fraction of hyperpolarized cells (purple) in a population of 1.4 x 10^6 cells. **(E)** Membrane potential fluctuation as a function of time (bottom) for a representative cell exhibiting No Hyperpolarization (NH) events. **(F)** Maximum membrane potential (ThT, a.u.) shows anti-correlation with the elongation rate (h^{-1}).

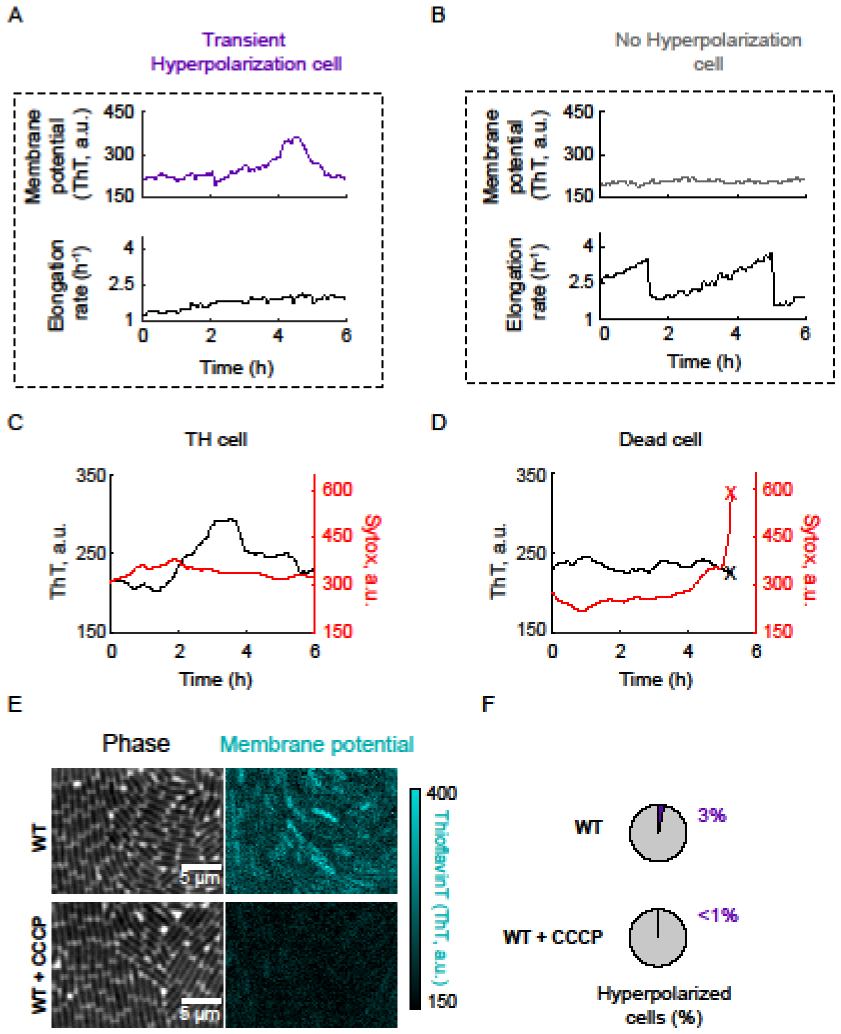

Figure 6.2 Thioflavin-T (ThT) reports hyperpolarized cells
(A) Membrane potential (top) and elongation rate (bottom) as a function of time for a single cell showing transient hyperpolarization. The same cell showed in Fig. 6.1d. **(B)** Membrane potential (top) and elongation rate (bottom) as a function of time for a cell showing no hyperpolarization. The same cell showed in Fig. 6.1F. **(C)** ThT (left axis) and Sytox green (right axis) signal as a function of time for a single cell. Transient hyperpolarization (increase in ThT signal) is not caused by cell death (no change in Sytox signal). **(D)** ThT (left axis) and Sytox green (right axis) as a function of time for a single cell not showing transient hyperpolarization. Cell death (increase in Sytox signal) is marked with a red X. **(E)** Snapshots of phase (right column) and ThT (left column) for cells in regular medium (top row) or in medium with 5µM CCCP (bottom row). **(F)** Fraction of hyperpolarized cells with and without CCCP.

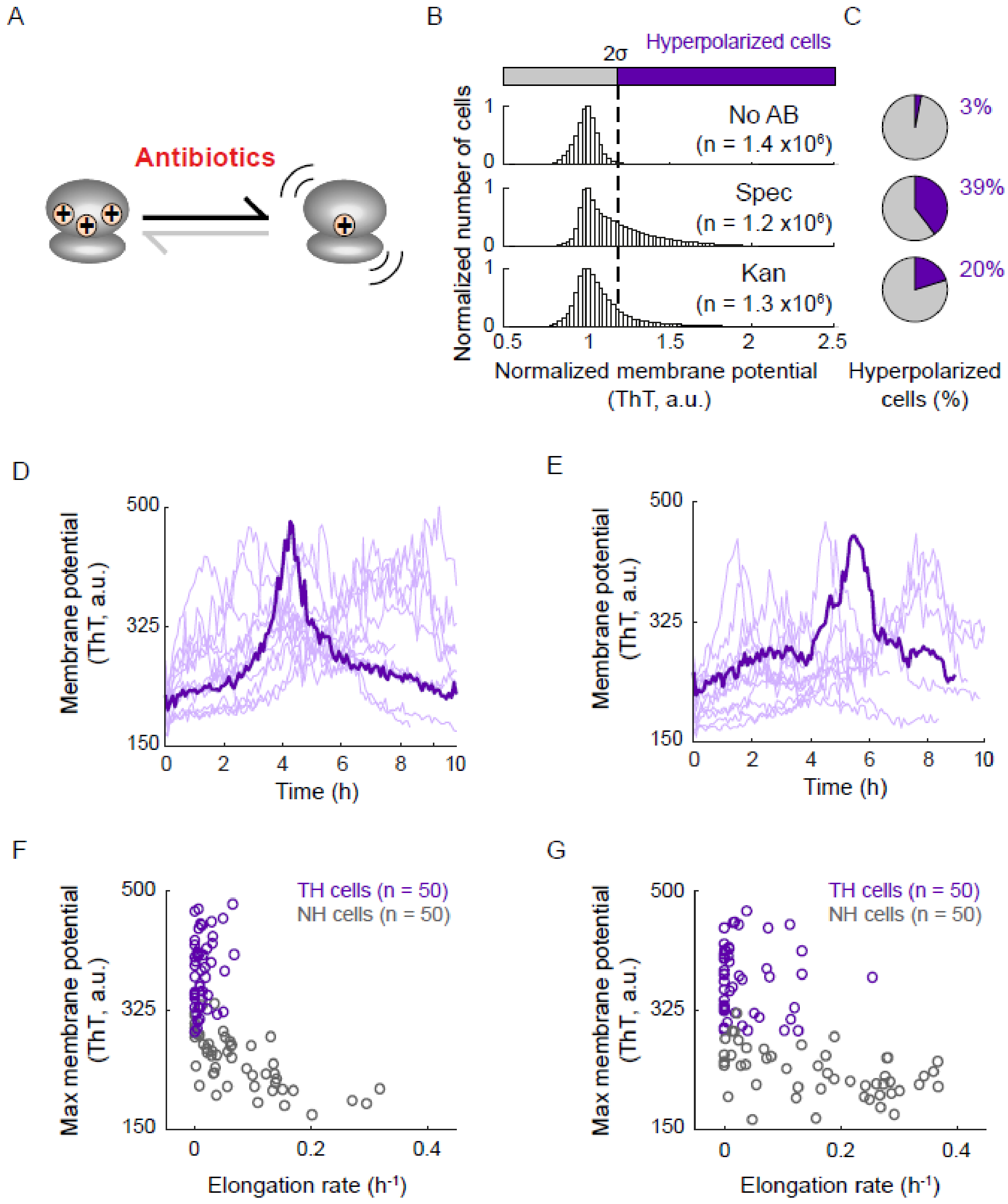

Figure 6.3 Ribosome-targeting antibiotics increase the fraction of transiently hyperpolarized cells.

(A) Antibiotics (such as spectinomycin and kanamycin) can perturb ribosomes. **(B)** Distribution of ThT signals in a population of cells in the absence of antibiotics (top) and in the presence of sub-lethal doses of spectinomycin (2 µg/ml, middle row) and kanamycin (0.5 µg/ml, bottom row). The dashed line represents two standard deviations from the mode, which we used as a cutoff to determine the fraction of hyperpolarized cells. **(C)** Pie charts show the statistics from (B), with the percent of cells exhibiting hyperpolarization shown in purple. **(D)** Time traces of transiently hyperpolarized cells in the presence of spectinomycin. **(E)** Time traces of transiently hyperpolarized cells in the presence of kanamycin. **(F-G):** Maximum membrane potential (ThT) as a function of elongation rate (h^{-1}) for TH and NH cells in the presence of spectinomycin (**F**) and kanamycin (**G**).

Figure 6.4 Genetic mutations of ribosomes modulate the fraction of transient hyperpolarized cells and elongation rates.

(A) Schemes showing the two ribosome perturbations. Left panel shows magnified view of L22 region. Different rRNA domains were indicated with different shade of gray (see Extended Data Fig. 4 for detail). Right panel shows magnified view of L34. Positively charged amino acids are indicated with orange color. There is no negatively charged amino acid in L34. **(B)** A cartoon illustrating how L34 deletion and L22 loop duplication perturb ribosomes. **(C)** Phase (left) and fluorescent (right) images of L22 loop duplication mutant. The scale bar is 10 μm. The color bar on the right illustrates the intensity range of the signal from ThT stained cells. **(D)** Membrane potential (ThT) fluctuation as a function of time for cells with L22 loop duplication. The pie chart shows the fraction of cells experiencing TH in a population of 7.3 x 10^5 cells. **(E)** Maximum membrane potential (ThT) as a function of elongation rate (h^{-1}) for WT and L22 loop duplication mutant. **(F)** Phase (left) and fluorescent (right) images of L34 deletion mutant. The distance and color scale set the same with (c). **(G)** Membrane potential (ThT) fluctuation as a function of time for L34 deletion mutant. The pie chart indicates the fraction of cells experiencing TH in a population of 1.1 x 10^6 cells. **(H)** Maximum membrane potential (ThT) as a function of elongation rate (h^{-1}) for WT and L34 deletion mutant.

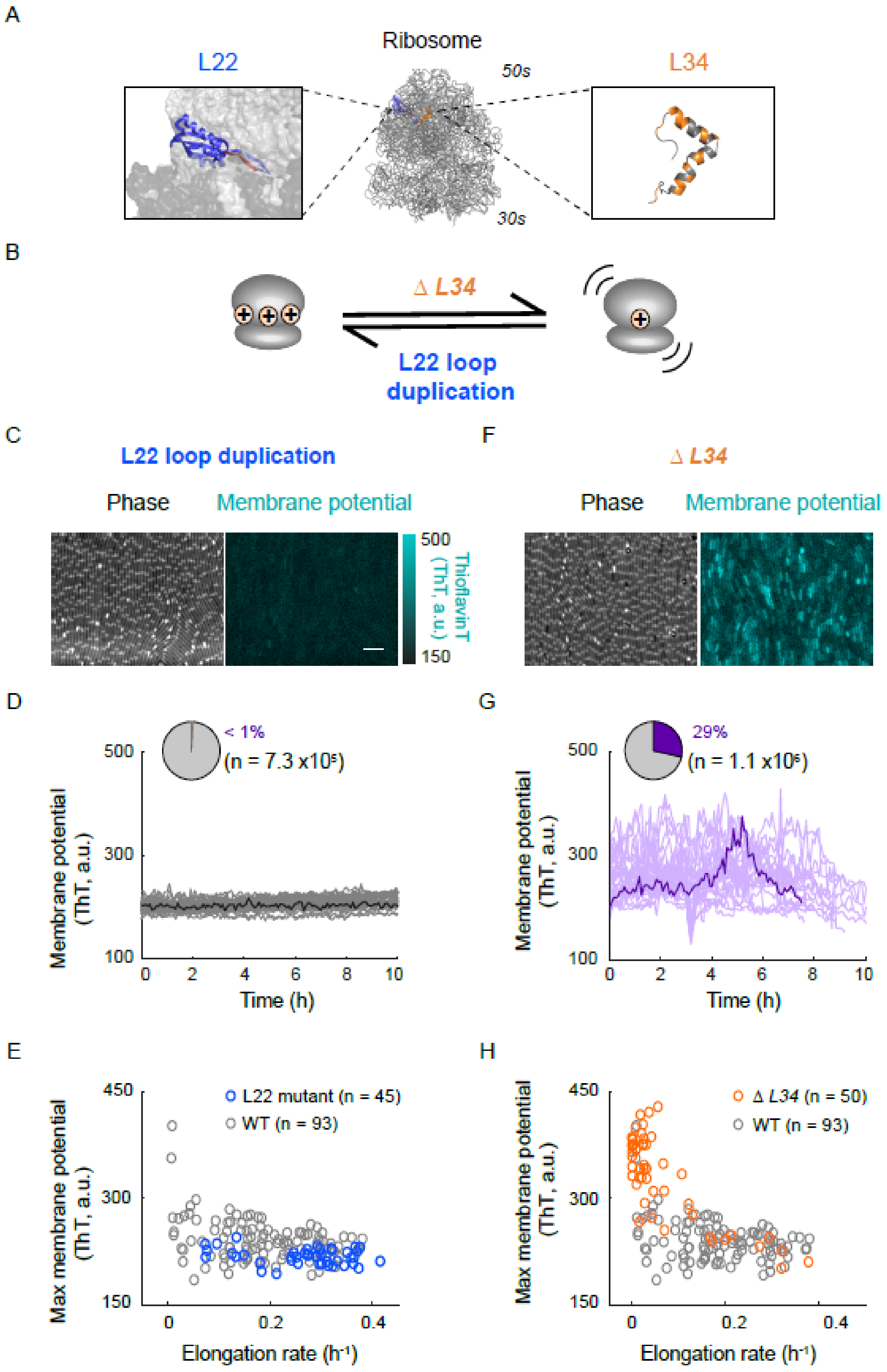
A
Ribosome
L22
L34
50s
30s
B
Δ L34
L22 loop duplication
C
L22 loop duplication
Phase
Membrane potential
500
Thioflavin T (ThT, a.u.)
150
F
Δ L34
Phase
Membrane potential
D
< 1%
(n = 7.3 x10^5)
500
300
100
Membrane potential (ThT, a.u.)
0
2
4
6
8
10
Time (h)
G
29%
(n = 1.1 x10^6)
500
300
100
Membrane potential (ThT, a.u.)
0
2
4
6
8
10
Time (h)
E
L22 mutant (n = 45)
WT (n = 93)
450
300
150
Max membrane potential (ThT, a.u.)
0
0.2
0.4
Elongation rate (h⁻¹)
H
Δ L34 (n = 50)
WT (n = 93)
450
300
150
Max membrane potential (ThT, a.u.)
0
0.2
0.4
Elongation rate (h⁻¹)

Figure 6.5 Magnesium ion plays an important role in hyperpolarization.
(A) Hyperpolarized cell fraction in absence of multivalent ions (middle) or absence of multivalent ions together with spectinomycin addition (bottom). **(B)** A schematic of ribosome structure with the location of magnesium ions. **(C)** Scheme showing the stabilization of ribosomes by magnesium addition. **(D)** Transient increase of ions in the presence of spectinomycin. Circles represent the timing at which single-cell hyperpolarization events occur. Time intervals during which excess ions are added are indicated with gray and black arrows, representing ion addition and removal. The type of ion in each case is indicated on the left (n > 20 for each condition). **(E)** Additional magnesium can reverse the effect of L34 deletion in a concentration-dependent manner. **(F)** Percentage of hyperpolarized cells decreases as a function of the concentration of magnesium in the media for L34 deletion mutant. **(G)** Elongation rate (h^{-1}) increases as a function of the concentration of magnesium in the media for L34 deletion mutant.

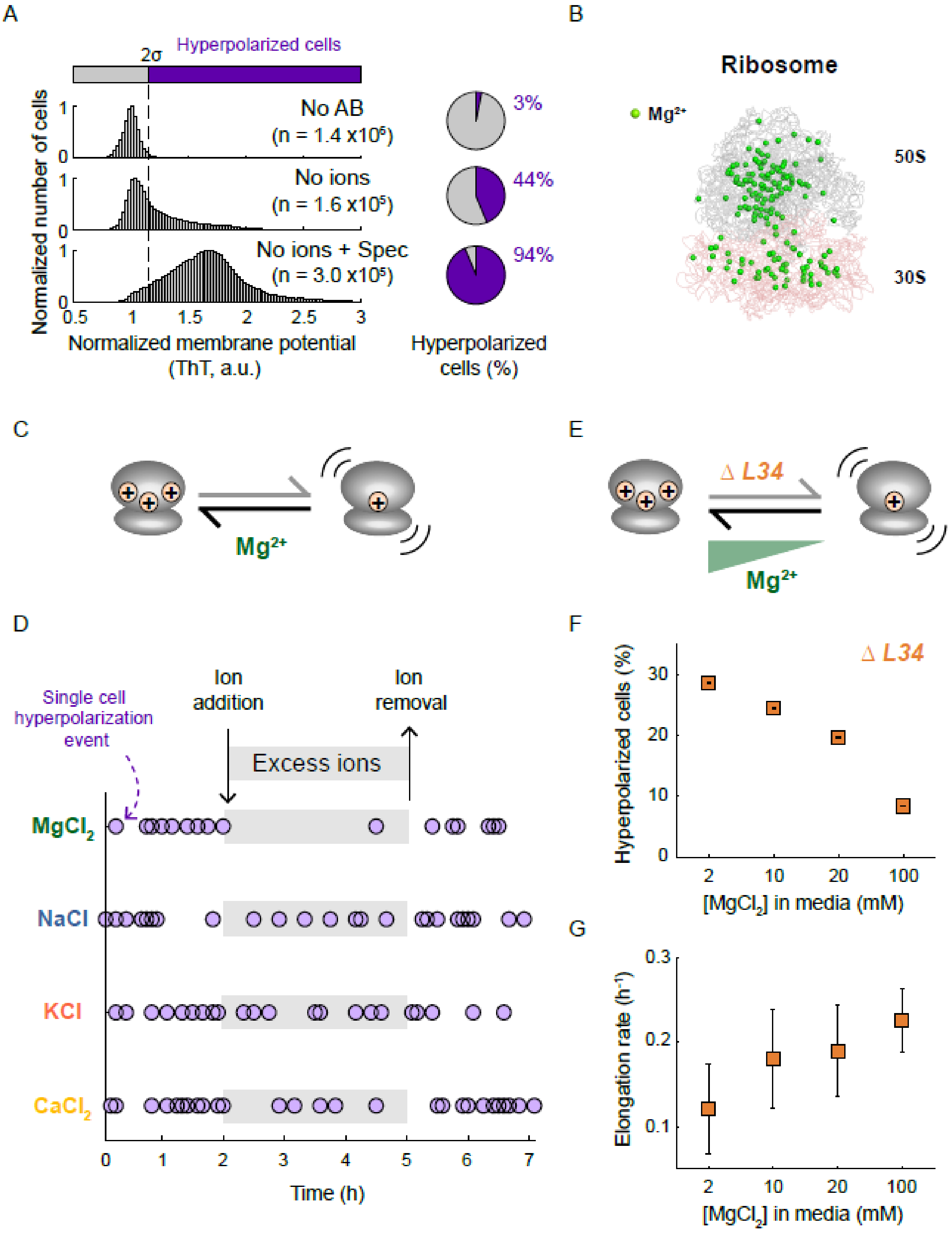
A
2σ
Hyperpolarized cells
Normalized number of cells
1
0
No AB
(n = 1.4 x10⁵)
3%
No ions
(n = 1.6 x10⁵)
44%
No ions + Spec
(n = 3.0 x10⁵)
94%
0.5
1
1.5
2
2.5
3
Normalized membrane potential
(ThT, a.u.)
Hyperpolarized
cells (%)
B
Ribosome
Mg²⁺
50S
30S
C
Mg²⁺
E
Δ L34
Mg²⁺
D
Single cell
hyperpolarization
event
Ion
addition
Ion
removal
Excess ions
MgCl₂
NaCl
KCl
CaCl₂
0
1
2
3
4
5
6
7
Time (h)
F
Δ L34
Hyperpolarized cells (%)
0
10
20
30
2
10
20
100
[MgCl₂] in media (mM)
G
Elongation rate (h⁻¹)
0.1
0.2
0.3
2
10
20
100
[MgCl₂] in media (mM)

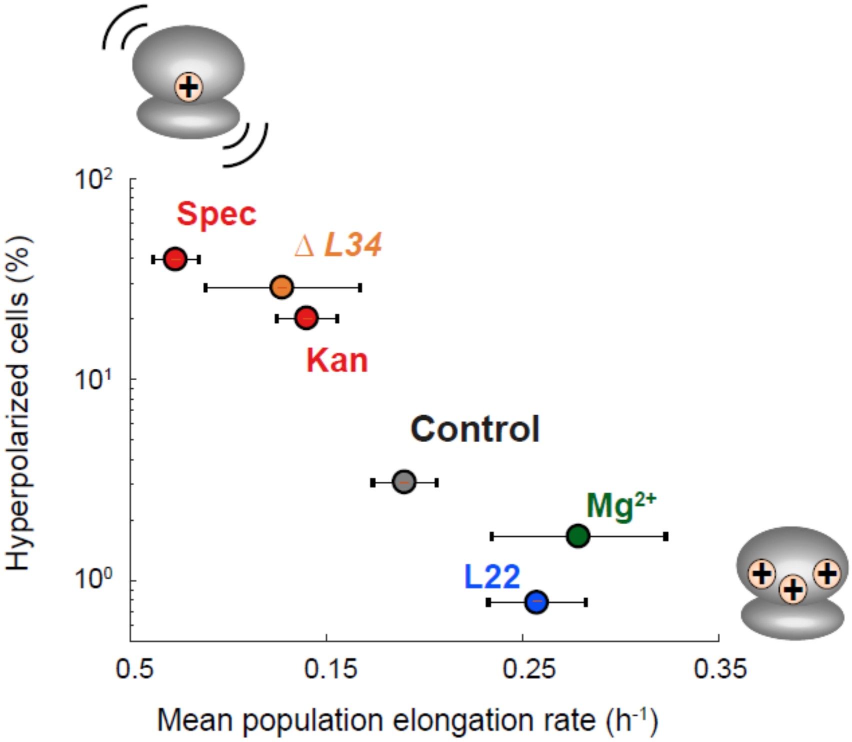

Figure 6.6 Chemical and genetic perturbations of the ribosome modulate both the membrane potential dynamics and elongation rate.

Summary of all perturbations in the study. Percentage of hyperpolarized cells in logarithmic scale as a function of mean population elongation rate (h^{-1}).

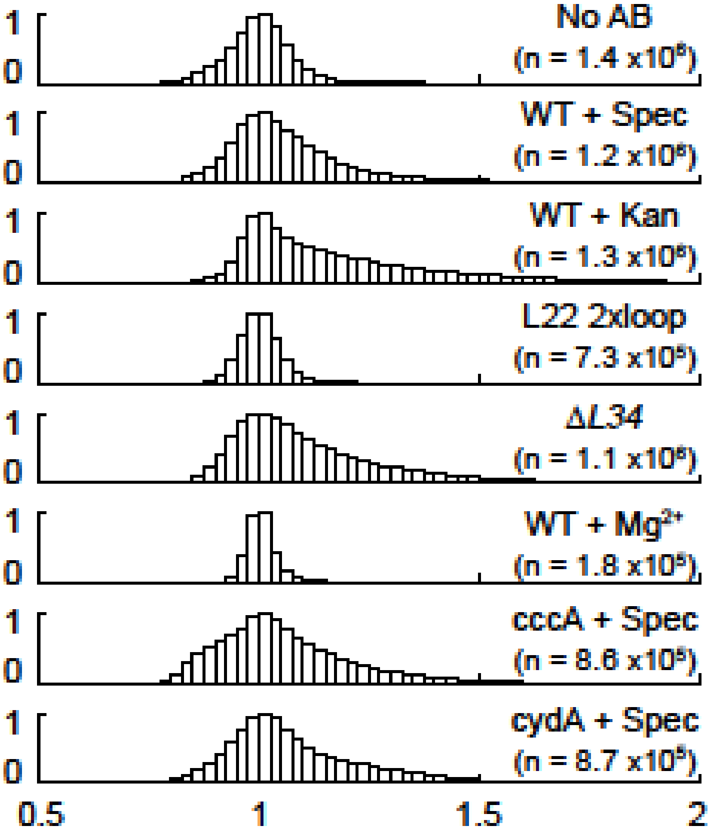

Figure 6.7 Membrane potential distribution in a population.
Histograms showing the distribution of cells with different membrane potential for (top to bottom): WT, WT in the presence of spectinomycin, WT in the presence of kanamycin, L22 loop duplication mutant, L34 deletion mutant, WT in the presence of 20 mM MgCl2, cccA deletion mutant, and cydA deletion mutant.

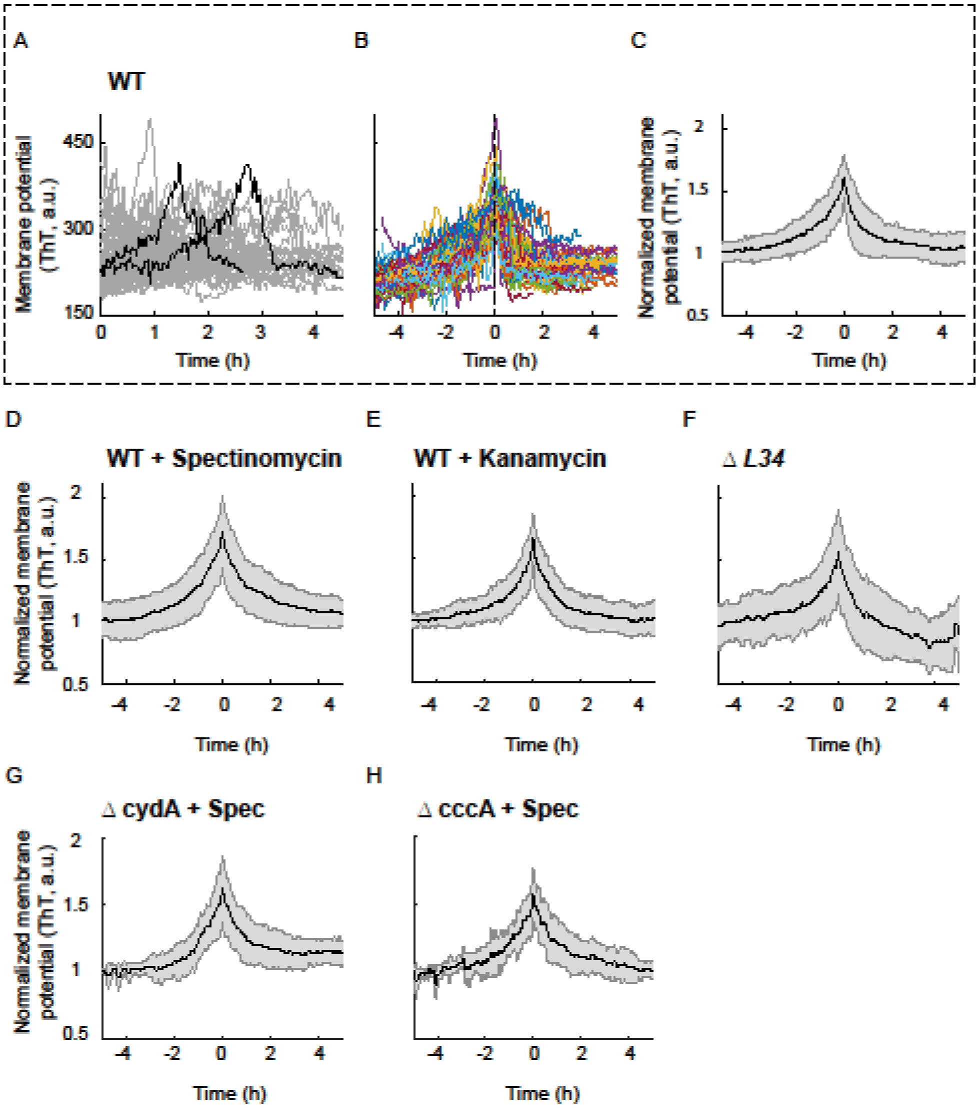

Figure 6.8 Aligned time traces with a transient hyperpolarization.
(A) Membrane potential as a function of time for individual cells in normal MSgg media. Time traces with transient hyperpolarization were intentionally picked for the analysis. **(B)** Time traces in (A) aligned by the time of the max ThT. **(C)** Average membrane potential change in time (black line) with standard deviation (gray area) were obtained from normalized and aligned time traces in (B). (**D-H):** Normalized and aligned membrane potential as a function of time for WT cells in the presence of 2µg/ml spectinomycin (D), for WT cells in the presence of 0.5 µg/ml kanamycin (E), for L34 deletion mutant (F), for cydA deletion mutant in the presence of 2µg/ml spectinomycin (G), and for cccA deletion mutant in the presence of 2µg/ml spectinomycin (H).

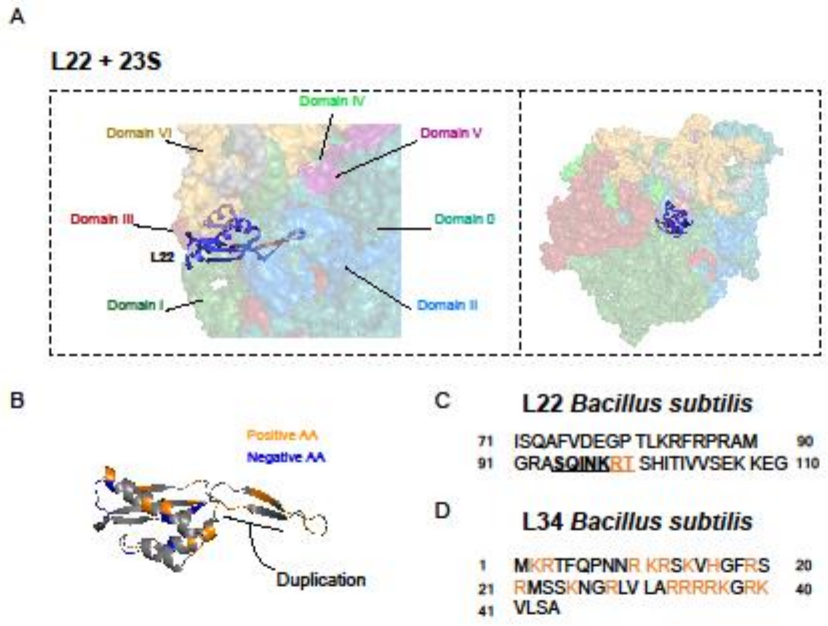

Figure 6.9 Detailed structural characteristics of ribosomal mutants.
(A) L22 protein is the only ribosomal protein that contact with all 6 domains of 23S rRNA. Below: duplicated amino acids in the loop marked in red and positively charged amino acids underlined. The structure is represented from PDB xxx. **(B),** Charge representation of L22 protein. **(C)** The duplicated L22 region is underlined. Positively charged amino acids are in orange **(D)** Amino acid sequence of the L34 protein. Positively charged amino acids are colored in orange.

IV

CONCLUSIONS AND FUTURE DIRECTIONS

7 Conclusions and Future directions

The dissertation thesis started off with two broad questions. 1. How cells cope with seemingly conflicting demands under stress, 2. How a cell can coordinate multiple and dynamic cellular processes to establish a right response to stress. In this section, I would like to discuss how each chapter could contribute to the answers and the future directions.

The first part of the thesis used *Bacillus subtilis* biofilms as a model system to answer the first question. It is worth note that a biofilm itself is a differentiated form from the free-living counterpart under stress (J. William Costerton et al. 1987). Why do bacteria form biofilms under stress? It has been known that a biofilm is much more resistant than free-living cells (Nickel et al. 1985; Gristina et al. 1987). At the same time, however, cells inside of a biofilm must compete for the limited amount of nutrients. How do cells solve this problem? To answer this question, we followed a biofilm development under a time-lapse microscope with fluorescent reporters of metabolic state. We found that nitrogen metabolic states are globally organized during the *B. subtilis* biofilm development (Fig. 2.1B). There has been a lot of speculations about metabolic organization inside of a biofilm and there are several suggestive data including ours described in Chapter 3 (Stewart and Franklin 2008; Dietrich et al. 2013; Rani et al. 2007), but this is the first visual representation of the global organization of a metabolic state in a biofilm.

The emergent pattern is counterintuitive because the nitrogen starvation reporter collectively turns on only at the periphery of a biofilm where cells are closer to the less depleted media. Interior cells lack the reporter expression and this is not due to the lack of ability to express the reporter protein (Fig. 2.1C and 2.2CD). Genetic mutants show that this pattern is directed by the TnrA, a central transcription factor of nitrogen metabolic genes, responding to an ammonium limitation (Fig. 2.2A, 2.3-6). Under this ammonia limiting condition, TnrA turns on many downstream genes to express active transporters and enzymes to ensure enough nitrogen source in the cell (Wray et al. 1996). Mixed biofilm experiments and a mathematical simulation demonstrated that the ammonia made by cells are shared with neighboring cells, coupling their metabolic states (Fig. 2.7-9, and Fig.A.1). It is interesting that the interior cells don't grow much, yet making enough metabolic intermediate and, in turn, modulate the metabolic states of the peripheral cells. In this way, cells in a biofilm can coordinate their growth and metabolic state under stress.

According to our study on sporulation described in Chapter 5 and many other's studies regarding cellular differentiation (Yasumura, Abe, and Tanaka 2008; Zhang et al. 2014; Zdena Palková and Vachova 2003), it seems very plausible that this global organization in metabolic states, or in other words growth, contribute to the cellular differentiation pattern in a biofilm. It's been known that biofilm formation promotes cellular differentiation and different cell types are located in the different regions of a biofilm (Vlamakis et al. 2008); still, it remains unclear what drives this cell type organization in a biofilm. Metabolic organizations in a biofilm and their effects on biofilm development would give us a better tool for biofilm control.

A limitation of this study is that a biofilm grows in 3D on MSgg-agar plate. It is apparent that the biofilm growth and cell density is one of the major factors driving this metabolic organization, but the ability to capture z-dimensional growth is very limited. Studies present in Chapter 3 and 4 overcome this shortcoming by using a growth chamber that limits z-dimensional growth and cells essentially grow in 2D. Based on my discovery in Chapter 2, we could hypothesize that the periodic growth halt of a biofilm periphery in a microfluidic chamber (Fig.3.1) might be due to ammonia limitation imposed by interior cells (Fig.3.2). Interior and periphery are dependent each other on their metabolic states because interior cells depend on peripheral cells for the glutamate uptake while peripheral cells depend on interior cells for ammonia production. This simpler system also allowed us to clearly demonstrate the biological benefit of sharing and coordinating nutrient consumptions in a biofilm (Fig. 3.4 and 3.11). This is such a clear demonstration of how cells coordinate different needs by forming a biofilm under stress.

The understanding of the growth oscillations was soon complemented by Arthur Prindle's study that showed electric communication within a biofilm (Prindle et al. 2015). This study provided not only the explanation of how the entire biofilm can synchronize their metabolic oscillation faithfully but also a new perfective to approach a biofilm physiology (I will discuss this point in depth later). Electrical communication enables long-distance synchronization without diminishing the signal amplitude and propagation outside of a biofilm. It also helped us to understand how multiple biofilms can coordinate themselves under stress, which is described in Chapter 4.

If a population of bacteria forms a biofilm as a stress response, some coordination inside a biofilm sounds reasonable to increase the general fitness. But what about multiple biofilms? Could cells in independent biofilms still coordinate their behaviors and get benefit under stress? In chapter 4, I described how independent biofilms can synchronize or anti-synchronize their metabolic oscillations under stress. In this study, we extended our understanding from a single biofilm to two nearby biofilms, which can affect each other by nutrient competition and electric communication (Fig. 4.1).

Utilizing various genetic mutants and a mathematical model, we could explain the observation of two biofilms that oscillate in phase and out of phase based on communication and competition strength (Fig.4.2). Specifically, starvation stress increases both competition and communication strength, but for different extents. The phase diagram, computed by the mathematical model and verified by experiments, shows that this is not a simple relationship. However, one can make a simple prediction out of it. Once the glutamate concentration, the major nitrogen source in the media, gets lower, biofilms will shift to anti-phase (Fig. 4.2). Furthermore, this anti-phase synchronization lessens nutrient competition between biofilms and let each biofilm grow as if they grow alone in the growth chamber (Fig. 4.3). This study provides another concrete example of a coordination strategy to handle tensions.

These *B.subtilis* biofilm studies initiate many interesting questions; Will there be oscillations in other bacterial biofilms? What about multi-species biofilms? Do these oscillations play any role in other signaling processes like neurons do, or differentiation processes of a biofilm? Most importantly, it clearly demonstrates that cells can not only communicate their metabolic state with the other cells through electrochemical signaling but also modulate others' state and thus initiate new dynamics. This way of communication method would go much further and faster than the communication based on the diffusion or exhaustion of molecules. Also, the signals are based on cells' metabolic need and communication capacity, and thus it's plausible that different species would generate entirely different dynamics. It is very exciting to see what can biofilms do more by effectively changing the electrochemical environment of neighbors.

One step further, neither glutamate nor potassium is specific to bacteria. Indeed, these are the dominant amino acid and ion in any cell (Newsholme et al. 2003; Milo et al. 2010). Recently, there has been an increasing attention to the effects of gut microbiota on the brain (Ridaura and Belkaid 2015; Zhu et al. 2017). Gut microbiota suggested as a potential regulator of neurodevelopment and is also known to be closely associated with various central nervous system disease including Parkinson’s disease and Alzheimer’s disease (Klingelhoefer and Reichmann 2015; Wu et al. 2017). Current studies are mostly focused on the composition and quantity of gut microbiomes. These are very valid points and will serve as a solid ground, but the main factor affects the host might be the electrochemical dynamics of microbiota rather than the exact composition or quantity.

The second part of the thesis asked about the coordination strategy between dynamic processes in a cell under stress. Sporulation is particularly a good example to investigate it because cells need to coordinate their differentiation program and cell cycle to survive under stress (Fig. 5.1). Moreover, both sporulation and cell cycle are individually very well characterized for their dynamics and numerous components involved in each process (Jeffery Errington 1993; Higgins and Dworkin 2012; Sharpe et al. 1998; Michael 2001).

In Chapter 5, I described a work mainly done by Jatin Narula and Anna Kuchina. In this work, we could unambiguously demonstrate that the sporulation process is coordinated with chromosome replication, cell cycle, by transient gene dosage imbalance during chromosomal replication (Fig. 5.3-4, D.1-2). Plainly, one gene is located closer to the starting point of the chromosomal replication while the other gene is located closer to the end. Then, the former gene will spend time with a double amount longer when the chromosomal replication gets slower. This transient gene dosage imbalance, together with the complicated dynamic genetic circuit, produces pulsatile behavior of the master regulator of sporulation and leads to the successful sporulation. Mutants that lost this coordination lead to sporulation defects with too early or too late cell divisions (Fig. 5.5), confirming the importance of this coordination.

It is well known that genes in the same regulatory network are frequently located close to each other and even form an operon in bacteria to facilitate the co-regulation (Doncic, Falleur-Fettig, and Skotheim 2011; Toettcher et al. 2009). Contrary, in chapter 5, I describe a counterexample that the genes in the same regulatory network for sporulation are in the almost opposite side of a chromosome and cell uses it as a regulatory tool to determine the timing. It is such a genius way to couple dynamic systems; utilizing their own dynamic features. Also, it seems obvious that there should be much more regulatory pathways that exploit this simple coupling mechanism. It would be a great future project to examine regulatory networks that implement gene-dosage effect in the regulatory mechanism.

It is also such a great example of the how a combination of a mathematical model and experiments complement each other beautifully. Biological systems often have too many players, multiple feedbacks, and complex outcomes to interpret intuitively. A mathematical model can help narrow down the most fundamental components to recapitulate the dynamics of interest by providing what kind of interactions are necessary to achieve specific features. On the other hand, experimental verifications are essential to confine the mathematical model since there could be always multiple ways to explain one phenomenon, but it’s hard to equally satisfy multiple characteristics. For instance, the inhibition of KinA by Sda (J. Veening, Murray, and Errington 2009) can explain the 0A~P pulses coupled with DNA replication, but it cannot explain the lack of pulsing our results with perturbing 0A~p-0F negative feedback (Fig. 5.3D).

Along with slowing down DNA replication, various stresses often interfere with ribosomes. In Chapter 6, I discussed how ribosome, one of the most ancient and crucial parts of a cell, can be coupled with another same kind, membrane potential. A ribosome comprises 65% ribosomal RNA (rRNA) and 35% ribosomal proteins (Kurland 1960). As one can imagine from the high fraction of rRNA in this small entity, a lot of ions (> 170 Mg^{2+} ions/a ribosome) are necessary to neutralize the negative charges and compact them (Schuwirth et al. 2005). Moreover, the number of ribosomes in a bacterium can range from 5,000 to 75,000 depending on its growth rate (Milo et al. 2010). If so, how do changes in ribosomes in a cell affect the magnesium or other ions in a cell, which can be translated to change in membrane potential (Fig.6.1A)?

Various perturbations on the ribosomes, from chemicals to genetic mutations, show that ribosomal perturbations can lead to a transient hyperpolarization of the membrane potential (Fig. 6.2-3). To my knowledge, this is the first time to show the coupling of ribosomes and membrane potential dynamics. How can ribosome perturbations alter membrane potential dynamics? We don’t know the full picture yet, but it is likely from a direct impact of magnesium ions bound to ribosomes. We ruled out several other possibilities including respiration (Fig. 6.2) and the potential influx of negative ions from the media (Fig. 6.4). On top of these, ion quenching results and the magnesium-dependency of hyperpolarized L34 disruption mutant fraction strongly suggest that magnesium is responsible for the membrane potential changes (Fig. 6.4).

This leads us to think about the number and dynamics of ions in a cell, especially magnesium ions. Magnesium ions are the predominant divalent cations in a cell and but their dynamics are often neglected because of the relatively high amount in both bound and free pool of magnesium ions and a rare occurrence of a significant change in free magnesium pool (Romani 2011). It is very different from the calcium regulation, which is usually maintained at very low concentration, and thus it is easy to detect transient changes in free ion concentrations (Dominguez 2004). Our results suggest a possibility that ribosomes act as a magnesium reservoir and cells use ribosomal bounding magnesium as a secondary messenger under stress. It would be meaningful to investigate other cellular processes that heavily rely on magnesium ions, such as replication and cell division, under the ribosomal stress condition.

This study instigates many new questions. For instance, what are the dynamics of magnesium ions and other ions during the transient hyperpolarization? Can there be any functional role? How are the neighboring cells affected by the ion efflux? Membrane potential is crucial for many cellular functions; nutrient uptake, ATP synthesis, and membrane protein positioning, to name a few. While ions play a critical role in all these, ion dynamics in a cell is largely mysterious. It is mainly because ions are too small to monitor and too many to notice small changes, yet still physiologically relevant. Visualization of ions itself inevitably perturbs the equilibrium, making it even harder to monitor their dynamics. It is recent that few ion reporters are introduced in the field. I believe the ability to monitor various ions in real time will vastly widen our perspectives on biology.

It is interesting that the main players of the stress responses were not made specifically for the stress response. Rather, a cell utilizes the dynamic characteristic of each cellular process to couple it with the other when needed. This makes sense because many stressful conditions would also limit the ability of a cell to produce or reproduce. Cells are in this conundrum again; production is significantly limited, yet it needs to produce signals to survive. In this situation, it is almost impossible to prepare tailored responses for different kinds of stresses. Instead, cells respond in a smarter way. Cells use the fact that in the end, all stresses will slow down the growth, and thus will change certain dynamic features of the existing processes. These cannot be understood if one approaches the phenomenon with a static or a linear view.

Throughout the dissertation thesis, we saw that we can learn much more if we start considering the dynamics and integrating dynamic relationships between the key players, which are often non-linear and thus non-intuitive. Apparently, it is meaningful to get informed of all players in the scene. It is also important to learn details of each component to understand a certain pathway. On top of these, investigating how dynamic processes operate together can lead us to understand how a living system, as a whole, perceives, processes, and reacts to the environmental challenges better. Quantitative analysis and mathematical modeling are the beginning. Furthermore, studies presented in the thesis exclaim the importance of ions with its vast number and dynamic features. It will be exciting to see whether and how the appreciation of ions leads to a new conceptual understanding of cellular coordination.

V

APPENDICES

Appendix A. Mathematical Model for Chapter 2

In our earlier work (Mather et al. 2010; Volfson et al. 2008), we developed a discrete agent-based model of bacterial populations. Here, in order to describe the dynamics of a growing bacterial biofilm, we adopt this model to simulate intracellular metabolic processes along with cell growth, division, and mechanical cell-cell interactions. Each cell in the population is modeled as a spherocylinder that can grow along its axis and divide once the conditions for the division are met. Each cell is endowed with a set of ordinary differential equations describing metabolic reactions and biomass growth, which use as input time-dependent parameters of the local extracellular concentrations of ammonium and glutamate. In turn, each cell serves as a localized source and/or a sink of the glutamate and ammonium that diffuses through the cell membrane and throughout the integration domain. The dynamics of extracellular compounds such as glutamate and ammonium are modeled by partial differential equations incorporating diffusion, dissipation, and local sources (cells).

As intracellular variables, we include the concentrations of glutamate, ammonium, active glutamate dehydrogenase (GDH), housekeeping proteins responsible for cell growth, and fluorescent marker *yfp* driven by *nasA* promoter (which we call in the following P_{nasA}-*yfp*).

For simplicity, we used a 2-D version of this model in which bacterial cells confined to a monolayer. Specifically, the equations for intracellular dynamics in each of the cells are

$$\frac{dG_i}{dt} = -\alpha G_i H_i - \delta G_i R_i + D_g(G(x_i,t) - G_i)$$

$$\frac{dA_i}{dt} = \alpha G_i H_i - \delta A_i R_i + D_a (A(x_i, t) - A_i)$$

$$\frac{dR_i}{dt} = \beta_R f_R - \gamma_R R_i$$

$$\frac{dH_i}{dt} = \beta_0 + \beta_H f_H - \gamma_H H_i$$

$$\frac{dY_i}{dt} = \beta_Y f_Y - \gamma_Y Y_i$$

Here $G_i(t), A_i(t), R_i(t), H_i(t), Y_i(t)$ are the intracellular concentrations of glutamate, ammonium, housekeeping proteins, GDH and P*nasA*-*yfp* in i -th cell, respectively. Variables $G(x_i, t), A(x_i, t)$ are extracellular concentrations of glutamate and ammonium at the location of the i -th cell. The meanings of each term in the equations are as follows.

$\alpha G_i H_i$: ammonium production rate from glutamate catalyzed by GDH.

$\delta G_i R_i$: glutamate consumption rate

$\delta A_i R_i$: ammonium consumption rate

$D_g (G(x_i, t) - G_i)$ and $D_a (A(x_i, t) - A_i)$: glutamate and ammonium diffusion through the cell membrane. D_g, D_a are cell membrane diffusion constants for glutamate and ammonium, respectively.

$\beta_R f_R$: synthesis rate of the housekeeping protein

$\gamma_R R_i$: degradation rate of the housekeeping protein

β_0 : basal synthesis rate of GDH. For wild-type cells, $\beta_0 = 0$; for cells over-expressing GDH we choose $\beta_0 = 10$

$\beta_H f_H$: biofilm-induced GDH synthesis rate

$\gamma_H H_i$: GDH degradation rate

$\beta_Y f_Y$: production rate of P$_{nasA}$-*yfp*

$\gamma_Y Y_i$: degradation rate of P$_{nasA}$-*yfp*

Functions f_R , f_H , and f_Y specify the functional form of synthesis rates of housekeeping proteins, GDH, and P$_{nasA}$-*yfp*, respectively. We assume that housekeeping protein synthesis is activated by glutamate and ammonium, and thus f_R has the form

$$f_R = \frac{G_i^{n_1}}{G_i^{n_1} + K_1^{n_1}} \frac{A_i^{n_2}}{A_i^{n_2} + K_2^{n_2}}$$

In wild-type cells, GDH synthesis only occurs in the interior of the biofilm. We assume that growth of extracellular polymeric substances triggers that transition. To model this accumulation, we introduce the local concentration of EPS $E(x,t)$ that is initially set to zero, but within the biofilm, it grows at a constant rate b_E. Function f_H for *i*-th cell switches from 0 to 1 when $E(x_i,t)$ at the position of the *i*-th cell reaches 1.

The synthesis of P$_{nasA}$-*yfp* is mostly repressed by ammonium, and thus we model it by choosing

$$f_Y = \frac{K_3^{n_3}}{A_i^{n_3} + K_3^{n_3}} .$$

The extracellular glutamate and ammonium concentrations $G(x_i,t), A(x_i,t)$ are governed by linear partial differential equations with linear diffusion, dissipation of localized sources and sinks (cells):

$$\partial_t G = D_g\left[\sum G_i \delta(\mathbf{x}-\mathbf{x}_i) - G\right] + \lambda(G_0 - G(x,t)) + D_G \nabla^2 G$$

$$\partial_t A = D_a\left[\sum A_i \delta(\mathbf{x}-\mathbf{x}_i) - A\right] + D_A \nabla^2 A - \delta_A A$$

Here D_G, D_A are diffusion constants for glutamate and ammonium in the media respectively. $\delta_A A$ is the dissipation term of extracellular ammonium, and term $\lambda(G_0 - G(x_i,t))$ describes the diffusion of glutamate from the substrate to the biofilm environment. In the simulation, we used 2D finite difference method with zero-flux boundary contains a square domain to approximate the diffusion of glutamate and ammonium.

We assume that when the concentration of housekeeping proteins is above a certain threshold (0.014 in the simulation), the cell length increases linearly in time with the rate r_N^i until it reaches a pre-defined “division length” l_d at which it is replaced by two coaxial cells with lengths $l_d/2$ touching each other. The division length of each cell is chosen at random at birth from a uniform distribution within the interval $[l_0-\Delta l, l_0+\Delta l]$ with $\Delta l = 0.01 l_0$. Cells interact with each other via normal and tangential forces computed from cell overlap via a variant of the well- established string-dashpot algorithm.

In biofilm growth simulation, the concentration of glutamate in the substrate is maintained constant $G_0 = 10$. For extracellular ammonium inside the biofilm, $\delta_A = 0$ due to the protection of the biofilm. Outside the biofilm, we assume that ammonium readily makes equilibrium with ambient ammonia which quickly diffuses away so that the concentration of ammonium is 0. Consider the thickness of the biofilm decreases at the edge of the biofilm when we plot the snapshot of the simulation of the biofilm, the P*nasA*-*yfp* expression is scaled by a factor of $\frac{d^5}{d^5+d_0^5}$, where d is the distance between the cell and the edge of the biofilm and $d_0=8$.

In the single-cell level experiments, the concentration of extracellular glutamate is much lower than that in the biofilm growth experiment. Furthermore, it was consumed slowly on the time scale of the experiment, and therefore in simulations we simply assumed it to be constant $G(x_i,t)=0.01$. Unlike the biofilm experiment where ammonium was trapped within the biofilm, in these experiments it can escape freely. We model this by the dissipation term in the equation for ammonium with $\delta_A=100$. Note that due to fast diffusion of ammonium and the relatively small size of the experimental domain, the concentration of ammonium throughout the region of simulation is nearly constant.

Appendix A, in full, contains materials being prepared for publication. Dong-yeon D. Lee, Liyang Xiong, San Ly, Lev Tsimring and Gürol M Süel. The dissertation author was the primary investigator and author of the material contains the chapter.

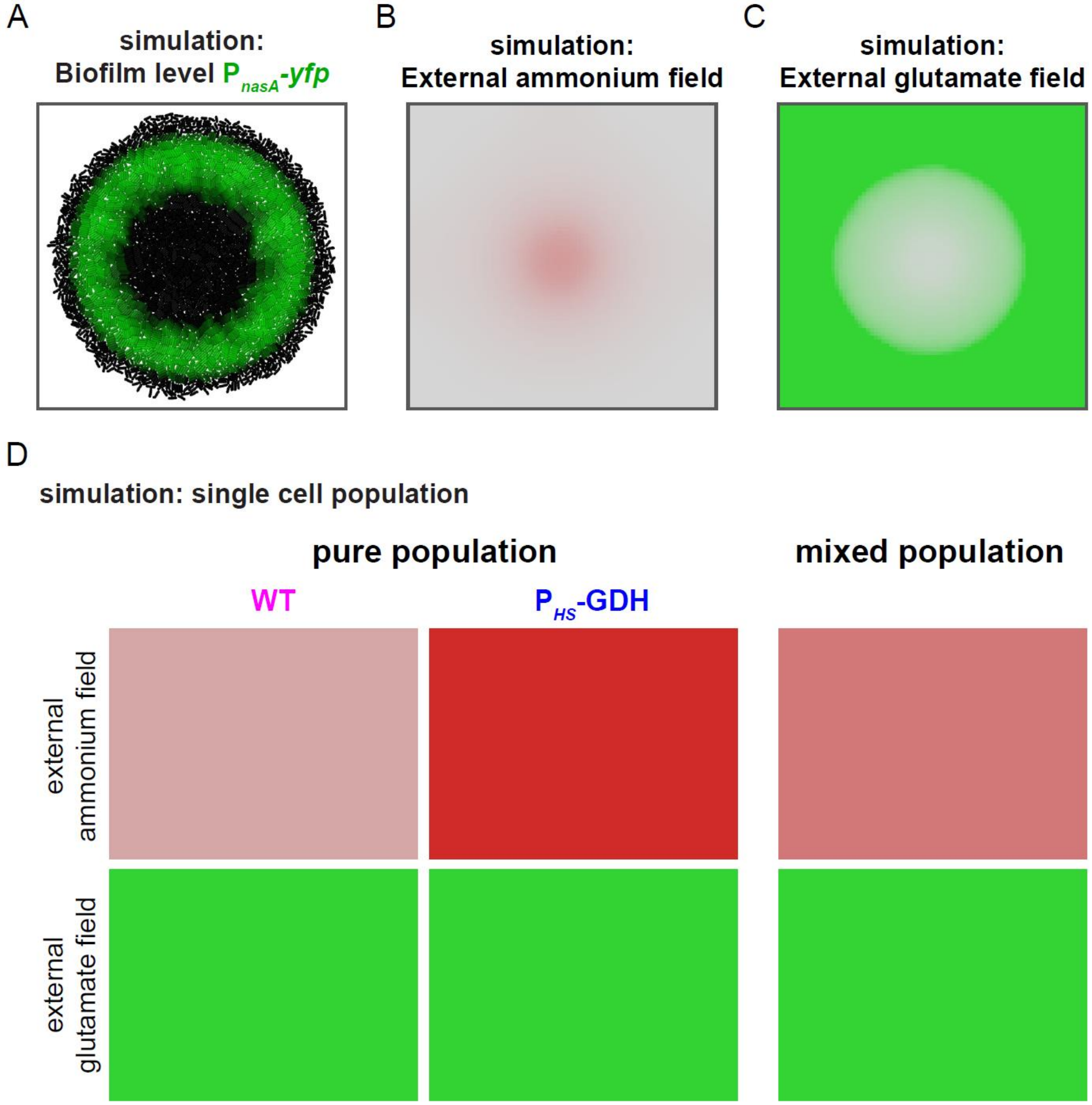

Figure A.1 Mathematical modeling of the spatiotemporal nitrogen metabolic regulation. **(A)** Ring pattern of nitrogen stress response in Figure 1B is generated by the mathematical model. **(B)** Model prediction of the extracellular ammonium concentration in biofilm simulation shown in A. **(C)** Model prediction of the extracellular glutamate concentration in biofilm simulation shown in A. **(D)** Extracellular ammonium (left) and glutamate (right) concentrations predicted in the model simulation for pure WT population (top), pure GDH overexpression population (middle) and mixed population in Figure 2.9C. The ammonium coupling at the single cell level was simulated using the same intracellular circuit parameters used in A.

Table A.1 Parameter values used in the model.

α	10
δ	50
λ	0.001
β_R	9
γ_R	1
β_H	0.9
γ_H	1
β_Y	0.4
γ_Y	0.4
D_G	200
D_A	2000
D_g	300
D_a	2000
K_1	1
K_2	0.01
K_3	0.009
n_1, n_2	10
n_3	5

Appendix B. Mathematical Model for Chapter 3

B.1 Model description

We describe the dynamics of biofilm growth in terms of two distinct populations, corresponding to the interior and the periphery of the biofilm. The two populations are assumed to be located in a moving frame of reference as the biofilm grows so that they are always located at the same distance from the physical edge of the biofilm (Fig. 3.10A).

The metabolic state of the biofilm is determined by the following quantities: 1) The concentrations of glutamate in the biofilm interior (G_i) and in the periphery (G_p); 2) the concentration of ammonium (A), which is assumed to be equal for the two populations due to its fast diffusion; 3) The concentration of active glutamate dehydrogenase (GDH) in the interior cells (H_i); and 4) the rate of biomass production, which is assumed to be given by the concentrations of housekeeping proteins (such as ribosomal proteins) in the interior (r_i) and in the periphery (r_p). The dynamics of these state variables are described by the following set of ordinary differential equations:

$$\frac{dA}{dt} = \alpha G_i H_i - \delta_A A(r_i + r_p)$$

$$\frac{dG_i}{dt} = D\left(G_p - G_i\right) - \alpha G_i H_i - \delta_G G_i r_i$$

$$\frac{dG_p}{dt} = D\left(G_i - G_p\right) + D_E\left(G_E - G_p\right) - \delta_G G_p r_p$$

$$\frac{dH_i}{dt} = \beta_H \frac{G_i^n}{K_H^n + G_i^n} - \gamma_H H_i$$

$$\frac{dr_i}{dt} = \beta_r A G_i - \gamma_r r_i$$

$$\frac{dr_p}{dt} = \beta_r A G_p - \gamma_r r_p$$

The terms in the equations are interpreted as follows:

- $\alpha G_i H_i$: ammonium production from glutamate, catalyzed by the enzyme GDH (Fig. 3.2A)
- $\delta_A A(r_i + r_p)$: ammonium consumption by interior and peripheral cells
- $\delta_G G_i r_i$ and $\delta_G G_p r_p$: glutamate consumption by interior and peripheral cells, respectively
- $D(G_p - G_i)$: glutamate diffusion between peripheral and interior regions
- $D_E(G_E - G_p)$: glutamate diffusion between the environment and the periphery of the biofilm
- $\beta_H \frac{G_i^n}{K_H^n + G_i^n}$: GDH activation in the interior cells
- $\gamma_H H_i$: GDH deactivation in the interior cells
- $\beta_r A G_i$ and $\beta_r A G_p$: production of housekeeping proteins in the interior and peripheral cells, respectively
- $\gamma_r r_i$ and $\gamma_r r_p$: degradation of housekeeping proteins in interior and peripheral cells, respectively

We make the following assumptions:

- Peripheral cells rely on ammonium synthesized by interior cells. As a simplification, we assume that only the interior cells have active GDH.
- Activation of GDH depends on the glutamate availability. Specifically, H_i is reduced when the concentration of available glutamate (G_i) is below a given threshold. This can be due to explicit regulatory interactions or simply as a consequence of the slowdown of cellular processes in the absence of nutrients.

- Consumption of ammonium and glutamate depends on the metabolic activity of the cell. The higher the concentration of housekeeping proteins – a proxy for the metabolic state of the cell – the faster the consumption of nutrients.
- The production of housekeeping proteins increases with the concentrations of glutamate and ammonium.

In order to extract from the model the population expansion, which can be measured experimentally, we consider that the dynamics of the cell density $\boldsymbol{\rho}$ of the two populations are given by:

$$\frac{d\rho_{i,p}}{dt} = \eta r_{i,p}\rho_{i,p}\left(1 - \frac{\rho_{i,p}}{K(G_{i,p})}\right) - \lambda_{i,p}\rho_{i,p}$$

The first term in the right-hand side is a logistic-growth term, where the maximal growth rate is considered to be proportional to the concentrations of housekeeping proteins r_i and r_p. Additionally, we assume that the carrying capacity K depends on the concentration of glutamate:

$$K(G) = \frac{G^m}{K_k^m + G^m}$$

Thus $K(G)$ varies between 0 and 1 depending on whether glutamate concentration is below or above a given threshold, denoted as K_k. Note that the cell density $\rho_{i,p}$ defined here is relative to the carrying capacity, therefore, both K and ρ are dimensionless.

The logistic-growth term in the density equation shown above describes the standard birth/death processes that occur in an unmoving bacterial population. In our system, however, the peripheral cells are always expanding into the open area outside of the biofilm. We represent this fact by adding an effective decay term, $-\lambda_{i,p}\rho_{i,p}$ in the density equation of the expanding population (i.e. the peripheral population for all situations considered, except in the case of chemical attack, where the peripheral population is eradicated and consequently the interior cells can expand). This decay term accounts for the effective loss of cells undergone locally by the biofilm front as it expands (in our moving reference frame) into the cell-free area surrounding it.

Given the above-described dynamics for the cell densities, the growth rate (measured experimentally as the area of non-zero local motion within the biofilm) is given by the logistic term, since this is the only term related to the actual growth of the population:

$$\mu_{i,p} = \eta r_{i,p}\rho_{i,p}\left(1-\frac{\rho_{i,p}}{K(G_{i,p})}\right)$$

B.2 Addition of glutamine to the media

Glutamine is synthesized by glutamine synthase (GS) in the cell, and it also regulates the activity of GS through negative feedback [27]. Therefore, external addition of glutamine reduces GS activity and consequently lowers its consumption of ammonium and glutamate (used to synthesize glutamine). Additionally, we assumed that glutamine inhibits either directly or indirectly GDH activity, affecting the production of ammonium from glutamate. This is implemented in the model as a non-competitive inhibition on the parameters α and δ. Specifically, the effective $\bar{\alpha}$ and $\bar{\delta}$ are given by:

$$\bar{\alpha} = \frac{\alpha}{\frac{[Gln]}{K_\alpha}+1}, \quad \overline{\delta_{A,G}} = \frac{\delta_{A,G}}{\frac{[Gln]}{K_\delta}+1}$$

Fig. 3.3f in the main text shows the model prediction: in agreement with the experimental observations, external addition of glutamine leads to the quenching of oscillation. A systematic analysis of the effect of glutamine addition is shown in Fig. 3.9B, where a bifurcation diagram of the peripheral glutamate concentration with respect to the added glutamine concentration is shown.

B.3 Addition of glutamate to the media

The concentration of glutamate in the external medium is explicitly defined in the model by the parameter G_E. Thus, supplementation with additional glutamate is represented by simply increasing the value of G_E. Fig. 3.3G in the main text shows the model prediction: consistent with the experimental observations, a moderate increase in external glutamate does not eliminate the oscillations. A systematic study also shows that further increasing glutamate leads to quenching of oscillations (Fig. 3.9C).

B.4 Addition of ammonium to the media

The concentration of ammonium is explicitly represented in the model with the variable A, and the addition of ammonium to the media can be represented as an additional creation term (α_0) in the ammonium equation:

$$\frac{dA}{dt} = \alpha G_i H_i - \delta_A A(r_i + r_p) + \boldsymbol{\alpha_0}$$

Fig. 3.3H in the main text shows the model prediction: in agreement with the experiments, externally adding ammonium quenches oscillation. We also systematically explored the effect of different ammonium concentrations through a bifurcation diagram of the system with respect to α_0 (Fig. 3.9D).

B.5 Overexpression of GDH in cells

We also investigated the effects of overexpressing GDH in the biofilm. The overexpression is implemented in the model by an additional creation term β_0 into the equation for GDH (H_i). Furthermore, since the overexpression is applied throughout the entire biofilm, we include active GDH for the peripheral cells (H_p), and consequently the production of ammonium from those cells. To that end, the differential equations for A, G_p and H_i are modified as shown below, and an equation for GDH in the peripheral cell population (H_p) is also added:

$$\frac{dA}{dt} = \alpha G_i H_i + \boldsymbol{\alpha G_p H_p} - \delta_A A\left(r_i + r_p\right)$$

$$\frac{dG_p}{dt} = D\left(G_i - G_p\right) + D_E\left(G_E - G_p\right) - \boldsymbol{\alpha G_p H_p} - \delta_G G_p r_p$$

$$\frac{dH_i}{dt} = \boldsymbol{\beta_0} + \beta_H \frac{G_i^n}{K_H^n + G_i^n} - \gamma_H H_i$$

$$\boldsymbol{\frac{dH_p}{dt} = \beta_0 - \gamma_H H_p}$$

Fig. 3.4E in the main text shows the model prediction: in agreement with the experiments, overexpressing GDH leads to quenching of oscillation. A systematic analysis of different levels of overexpression is shown in the bifurcation diagram in the Fig. 3.9E.

B.6 Addition of hydrogen peroxide to the media

Hydrogen peroxide is a strong oxidizer that can kill the cells on the periphery of the biofilm. Dead cells in the biofilm will still affect glutamate diffusion but will be metabolically inactive. Thus, the killing is implemented in the model by removing the production term of housekeeping proteins in the peripheral cell population. Additionally, a new negative term in the cellular density equation is introduced to account for cell death. To that end, the differential equations for r_p and ρ_p are modified as shown below:

$$\frac{dr_p}{dt} = -\gamma_r r_p$$

$$\frac{d\rho_p}{dt} = \eta r_p \rho_p \left(1 - \frac{\rho_p}{K(G_p)}\right) - \boldsymbol{\lambda_{H_2 0_2} \rho_p} - \lambda_p \rho_p$$

The new term is also added to the equation for the rate of population expansion:

$$\mu_p = \eta r_p \rho_p \left(1 - \frac{\rho_p}{K(G_p)}\right) - \boldsymbol{\lambda_{H_2O_2}\rho_p}$$

Finally, in the case of GDH overexpression, hydrogen peroxide entirely eliminates GDH production in the peripheral cell population, and the differential equation for H_p becomes:

$$\frac{dH_p}{dt} = -\gamma_H H_p$$

Fig. 3.4H in the main text shows the model prediction on the average growth rate and death in interior and peripheral populations after the addition of hydrogen peroxide, for both wild-type and GDH overexpressing biofilms.

B.7 Effect of varying the ratio of interior to peripheral cells

As a consequence of biofilm expansion, the relative size of interior and peripheral cell populations changes over time. Since the variables of the mathematical model represent intensive quantities (their value does not depend on the total volume) most of the equations would not be affected by changes in the relative size of both cell populations. The only exception is the equation for ammonium, as it describes the concentration of this species in the whole biofilm, taking into account reactions that occur exclusively in one or the other population region. In this case, the relative size of each one of these two regions will modulate the relative effect of these reactions.

To explore the effects of changes in the relative sizes of the two populations, we define f_i as the fraction of the size of the interior population over the whole biofilm population. This parameter allows us to distinguish the contributions of the interior and peripheral regions to both the production and the consumption of ammonium:

$$\frac{dA}{dt} = f_i \alpha G_i H_i - \delta_A A\big(f_i r_i + (1 - f_i)\, r_p\big)$$

This equation allows us to determine the effect of an increase in f_i (such as the one that occurs in the biofilm as it expands) on the growth oscillations reported above. Fig. 3.10F shows that the oscillations persist for a wide range of f_i values, with a period that increases only slightly with f_i, in agreement with the experimental observations.

B.8 Sensitivity analysis

Fig. 3.10G and H show how changes in each one of the intrinsic parameters of the model affect the period and the modulation depth of the oscillations. The values of the parameters were scanned from 50% to 150% of its original value. Whenever a modulation depth lower than 2% was measured the system was considered to be non-oscillating and labeled in gray in the color plot.

Appendix B, in full, is a reprint of the material *Jintao Liu, Arthur Prindle*, Jacqueline Humphries*, Marçal Gabalda-Sagarra*, Munehiro Asally*,* ***Dong-yeon D. Lee****, San Ly, Jordi Garcia-Ojalvo, and Gürol M. Süel. "Metabolic co-dependence gives rise to collective oscillations within biofilms" Nature vol. 523, 550–554. 2015 (*equal contribution).* The dissertation author participated in discussions, some of the experimental designs, and strain construction.

Figure B.1 Mathematical model of biofilm growth.

(A) The model describes the dynamics of two cell populations in a biofilm, interior and peripheral. As the biofilm grows, there is a constant distance between the interior population and the biofilm edge. **(B-E)** Bifurcation diagrams showing systematic analysis on the effects of external glutamine, external glutamate, ammonium uptake, and GDH overexpression respectively. The red lines correspond to the extrema of oscillations in peripheral glutamate (stable limit cycle). The solid black line denotes stable fixed point. The dashed black line corresponds to an unstable fixed point. The vertical gray lines highlight the state of the system for each nutrient addition experiment shown in Fig. 3.3 of the main text. **(F)** Model prediction of oscillation period as a function of interior cell fraction in the whole biofilm. **(G-H)** Sensitivity analysis of oscillation period and modulation depth to changes in model parameters. The modulation depth is defined as the amplitude of the oscillations divided by the mean value. Gray color denotes parameter regions where the system does not oscillate.

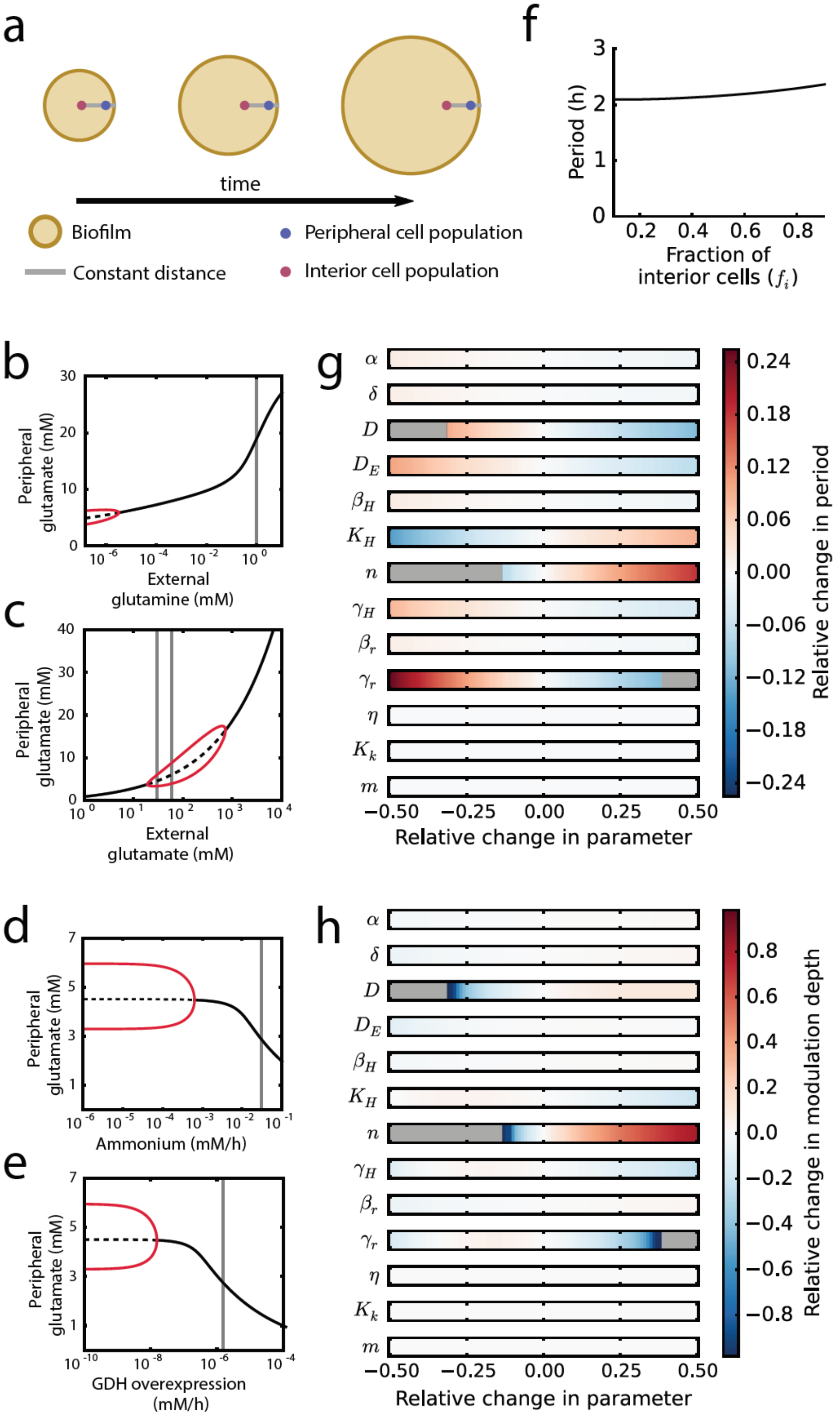
a
time
Biofilm
Constant distance
Peripheral cell population
Interior cell population
f
Period (h)
0
1
2
3
0.2
0.4
0.6
0.8
Fraction of interior cells (f_i)
b
Peripheral glutamate (mM)
0
10
20
30
10^{-6}
10^{-4}
10^{-2}
10^{0}
External glutamine (mM)
c
Peripheral glutamate (mM)
0
10
20
30
40
10^{0}
10^{1}
10^{2}
10^{3}
10^{4}
External glutamate (mM)
d
Peripheral glutamate (mM)
1
3
5
7
10^{-6}
10^{-5}
10^{-4}
10^{-3}
10^{-2}
10^{-1}
Ammonium (mM/h)
e
Peripheral glutamate (mM)
1
3
5
7
10^{-10}
10^{-8}
10^{-6}
10^{-4}
GDH overexpression (mM/h)
g
α
δ
D
D_E
β_H
K_H
n
γ_H
β_r
γ_r
η
K_k
m
−0.50
−0.25
0.00
0.25
0.50
Relative change in parameter
0.24
0.18
0.12
0.06
0.00
−0.06
−0.12
−0.18
−0.24
Relative change in period
h
α
δ
D
D_E
β_H
K_H
n
γ_H
β_r
γ_r
η
K_k
m
−0.50
−0.25
0.00
0.25
0.50
Relative change in parameter
0.8
0.6
0.4
0.2
0.0
−0.2
−0.4
−0.6
−0.8
Relative change in modulation depth

Table B.1 Parameter values used in the model.

	Description	Value	Units
α	Glutamate dehydrogenation coefficient	50	μM^{-1} h^{-1}
δ_A	Ammonium consumption coefficient	4	μM^{-1} h^{-1}
δ_G	Glutamate consumption rate	4	μM^{-1} h^{-1}
D	Glutamate diffusion constant within the biofilm.	0.4	h^{-1}
D_E	Glutamate diffusion constant between biofilm and exterior	0.6	h^{-1}
G_E	Glutamate concentration in the external medium	30	mM
β_H	Maximal activation rate of GDH	50	μM h^{-1}
γ_H	Deactivation rate of GDH	7.5	h^{-1}
K_H	GDH activation threshold	7.2	mM
n	Hill coefficient for GDH activation	7	
β_r	Expression coefficient of ribosomal/housekeeping proteins.	0.14	mM^{-1} h^{-1}
γ_r	Degradation rate of ribosomal/housekeeping proteins	2	h^{-1}
η	Population growth rate coefficient	100	mM^{-1}
K_K	Glutamate threshold for carrying capacity	0.85	mM
m	Hill coefficient for carrying capacity	12	
λ_i	Expansion rate of interior cells	0	h^{-1}
λ_p	Expansion rate of peripheral cells	0.032	h^{-1}
$[Gln]$	Concentration of glutamine in the medium	1	mM
K_α	Glutamine inhibition threshold on GDH activity	$5\cdot10^{-8}$	mM
K_δ	Glutamine inhibition threshold on GS activity	$5\cdot10^{-2}$	mM
α_0	Rate of ammonium entering the biofilm from the external medium	0.03	mM h^{-1}
β_0	Expression rate of GDH from the additional copy of the gene	$1.5\cdot10^{-6}$	mM h^{-1}
$\lambda_{H_2O_2}$	Death rate due to hydrogen peroxide	5	h^{-1}

Appendix C. Mathematical Model for Chapter 4

We use a minimal model to analyze the interplay of competition for nutrients and communication between oscillating biofilms, and the effect of this interplay on biofilm growth. We modeled each biofilm as a core phase oscillator defined by a phase variable θ_i, representing the oscillations in the stress level (quantified by $1+\sin\theta_i$) that periodically occur within the biofilm and that result in growth oscillations (*5*, *15*). The model reads (where the index i = 1, 2 denotes each of the two biofilms):

$$\frac{d\theta_i}{dt} = \omega_0 + \Delta\omega(G,\theta_i) + K(G)\sin(\theta_{3-i} - \theta_i) \tag{1}$$

$$\frac{dG}{dt} = b(G_t - G) - C(G,\theta_1) - C(G,\theta_2) - \delta_G r_1 G - \delta_G r_2 G \tag{2}$$

$$\frac{dr_i}{dt} = C(G,\theta_i) - \frac{\delta_r r_i}{k_r + r_i} \tag{3}$$

Equation (1) describes the phase dynamics of the two oscillators, which are coupled in a standard Kuramoto-like (*20*) form with a coupling strength that depends on the amount of glutamate:

$$K(G) = \frac{K_0 G}{k_\theta + G}$$

The coupling strength K_0 depends on the efficiency of electrical signaling between the biofilms (and is thus decreased in the *trkA* deletion mutant, see parameter table below) and on the distance between the biofilms. The intrinsic frequency of each oscillator has a basal value ω_0, and is assumed to increase during the stress buildup phase as glutamate concentration decreases:

$$\Delta\omega(G,\theta_i) = \frac{\Delta\omega_0}{1+G/k_\omega}\cos\theta_i H(\cos\theta_i)$$

In this expression $H(x)$ is the Heaviside function, which ensures that the frequency changes only during the part of the oscillation where the stress increases, which corresponds to $(\sin\theta_i)' = \cos\theta_i > 0$ (the additional $\cos\theta_i$ factor is added for continuity).

Equation (2) describes the dynamics of the total glutamate available to the two biofilms. First, we model the addition of glutamate in the microfluidic device with the term $b(G_t - G)$. Second, we represent the consumption of glutamate for biomass production by each biofilm via the function $C(G,\theta_i)$, which saturates with G and increases with diminishing stress (which is represented by a factor $1-\sin\theta_i$):

$$C(G,\theta_i) = \frac{aG}{k_G + G}(1-\sin\theta_i)$$

Finally, glutamate is also assumed to be spent in generic metabolic tasks, modeled by the term $-\delta_G r_i G$. The existence of the consumption terms in the glutamate equation represents the competition between the two biofilms.

Equation (3) describes the rate of biomass production by the biofilms.

The simulations are started from initial conditions $\theta_1 = 0$, $\theta_2 = 0.1$, $G = G_t$, $r_1 = r_2 = 0$. Integration of the model is performed with the *odeint* function from the Python SciPy package. Measurements are taken at steady state. The average growth rate is calculated as the time average of r_1 and r_2 over the last 800 time units. The phase difference is measured as the average distance between the two nearest peaks of the two $\sin\theta_i$ signals normalized by the instantaneous period, for the last 100 time units. The model parameters are given in the Table C.1 below.

Appendix C, in full, is a reprint of the material *Jintao Liu, Rosa Martinez-Corral*, Arthur Prindle*, **Dong-yeon D. Lee**, Joseph Larkin, Marçal Gabalda-Sagarra, Jordi Garcia-Ojalvo, Gürol M. Süel. "Coupling between distant biofilms and emergence of nutrient time-sharing" Science, vol. 356, Issue 6338, 638-642. 2017 (*equal contribution).* The dissertation author participated in discussions, strain constructions, experiments for supplementary materials, and reviewer responses.

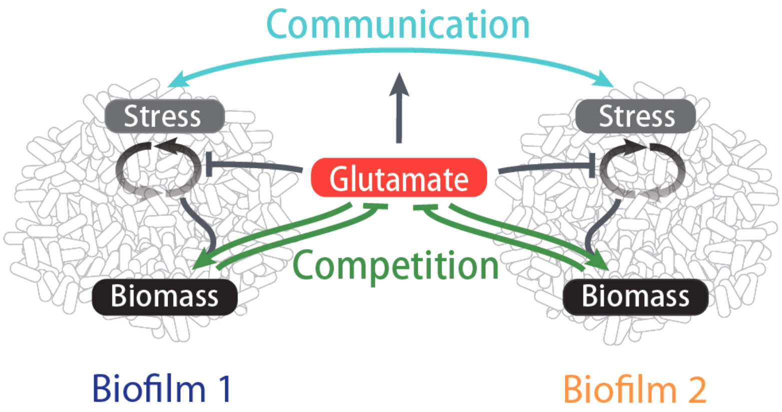

Figure C.1 Schematic of a mathematical model describing the interactions between two biofilms.

Each biofilm was modeled as a phase oscillator, representing oscillations in metabolic stress. We assumed two biofilms were coupled by competition for glutamate and communication through electrical signaling. In addition, we assumed that communication increased with the concentration of glutamate in the medium, as the activity of the potassium ion channel underlying electrical signaling is regulated by glutamate availability.

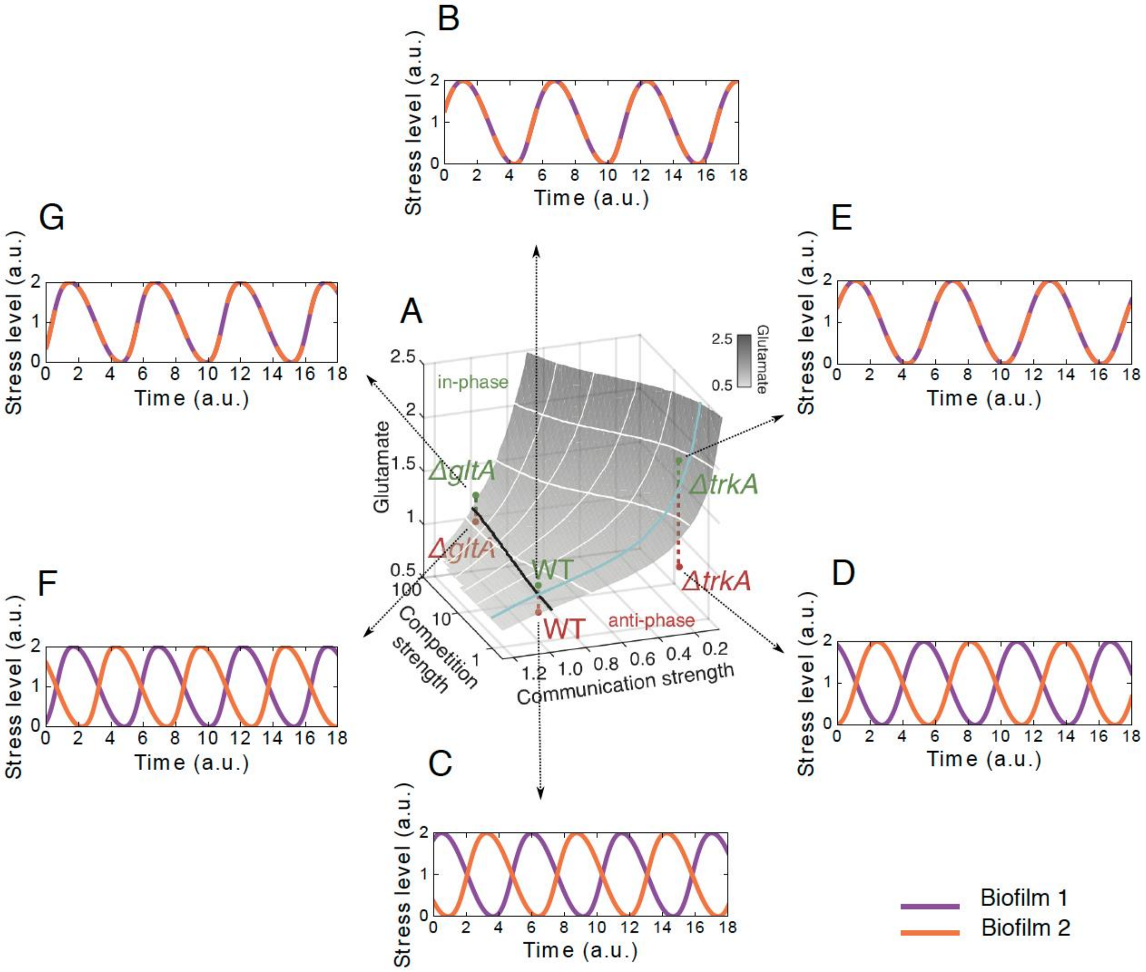

Figure C.2 Synchronization between biofilms is governed by communication and competition.
(A) Phase diagram computed using a mathematical model of coupled phase oscillators (see supplementary text on modeling). The gray-shaded surface depicts the boundary between regions of in-phase oscillations and anti-phase oscillations. **(B-G)** Model time traces from different regions of the phase diagram, which correspond to different experiments discussed in the main text: wild-type **(B-C)**, Δ*trkA* **(D-E)**, and Δ*gltA* **(F-G)** biofilms. For each strain, the model predicted that biofilm pairs oscillate in-phase at relatively high glutamate concentration and oscillate in anti-phase at relatively low glutamate concentration.

Table C.1 Parameter values used in the model.

Parameter	Description	Value (a.u.)
ω_0	Basal intrinsic frequency	1
$\Delta\omega_0$	The maximal glutamate-induced frequency shift	1
k_ω	Glutamate threshold inhibition of frequency shift	0.19
K_0	Maximum coupling (communication) strength	0.073 (baseline level) 0.016 (*trkA* mutation)
k_θ	The threshold for glutamate modulation of coupling strength	0.29
a	Maximum glutamate consumption rate	1.78
k_G	Saturation threshold for glutamate consumption	0.01
δ_r	Biomass degradation rate	4.46
k_r	Saturation threshold for biomass degradation	1.27
b	Glutamate flow rate	6.37
δ_G	Glutamate consumption rate	1.2 (baseline level) 80 (*gltA* deletion)
G_t	External glutamate concentration	1 (baseline level)

Appendix D. Mathematical Model for Chapter 5

D.1 Mathematical Model of the Sporulation Phosphorelay

We extended a previous mathematical model of sporulation phosphorelay network (Narula et al., 2012) to uncover the mechanism of pulsatile 0A activation. For this purpose, we employed a deterministic model of the phosphorelay network with ordinary-differential equations describing the concentration of the phosphorelay proteins and their complexes as a function of time.

Our model can be subdivided into the following two parts: (i) the post-translational interactions that describe the phosphorylation/dephosphorylation of phosphorelay species and (ii) the transcriptional feedback interactions that control the expression of the phosphorelay proteins. Below we describe the reactions and associated assumptions and parameter values for each of these parts separately.

D.1.1 Post-translational interactions in the phosphorelay

The activity of the sporulation master regulator is controlled by the sporulation phosphorelay through post-translational phosphorylation/dephosphorylation reactions. Specifically, phosphoryl groups are transferred from the major sporulation kinase KinA to Spo0A (0A) via the phosphotransferases Spo0B (0B) and Spo0F (0F) (Eswaramoorthy et al., 2010; Hoch, 1993). Phosphorylated 0F and 0A are subject to negative regulation by phosphatases Rap and Spo0E (0E), respectively. Our model of these post-translational interactions in the phosphorelay includes the following reactions (R1-R7):

$$\mathrm{KinA}\ \underset{k_{dp}}{\overset{\mathrm{k_p}}{\rightleftarrows}}\ \mathrm{KinA_p} \qquad \text{(R1)}$$

$$\mathrm{KinA_p} + \mathrm{0F}\ \underset{k_1}{\overset{k_b}{\rightleftarrows}}\ \mathrm{Kin}A_p\colon 0F\ \underset{k_b}{\overset{k_2}{\rightleftarrows}}\ \mathrm{Kin}A_p + 0F_p \qquad \text{(R2)}$$

$$\mathrm{KinA} + \mathrm{0F}\ \underset{k_1}{\overset{k_b}{\rightleftarrows}}\ \mathrm{KinA\colon 0F} \qquad \text{(R3)}$$

$$\mathrm{0F_p} + \mathrm{0B}\ \underset{k_3}{\overset{k_b}{\rightleftarrows}}\ \mathrm{0F_p\colon 0B}\ \underset{k_b}{\overset{k_4}{\rightleftarrows}}\ \mathrm{0F} + 0B_p \qquad \text{(R4)}$$

$$0B_p + \mathrm{0A}\ \underset{k_5}{\overset{k_b}{\rightleftarrows}}\ 0B_p\colon \mathrm{0A}\ \underset{k_b}{\overset{k_6}{\rightleftarrows}}\ \mathrm{0B} + 0A_p \qquad \text{(R5)}$$

$$0F_p + \mathrm{Rap}\ \underset{k_{ubr}}{\overset{k_b}{\rightleftarrows}}\ 0F_p\colon \mathrm{Rap}\ \xrightarrow{k_r}\ \mathrm{0F} + Rap \qquad \text{(R6)}$$

$$0A_p + \mathrm{0E}\ \underset{k_{ube}}{\overset{k_b}{\rightleftarrows}}\ 0A_p\colon \mathrm{0E}\ \xrightarrow{k_e}\ \mathrm{0A} + \mathrm{0E} \qquad \text{(R7)}$$

Here 0F, 0B, 0A, and 0E refer to the proteins Spo0F, Spo0B, Spo0A and Spo0E respectively. Subscript P marks phosphorylated forms of the proteins, colon denotes protein complexes and each rate constant is introduced above its corresponding reaction arrow. Reaction R3 was included in our model to account for the substrate inhibition effect of Spo0F on the kinase KinA. All post-translational reactions were modeled with mass-action kinetics. Table D.1 shows the parameter values used in this model. Binding rates k_b for all reactions were assumed to be diffusion-limited with rate constant 0.5 $nM^{-1}hr^{-1}$. Dephosphorylation by 0E and Rap were assumed to have catalytic rate constants 100 hr^{-1} based on (Stephenson and Perego, 2002). All other rate constants were estimated from the in vitro measurements of phosphorelay kinetics (Grimshaw et al., 1998). These parameter values have an order of magnitude agreement with the parameters used in other models (Bischofs et al., 2009; Sen et al., 2011).

D.1.2 Protein production and degradation in the phosphorelay

For modeling the expression of phosphorelay proteins, we assumed that binding-unbinding of transcription factors from their promoters is fast and therefore rates of transcription can be modeled with appropriate Hill-functions.

The production of the phosphorelay genes kinA, 0F, and 0Ais regulated by $0A_P$ both directly and indirectly (via σ_H), thereby forming multiple feedback loops (Fujita and Sadaie, 1998; Weir et al., 1991). To model the delay induced by the indirect feedback we assumed that $0A_P$ levels control the expression an intermediate regulator S which in turn controls the transcription of kinA, 0F, and 0A (similar to (Levine et al., 2012)). The regulation of kinA, 0F, and 0Atranscription by the intermediate regulator was modeled with the generic Hill-function:

$$v = v^0 + v^{max}\frac{[S]^m}{K^m + [S]^m}$$

Here v^0 and v^{max} represent the basal and maximal rate of transcription, respectively. K and m represent the half-maximal binding constant and the Hill-exponent, respectively. For simplicity, the rate of expression of the intermediate regulator was assumed to be linearly dependent on $0A_P$. For spo0B, spo0E, and rap we assumed constant rates of transcription.

The specific rate expressions and parameter values used are described in Table D.1

For the simulations of the i0F strains (Figures 5.3CD), the 0F expression rate was fixed at 4 μMhr^{-1} and 10 μMhr^{-1} for comparisons to 5μM IPTG induction and 20μM IPTG induction respectively.

The rate of transcription of all genes in the model were also assumed to be proportional to the gene copy number and cell growth rate according to the following equation: $v = gv_p$ Where v is the actual rate of gene expression, v_P represents the expressions described for each gene in Table D.1, g is the gene copy number. The combined Protein Dilution/Degradation rate constant for all proteins was fixed at $0.7hr^{-1}$.

D.1.3 Steady state response of phosphorelay

To determine the effect of the substrate inhibition of KinA by 0F on our model results, we decoupled the transcriptional feedback from $0A_P$ to kinA, 0F, and 0A in our model and studied the response post-translational interactions in the phosphorelay in isolation. We kept the rate of 0A transcription fixed at $4\mu Mh^{-1}$ for these simulations and calculated the steady state $0A_P$ concentrations at different combinations of total KinA and 0F concentrations ($[KinA]_T$ and $[0F]_T$). As shown in the contour plot of Figure 5.7B, steady-state $0A_P$ levels always increased with increasing $[KinA]_T$. However, when the substrate inhibition of KinA by 0F (reaction R3) was included in the model, steady-state $0A_P$ levels depended non-monotonically on $[0F]_T$ concentrations and decreased at high 0F levels. Plotting the steady state $0A_P$ concentrations as a function of the $[0F]_T/[KinA]_T$ ratio (Figure 5.7C) at different fixed levels of $[KinA]_T$ showed that $[0A_P]$ decreases ultrasensitively as this ratio becomes greater than one. Moreover, the ultrasensitivity of this decrease (measured by Hill- exponent) increases at higher $[KinA]_T$. These results suggest that the substrate inhibition of KinA by 0F makes the post-translational response of the phosphorelay highly sensitive to the ratio of 0F and kinA transcription rates. All steady-state responses were calculated using the CL_MATCONT bifurcation package for MATLAB (Dhooge et al., 2003).

A similar procedure was used for Figure 5.2B, to demonstrate the effect of substrate inhibition on the phosphorelay response in a mutant where 0F expression is externally induced. For this simulation, we decoupled the transcriptional feedback from $0A_P$ to 0F and independently varied the 0F expression rate to calculate the steady-state $0A_P$ concentrations as a function of increasing 0F concentrations. As shown in Figure 5.2B, when the substrate inhibition of KinA by 0F (reaction R3) was included in the model, steady-state $0A_P$ levels and the P_{0A} promoter activity decreased ultrasensitively as 0F expression was increased. In contrast, when reaction R3 was excluded, $0A_P$ levels and P_{0A} promoter activity were far less sensitive to high 0F concentrations. These modeling results were compared to measurements of P_{0A} promoter activity in the $i0F^{amyE}$ strain where 0F is expressed solely from an IPTG inducible promoter. As shown in Figure 5.2B, P_{0A} promoter activity in the $i0F^{amyE}$ strain decreases ultrasensitively at high IPTG levels thus confirming the substrate inhibition effect. These steady state calculations were all done with the CL_MATCONT bifurcation package.

D.1.4 Time-Course Simulations

All simulations of the phosphorelay response (Figures 5.3, D.1) were done using the *ode15s* solver of MATLAB. The cell-cycle duration, Tcyc was fixed at 8hrs and the DNA replication periods were modeled with a fixed 2 hour time duration. All origin-proximal genes (P_{0A} and P_{0F} reporters, 0F in WT, P_{hsp}-0F in $i0F^{amyE}$ and kinA in *Trans-kinA*^{amyE}) were assumed to be replicated at the start of the DNA replication period and all terminus proximal genes (kinA, 0B, 0A, P_{hsp}-0F in *i0F*^{gltA}, 0F in Trans-0F^{gltA}) were assumed to be replicated at the end of the DNA replication time-window. For simplicity, replication was assumed to start immediately after cell division.

In Figure D.1, we mimic the effect of increasingly severe nutrient deprivation over multiple cell-cycles spent in starvation conditions by varying the KinA autophosphorylation rate, k_p. As shown in Figure D.1, increasing k_p leads to increasing $0A_P$ levels and P_{0A} promoter activity similar to the increases seen in experimental results of Figure 5.4. k_p is not the only parameter that can affect $0A_P$ levels in this fashion. Changes in other parameters including 0A dephosphorylation rate, protein dilution rate etc. can have a similar effect (not shown). Notably however whereas changes in these parameters can affect quantitative aspects of our results such as the $0A_P$ pulse amplitude, the qualitative features of our results (i.e. pulsing in WT; no pulsing in *Trans-0F*^{gltA} and *i0F*^{gltA} etc.) are robust to such parameter variations.

In modeling the participation of KinB in the phosphorelay, for simplicity, we assumed that KinA and KinB are identical except that each is active in different environmental conditions so that their kinase activities do not overlap. Accordingly, we assumed that KinB expression can be described by the same Hill-equation and parameters as those used for KinA in Figure D.1. We also assumed that KinB has the same post-translational reactions and parameters as KinA. Our assumption of KinB substrate inhibition by excess 0F is justified based on the observation that 0F overexpression decreases sporulation about 1000-fold -a much stronger effect than that of KinA deletion (Figure 5.7A). KinB simulations differ from KinA simulations in one respect kinB is located closer to oriC than kinA (Figure D.1A). Taking this into account, kinBwas replicated 1 hour after the initiation of DNA replication in contrast to kinA which is replicated 2 hours after initiation (compare gene dosage curves for kinA and kinB in Figure D.1D). As a result, the transient period during which substrate inhibition by 0F blocks 0A activation is shorter for KinB. Our mathematical model shows that this the transient period is sufficient to trigger pulsing albeit of lower amplitude (Figure D.1E). Similar to KinA simulations the cell-cycle duration, Tcyc was fixed at 8hrs and DNA replication periods were modeled with a fixed 2 hour time duration. All origin-proximal genes (P_{0A} and P_{0F} reporters and 0F) were assumed to be replicated at the start of the DNA replication period and all terminus proximal genes (0B and 0A) were assumed to be replicated at the end of the DNA replication time-window.

D.2 Simplified Minimal Model of Spo0A Activation

To identify the minimum design features of the sporulation phosphorelay that enable the gene dosage-dependent $0A_P$ pulsing response, we also constructed the following simplified model:

$$\frac{\mathrm{d}[0\mathrm{A_p}]}{\mathrm{dt}} = \in (v_{A_p} F([S]) * G([0F]) * H([0F]) - [0A_p])$$

$$\frac{d[0\mathrm{F}]}{dt} = g_{0F} * (v_{0F}^{0} + v_{0F}^{m} \frac{[S]^p}{K_{0F}^{p} + [S]^p}) - [0F]$$

$$\frac{d[\mathrm{S}]}{dt} = [0A_p] - [S]$$

$$\mathrm{G(0F)} = \frac{[0F]^n}{K_{A_p1}^{n} + [0F]^n}, H(0F) = \frac{K_{A_p2}^{m}}{K_{A_p2}^{m} + ([0F]/[KinA]^m}, \qquad F(S) = \frac{[S]^r}{K_{A_p3}^{r} + [S]^r}$$

This minimal model consists of only three variables: [0Ap] (Spo0A~P), [0F] (Spo0F) and the transcriptional delay variable S. To capture the non-monotonic dependence of $0A_P$ on 0F (see Figure 5.7C) we modeled $0A_P$ production as the product of two functions: G([0F]) and H([0F]). G([0F]) is an increasing function which captures the activation of 0A by low levels of 0F and H([0F]) captures the ultrasensitive repression of $0A_P$ for [0F]/[KinA] greater than one. The additional function F([0Ap]) models the positive feedback from 0AP to itself via the activation of spo0A expression although this is not essential for the minimal pulsing model as we describe below. 0F production is modeled with a Hill-function dependent on the delayed $0A_P$ variable S similar to the full model in the previous section. KinA production rate was assumed to be fixed for the minimal model and [KinA] was used as a time-varying signal which was calculated from the solution of the following equation:

$$\frac{d[KinA]}{dt} = g_{kinA} * v_{kinA} - \ [KinA]$$

Where g_{kinA} = 1 (tmodTcyc) < Trep or g_{kinA} = 2 (tmodTcyc) ≥ Trep and Trep and Tcyc represent the replication period and cell-cycle duration respectively.

0F and *kinA* gene copy numbers g_{0F} and g_{kinA} control the inputs for the minimal model. As shown in Figure D.2A the WT and *Trans-0F*^{gltA} versions of this model differ in that DNA replication affects the only g_{kinA} in WT whereas it affects both g_{0F} and g_{kinA} in Trans-0F^{gltA}. Figure D.2B shows how the nullclines for [0Ap] and [0F] in the minimal model change depending on g_{0F} and g_{kinA}. These nullclines are helpful in gaining insight into the *kinA:0F* ratio dependent pulsing of $0A_P$. As shown in Figure D.2BC, although at the start of DNA replication (g_{0F}=2 and g_{kinA}=2) the both WT and *Trans-0F*^{gltA} are at the same starting point, they approach different asymptotic steady states during DNA replication.

Specifically,[0F] decreases in both WT and *Trans-0F*^{gltA} but [0A$_P$] levels decrease only in WT. Once DNA replication is completed, copy numbers return to their original values (g_{0F}=2 and g_{kinA}=2), forcing the system to return to the starting point. In WT the decrease in [0A$_P$] levels delays the [0F] increase, thereby allowing [0A$_P$] to overshoot and produce a pulse of [0A$_P$]. In contrast, increase in [0F] is not delayed in *Trans-0F*^{gltA} preventing a [0A$_P$] pulse.

The minimal model is able to produce *kinA:0F* ratio dependent pulsing of 0A$_P$ because it includes a delayed ultrasensitive negative feedback loop between 0A$_P$ and 0F similar to the full phosphorelay model. To demonstrate that both the delay and ultrasensitivity are essential for pulsing we constructed minimal model variants that lack these features (Figure D.2D). As shown in Figure D.2EFG, in the absence of delay, 0F accumulates rapidly and prevents the 0A$_P$ overshoot and pulsing despite the decrease in 0A$_P$ during DNA replication. In the absence of ultrasensitivity, kinA gene copy number change during DNA replication does not change 0A$_P$ significantly and as a result, no 0A$_P$ pulse is produced.

We also used the minimal model to test the effect of the addition of a weak positive feedback from 0A$_P$ to itself (Figure D.2D). As shown in Figure D.2E, the positive feedback increases the ultrasensitivity of the dependence on 0A$_P$ on the [0F]/[KinA] ratio. As a result, the decrease in 0A$_P$ during replication and the consequent increase after replication is completed are both exaggerated relative to the minimal model that lacks the positive feedback (Figure D.2 EFG). This leads us to conclude that although positive feedback can enhance the amplitude of but is not essential for *kinA:0F* ratio dependent pulsing of 0A$_P$. This result agrees with the observations of Levine and Chastanet who have shown that substitution of the native $0A_P$ regulated P_{0A} promoter with an IPTG-inducible promoter for 0A production does not significantly affect $0A_P$ or sporulation dynamics (Chastanet et al., 2010; Levine et al., 2012).

The minimal model parameters were fixed as given are available online.

All simulations of the minimal model were done using the *ode15s* solver of MATLAB similar to the full phosphorelay model. The cell-cycle duration, Tcyc was fixed at 6hrs and DNA replication period durations, Trep were set to 2hrs.

Appendix D, in full, is a reprint of the material *Jatin Narula*, Anna Kuchina*,* ***Dong-yeon D. Lee****, Masaya Fujita, Gürol M. Süel, Oleg A. Igoshin. "Chromosomal Arrangement of Phosphorelay GenesCouples Sporulation and DNA Replication" Cell 162, 328–337. 2015 (*equal contribution).* The dissertation author performed experiments regarding translocated *kinA* strains, which were used in Figure 5.4, 5.5, and 5.8.

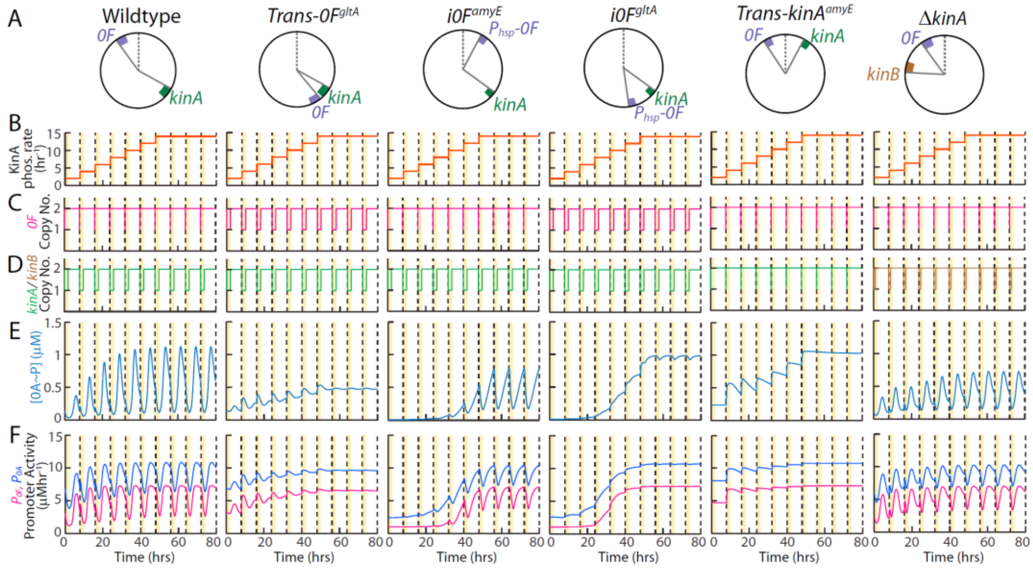

Figure D.1 Changes in *kinA* and *0F* gene dosages and KinA autophosphorylation rate was used as inputs to the mathematical model to study the response of the phosphorelay. Yellow shaded regions and dashed vertical lines in **(B)**–**(F)** represent DNA replication periods and cell divisions respectively. **(A)** Chromosomal arrangements of *0F* and *kinA* in Wild-type (WT) *B. subtilis* and mutant strains: *Trans-0F*^{gltA}, *i0F*^{amyE}, *i0F*^{gltA}, *ΔkinA*. *0F* is located close to the origin of replication in WT and *i0F*^{amyE} strains and close to the terminus in the *Trans-0F*^{gltA} and *i0F*^{gltA}. *kinA* is located close to the terminus in all strains except *Trans-kinA*^{amyE}. *kinB* is located about 60 degrees further from *oriC* than *0F*. Note that *0F* is expressed from the IPTG-inducible *Phsp* promoter, rather than the native 0A-P-regulated P_{0F} promoter in the inducible *i0F*^{amyE} and *i0F*^{gltA} strains. **(B)** KinA/KinB autophosphorylation rate was increased over multiple cell-cycles to mimic the effect of increasing starvation. **(C)** Changes in *0F* gene dosage in the WT and mutant strains. In WT, *i0F*^{amyE,} and *Trans-kinA*^{amyE}, *0F* is replicated soon after cell division due to its position close to the chromosome origin in these strains. The translocation of *0F* close to the terminus in *Trans-0F*^{gltA} and *i0F*^{gltA} strains delays its replication so that it is replicated at the end of the DNA replication period in each cell-cycle. **(D)** Changes in *kinA/kinB* gene dosage in the WT and mutant strains. *kinA* is replicated at the end of the DNA replication period due to its position close to the chromosome terminus in all strains except *Trans-kinA*^{amyE}. Translocation of *kinA* close to the origin in *Trans-kinA*^{amyE} results in *kinA* being replicated at the start of the DNA replication period in each cell-cycle. Note that *kinA* and *0F* gene dosage trajectories are identical in the *Trans-kinA*^{amyE}, *Trans-0F*^{gltA} and *i0F*^{gltA} strains. Since *kinB* is located closer to oriC than kinA it is replicated earlier. As a result, *kinB:0F* imbalance window is smaller. **(E)** Model simulation results showing the time course of 0A-P concentrations in WT and mutant strains. Note that 0A-P pulses in WT but does not pulse or increase significantly in the fluctuates in the *Trans-0F*^{gltA} mutant that lacks the transient change in kinA:0F gene dosage ratio. 0A-P does not pulse in the inducible strains *i0F*^{amyE} and *i0F*^{gltA} but it fluctuates in *i0F*^{amyE} due to the decrease in kinA:0F gene dosage ratio during DNA replication. 0A-P does not pulse in *Trans-kinA*^{amyE} that also lacks the transient change in *kinA:0F* gene dosage ratio. The pulse amplitude of 0A-P in WT and the level of 0A-P in the mutants increases with increasing KinA autophosphorylation rate (compare with experimental data from Fig. 5.4). Pulse amplitudes are reduced in the *ΔkinA* as a result of the smaller transient kinB:0F imbalance window. **(F)** Model simulation results similar to **(E)** showing the time course of P_{0A} (blue curves) and P_{0F} (pink curves) promoter activities in WT and mutant strains.

Figure D.2 Simplified Models of 0A Activation Explain the Mechanism of 0A~P Pulsing. **(A–C)** Illustration of the transient *kinA:0F* imbalance dependent mechanism of 0A~P pulsing with a minimal model of 0A activation. **(A)** Design of the minimal model of 0A activation. In the minimal model, 0A~P production is activated/inhibited by 0F depending on the KinA level which acts as the signal to the model. In addition, 0A~P activates 0F production with a delay forming an ultrasensitive delayed negative-feedback loop. Note that gene copy number variation affects only the KinA signal in Wild-type (left) and both KinA and 0F in the *Trans-0F*^{gltA} mutant. **(B)** Nullclines and dynamics of the minimal model response to DNA replication. The cyan and black lines represent the nullclines for the differential equations of [0A~P] and [0F] respectively. Blue curves show the trajectory of the minimal model response to DNA replication. Gray arrows show the derivative vector field of the minimal model. [0F] nullclines show that [0F] increases as a function of [0A~P]. [0A~P] nullclines (cyan lines) show that it decreases at high levels of [0F] similar to the results in Fig. 5.7C. Note that the [0A~P] and [0F] nullclines depend on the kinA copy number and the 0F copy number respectively. In both WT (left) and *Trans-0F*^{gltA} (right), trajectories start from the same point (red dots; *2xkinA* and *2x0F* copies). Then, during DNA replication (yellow panels), either only *kinA* copy number is reduced to 1 (WT) or both *kinA* and *0F* copy numbers are reduced to 1 (*Trans-0F*^{gltA}). These changes force the system to move toward the new steady states (green dots). Note that whereas [0F] decreases in both WT and *Trans-0F*^{gltA}, [$0A_P$] levels decrease only in WT. Once DNA replication is completed, copy numbers return to their original values, forcing the system to turn around and return to the starting point (red dots). As a result of the decrease in [$0A_P$] levels, the increase in [0F] is delayed in WT allowing [$0A_P$] to overshoot and a high level of [$0A_P$] accumulates before the increase in [0F] blocks 0A phosphorylation (black dot in WT). In contrast, increase in [0F] is not delayed in *Trans-0F*^{gltA} preventing a [$0A_P$] overshoot (black dot in *Trans-0F*^{gltA}). **(C)** Time-course representation of the trajectories in (B) showing how only WT (left) and not *Trans-0F*^{gltA} is able to produce a pulse of [$0A_P$] in response to DNA replication. **(D–G)** Identification of the design features essential for 0A~P pulsing. **(D)** Variations of the minimal model design (from left to right): WT (delayed ultrasensitive negative feedback), WT without delayed feedback, WT without ultrasensitive feedback, WT with positive feedback. **(E)** Nullclines and dynamics of the various minimal models' response to DNA replication. The cyan and black lines represent the nullclines for the differential equations of [0A~P] and [0F] respectively. Dashed and solid cyan lines represent [0A~P] nullclines for *1xkinA* and *2xkinA* respectively. Blue curves show the trajectory of the minimal model response to DNA replication. Gray arrows show the derivative vector field of the minimal model. **(F and G)** Time-course representation of the DNA replication driven KinA signal **(F)** used for running the minimal models and the 0A~P response **(G)** that results. Note that both delay and ultrasensitivity of the negative feedback are essential for pulsing. Positive feedback is not essential but enhances the 0A~P pulsing amplitude.

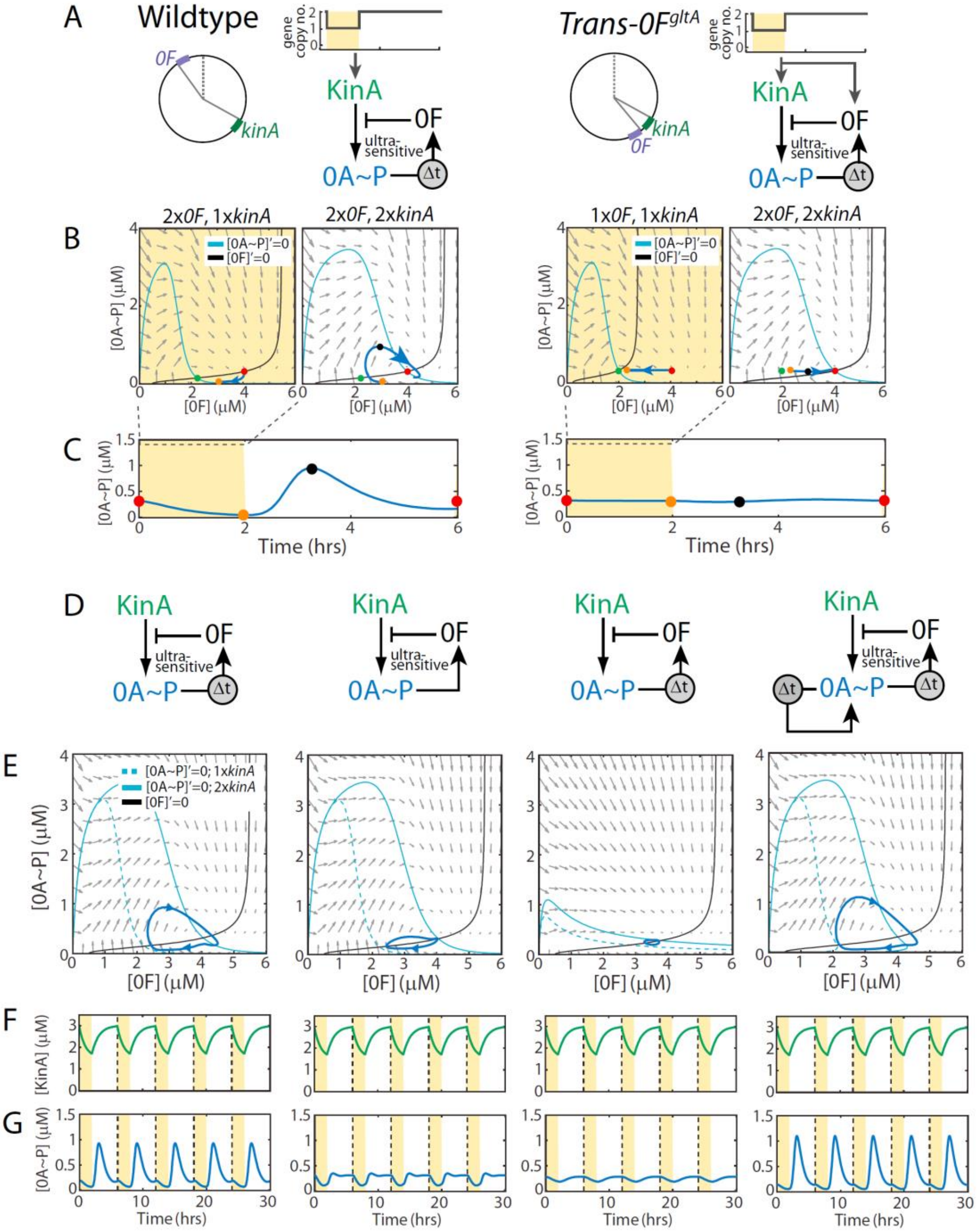
A
Wildtype
gene copy no.
2
1
0
0F
kinA
KinA
0F
ultra-sensitive
0A~P
Δt
Trans-0F^gltA
B
2x0F, 1xkinA
2x0F, 2xkinA
1x0F, 1xkinA
2x0F, 2xkinA
[0A~P]'=0
[0F]'=0
[0A~P] (μM)
[0F] (μM)
C
[0A~P] (μM)
Time (hrs)
D
KinA
0F
ultra-sensitive
0A~P
Δt
E
[0A~P]'=0; 1xkinA
[0A~P]'=0; 2xkinA
[0F]'=0
[0A~P] (μM)
[0F] (μM)
F
[KinA] (μM)
G
[0A~P] (μM)
Time (hrs)

Table D.1 Parameter values used for post-translational interactions

Parameters for Transcription/Translation is available online.

Parameter	Reaction	Description	Value
k_p	KinA → $KinA_p$	KinA auto-phosphorylation	8 hr-1
k_{dp}	$KinA_p$ → KinA	KinA dephosphorylation	2 hr^{-1}
k_b		Diffusion-limited binding rate constant	0.5 $nM^{-1}hr^{-1}$
k_i	KinA:0F → KinA+0F	KinA:0F complex dissociation	80 hr^{-1}
k_1	$KinA_p$:0F→ $KinA_p$+0F	$KinA_P$:0F complex dissociation	300 hr^{-1}
k_2	$KinA_p$:0F→ KinA+$0F_p$	0F phosphorylation	300 hr^{-1}
k_3	$0F_p$:0B→ $0F_p$+0B	$0F_P$:0B complex dissociation	500 hr^{-1}
k_4	$0F_p$:0B→ 0F+$0B_p$	0F to 0B phosphotransfer	800 hr^{-1}
k_5	$0B_p$:0A→ $0B_p$+0A	$0B_P$:0A complex dissociation	200 hr^{-1}
k_6	$0B_p$:0A→ 0B+$0A_p$	0B to 0A phosphotransfer	800 hr^{-1}
k_{ubr}	$0F_p$:Rap→ $0F_p$+Rap	$0F_P$:Rap complex dissociation	100 hr^{-1}
k_r	$0F_p$:Rap→ 0F+Rap	$0F_P$ dephosphorylation	20 hr^{-1}
k_{ube}	$0A_p$:0E→ $0A_p$+0E	$0A_P$:0E complex dissociation	100 hr^{-1}
k_e	$0A_p$:0E→ 0A+0E	$0A_P$ dephosphorylation	20 hr^{-1}

REFERENCES

Akanuma, Genki, Ako Kobayashi, Shota Suzuki, Fujio Kawamura, Yuh Shiwa, Satoru Watanabe, Hirofumi Yoshikawa, Ryo Hanai, and Morio Ishizuka. 2014. “Defect in the Formation of 70S Ribosomes Caused by Lack of Ribosomal Protein L34 Can Be Suppressed by Magnesium.” *Journal of Bacteriology* 196 (22): 3820–30. https://doi.org/10.1128/JB.01896-14.

Anyan, Morgen E., Aboutaleb Amiri, Cameron W. Harvey, Giordano Tierra, Nydia Morales-Soto, Callan M. Driscoll, Mark S. Alber, and Joshua D. Shrout. 2014. “Type IV Pili Interactions Promote Intercellular Association and Moderate Swarming of *Pseudomonas Aeruginosa*.” *Proceedings of the National Academy of Sciences* 111 (50): 18013–18. https://doi.org/10.1073/pnas.1414661111.

Appleby, Jeryl L., John S. Parkinson, and Robert B. Bourret. 1996. “Signal Transduction via the Multi-Step Phosphorelay: Not Necessarily a Road Less Traveled.” *Cell* 86 (6): 845–48. https://doi.org/10.1016/S0092-8674(00)80158-0.

Asally, Munehiro, Mark Kittisopikul, Pau Rué, Yingjie Du, Zhenxing Hu, Tolga Çağatay, Andra B Robinson, Hongbing Lu, Jordi Garcia-Ojalvo, and Gürol M Süel. 2012. “Localized Cell Death Focuses Mechanical Forces during 3D Patterning in a Biofilm.” *Proceedings of the National Academy of Sciences of the United States of America* 109 (46): 18891–96. https://doi.org/10.1073/pnas.1212429109.

Ban, Nenad, Poul Nissen, Jeffrey Hansen, Peter B. Moore, and Thomas A. Steitz. 2000. “The Complete Atomic Structure of the Large Ribosomal Subunit at 2.4 Å Resolution.” *Science* 289 (5481): 905–20. https://doi.org/10.1126/science.289.5481.905.

Belitsky, Boris R, and Abraham L Sonenshein. 1998. “Role and Regulation of Bacillus Subtilis Glutamate Dehydrogenase Genes” 180 (23): 6298–6305.

Bemer, R. 1957. “How to Consider a Computer.” *Automatic Control Magazine* March: 66–69.

Ben-Jacob, Eshel, Inon Cohen, and Herbert Levine. 2000. “Cooperative Self-Organization of Microorganisms.” *Advances in Physics* 49 (4): 395–554. https://doi.org/10.1080/000187300405228.

Berk, Veysel, Jiunn C N Fong, Graham T Dempsey, Omer N Develioglu, Xiaowei Zhuang, Jan Liphardt, Fitnat H Yildiz, and Steven Chu. 2012. “Molecular Architecture and Assembly Principles of Vibrio Cholerae Biofilms.” *Science* 337 (236): 236–39. https://doi.org/10.1126/science.1222981.

Blanc-Potard, Anne Beatrice, Nara Figueroa-Bossi, and Lionello Bossi. 1999. “Histidine Operon Deattenuation in DnaA Mutants of Salmonella Typhimurium Correlates with a Decrease in the Gene Dosage Ratio between TRNA(His) and Histidine Biosynthetic Loci.” *Journal of Bacteriology* 181 (9): 2938–41.

Blencke, Hans-Matti, Georg Homuth, Holger Ludwig, Ulrike Mäder, Michael Hecker, and Jörg Stülke. 2003. “Transcriptional Profiling of Gene Expression in Response to Glucose in Bacillus Subtilis: Regulation of the Central Metabolic Pathways.” *Metabolic Engineering* 5 (2): 133–49. https://doi.org/10.1016/S1096-7176(03)00009-0.

Block, Dena H S, Razika Hussein, Lusha W. Liang, and Han N. Lim. 2012. “Regulatory Consequences of Gene Translocation in Bacteria.” *Nucleic Acids Research* 40 (18): 8979–92. https://doi.org/10.1093/nar/gks694.

Boogerd, Fred C, Hongwu Ma, Frank J Bruggeman, Wally C van Heeswijk, Rodolfo García-Contreras, Douwe Molenaar, Klaas Krab, and Hans V Westerhoff. 2011. “AmtB-Mediated NH3 Transport in Prokaryotes Must Be Active and as a Consequence Regulation of Transport by GlnK Is Mandatory to Limit Futile Cycling of NH4(+)/NH3.” *FEBS Letters* 585 (1). Federation of European Biochemical Societies: 23–28. https://doi.org/10.1016/j.febslet.2010.11.055.

Branda, S S, J E González-Pastor, S Ben-Yehuda, R Losick, and R Kolter. 2001. “Fruiting Body Formation by Bacillus Subtilis.” *Proceedings of the National Academy of Sciences of the United States of America* 98 (20): 11621–26. https://doi.org/10.1073/pnas.191384198.

Browne, Hilary P., Samuel C. Forster, Blessing O. Anonye, Nitin Kumar, B. Anne Neville, Mark D. Stares, David Goulding, and Trevor D. Lawley. 2016. “Culturing of ‘unculturable’ Human Microbiota Reveals Novel Taxa and Extensive Sporulation.” *Nature* 533 (7604). Nature Publishing Group: 543–46. https://doi.org/10.1038/nature17645.

Bryers, James D. 2008. “Medical Biofilms.” *Biotechnology and Bioengineering* 100 (1): 1–18. https://doi.org/10.1002/bit.21838.

Burbulys, David, Kathleen A. Trach, and James A. Hoch. 1991. “Initiation of Sporulation in B. Subtilis Is Controlled by a Multicomponent Phosphorelay.” *Cell* 64 (3): 545–52. https://doi.org/10.1016/0092-8674(91)90238-T.

Cai, Long, Chiraj K. Dalal, and Michael B. Elowitz. 2008. “Frequency-Modulated Nuclear Localization Bursts Coordinate Gene Regulation.” *Nature* 455 (7212): 485–90. https://doi.org/10.1038/nature07292.

Castorph, Helga, and Diethelm Kleiner. 1984. “Some Properties of a Klebsiella Pneumoniae Ammonium Transport Negative Mutant (Amt-).” *Archives of Microbiology* 139 (2–3): 245–47. https://doi.org/10.1007/BF00402008.

Celiker, Hasan, and Jeff Gore. 2012. “Competition between Species Can Stabilize Public-Goods Cooperation within a Species.” *Molecular Systems Biology* 8 (November). https://doi.org/10.1038/msb.2012.54.

Chapman, J W, and P J Piggot. 1987. “Analysis of the Inhibition of Sporulation of *Bacillus Subtilis* Caused by Increasing the Number of Copies of the Spo0F Gene.” *Journal of General Microbiology* 133 (8): 2079–88. https://doi.org/10.1099/00221287-133-8-2079.

Chastanet, A., D. Vitkup, G.-C. Yuan, T. M. Norman, J. S. Liu, and R. M. Losick. 2010. “Broadly Heterogeneous Activation of the Master Regulator for Sporulation in Bacillus Subtilis.” *Proceedings of the National Academy of Sciences* 107 (18): 8486–91. https://doi.org/10.1073/pnas.1002499107.

Chiba, Shinobu, Anne Lamsa, and Kit Pogliano. 2009. “A Ribosome-Nascent Chain Sensor of Membrane Protein Biogenesis in Bacillus Subtilis.” *EMBO Journal* 28 (22). Nature Publishing Group: 3461–75. https://doi.org/10.1038/emboj.2009.280.

Clarkson, Joanna, Jwu Ching Shu, David A. Harris, Iain D. Campbell, and Michael D. Yudkin. 2004. “Fluorescence and Kinetic Analysis of the SpoIIAB Phosphorylation Reaction, A Key Regulator of Sporulation in Bacillus Subtilis.” *Biochemistry* 43 (11): 3120–28. https://doi.org/10.1021/bi036014+.

Cole, John a, Lars Kohler, Jamila Hedhli, and Zaida Luthey-Schulten. 2015. “Spatially-Resolved Metabolic Cooperativity within Dense Bacterial Colonies.” *BMC Systems Biology* 9 (1): 1–17. https://doi.org/10.1186/s12918-015-0155-1.

Commichau, Fabian M, Katrin Gunka, Jens J Landmann, and Jörg Stülke. 2008. “Glutamate Metabolism in Bacillus Subtilis : Gene Expression and Enzyme Activities Evolved To Avoid Futile Cycles and To Allow Rapid Responses to Perturbations of the System.” *Journal of Bacteriology* 190 (10): 3557–64. https://doi.org/10.1128/JB.00099-08.

Cong, Xiaomei, Wanli Xu, Rachael Romisher, Samantha Poveda, Shaina Forte, Angela Starkweather, and Wendy A. Henderson. 2016. “Gut Microbiome and Infant Health: Brain-Gut-Microbiota Axis and Host Genetic Factors.” *The Yale Journal of Biology and Medicine* 89 (3): 299. https://doi.org/10.12932/AP0803.

Costerton, J. W. 1999. “Bacterial Biofilms: A Common Cause of Persistent Infections.” *Science* 284 (5418): 1318–22. https://doi.org/10.1126/science.284.5418.1318.

Costerton, J. William, K.-J. Cheng, Gill G. Greesy, Timothy I. Ladd, J. Curtis Nickel, Mrinal Dasgupta, and Thomas J. Marrie. 1987. “Bacterial Biofilms in Nature and Disease.” *Ann. Rev. Microbiol.* 41: 435–64.

Davies, David. 2003. “Understanding Biofilm Resistance to Antibacterial Agents.” *Nature Reviews. Drug Discovery* 2 (2): 114–22. https://doi.org/10.1038/nrd1008.

Davies, David G., Matthew R. Parsek, James P. Pearson, Barbara H. Iglewski, J. W. Costerton, and E. P. Greenberg. 1998. “The Involvement of Cell-to-Cell Signals in the Development of a Bacterial Biofilm.” *Science* 280 (5361): 295–98. https://doi.org/10.1126/science.280.5361.295.

Davis, B D. 1987. “Mechanism of Bactericidal Action of Aminoglycosides.” *Microbiological Reviews* 51 (3): 341–50. https://doi.org/0146-0749/87/030341-10$02.00/0.

Detsch, C. 2003. “Ammonium Utilization in Bacillus Subtilis: Transport and Regulatory Functions of NrgA and NrgB.” *Microbiology* 149 (11): 3289–97. https://doi.org/10.1099/mic.0.26512-0.

Dietrich, Lars E P, Chinweike Okegbe, Alexa Price-Whelan, Hassan Sakhtah, Ryan C Hunter, and Dianne K Newman. 2013. “Bacterial Community Morphogenesis Is Intimately Linked to the Intracellular Redox State.” *Journal of Bacteriology* 195 (7): 1371–80. https://doi.org/10.1128/JB.02273-12.

Dominguez, Delfina C. 2004. “Calcium Signalling in Bacteria.” *Molecular Microbiology* 54 (2): 291–97. https://doi.org/10.1111/j.1365-2958.2004.04276.x.

Doncic, Andreas, Melody Falleur-Fettig, and Jan M. Skotheim. 2011. “Distinct Interactions Select and Maintain a Specific Cell Fate.” *Molecular Cell* 43 (4). Elsevier Inc.: 528–39. https://doi.org/10.1016/j.molcel.2011.06.025.

Donlan, Rodney M, and J William Costerton. 2002. “Biofilms: Survival Mechanisms of Clinically Relevant Microorganisms.” *Clinical Microbiology Reviews* 15 (2): 167–93. https://doi.org/10.1128/CMR.15.2.167.

Dubnau, D. 1991. “The Regulation of Genetic Competence in Bacillus Subtilis.” *Molecular Microbiology* 5 (1): 11–18. https://doi.org/10.1111/j.1365-2958.1991.tb01820.x.

Dunny, Gary M., and Bettina A. B. Leonard. 1997. “Cell-Cell Communication in Gram-Positive Bacteria.” *Annual Review of Microbiology* 51 (1): 527–64. https://doi.org/10.1146/annurev.micro.51.1.527.

Eldar, A. 2011. “Social Conflict Drives the Evolutionary Divergence of Quorum Sensing.” *Proceedings of the National Academy of Sciences* 108 (33): 13635–40. https://doi.org/10.1073/pnas.1102923108.

Errington, Jeff. 2003. “Regulation of Endospore Formation in Bacillus Subtilis.” *Nature Reviews Microbiology* 1 (2): 117–26. https://doi.org/10.1038/nrmicro750.

Errington, Jeffery. 1993. “Bacillus Subtilis Sporulation : Regulation of Gene Expression and Control of Morphogenesis.” *Microbiological Reviews* 57 (1): 1–33.

Eswaramoorthy, P., D. Duan, J. Dinh, A. Dravis, S. N. Devi, and M. Fujita. 2010. “The Threshold Level of the Sensor Histidine Kinase KinA Governs Entry into Sporulation in Bacillus Subtilis.” *Journal of Bacteriology* 192 (15): 3870–82. https://doi.org/10.1128/JB.00466-10.

Eswaramoorthy, Prahathees, Daniel Duan, Jeffrey Dinh, Ashlee Dravis, Seram Nganbiton Devi, and Masaya Fujita. 2010. “The Threshold Level of the Sensor Histidine Kinase KinA Governs Entry into Sporulation in Bacillus Subtilis.” *Journal of Bacteriology* 192 (15): 3870–82. https://doi.org/10.1128/JB.00466-10.

Ferraris, Ronaldo P., Jun-yong Choe, and Chirag R. Patel. 2018. “Intestinal Absorption of Fructose.” *Annual Review of Nutrition* 38 (4): 1–27.

Fisher, Susan H., and Abraham L Sonenshein. 1977. “Glutamine-Requiring Mutants of Bacillus Subtilis.” *Biochemical and Biophysical Research Communications* 79 (3): 987–95.

Freilich, Shiri, Raphy Zarecki, Omer Eilam, Ella Shtifman Segal, Christopher S. Henry, Martin Kupiec, Uri Gophna, Roded Sharan, and Eytan Ruppin. 2011. “Competitive and Cooperative Metabolic Interactions in Bacterial Communities." *Nature Communications* 2. Nature Publishing Group: 589. https://doi.org/10.1038/ncomms1597.

Friend, James, and Leslie Yeo. 2010. "Fabrication of Microfluidic Devices Using Polydimethylsiloxane." *Biomicrofluidics* 4 (2): 1–5. https://doi.org/10.1063/1.3259624.

Fujita, Masaya, and Richard Losick. 2005. "Evidence That Entry into Sporulation in Bacillus Subtilis Is Mediated by Gradual Activation of a Master Regulator." *Genes Dev.* 19: 2236–2244. https://doi.org/10.1101/gad.1335705.of.

Görlach, Agnes, Katharina Bertram, Sona Hudecova, and Olga Krizanova. 2015. "Calcium and ROS: A Mutual Interplay." *Redox Biology* 6: 260–71. https://doi.org/10.1016/j.redox.2015.08.010.

Gregor, T, K Fujimoto, N Masaki, and S Sawai. 2010. "The Onset of Collective Behavior in Social Amoeba." *Science* 328 (May): 1021–25. https://doi.org/10.1126/science.1183415.

Grimshaw, Charles E., Shaoming Huang, Conrad G. Hanstein, Mark A. Strauch, David Burbulys, Ling Wang, James A. Hoch, and John M. Whiteley. 1998. "Synergistic Kinetic Interactions between Components of the Phosphorelay Controlling Sporulation in Bacillus Subtilis." *Biochemistry* 37 (5): 1365–75. https://doi.org/10.1021/bi971917m.

Gristina, Anthony G., Cherri D. Hobgood, Lawrence X. Webb, and Quentin N. Myrvik. 1987. "Adhesive Colonization of Biomaterials and Antibiotic Resistance." *Biomaterials* 8 (6): 423–26. https://doi.org/10.1016/0142-9612(87)90077-9.

Gunka, Katrin, and Fabian M Commichau. 2012. "Control of Glutamate Homeostasis in Bacillus Subtilis: A Complex Interplay between Ammonium Assimilation, Glutamate Biosynthesis and Degradation." *Molecular Microbiology* 85 (2): 213–24. https://doi.org/10.1111/j.1365-2958.2012.08105.x.

Haima, Peter, Sierd Bron, and Gerard Venema. 1987. "The Effect of Restriction on Shotgun Cloning and Plasmid Stability in Bacillus Subtilis Marburg." *MGG Molecular & General Genetics* 209 (2): 335–42. https://doi.org/10.1007/BF00329663.

Hall-Stoodley, Luanne, J William Costerton, and Paul Stoodley. 2004. "Bacterial Biofilms: From the Natural Environment to Infectious Diseases." *Nature Reviews. Microbiology* 2 (2): 95–108. https://doi.org/10.1038/nrmicro821.

Hallatschek, Oskar, Pascal Hersen, Sharad Ramanathan, and David R Nelson. 2007. "Genetic Drift at Expanding Frontiers Promotes Gene Segregation." *Proc. Natl. Acad. Sci. USA* 104 (50): 19926–30. https://doi.org/10.1073/pnas.0710150104.

Harcombe, William R. R, William J. J Riehl, Ilija Dukovski, Brian R. R Granger, Alex Betts, Alex H. H Lang, Gracia Bonilla, et al. 2014. "Metabolic Resource Allocation in Individual Microbes Determines Ecosystem Interactions and Spatial Dynamics."

Cell Reports, April, 1–12. https://doi.org/10.1016/j.celrep.2014.03.070.

Hauser, P M, and J Errington. 1995. "Characterizaton of Cell Cycle Events during the Onset of Sporulation in Bacillus Subtilis." *J Bacteriol* 177 (14): 3923–31.

Hense, Burkhard a, Johannes Müller, Christina Kuttler, and Anton Hartmann. 2012. "Spatial Heterogeneity of Autoinducer Regulation Systems." *Sensors (Basel, Switzerland)* 12 (4): 4156–71. https://doi.org/10.3390/s120404156.

Hibbing, Michael E., Clay Fuqua, Matthew R. Parsek, and S. Brook Peterson. 2010. "Bacterial Competition: Surviving and Thriving in the Microbial Jungle." *Nature Reviews Microbiology* 8 (1): 15–25. https://doi.org/10.1038/nrmicro2259.

Higgins, Douglas, and Jonathan Dworkin. 2012. "Recent Progress in Bacillus Subtilis Sporulation." *FEMS Microbiology Reviews* 36 (1): 131–48. https://doi.org/10.1111/j.1574-6976.2011.00310.x.

Humphries, Jacqueline, Liyang Xiong, Jintao Liu, Arthur Prindle, Fang Yuan, Heidi A. Arjes, Lev Tsimring, and Gürol M. Süel. 2017. "Species-Independent Attraction to Biofilms through Electrical Signaling." *Cell* 168 (1–2): 200–209. https://doi.org/10.1016/j.cell.2016.12.014.

Igoshin, Oleg A., Rui Alves, and Michael A. Savageau. 2008. "Hysteretic and Graded Responses in Bacterial Two-Component Signal Transduction." *Molecular Microbiology* 68 (5): 1196–1215. https://doi.org/10.1111/j.1365-2958.2008.06221.x.

Igoshin, Oleg A., Chester W. Price, and Michael A. Savageau. 2006. "Signalling Network with a Bistable Hysteretic Switch Controls Developmental Activation of the ??F Transcription Factor in Bacillus Subtilis." *Molecular Microbiology* 61 (1): 165–84. https://doi.org/10.1111/j.1365-2958.2006.05212.x.

Irnov, Irnov, and Wade C Winkler. 2010. "A Regulatory RNA Required for Antitermination of Biofilm and Capsular Polysaccharide Operons in Bacillales." *Molecular Microbiology* 76 (3): 559–75. https://doi.org/10.1111/j.1365-2958.2010.07131.x.

Jarmer, Hanne, Randy Berka, Steen Knudsen, and Hans H. Saxild. 2002. "Transcriptome Analysis Documents Induced Competence of Bacillus Subtilis during Nitrogen Limiting Conditions." *FEMS Microbiology Letters* 206 (2): 197–200. https://doi.org/10.1016/S0378-1097(01)00525-0.

Jayakumar, A., I. Schulman, D. MacNeil, and E. M. Barnes. 1986. "Role of Escherichia Coli GlnALG Operon in Regulation of Ammonium Transport." *Journal of Bacteriology* 166 (1): 281–84. https://doi.org/10.1128/jb.166.1.281-284.1986.

Keiler, Kenneth C. 2015. "Mechanisms of Ribosome Rescue in Bacteria." *Nature Reviews Microbiology* 13 (5): 285–97. https://doi.org/10.1038/nrmicro3438.

Kim, Hyun J., Agnes Roux, and Abraham L. Sonenshein. 2002. "Direct and Indirect Roles of CcpA in Regulation of Bacillus Subtilis Krebs Cycle Genes." *Molecular Microbiology* 45 (1): 179–90. https://doi.org/10.1046/j.1365-2958.2002.03003.x.

Kim, Minsu, Zhongge Zhang, Hiroyuki Okano, Dalai Yan, Alexander Groisman, and

Terence Hwa. 2012. “Need-Based Activation of Ammonium Uptake in Escherichia Coli.” *Molecular Systems Biology* 8 (616). Nature Publishing Group: 616. https://doi.org/10.1038/msb.2012.46.

Klein, Daniel J, Peter B Moore, and Thomas a Steitz. 2004. “The Contribution of Metal Ions to the Structural Stability of the Large Ribosomal Subunit.” *RNA Society*, no. McCarthy 1962: 1366–79. https://doi.org/10.1261/rna.7390804.2.

Kleiner, D. 1985. “Bacterial Ammonium Transport.” *FEMS Microbiology Letters* 32 (2): 87–100. https://doi.org/10.1016/0378-1097(85)90059-X.

Klingelhoefer, Lisa, and Heinz Reichmann. 2015. “Pathogenesis of Parkinson Disease - The Gut-Brain Axis and Environmental Factors.” *Nature Reviews Neurology* 11 (11). Nature Publishing Group: 625–36. https://doi.org/10.1038/nrneurol.2015.197.

Klumpp, Stefan, Zhongge Zhang, and Terence Hwa. 2009. “Growth Rate-Dependent Global Effects on Gene Expression in Bacteria.” *Cell* 139 (7). Elsevier Ltd: 1366–75. https://doi.org/10.1016/j.cell.2009.12.001.

Kobayashi, Kazuo. 2007. “Gradual Activation of the Response Regulator DegU Controls Serial Expression of Genes for Flagellum Formation and Biofilm Formation in Bacillus Subtilis.” *Molecular Microbiology* 66 (2): 395–409. https://doi.org/10.1111/j.1365-2958.2007.05923.x.

Kohanski, Michael a, Daniel J Dwyer, Jamey Wierzbowski, Guillaume Cottarel, and James J Collins. 2008. “Mistranslation of Membrane Proteins and Two-Component System Activation Trigger Antibiotic-Mediated Cell Death.” *Cell* 135 (4). Elsevier Inc.: 679–90. https://doi.org/10.1016/j.cell.2008.09.038.

Kragh, Kasper N., Jaime B. Hutchison, Gavin Melaugh, Chris Rodesney, Aled E. L. Roberts, Yasuhiko Irie, Peter Ø Jensen, et al. 2016. “Role of Multicellular Aggregates in Biofilm Formation.” *MBio* 7 (2): e00237-16. https://doi.org/10.1128/mBio.00237-16.

Kralj, Jm, Dr Hochbaum, Ad Douglass, and Ae Cohen. 2011. “Electrical Spiking in Escherichia Coli Probed with a Fluorescent Voltage-Indicating Protein.” *Science* 333 (July): 345–48. https://doi.org/10.1126/science.1204763.

Kuchina, Anna, Lorena Espinar, Tolga Çağatay, Alejandro O Balbin, Fang Zhang, Alma Alvarado, Jordi Garcia-Ojalvo, and Gürol M Süel. 2011. “Temporal Competition between Differentiation Programs Determines Cell Fate Choice.” *Molecular Systems Biology* 7 (557): 557. https://doi.org/10.1038/msb.2011.88.

Kuchina, Anna, Lorena Espinar, Jordi Garcia-Ojalvo, and Gürol M Süel. 2011. “Reversible and Noisy Progression towards a Commitment Point Enables Adaptable and Reliable Cellular Decision-Making.” *PLoS Computational Biology* 7 (11): e1002273. https://doi.org/10.1371/journal.pcbi.1002273.

Kurland, C. G. 1960. “Molecular Characterization of Ribonucleic Acid from Escherichia Coli Ribosomes: I. Isolation and Molecular Weights.” *Journal of Molecular Biology* 2 (2). Academic Press Inc. (London) Ltd.: 83–91. https://doi.org/10.1016/S0022-

2836(60)80029-0.

Landecker, Hannah. 2009. “Seeing Things : From Microcinematography to Live Cell Imaging.” *Nature Methods* 6 (10). Nature Publishing Group: 707–9. https://doi.org/10.1038/nmeth1009-707.

Lane, N. 2015. “The Unseen World: Reflections on Leeuwenhoek (1677) ‘Concerning Little Animals.’” *Philosophical Transactions of the Royal Society B: Biological Sciences* 370 (1666): 20140344–20140344. https://doi.org/10.1098/rstb.2014.0344.

LeDeaux, John R., Namyi Yu, and Alan D Grossman. 1995. “Different Roles for KinA , KinB , and KinC in the Initiation of Sporulation in Bacillus Subtilis . Different Roles for KinA , KinB , and KinC in the Initiation of Sporulation in Bacillus Subtilis” 177 (3): 861–63. https://doi.org/10.1128/jb.177.3.861-863.1995.

Levine, Joe H, Michelle E Fontes, Jonathan Dworkin, and Michael B Elowitz. 2012. “Pulsed Feedback Defers Cellular Differentiation.” *PLoS Biology* 10 (1): e1001252. https://doi.org/10.1371/journal.pbio.1001252.

Liu, Jintao, Rosa Martinez-Corral, Arthur Prindle, Dong-yeon D. Lee, Joseph Larkin, Marçal Gabalda-Sagarra, Jordi Garcia-Ojalvo, and Gürol M. Süel. 2017. “Coupling between Distant Biofilms and Emergence of Nutrient Time-Sharing.” *Science* 356 (6338): 638–42. https://doi.org/10.1126/science.aah4204.

Liu, Jintao, Arthur Prindle, Jacqueline Humphries, Marcal Gabalda-Sagarra, Munehiro Asally, Dong-yeon D. Lee, San Ly, Jordi Garcia-Ojalvo, and Gürol M. Süel. 2015. “Metabolic Codependence Gives Rise to Collective Oscillations within Microbial Communities.” *Nature* 523 (7562): 550–54. https://doi.org/doi:10.1038/nature14660.

López, Daniel, and Roberto Kolter. 2010. “Extracellular Signals That Define Distinct and Coexisting Cell Fates in Bacillus Subtilis.” *FEMS Microbiology Reviews* 34 (2): 134–49. https://doi.org/10.1111/j.1574-6976.2009.00199.x.

Ma, Wenzhe, Ala Trusina, Hana El-samad, Wendell a Lim, and Chao Tang. 2009. “Defining Network Topologies That Can Achieve Biochemical Adaptation.” *Cell* 138 (4). Elsevier Ltd: 760–73. https://doi.org/10.1016/j.cell.2009.06.013.

Mather, William, Octavio Mondragón-Palomino, Tal Danino, Jeff Hasty, and Lev S. Tsimring. 2010. “Streaming Instability in Growing Cell Populations.” *Physical Review Letters* 104 (20): 208101. https://doi.org/10.1103/PhysRevLett.104.208101.

Megason, Sean G., and Scott E. Fraser. 2007. “Imaging in Systems Biology.” *Cell* 130 (5): 784–95. https://doi.org/10.1016/j.cell.2007.08.031.

Michael, W M. 2001. “Cell Cycle: Connecting DNA Replication to Sporulation in Bacillus.” *Current Biology : CB* 11 (11): R443-5. http://www.ncbi.nlm.nih.gov/pubmed/11516668.

Middleton, Rebecca, and Antje Hofmeister. 2004. “New Shuttle Vectors for Ectopic Insertion of Genes into Bacillus Subtilis.” *Plasmid* 51 (3): 238–45. https://doi.org/10.1016/j.plasmid.2004.01.006.

Milo, Ron, Paul Jorgensen, Uri Moran, Griffin Weber, and Michael Springer. 2010. "BioNumbers The Database of Key Numbers in Molecular and Cell Biology." *Nucleic Acids Research* 38 (suppl 1): D750–53. https://doi.org/10.1093/nar/gkp889.

Morikawa, Masaaki. 2006. "Beneficial Biofilm Formation by Industrial Bacteria Bacillus Subtilis and Related Species." *Journal of Bioscience and Bioengineering* 101 (1): 1–8. https://doi.org/10.1263/jbb.101.1.

Nadell, Carey D., Knut Drescher, and Kevin R. Foster. 2016. "Spatial Structure, Cooperation and Competition in Biofilms." *Nature Reviews Microbiology* 14 (9): 589–600. https://doi.org/10.1038/nrmicro.2016.84.

Nakano, M M, F Yang, P Hardin, and P Zuber. 1995. "Nitrogen Regulation of NasA and the NasB Operon, Which Encode Genes Required for Nitrate Assimilation in Bacillus Subtilis." *Journal of Bacteriology* 177 (3): 573–79. http://jb.asm.org/content/177/3/573.long.

Narula, Jatin, Seram N Devi, Masaya Fujita, and Oleg a Igoshin. 2012. "Ultrasensitivity of the Bacillus Subtilis Sporulation Decision." *Proceedings of the National Academy of Sciences of the United States of America* 109 (50): E3513-22. https://doi.org/10.1073/pnas.1213974109.

Newsholme, P, M M R Lima, J Procopio, T C Pithon-Curi, S Q Doi, R B Bazotte, and R Curi. 2003. "Glutamine and Glutamate as Vital Metabolites." *Brazilian Journal of Medical and Biological Research = Revista Brasileira de Pesquisas Médicas e Biológicas / Sociedade Brasileira de Biofísica ... [et Al.]* 36 (2): 153–63. http://www.ncbi.nlm.nih.gov/pubmed/12563517.

Nickel, J C, I Ruseska, J B Wright, and J W Costerton. 1985. "Tobramycin Resistance of Cells of Pseudomonas Aeruginosa Growing as Biofilm on Urinary Catheter Material." *Antimicrob Agents Chemother* 27 (4): 619–24. https://doi.org/10.1128/AAC.27.4.619.

Nijland, Reindert, and J Grant Burgess. 2010. "Bacterial Olfaction." *Biotechnology Journal* 5 (9): 974–77. https://doi.org/10.1002/biot.201000174.

Oliveira, Nuno M., Rene Niehus, and Kevin R. Foster. 2014. "Evolutionary Limits to Cooperation in Microbial Communities." *Proceedings of the National Academy of Sciences* 111 (50): 17941–46. https://doi.org/10.1073/pnas.1412673111.

Palková, Z, B Janderová, J Gabriel, B Zikánová, M Pospísek, and J Forstová. 1997. "Ammonia Mediates Communication between Yeast Colonies." *Nature* 390 (6659): 532–36. https://doi.org/10.1038/37398.

Palková, Zdena, and Libuse Vachova. 2003. "Ammonia Signaling in Yeast Colony Formation." *International Review of Cytology* 225 (January): 229–72. http://www.ncbi.nlm.nih.gov/pubmed/12696594.

Parsek, Matthew R, and Pradeep K. Singh. 2003. "Bacterial Biofilms: An Emerging Link to Disease Pathogenesis." *Annual Review of Microbiology* 57: 677–701. https://doi.org/10.1146/annurev.micro.57.030502.090720.

Perego, M., C. F. Higgins, S. R. Pearce, M. P. Gallagher, and J. a. Hoch. 1991. “The Oligopeptide Transport System of Bacillus Subtilis Plays a Role in the Initiation of Sporulation.” *Molecular Microbiology* 5 (1): 173–85. https://doi.org/10.1111/j.1365-2958.1991.tb01838.x.

Perego, M, S P Cole, D Burbulys, K Trach, and J A Hoch. 1989. “Characterization of the Gene for a Protein-Kinase Which Phosphorylates the Sporulation-Regulatory Proteins Spo0a and Spo0f of Bacillus-Subtilis.” *Journal Of Bacteriology* 171 (11): 6187–96.

Persat, Alexandre, Carey D. Nadell, Minyoung Kevin Kim, Francois Ingremeau, Albert Siryaporn, Knut Drescher, Ned S. Wingreen, Bonnie L. Bassler, Zemer Gitai, and Howard A. Stone. 2015. “The Mechanical World of Bacteria.” *Cell* 161 (5). Elsevier Inc.: 988–97. https://doi.org/10.1016/j.cell.2015.05.005.

Pontes, Mauricio H., Anastasia Sevostyanova, and Eduardo A. Groisman. 2015. “When Too Much ATP Is Bad for Protein Synthesis.” *Journal of Molecular Biology* 427 (16). Elsevier B.V.: 2586–94. https://doi.org/10.1016/j.jmb.2015.06.021.

Prindle, Arthur, Jintao Liu, Munehiro Asally, San Ly, Jordi Garcia-Ojalvo, and Gürol M. Süel. 2015. “Ion Channels Enable Electrical Communication in Bacterial Communities.” *Nature* 527 (7576): 59–63. https://doi.org/10.1038/nature15709.

Rani, Suriani Abdul, Betsey Pitts, Haluk Beyenal, Raaja Angathevar Veluchamy, Zbigniew Lewandowski, William M. Davison, Kelli Buckingham-Meyer, and Philip S Stewart. 2007. “Spatial Patterns of DNA Replication, Protein Synthesis, and Oxygen Concentration within Bacterial Biofilms Reveal Diverse Physiological States.” *Journal of Bacteriology* 189 (11): 4223–33. https://doi.org/10.1128/JB.00107-07.

Rasmussen, Howard, Pamela Jensen, William Lake, and David B.P. Goodman. 1976. “Calcium Ion as Second Messenger.” *Clinical Endocrinology* 5: 11–27.

Ridaura, Vanessa, and Yasmine Belkaid. 2015. “Gut Microbiota: The Link to Your Second Brain.” *Cell* 161 (2). Elsevier Inc.: 193–94. https://doi.org/10.1016/j.cell.2015.03.033.

Riddell, John Leonard. 1854. “On the Binocular Microscope.” *Q J Microsc Sci.* 2: 18–24.

Romani, Andrea M.P. 2011. “Cellular Magnesium Homeostasis.” *Archives of Biochemistry and Biophysics* 512 (1). Elsevier Inc.: 1–23. https://doi.org/10.1016/j.pestbp.2011.02.012.Investigations.

Schindler, J, and M Sussman. 1977. “Ammonia Determines the Choice of Morphogenetic Pathways in Dictyostelium Discoideum.” *Journal of Molecular Biology* 116 (1): 161–69. https://doi.org/10.1016/0022-2836(77)90124-3.

Schultz, Daniel, Peter G Wolynes, Eshel Ben Jacob, and José N Onuchic. 2009. “Deciding Fate in Adverse Times: Sporulation and Competence in Bacillus Subtilis.” *Proceedings of the National Academy of Sciences of the United States of America* 106 (50): 21027–34. https://doi.org/10.1073/pnas.0912185106.

Schuwirth, Barbara S., Maria A. Borovinskaya, Cathy W. Hau, Wen Zhang, Anton Vila-Sanjurjo, James M. Holton, and Jamie H. Doudna Cate. 2005. “Structures of the Bacterial Ribosome at 3.5Å Resolution.” *Science* 310: 827–34.

Scott, Matthew, Eduard M Mateescu, Zhongge Zhang, and Terence Hwa. 2010. “Interdependence of Cell Growth Origins and Consequences.” *Science* 330 (November).

Sen, Shaunak, Jordi Garcia-Ojalvo, and Michael B. Elowitz. 2011. “Dynamical Consequences of Bandpass Feedback Loops in a Bacterial Phosphorelay.” *PLoS ONE* 6 (9). https://doi.org/10.1371/journal.pone.0025102.

Shapiro, James A. 1998. “Thinking About Bacterial Populations as Multicellular Organisms.” *Annual Review of Microbiology* 52 (1): 81–104. https://doi.org/10.1146/annurev.micro.52.1.81.

Sharpe, Michaela E, Philippe M Hauser, Robert G Sharpe, Michaela E Sharpe, Philippe M Hauser, and Robert G Sharpe. 1998. “Bacillus Subtilis Cell Cycle as Studied by Fluorescence Microscopy : Constancy of Cell Length at Initiation of DNA Replication and Evidence for Active Nucleoid Partitioning Bacillus Subtilis Cell Cycle as Studied by Fluorescence Microscopy : Constancy Of.” *Journal of Bacteriology* 180 (3): 547–55.

Singleton, C. K., J. H. Kirsten, and C. J. Dinsmore. 2006. “Function of Ammonium Transporter A in the Initiation of Culmination of Development in Dictyostelium Discoideum.” *Eukaryotic Cell* 5 (7): 991–96. https://doi.org/10.1128/EC.00058-06.

Slager, Jelle, Morten Kjos, Laetitia Attaiech, and Jan Willem Veening. 2014. “Antibiotic-Induced Replication Stress Triggers Bacterial Competence by Increasing Gene Dosage near the Origin.” *Cell* 157 (2). Elsevier Inc.: 395–406. https://doi.org/10.1016/j.cell.2014.01.068.

Stannek, Lorena, Martin J. Thiele, Till Ischebeck, Katrin Gunka, Elke Hammer, Uwe Völker, and Fabian M. Commichau. 2015. “Evidence for Synergistic Control of Glutamate Biosynthesis by Glutamate Dehydrogenases and Glutamate in *B Acillus Subtilis*.” *Environmental Microbiology*, n/a-n/a. https://doi.org/10.1111/1462-2920.12813.

Stewart, Philip S, and Michael J Franklin. 2008. “Physiological Heterogeneity in Biofilms.” *Nature Reviews. Microbiology* 6 (3): 199–210. https://doi.org/10.1038/nrmicro1838.

Stoodley, P, K Sauer, D G Davies, and J W Costerton. 2002. “Biofilms as Complex Differentiated Communities.” *Annual Review of Microbiology* 56 (January): 187–209. https://doi.org/10.1146/annurev.micro.56.012302.160705.

Strachey, C. 1959. “Time Sharing in Large Fast Computers.” *Proc. Intl. Conf. on Information Processing* June: 336–41.

Su’etsugu, Masayuki, and Jeff Errington. 2011. “The Replicase Sliding Clamp Dynamically Accumulates behind Progressing Replication Forks in Bacillus Subtilis

Cells." *Molecular Cell* 41 (6). Elsevier Inc.: 720–32. https://doi.org/10.1016/j.molcel.2011.02.024.

Süel, Gürol M, Jordi Garcia-Ojalvo, Louisa M Liberman, and Michael B Elowitz. 2006. "An Excitable Gene Regulatory Circuit Induces Transient Cellular Differentiation." *Nature* 440 (23): 545–50. https://doi.org/10.1038/nature04588.

Tempest, D W, J L Meers, and C M Brown. 1970. "Influence of Environment on the Content and Composition of Microbial Free Amino Acid Pools." *Journal of General Microbiology* 64 (2): 171–85. http://www.ncbi.nlm.nih.gov/pubmed/4995906.

Toettcher, Jared E, Alexander Loewer, Gerard J Ostheimer, Michael B Yaffe, and Bruce Tidor. 2009. "Distinct Mechanisms Act in Concert to Mediate Cell Cycle Arrest." *Pnas* 106 (3): 785–90. https://doi.org/10.1073/pnas.0806196106.

Veening, Jan-Willem, Eric J Stewart, Thomas W Berngruber, François Taddei, Oscar P Kuipers, and Leendert W Hamoen. 2008. "Bet-Hedging and Epigenetic Inheritance in Bacterial Cell Development." *Proceedings of the National Academy of Sciences of the United States of America* 105 (11): 4393–98. https://doi.org/10.1073/pnas.0700463105.

Veening, Jw, Heath Murray, and Jeff Errington. 2009. "A Mechanism for Cell Cycle Regulation of Sporulation Initiation in Bacillus Subtilis." *Genes & Development*, 1959–70. https://doi.org/10.1101/gad.528209.tation.

Vlamakis, Hera, Claudio Aguilar, Richard Losick, and Roberto Kolter. 2008. "Control of Cell Fate by the Formation of an Architecturally Complex Bacterial Community." *Genes and Development* 22 (7): 945–53. https://doi.org/10.1101/gad.1645008.

Vlamakis, Hera, Yunrong Chai, Pascale Beauregard, Richard Losick, and Roberto Kolter. 2013. "Sticking Together: Building a Biofilm the Bacillus Subtilis Way." *Nature Reviews. Microbiology*, no. January (January). Nature Publishing Group. https://doi.org/10.1038/nrmicro2960.

Volfson, Dmitri, Scott Cookson, Jeff Hasty, and Lev S Tsimring. 2008. "Biomechanical Ordering of Dense Cell Populations." *Proceedings of the National Academy of Sciences of the United States of America* 105 (40): 15346–51. https://doi.org/10.1073/pnas.0706805105.

Wang, Jue D., and Petra A. Levin. 2009. "Metabolism, Cell Growth and the Bacterial Cell Cycle." *Nature Reviews Microbiology* 7 (11). Nature Publishing Group: 822–27. https://doi.org/10.1038/nrmicro2202.

Wang, Ling, Roberto Grau, Marta Perego, and James a. Hoch. 1997. "A Novel Histidine Kinase Inhibitor Regulating Development in Bacillus Subtilis." *Genes and Development* 11 (19): 2569–79. https://doi.org/10.1101/gad.11.19.2569.

Wang, Zeneng, and Yongzhong Zhao. 2018. "Gut Microbiota in Cardiovascular Health and Disease." *Protein Cell*, March. Higher Education Press. https://doi.org/https://doi.org/10.1007/s13238-018-0549-0.

Waters, Christopher M., and Bonnie L. Bassler. 2005. "QUORUM SENSING: Cell-to-

Cell Communication in Bacteria." *Annual Review of Cell and Developmental Biology* 21 (1): 319–46. https://doi.org/10.1146/annurev.cellbio.21.012704.131001.

Wilking, James N, Vasily Zaburdaev, Michael De Volder, Richard Losick, Michael P Brenner, and David A Weitz. 2013. "Liquid Transport Facilitated by Channels in Bacillus Subtilis Biofilms." *Proceedings of the National Academy of Sciences* 110 (3): 848–52.

Wingreen, Ned S., and Simon A. Levin. 2006. "Cooperation among Microorganisms." *PLoS Biology* 4 (9): 1486–88. https://doi.org/10.1371/journal.pbio.0040299.

Wray, L V, J M Zalieckas, and S H Fisher. 2001. "Bacillus Subtilis Glutamine Synthetase Controls Gene Expression through a Protein-Protein Interaction with Transcription Factor TnrA." *Cell* 107 (4): 427–35. https://doi.org/10.1016/S0092-8674(01)00572-4.

Wray, Lewis V., Amy E. Ferson, Kelllie Rohrer, and Susan H. Fisher. 1996. "TnrA, a Transcription Factor Required for Global Nitrogen Regulation in Bacillus Subtilis." *Proceedings of the National Academy of Sciences of the United States of America* 93 (17): 8841–45. http://www.pnas.org/content/93/17/8841.long.

Wray, Lewis V, and Susan H Fisher. 2005. "A Feedback-Resistant Mutant of Bacillus Subtilis Glutamine Synthetase with Pleiotropic Defects in Nitrogen-Regulated Gene Expression." *The Journal of Biological Chemistry* 280 (39): 33298–304. https://doi.org/10.1074/jbc.M504957200.

Wu, Shih Cheng, Zih Syuan Cao, Kuo Ming Chang, and Jyh Lyh Juang. 2017. "Intestinal Microbial Dysbiosis Aggravates the Progression of Alzheimer's Disease in Drosophila." *Nature Communications* 8 (1). Springer US: 1–8. https://doi.org/10.1038/s41467-017-00040-6.

Xavier, Joao B., and Kevin R. Foster. 2007. "Cooperation and Conflict in Microbial Biofilms." *Proceedings of the National Academy of Sciences* 104 (3): 876–81. https://doi.org/10.1073/pnas.0607651104.

Yamamoto, Tatsuya, Yoshihiro Shimizu, Takuya Ueda, and Yoshitsugu Shiro. 2010. "Mg $^{2+}$ Dependence of 70 S Ribosomal Protein Flexibility Revealed by Hydrogen/Deuterium Exchange and Mass Spectrometry." *Journal of Biological Chemistry* 285 (8): 5646–52. https://doi.org/10.1074/jbc.M109.081836.

Yasumura, Ayako, Sadanobu Abe, and Teruo Tanaka. 2008. "Involvement of Nitrogen Regulation in Bacillus Subtilis DegU Expression." *Journal of Bacteriology* 190 (15): 5162–71. https://doi.org/10.1128/JB.00368-08.

Yildiz, Fitnat H., and Karen L. Visick. 2009. "Vibrio Biofilms: So Much the Same yet so Different." *Trends in Microbiology* 17 (3): 109–18. https://doi.org/10.1016/j.tim.2008.12.004.

Yoshida, Ken-ichi, Hirotake Yamaguchi, Masaki Kinehara, Yo-hei Ohki, Yoshiko Nakaura, and Yasutaro Fujita. 2003. "Identification of Additional TnrA-Regulated Genes of Bacillus Subtilis Associated with a TnrA Box." *Molecular Microbiology*

49 (1): 157–65. https://doi.org/10.1046/j.1365-2958.2003.03567.x.

Zeigler, Daniel R., Zoltán Prágai, Sabrina Rodriguez, Bastien Chevreux, Andrea Muffler, Thomas Albert, Renyuan Bai, Markus Wyss, and John B. Perkins. 2008. “The Origins of 168, W23, and Other Bacillus Subtilis Legacy Strains.” *Journal of Bacteriology* 190 (21): 6983–95. https://doi.org/10.1128/JB.00722-08.

Zhang, Wenbo, Agnese Seminara, Melanie Suaris, Michael P Brenner, David a Weitz, and Thomas E Angelini. 2014. “Nutrient Depletion in Bacillus Subtilis Biofilms Triggers Matrix Production.” *New Journal of Physics* 16 (1): 015028. https://doi.org/10.1088/1367-2630/16/1/015028.

Zhu, Xiqun, Yong Han, Jing Du, Renzhong Liu, Ketao Jin, and Wei Yi. 2017. “Microbiota-Gut-Brain Axis and the Central Nervous System.” *Oncotarget* 8 (32): 53829–38. https://doi.org/10.18632/oncotarget.17754.